



# **Microstructure and mechanical properties of tin-based alloys for miniature detonating cords**

A thesis submitted for the degree of

Doctor of Philosophy

By

**Guangyu Liu**

Department of Mechanical, Aerospace and Civil Engineering

College of Engineering, Design and Physical Sciences

Brunel University London

Uxbridge, UB8 3PH

United Kingdom

March 2019

Supervision: Dr. Shouxun Ji

Prof. Zhongyun Fan

## Abstract

Miniature detonating cord (MDC), a typical linear explosive device, is primarily used in aircraft canopy severance systems. MDCs are typically flexible cylindrical cords with an explosive core and a robust sheath/cladding material. In practical applications, upon detonation, the MDC which is bonded to the inside of canopy propels the sheath outward at a high velocity, thereby penetrating or shattering the canopy transparency to clear an escape path. Conventionally, the materials for explosive core are pentaerythritol tetranitrate (PETN), cyclotrimethylenetrinitramine (RDX), cyclotetr-amethylenetetranitramine (HMX), or hexanitrostilbene (HNS).

For decades, the sheath materials of MDCs were made by antimonial or non-antimonial lead, due to high density, good ductility, and relative ease of manufacturing. However, owing to the environmental and human health concerns regarding lead poisoning and the increasingly strict requirement in environmental legislations, the replacement of lead has been compulsory for recent development of new generation metallic sheath materials for MDCs in aerospace industry. The present study aims to study the feasibility and reliability of developing a cost-effective and easy-manufacturing lead-free tin-based alloy, which is suitable as the sheath materials of MDCs for the clearance of aircraft canopies.

The materials requirement was analysed and Sn-Cu based alloys were firstly chosen as potential candidates. The Sn-Cu alloys (0.3-1.0wt.%Cu) were prepared by casting and rolling. Microstructures of as-cast Sn-Cu alloys comprised Sn solutions with  $\text{Cu}_6\text{Sn}_5$  intermetallic phase in the matrix. The as-rolled hypoeutectic Sn-Cu alloys (0.3-0.5wt.%Cu) offered the yield strength from 26.1 to 31.9 MPa, UTS from 30.1 to 34 MPa and elongation from 86.4 to 87.5%, which were found to be appropriate for the sheath. Particularly, the Sn-Cu alloys exhibited nonwork-hardening phenomenon under tensile stress, which could benefit sheath manufacturing and subsequent processing after assembly with high-energy explosive materials.

Another achievement is understanding the deformation mechanisms and microstructure characteristics of the Sn-Cu alloy under rolling, which involves boundary formation, dynamic restoration, twinning, and recrystallization texture. A bimodal grain structure was well established after rolling, ascribed to the dislocation activities and dynamic restorations including dynamic recovery (DRV) and dynamic recrystallization (DRX). The  $\text{Cu}_6\text{Sn}_5$  particle-

stimulated nucleation (PSN) was found as the major mechanism of DRX, which was also the dominant cause of forming of  $\langle 001 \rangle // RD$  oriented nuclei. Additionally, DRX nuclei are formed along the existing boundaries, resulting in a necklace structure via continuous dynamic recrystallization (CDRX).  $\{301\}$  and  $\{101\}$  twins were identified as additional significant microstructure features.

Due to the microstructural inhomogeneity of Sn-Cu alloys subjected to rolling, alternative tin alloys were also developed for applications. The assessment of the mechanical properties of Sn-3Zn- $x$ Bi (Bi: 0-5wt.%) alloys processed by rolling were undertaken to explore their feasibility as sheath materials. Effects of Bi on the microstructure and mechanical properties of Sn-Zn were studied. Bi significantly refined the as-cast microstructure, altering the configuration of Sn-Zn eutectic from well-aligned Zn-rich needles to misaligned Zn-rich flakes. After deformation, secondary phases such as Zn-rich precipitates and Bi particles, and Bi solutes were critical to grain refinement because these secondary phase particles provided more sites for nucleation and more obstacles to growth of new recrystallized grains. Tensile results confirmed that Bi addition enhanced both strength and ductility of the rolled Sn-Zn-Bi alloys. The Sn-3Zn-5Bi alloy possessed superior strength and ductility (UTS: 84.4 MPa; Yield strength: 68.3 MPa; Elongation: 75.2%) due to its finest and most homogeneous equiaxed grains.

The corrosion properties of Sn-3Zn- $x$ Bi ( $x=0, 1, 3, 5, 7$  wt.%) alloys were investigated to explore the effect of Bi on the corrosion performance of the Sn-Zn alloy. Results indicated that the addition of 1 wt.% Bi increased the corrosion susceptibility of the Sn-3Zn alloy, mainly attributed to the coarsened and more uniformly distributed corrosion-vulnerable Zn-rich precipitates, while further increasing the Bi contents decreased the corrosion susceptibility of Sn-3Zn- $x$ Bi alloys due to the higher fraction of nobler Bi particles serving as anodic barriers. The Sn-3Zn-7Bi possessed the best corrosion resistance among all tested alloys. The role of Bi on the corrosion properties was considerably discussed.

Finally, numerical performance simulations and proof tests were conducted using Ansys AUTODYN-2D to verify the reliability of the tin alloys for the cord sheaths. The cut depths of the cords sheathed by varied metals/alloys incorporating Pb, Pb-Sb, Sn, Sn-Cu, Sn-Zn-Bi, Al, Cu, and Ta were attained. Simulation results indicated that newly developed tin sheathed cords showed similar cut depths compared with lead. Proof firings demonstrated that the Sn-Zn-Bi

sheathed cords fulfilled the requirement of cut depths against acrylic and aluminium targets, confirming the successful development of Sn-Zn-Bi for the MDCs in the specific application.

**Key words:** Miniature detonating cords; Tin-based alloys; Microstructure; Mechanical properties; Corrosion; Simulation

## **Acknowledgment**

I would like to acknowledge a great debt to Dr. Shouxun Ji and Prof. Zhongyun Fan for offering me such a wonderful opportunity to pursue my PhD at BCAST, Brunel University London. Their continuous support and guidance helped me throughout the whole PhD journey from start to finish of the research.

I express my sincere gratitude to Dr. Yan Huang and Dr. Xinliang Yang for the supportive guidance on EBSD operation and data analysis using OIM. Dr. Sajjad Amirkhanlou is greatly thanked for providing valuable suggestions on microstructural characterization of Sn-Zn-Bi alloys processed by rolling. I am very grateful to Dr. Shohreh Khorsand for supportive guidance on electrochemical measurements and on knowledge of corrosion. I thank Dr. Feng Gao for the support on Pandat modelling. Dr. David Holland (Fluid Gravity Engineering Ltd) is sincerely appreciated for his help in numerical simulations. Special thanks are due to Yaqiong Wang (Queen Mary University) for providing instruments and helping conduct EIS tests.

I am grateful to Steve Cook, Jon Gadd, Peter Lloyd, Graham Mitchell, and Samantha Melvin who offered support in BCAST laboratories. I thank ETC staff, Dr. Ashley Hawkins, Dr Lorna Anguilano, Dr. Nico Nelson, and Nita Varma for the assistance in using characterization facilities. Besides, my sincere thanks to my friendly colleagues Dr. Yijie Zhang, Dr. Xixi Dong, Dr. Xiangzhen Zhu, Dr. Feng Wang, Shihao Wang, Jiao Fang, Qing Cai for their support and help during experimental work and research.

Most importantly, I would very much like to acknowledge my loving parents, without their support and love none of this work would be possible.

# Table of Contents

Abstract.....	i
Acknowledgment .....	iv
Table of Contents.....	v
Symbols.....	ix
Abbreviations.....	xi
List of Publications .....	xiii
Chapter 1 Introduction .....	1
1.1 Background and Motivation .....	1
1.2 Research Objectives.....	3
1.3 Thesis Outline .....	3
Chapter 2 Literature Review .....	6
2.1 Linear Detonating and Explosive Device .....	6
2.1.1 Terminology.....	6
2.1.2 Classification and Application.....	7
2.2 Miniature Detonating Cords .....	13
2.2.1 Configuration .....	13
2.2.2 Manufacturing Routes.....	14
2.3 Penetration and Cutting Process of Explosive Charges.....	16
2.3.1 Penetration Process of Shaped Charges .....	16
2.3.2 Cutting Process of Linear Shaped Charges.....	18
2.3.3 Factors Influencing the Cutting Performance .....	21
2.4 Importance of Sheath .....	24
2.4.1 Density of Sheath Materials.....	26
2.4.2 Ductility of Sheath Materials .....	27
2.5 Selection and Criteria of Sheath Materials .....	28
2.5.1 Materials for Shaped Charge Liners .....	28
2.5.2 Tin Alloys for the Sheath Materials of Linear Explosive Cords .....	29
2.5.3 Selection Criteria .....	32
Chapter 3 Methodology .....	34
3.1 Materials Preparation .....	34

3.1.1 Alloy Casting .....	34
3.1.2 Alloy Processing .....	35
3.2 Microstructure Characterization .....	36
3.2.1 Metallographic Surface Preparation .....	36
3.2.2 Optical Microscopy.....	37
3.2.3 Electron Microscopy .....	38
3.2.4 X-Ray Diffraction .....	39
3.3 Mechanical Property Measurements.....	40
3.3.1 Tensile Tests .....	40
3.3.2 Vickers Harness .....	41
3.4 Electrochemical Measurements .....	41
3.4.1 Potentiodynamic Polarization .....	41
3.4.2 Electrochemical Impedance Spectroscopy .....	42
3.5 Numerical Simulation and Proof Test.....	42
Chapter 4 Microstructure and Mechanical Properties of Sn-Cu Alloys for Miniature Detonating Cords.....	43
4.1 Introduction.....	43
4.2 Microstructure and Hardness of As-cast Sn-Cu Alloys.....	43
4.2.1 Solidification Microstructure .....	43
4.3 Microstructure and Mechanical Properties of Sn-Cu Alloys after Rolling.....	52
4.3.1 Microstructural Evolution of Sn-1.0wt.%Cu during Rolling.....	52
4.3.2 Mechanical Properties of the Sn-Cu Alloys after Rolling .....	55
4.3.3 Fractograph Characterization .....	58
4.4 Relation between Microstructure and Mechanical Properties .....	60
4.4.1 Strengthening in Sn-Cu Alloys .....	60
4.4.2 Strain Softening .....	60
4.5 Summary .....	62
Chapter 5 Microstructure, Dynamic Restoration and Recrystallization Texture of Sn-0.5wt.%Cu Processed by Rolling.....	63
5.1 Introduction.....	63
5.2 Microstructure prior to Rolling.....	64
5.3 Microstructure after Rolling .....	66
5.3.1 Bimodal Grain Structure .....	67
5.3.2 Dynamic Restoration .....	70

5.3.3 Twinning .....	76
5.3.4 Recrystallization Texture .....	79
5.4 Summary .....	82
Chapter 6 Microstructure and Mechanical Properties of Sn-Zn-Bi Alloys Processed by Rolling .....	83
6.1 Introduction .....	83
6.2 Solidification Microstructure .....	84
6.2.1 Solidification Microstructure of Cast Sn-3Zn .....	85
6.2.2 Solidification Microstructure of Cast Sn-3Zn-xBi .....	86
6.3 Microstructural Evolution under Rolling .....	90
6.3.1 Evolution of Primary $\beta$ -Sn Phase, Eutectics and Precipitates .....	90
6.3.2 Grain Refinement .....	93
6.3.3 Correlation between the Microstructure and Mechanical Properties .....	101
6.4 Summary .....	106
Chapter 7 Electrochemical Corrosion Performance of Sn-Zn-Bi Alloys .....	107
7.1 Introduction .....	107
7.2 Microstructure of Sn-3Zn-xBi Prior to Corrosion Measurements .....	109
7.3 Electrochemical Measurements of Sn-3Zn-xBi .....	111
7.3.1 Potentiodynamic Polarization Curves .....	111
7.3.2 Electrochemical Impedance Spectroscopy .....	113
7.4 Corrosion Products Characterization .....	117
7.4.1 Surface Characterization .....	117
7.4.2 Cross Section Characterization .....	121
7.5 Effects of Bi on the Corrosion Resistance of Sn-Zn .....	124
7.6 Electrochemical Measurements of Pb/Pb-5Sb .....	127
7.6 Summary .....	129
Chapter 8 Performance Simulations and Proof of Sn-Zn-Bi MDCs .....	131
8.1 Introduction .....	131
8.2 Performance Simulations .....	131
8.2.1 Geometrical Setup .....	131
8.2.2 Material Models and Parameters .....	132
8.2.3 Solvers and Boundary Conditions .....	137
8.2.4 Simulation Results .....	139
8.3 Proof Tests .....	149

8.4 Summary .....	155
Chapter 9 Conclusions .....	156
Chapter 10 Suggestions for Future Work .....	158
References .....	159

## Symbols

<b>Symbols</b>	<b>Meaning</b>
$g$	Gravitational acceleration
$M$	Liner mass
$C$	Explosive mass
$D$	Maximum penetration depth
$v_{jt}$	Velocity of jet tip
$v_{js}$	Velocity of jet rearward tail
$\rho_j$	Density of the jet
$\rho_t$	Density of the target
$t$	Particulation time
$P$	Pressure
$V$	Relative volume, $\rho/\rho_o$
$e$	Specific energy
$\rho$	Reference density
$\rho_o$	Density at zero pressure
$C_p$	Specific heat at constant pressure
$C_v$	Specific heat at constant volume
$\gamma$	Polytropic index, $C_p/C_v$
$\sigma_y$	Yield stress
$\varepsilon_p$	Equivalent plastic strain
$\dot{\varepsilon}^*$	Equivalent strain rate
$T^{*m}$	Reduced temperature in J-C model
$d$	Grain size
$i_{\text{corr}}$	Corrosion current density
$i_{\text{pass}}$	Passivation current density
$E_{\text{corr}}$	Corrosion potential
$i_{\text{cc}}$	Critical current density
$f$	Frequency
$ Z $	Electrochemical impedance
$R_s$	Uncompensated electrolyte resistance
$R_1$	Resistance of the corrosion product layer
$\text{CPE}_1$	Capacitance of the corrosion product layer

$R_{ct}$	Resistance of the electrical double layer
$CPE_{dl}$	Capacitance of the electrical double layer
$R_w$	Transport resistance
$C_0$	Sound speed
$U_s$	Shock velocity
$U_p$	Velocity of particles behind the shock
$m_i$	Mass proportion of the element $i$

## Abbreviations

<b>Abbreviations</b>	<b>Meaning</b>
MDC	Miniature detonating cord
EBSD	Electron backscattered diffraction
DRX	Dynamic recrystallization
EIS	Electrochemical impedance spectroscopy
SEM	Scanning electron microscopy
EDS	Energy dispersive X-ray analyser
OM	Optical microscopy
XRD	X-ray diffraction
TNT	Trinitrotoluene
PETN	Pentaerythritol tetranitrate
HNS	Hexanitrostilbene
RDX	Cyclotrimethylenetrinitramine
HMX	Cyclotetramethylenetetranitramine
DIPAM	Dipicramide; diaminohexanitrobiphenyl
SC	Shaped charge
LSC	Linear shaped charge
MDF	Mild detonating fuse
RSJ	Rolled steel joists
EFP	Explosively formed projectile
YS	Yield strength
UTS	Ultimate tensile strength
El	Elongation
ICP-AES	Inductively coupled plasma atomic emission spectroscopy
RD	Rolling direction
TD	Transverse direction
ND	Normal direction
OIM	Orientation imaging microscopy
OCP	Open circuit potential
EOS	Equation of state
JWL	Jones-Wilkins-Lee
J-C Model	Johnson-Cook strength model

IPF	Inverse pole figure
IQ	Image quality
HAGB	High-angle grain boundary
LAGB	Low-angle grain boundary
BCT	Body-centred tetragonal
DDRX	Discontinuous dynamic recrystallization
GOS	Grain orientation spread
DRV	Dynamic recovery
SFE	Stacking fault energy
PSN	Particle-stimulated nucleation
PDZ	Particle deformation zone
CDRX	Continuous dynamic recrystallization
ITB	Incoherent twin boundary
TB	Twin boundary
SRX	Static recrystallization
EC	Equivalent circuit
CPE	Constant phase element
SHE	Standard hydrogen electrode
R_SZB-MDC	Round Sn-Zn-Bi miniature detonating cord
C_SZB-MDC	Chevron Sn-Zn-Bi miniature detonating cord

## List of Publications

- Guangyu Liu, Shouxun Ji, Luke Grechcini, Andrew Bentley, Zhongyun Fan. Microstructure and mechanical properties of Sn-Cu alloys for detonating and explosive cords. *Materials Science and Technology*, 2017, 33(16) 1907-1918.
- Guangyu Liu, Shouxun Ji. Effect of Bi on the microstructure and mechanical properties of Sn-Zn alloys processed by rolling, *Materials Characterization*, 2018, 137, 39-49.
- Guangyu Liu, Shouxun Ji. Microstructure, restoration, and recrystallization texture of Sn-0.5wt.%Cu alloy after rolling. *Materials Characterization*, 2019, 150, 174-183.
- Guangyu Liu, Shohreh Khorsand, Shouxun Ji. Electrochemical corrosion behaviour of Sn-Zn-xBi lead-free soldering alloys in 0.5 M NaCl solution. *Journal of Materials Science and Technology*, 2019, In press.

# Chapter 1 Introduction

## 1.1 Background and Motivation

Canopy transparency severance/fracture systems are designed primarily for use in emergency escape of pilots or crew through the cockpit of an aircraft. An ejection seat is well known as the effective apparatus to assist evacuation, in case of an aircraft malfunction or combat damage [1]. Upon actuation, the seat is explosively ejected and once a safe height is attained there is automatic parachute deployment. When an ejection seat is jettisoned from the cockpit of an aircraft, it must pass through the region occupied by the transparent canopy of the aircraft. For decades, a prominent method of ejection through the canopy relies on the initial upward seat movement where a projection on top of the seat acts as a canopy breaker forming an egress opening. However, in this approach there is no guarantee that the canopy will be broken in a manner to give a hole of the appropriate size and shape. Additionally, the collision between the seat and the canopy pose a risk of injury of the ejected crew.

As an approach of overcoming this problem a linear explosive device has been employed, known as “miniature detonating cord” or “flexible linear shaped charge”. This device is bonded to the inner surface of the canopy transparency along the pre-designed fracture patterns, as shown in Figure 1.1. When the device is detonated, the transparency which is generally made of acrylic or polycarbonate absorbs blast energy and is subsequently severed or broken up. The explosive content of the cord is dependent on energy requirements for a given canopy transparency and which is contained in the core of a tube sheath, with metals being the preferred sheath material. Sometimes as a protection against the ingress of moisture and cracking, and to allow better handle-ability, it is applicable that the cord is sheathed by an outer sheath of plastic.

In modern military and commercial applications, a canopy transparency of fast jet powered aircrafts is not just used for a separation of the crews against air, but plays an increasingly significant role in ensuring the safety during flight. It is required to provide complete air tightness, good visibility and effective protection of the pilots and crews against any possible impacts, such as bird strike. In this sense, the strength of the transparency is preferably designed as high as possible. Also, the transparency is getting larger in thickness. This surely provides more reliable protection for the crew against potential physical damages from outside of cockpits. Furthermore, during the high-speed flight a better visibility is greatly desirable for

the crew. This requires better design of the severance pattern, and for explosive cords of smaller dimensions without sacrificing the cutting efficiency or reducing the shattering energy.



Figure 1.1 Photo showing the configuration of the linear explosive device bonded to a transparent canopy of an aircraft [2].

The increased strength and thickness, associated with the increasingly strict visibility requirements of the canopy transparency pose enormous difficulties to the severance of the canopy, particularly under the condition that less explosive core can be loaded into the cords of reduced dimensions. Therefore, the sheath of linear explosive cords becomes a critical component to deal with this task, as the sheath will be shattered under explosive output, generating a sharp shattering force to cut the targets.

Conventionally, the metallic sheath materials for linear explosive cords are made of antimonial or non-antimonial lead due to its high density and good ductility. However, lead introduces health and environmental hazards. So, it is becoming compulsory to remove lead from various applications and industries. Therefore, it is essential to find suitable replacement materials. The present study aims to develop lead-free alloys for use in the sheath material of linear explosive cords for aircraft canopy severance systems. The effort is associated with material preparations by casting and mechanical processing. The challenge focuses on investigations of the new alloys in terms of the microstructural characteristics, mechanical behaviours, corrosion properties, and performance simulations.

## 1.2 Research Objectives

The major objectives of the present study are:

- To explore the relationship between the composition, processing, microstructure and mechanical properties of the Sn-(0.3-1.0wt.%)Cu alloys.
- To study the microstructural features and deformation mechanisms of the Sn-0.5wt.%Cu alloy processed by rolling.
- To investigate the effect of Bi on the microstructural evolution and mechanical properties of Sn-Zn-Bi alloys processed by rolling.
- To investigate the corrosion performance of Sn-Zn and Sn-Zn-Bi, and the effect of Bi on the corrosion properties of the Sn-Zn alloy.
- To assess the cutting performance of miniature detonating cords sheathed by newly developed tin alloys through numerical simulations.
- To prove the reliability of Sn-Zn-Bi sheathed MDCs for the aircraft canopy severance systems.

## 1.3 Thesis Outline

Following the introduction in Chapter 1, the literatures review will be given in Chapter 2, in which an introduction of the linear detonating and explosive devices and their fundamental applications are given. A special linear explosive device which is primarily used for severing the target or structure is described, including the configuration, manufacturing process, cutting process, and the factors affecting the cutting performance. Especially, the significance of sheath materials for linear explosive cords are interpreted. Potential metals or alloys which are suitable sheath materials are reviewed from the perspective of the mechanical properties and density, based on the reference data from the candidate materials for the liners of shaped charges.

In Chapter 3, the research methodology including alloy casting and processing, microstructure characterization, properties measurements, and simulation modelling are described. Details of the experimental procedures, examination equipment and techniques are given.

Chapter 4 presents the development of the Sn-Cu alloys including Sn-0.3wt.%, Sn-0.5wt.%Cu, Sn-0.7wt.%Cu, and Sn-1.0wt.%Cu that meet the requirement of mechanical properties, in particular ductility for the application as the sheath of the linear explosive cords. It investigates

the microstructural evolution and mechanical properties of Sn-Cu alloys with different compositions under the conditions from casting to rolling.

Chapter 5 presents the microstructural characteristics and deformation mechanisms of the Sn-0.5wt.%Cu alloy processed by rolling at room temperature. The microstructure, grain boundaries, dynamic restorations, twinning, and recrystallization texture are characterized by electron backscattered diffraction (EBSD) technique. Dynamic recrystallization (DRX) phenomenon and the effect of  $\text{Cu}_6\text{Sn}_5$  particles on the microstructural evolution are thoroughly discussed. The structural inhomogeneity including bimodal grain structure and texture introduced by rolling is observed. This inhomogeneous microstructural feature is deemed detrimental to the cutting performance of the cords.

Chapter 6 investigates the feasibility of developing a cost-effective and easy-manufacturing Sn-Zn-Bi alloys, which meet the requirement of mechanical properties, especially ductility for the application of sheath materials. For the first time, the microstructure and mechanical properties of Sn-3Zn, Sn-3Zn-1Bi, and Sn-3Zn-5Bi alloys (in mass percent) processed by rolling were studied using EBSD techniques. Results indicate that Bi can enhance both the strength and ductility of the rolled Sn-Zn-Bi alloys. The relationship between the microstructure and tensile properties of rolled specimens are discussed in association with the influence of Bi solutes and secondary phases on the refinement of dynamic crystallized microstructure.

Chapter 7 studies the reliability of developing Sn-Zn-Bi alloys as the sheath materials from the perspective of corrosion properties. The electrochemical corrosion behaviour of Sn-3Zn- $x$ Bi ( $x=0, 1, 3, 5, 7$  wt.%) alloys are investigated using potentiodynamic polarization and electrochemical impedance spectroscopy (EIS) techniques. The corrosion performance of the Sn-Zn-Bi alloys and the effect of Bi on the corrosion properties will be described. The corrosion resistance of current Pb/Pb-5Sb will be given, to provide reference data. The corrosion mechanism of the Sn-Zn-Bi alloys will be discussed in detail through microstructure examination on the surface and cross section of the alloys after corrosion measurements, using X-ray diffraction and scanning electron microscopy (SEM) equipped with energy dispersive X-ray spectroscopy (EDS).

Chapter 8 presents performance simulations of the antimonial lead Sn based alloys including Sn, Sn-Cu, and Sn-Zn-Bi alloys. The cut depth of the cords against an aluminium target

(Al7039) are compared for different metal sheath materials. Besides, the proof results of the cords sheathed with Sn-Zn-Bi against acrylic and or aluminium plate targets are presented.

Chapter 9 presents the main conclusions of the present study. Suggestions for future work of the developed alloy are given in Chapter 10.

## Chapter 2 Literature Review

### 2.1 Linear Detonating and Explosive Device

#### 2.1.1 Terminology

A linear detonating and explosive device is generally constructed with a secondary high explosive core, over its length, and a sheath or cladding to wrap/encase the explosive material and to provide confinement. Typical explosive materials used chronologically vary from trinitrotoluene (TNT), to pentaerythritol tetranitrate (PETN), cyclotrimethylenetrinitramine (RDX), cyclotetramethylenetetranitramine (HMX), and hexanitrostilbene (HNS) [3, 4]. The sheath is often made of textile braided materials, flexible plastic, or metals depending on different applications [5, 6, 7]. Figure 2.1 shows typical linear detonating and explosive products including textile, plastic, or metal sheathed cords and metal-clad linear shaped charges. Literally, according to the term “*detonating and explosive*”, the device generally provides two functions: one is related to transmission of detonation and another is associated with explosive energy output.

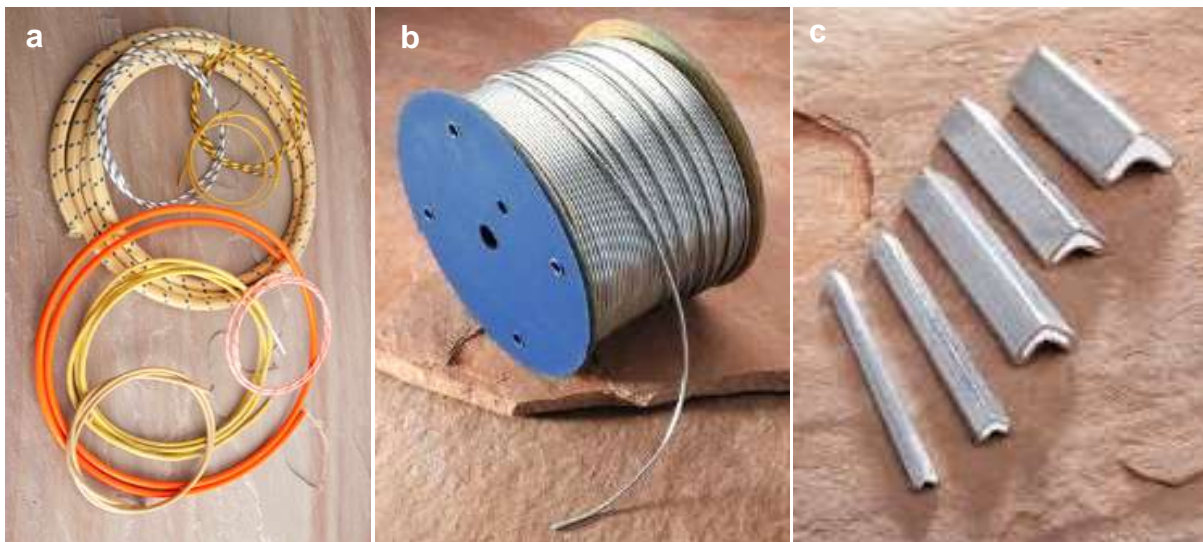


Figure 2.1 The linear detonating and explosive products. (a) textile braided or plastic sheathed cords, (b) metal sheathed detonating fuse [8], (c) metal-clad linear shaped charges [8].

The devices are extensively used for transmitting detonation from point to point, to control delay or to synchronize multiple explosive events on a plane, sphere or cylinder, such as the flexible detonating cords [5, 6]. Besides, they are also for use in severing, cutting, fracturing, or impacting target structures in the wide range of commercial and military applications, such as mining, demolition, and military launch and aircrafts [9]. In aspects of detonation transmission, once initiated, a detonation front propagates along its entire length without interruption, at a characteristic velocity with good repeatability, within the range of 7000 to 12000 ms<sup>-1</sup>, depending on the configuration [10, 11]. This is very useful for the simultaneous detonation of the explosive device with a very limited time delay. Also, these relatively lower detonation velocities are often used for time delays in the applications where sequential explosive missions are required. However, linear detonating and explosive devices are also proved to do useful work with the energy released by the device itself. In this aspect, it is often used for cutting or severance of targets, such as miniature detonating cords (MDCs) which are primarily used in aircraft canopy severance systems.

### *2.1.2 Classification and Application*

In specific, when it comes to transmission of detonation, the linear detonating and explosive devices generally feature in small dimensions, with the cross section of a few millimetres. Also, the explosive core is primarily enclosed in a textile sheath and wrapped in flexible plastic. For example, a great deal of textile-wrapped detonating cords is extensively used in the petroleum exploration and production industry to initiate other explosive components used in various downhole tools [3]. The textile wrapping provides a highly flexible structure that can be easily threaded through perforating guns.

On the other hand, when the devices are used for the purposes of fracturing, the sheath or the liner is more likely to be made of metallic materials with relatively high density, such as copper and lead [12], because these highly dense sheath materials can provide larger momentum for breaking targets. The corresponding dimensions are dependent on the specific applications. Both small linear explosive devices like the mild detonating fuse or cord (MDF) and larger ones such as linear shaped charges (LSCs) are applicable. Therefore, according to the difference in the configuration and functions the linear detonating and explosive devices are usually classified into two categories, i.e. detonation-transmitting dominated domains and target-severing dominated fields [13, 1].

## Fuse

One of the well-known linear detonating devices is the fuse [14]. In common usage, the word *fuse* is used indiscriminately. However, when being specific and particularly in the mining, demolition, and military domains, the term *fuse* describes a simple initiating or igniting device for the detonation of explosive components such as blasting caps and explosive charges [15]. The simplest form of fuse might be the burning fuse, which originated from China, approximately in the 10<sup>th</sup> century [16]. This specific ancient fuse consists of lightweight paper filled with loose gunpowder, and serves as a means of delaying ignition in fireworks and hand grenades, as shown in Figure 2.2.



Figure 2.2 A smoke bomb with a lit fuse [17].

Burning fuses or ignition fuses, while burning at a relatively rapid velocity of 5-25 seconds/foot, is characterized by an external flame and/or sparks emanating radially from the fuse [14]. This has disadvantages. For example, it is not applicable underwater or in the occasions where surroundings should not be influenced by the flash fire flame. To overcome these drawbacks, another version of a higher quality fuse is produced, which is known as the safety fuse [14]. A safety fuse consists of an elongated wrapping having the shape of a tubular, rigid or flexible tube or duct filled with a quantity of explosive or other reactive substance, normally black powder, distributed along the entire duct, as shown in Figure 2.3.

The explosive core occupies a portion only of the cross-sectional area of the channel otherwise filled by gas of the duct. An appropriate outer wrapping or coating treatment can make the safety fuse water-resistant and can even make them burn reliably underwater once lit. The safety fuse is distinguished generally from ignition fuses in that it burns at a relatively slow rate of 30-40 seconds/foot, and that the burning is confined within the fuse envelope until it reaches the end of the fuse where it emerges as a characteristic end spit [15]. Once ignited, safety fuses can burn underwater, and have no external flame that might ignite methane or other fuels such as might be found in mines or other industry.

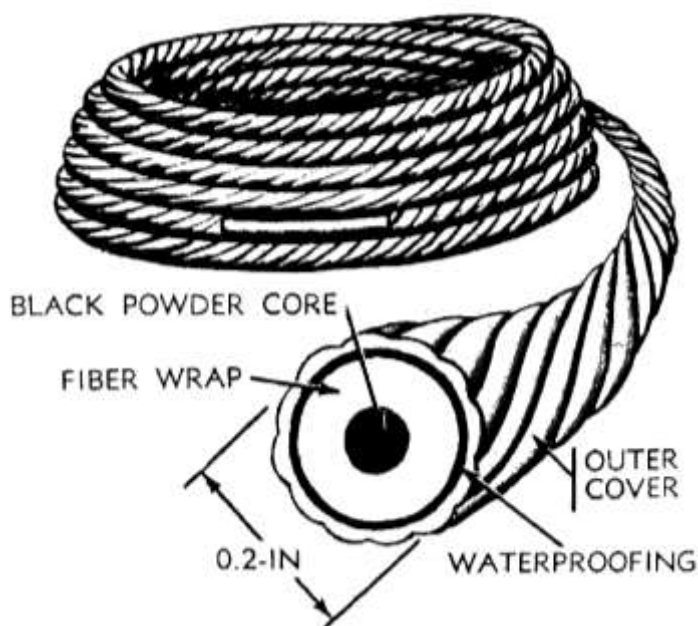


Figure 2.3 Photo of a waterproofing safety fuse [18].

The initiating fuses are extensively used in modern pyrotechnics because they burn at a uniform rate, with an easily visible external flame and moderate transferring speed from the ignition point to the end of the fuse. While, due to inevitable variations in velocity of propagation of detonation in the loose powder fuse ignition, a scattering of the moments of the ignition of the various charges is caused. This renders impossible or at least difficult to apply this type of ignition to the ignition with very short intervals in some specific applications. To deal with this type of issues, modern day safety fuses are often used in mining and military operations, to provide a time-delay before ignition, and they are often used to initiate an explosive detonator, thereby starting an explosive chain reaction to detonate a larger more stable main charge [19].

## **Detonating cords/fuses**

A detonating cord or detonating fuse, different from the *fuse* mentioned above, is another typically widely-used linear detonating and explosive device. It comprises a solid core of high explosive encased in a protective thin, flexible plastic, or metallic tube [20]. Normally, the diameter of detonating cords is less than 3 mm, and the diameter of explosive is less than 2 mm [21]. A typical explosive core for detonating cords is pentaerythritol tetranitrate, PETN, and typical core sizes ranges from about 5 grains of explosive per linear foot of cord (gr/ft) to around 400 gr/ft [11].

As the transmission medium, detonating cords possess a high exploding rate, any common length of detonating cord appears to explode instantaneously. In this way, detonating cords are likely regarded as the high-speed fuses which explode, rather than burn, and are more suitable for detonating high explosives. The sufficiently high detonation velocity guarantee simultaneous detonation for synchronizing multiple charges even though the charges are placed at different distances from the point of initiation. This is particularly useful for demolitions when structural elements need to be destroyed sequentially in the temporal and spatial domains.

When loaded with proper explosive materials, these low-yield detonating cords can be used as precision cutting charges to remove cables, pipes, wiring, fibre optics, and other utility bundles by placing one or more complete wraps around the targets [22]. Higher-yield detonating cords can be used to cut down small trees, although the process is very uneconomical in comparison with cutting by using bulk explosive, or even a chainsaw. High-yield detonating cords placed by divers has been used to remove old dock pilings and other underwater obstructions. Besides, detonating cords are also employed directly in building demolition where thin concrete slabs need be broken via channels drilled parallel to the surface, an advantage over dynamite is that a lower minimum of explosive force may be used and smaller diameter holes are sufficient to contain the explosive. They perform various functions in space and military systems, such as stage separations in rockets, missiles [23] and pilot ejection from aircraft [24].

## **Linear shaped charge**

When it comes to linear explosive devices in applications from burning, detonating, exploding, and fracturing, another widely used product in commercial and military applications is the linear shaped charge (LSC) [25]. The major use of LSCs is cutting metal or robust target in

separation systems. Slightly different from fuses or detonating cords, LSCs often have a larger dimension in diameter and a smaller size in length. Also, a LSC often has the specific cross section of chevron instead of circular.

Figure 2.4 shows the cross section of a typical linear shaped charge, which is composed of a liner with inverted V-shaped chevron profile and a seamless metal sheath [26]. The inverted V-shaped liner is surrounded by explosive, and the explosive is encased within a suitable sheath that serves to protect the explosive and to confine it upon detonation. The metallic sheaths are usually made from lead, aluminium, copper, or silver [26]. Lead LSCs are flexible while the others are stiff. Aluminium is lighter than others in LSCs of the same explosive core load. A lighter linear shaped charge is highly desirable in some certain military application where the LSC weight should be minimized to enable man-portability and the LSC can be carried easily for parachute.

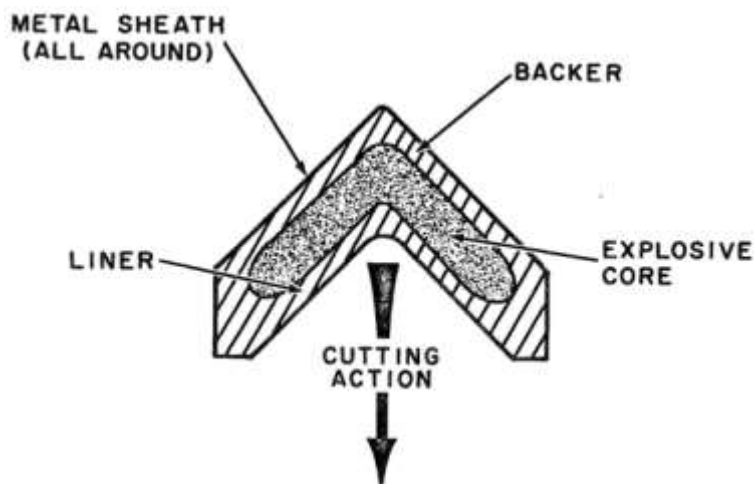


Figure 2.4 Cross section of a typical linear shaped charge (LSC) [26].

Upon detonation of an explosive element in the LSC, the focusing of explosive high-pressure wave as it becomes incident to the side wall causes the metal liner or sheath to form a metal slug which is projected as a knife-like cutting jet towards the target [27]. The cutting jet is linear, along a longitudinal axis of the charge, and therefore cuts the target in its path to a depth along a line defined by a configuration of the charge. The typical process of the liner collapse and jetting of a LSC is illustrated in Figure 2.5. The shape and depth of the cut may be finely controlled, by selecting appropriate dimensions and explosive loadings in the charge. For the cutting of complex geometries, there are also flexible versions of the linear shaped charges,

with a lead or high-density foam sheath and a ductile/flexible liner material, which also is often lead.

Linear shaped charges have numerous and varied applications, both in civil and military, where a clean and controlled cut is required. Because of the high cutting power, linear shaped charges may be used to cut concrete or metallic structures, such as cutting the rolled steel joists (RSJ), breaching walls, and demolishing building structures [28]. The precision of the line and depth of the cut allows for delicate cutting operations, for example, the LSCs are suitable for the purposes of cutting bomb casings during explosive ordinance disposal, achieved by wrapping the linear shaped charge around the bomb casing at the location of the desired cut [29].

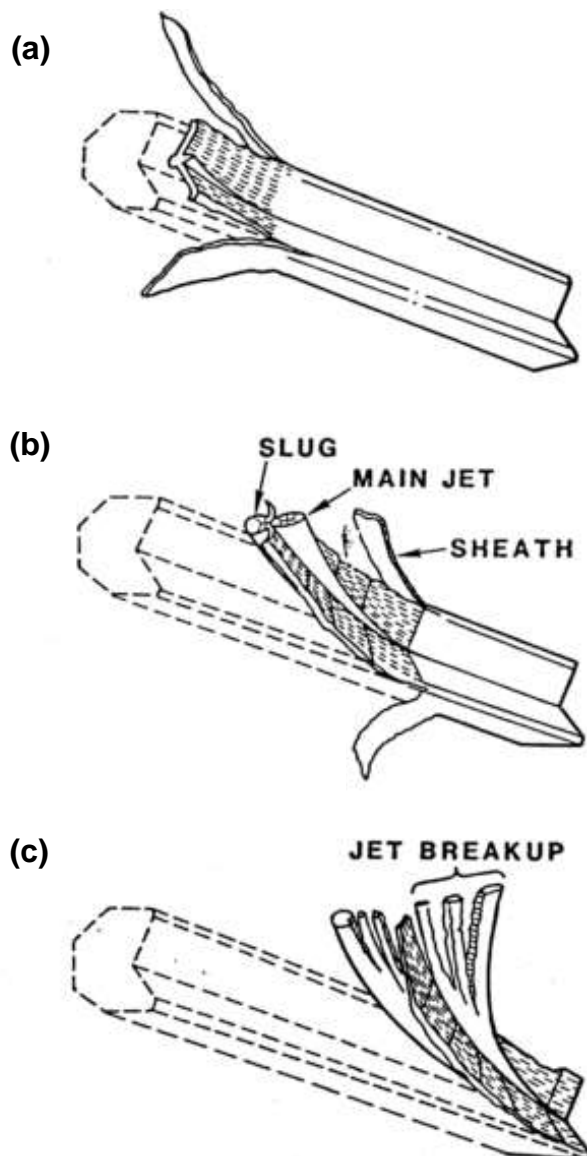


Figure 2.5 Linear shaped charge collapse and jetting process [30].

## 2.2 Miniature Detonating Cords

Functions and applications of linear detonating and explosive devices range from detonation transmission such as ignition fuses and safety fuses, to exploding and fracturing such as detonating cords and LSCs. The size of these devices differs vastly from a few millimetres (fuses and detonating cords) to tens of centimetres (LSCs). In the present study, the topic is focused on linear explosive devices of small dimensions and those operate greatly associated with exploding and fracturing domains.

### 2.2.1 Configuration

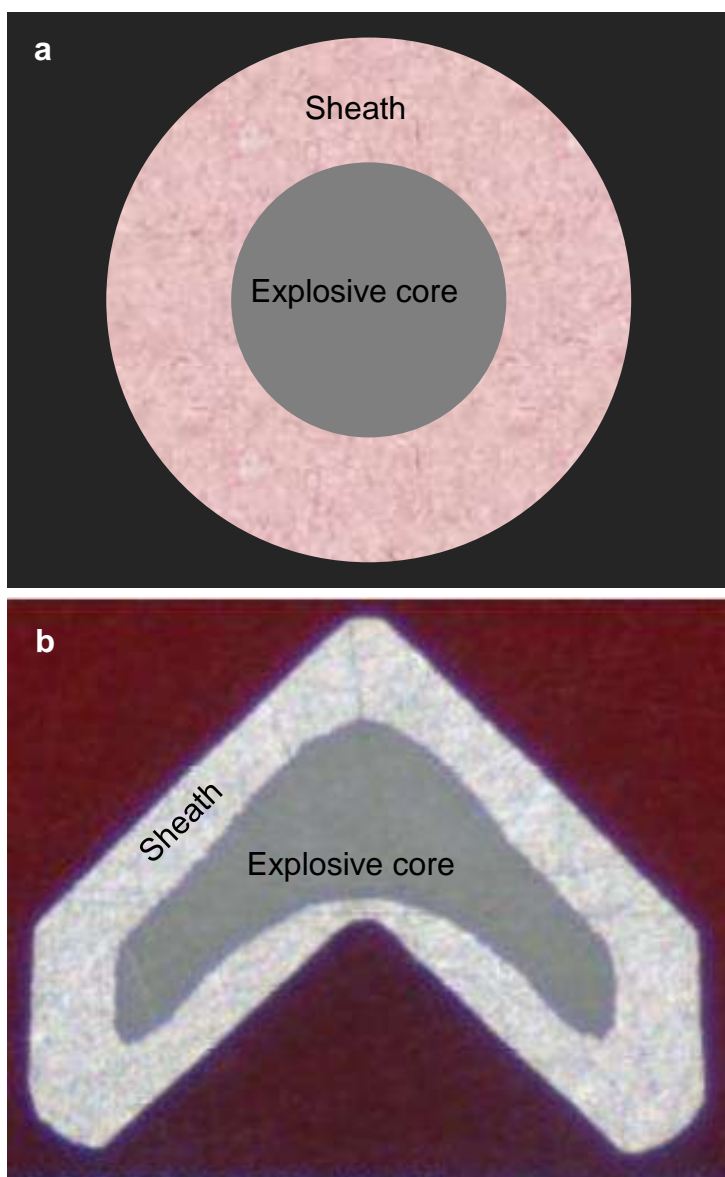


Figure 2.6 The schematic figure showing the cross section of typical miniature detonating cords with (a) round, and (b) chevron shape.

The miniature detonating cords (MDCs) are, in fact, a specific form of linear detonating and explosive devices. They are characterized as miniature dimensions. Hereafter, the MDCs mainly detonate the linear explosive devices that are particularly for use in structure cutting or severing, rather only for transmission of detonation. So, in comparison with other common linear detonating and explosive devices (detonating cord or LSCs), the MDCs generally display several unique characteristics, which include a smaller dimension in diameters ( $< 3\text{mm}$ ), a higher detonating velocity ( $> 6000\text{m/s}$ ) to guarantee simultaneous explosion throughout the entire length, and higher explosive loadings to ensure greater energy output.

Figure 2.6 presents the cross sections of a typical miniature detonating cord configured with two shapes: round and chevron. The sheath is often made of metallic materials such as lead, aluminium, silver, and copper, which is used as the housing or containment and more importantly to release momentum or energy in the form of shattering forces to cut the target. The explosive materials are normally the secondary explosives, for example, hexanitrostilbene (HNS), cyclotrimethylenetrinitramine (RDX), pentaerythritol tetranitrate (PETN), or cyclotetramethylenetetranitramine (HMX).

### *2.2.2 Manufacturing Routes*

The manufacture of metal sheathed linear detonating and explosive cords can be traced back to the early 1900's, by filling a lead tube with TNT and then drawing the tube down to wire sizes using wire drawing equipment [4]. Nowadays, although many high explosive materials and various types of sheath metals have emerged for linear explosive cords, the basic techniques for manufacturing those products remain unchanged. A typical manufacturing route comprising the steps of:

- (1) Preparing a metal tube by casting and subsequent drawing, extrusion or swaging.
- (2) Filling the tube with high explosive materials.
- (3) Drawing, rolling, or extruding the explosive-loaded sheath tube out to extend its length, reduce its diameter and compress the explosive contained.
- (4) If applicable, rolling the explosive-loaded cords into a desired shape with a specific cross section, such as a chevron configuration.

An example of conventional manufacturing process of a linear explosive cord with a chevron-shaped cross section is presented in Figure 2.7, where the round sheath tube was made from

Al, Cu, or Pb. The explosive cord included RDX, HNX, or DIPAM (dipicramide; diaminohexanitrobiphenyl). Figure 2.8 shows another typical cross section of the linear shaped cord or charge used for aircraft canopy severance systems.

The manufacturing process poses a reasonable demand for good ductility or workability of the sheath materials. On one hand, it is quite understandable that a metal sheath of high ductility will largely reduce the risks of fracture when it is under drawing or rolling together with the explosive core. A soft sheath tube with good workability can also provide ease of mechanical processing.

On the other hand, an explosive core made of any explosive materials has a critical diameter. Below the critical diameter, propagation of a detonation wave front along the core will not occur, and this critical diameter is known to decrease as the density of the explosive increases. Since a small MDC is desirable to offer a good flexibility and to facilitate good visibility of the cockpit, the explosive core is preferably compacted so that it has a sufficient density to allow the detonating cord to have a small diameter. A sheath tube of good ductility ensures that the drawing process will not cause over compaction of the explosive materials when the tube is radially compacted, which can avoid reducing the reliability of detonation.

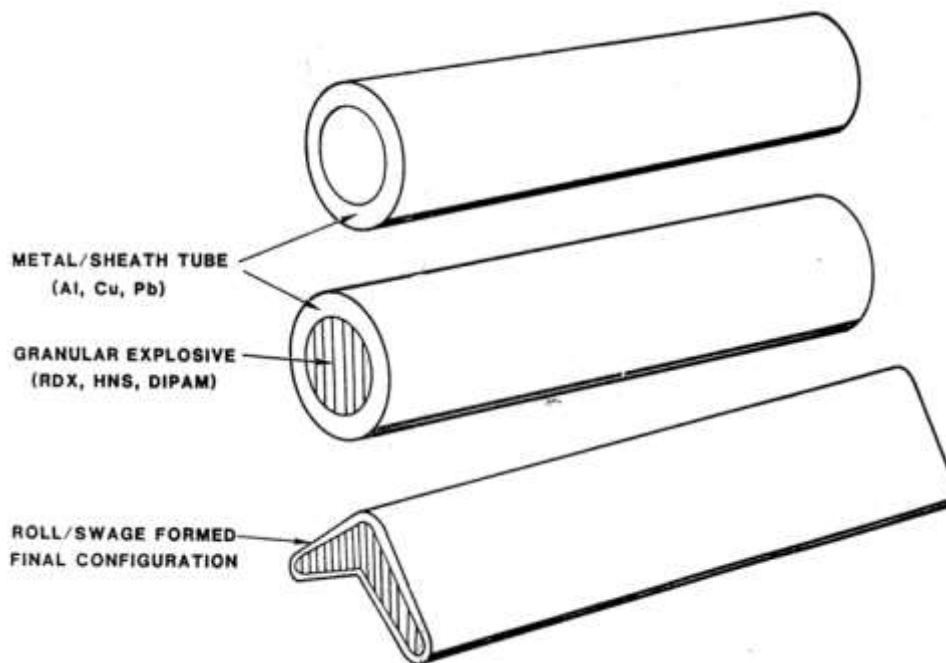


Figure 2.7 Schematics of manufacture of the linear detonation and explosive cords [30].

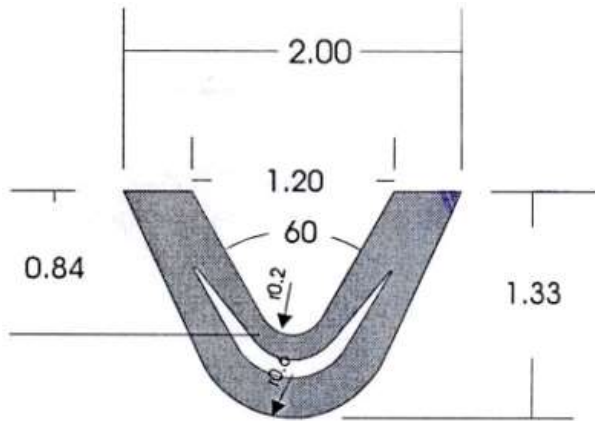


Figure 2.8 Cross section of linear detonation shaped charge for aircraft canopy severance systems [31].

## 2.3 Penetration and Cutting Process of Explosive Charges

### 2.3.1 Penetration Process of Shaped Charges

In this section, the penetration process of shaped charges will be introduced, which can provide general reference on cutting process of linear explosive cords. A shaped charge is a device that can focus explosive output in a specific direction. It is typically a cylindrical explosive charge with a hollow cavity at one end and a detonator at the other. Shaped charges are also called “*hollow charges*” or appear as explosively formed projectiles (EFPs) [32]. The shape of the hollow cavity may be conical, hemi-spherical, or tulip-shaped. The cavity of a shaped charge is usually lined with a metallic liner which is made by copper, steel, aluminium, and so on [32].

Figure 2.9 shows the scheme of a typical shaped charge and associated penetration principle towards a target plate [33]. The charge is constructed with a detonator, a high explosive, and a conical liner. Once detonated, the gaseous products generated in the detonation process can exert extremely intense, focused, localized pressure, and shock waves [34]. When this high pressure (200-300kbar) detonation shock engulfs the liner, the liner is softened or liquefied and consequently collapses and moves towards the charge axis of symmetry, and forms a metal jet with extremely high kinetic energy [32]. If the metal jet is directed towards a target, due to the high velocity of the jet, the stagnation pressure exceeds the strength of any known materials and can easily penetrate even the hardest material.

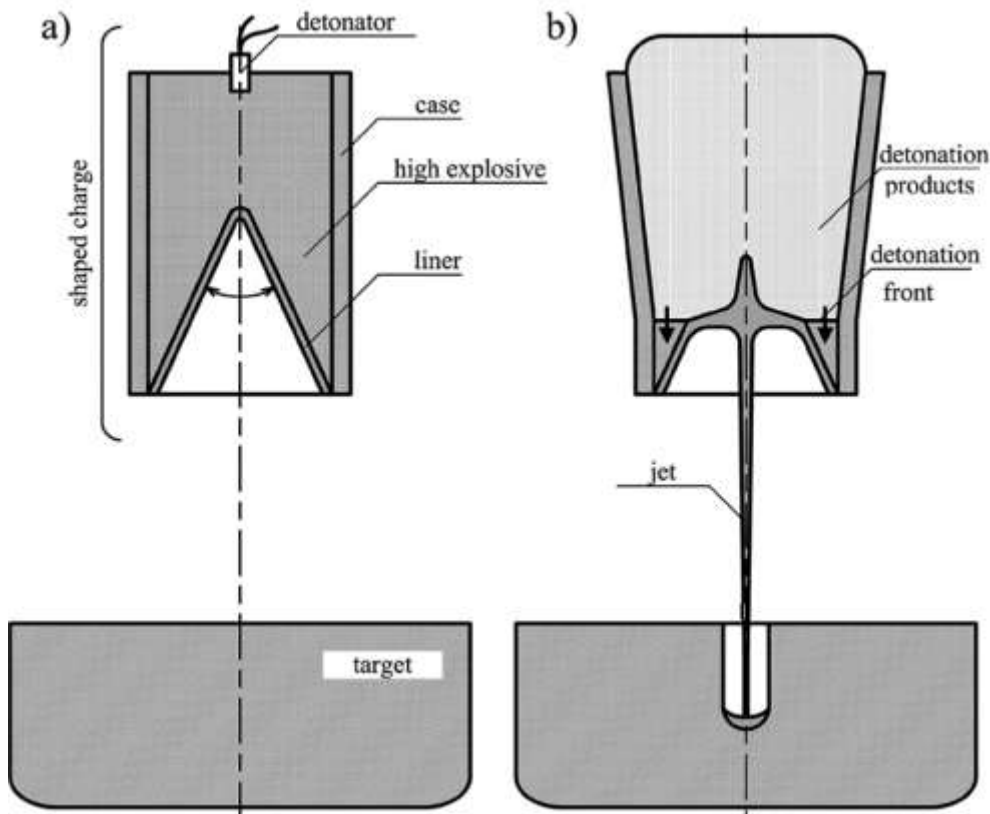


Figure 2.9 (a) Scheme of a shaped charge and (b) the associated penetration principle [33].

Figure 2.10 shows the flash X-ray of a collapsing of a copper liner after detonation [35]. The velocity of jet tip reaches  $10 \text{ km s}^{-1}$  after detonation for  $40 \mu\text{s}$ , giving a cone tip acceleration of about 25 million  $g$ . At this acceleration the tip would reach the speed of light, if possible, in around 1.5 seconds. But of course, it reaches a terminal velocity after only 40 millionths of a second. It is difficult to think of any other terrestrial event as fast as a shaped charge jet tip. The rearward tail, called a “slug” normally has a slower velocity of 2 to  $5 \text{ km s}^{-1}$ . The velocity gradient along the length of the jet lead to stretching of the jet, which ultimately fractures the jet due to severe elongation, if uninterrupted.

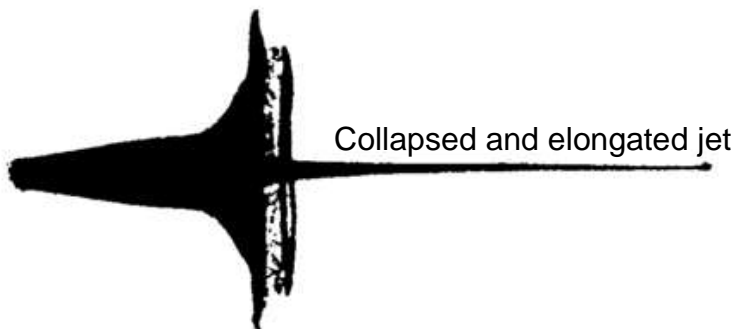


Figure 2.10 Flash X-ray of a collapsing copper cone liner [35].

### *2.3.2 Cutting Process of Linear Shaped Charges*

The jet formation process of a linear shaped charge (LSC) has been assumed to be the similar process as the traditional conical shaped charges based on the Birkhoff theory [36]. The theory in general describes the formation process of jets from conical and wedge-shaped liners, suggesting the jets will be based on classical hydrodynamics of perfect fluids regardless of the strength of the liner. Instead of top-down or left-right initiation, the propagation of the detonation in LSCs travels in a direction normal to the direction of jet travel. In the case of conical shaped charges, the jet formation process is comparatively straight forward because the jet and flight occurs only in an axial direction. For the linear explosive charge, it has no such single-axial jet projection. Instead, the jet forms as a group of elongated knife blade-shaped jet particles along the length. Thus, the jet formation process of LSCs is somewhat different from that of conical shaped charges.

Figure 2.11 presents simulation micrographs showing the evolution of a LSC after detonation in the time interval of 0-12  $\mu\text{m}$ , where a commercially manufactured 1200 gr/ft LSC and a mild steel target are numerically simulated using AUTODYN [37]. The long high explosive charge along the length of the LSC needs to be initiated from one end, in accordance to common practice, creating a gradual flat liner collapse in the lateral direction [38]. This planar jet causes a significant reduction in the penetration performance of typical LSCs ranging only a few inches [39].

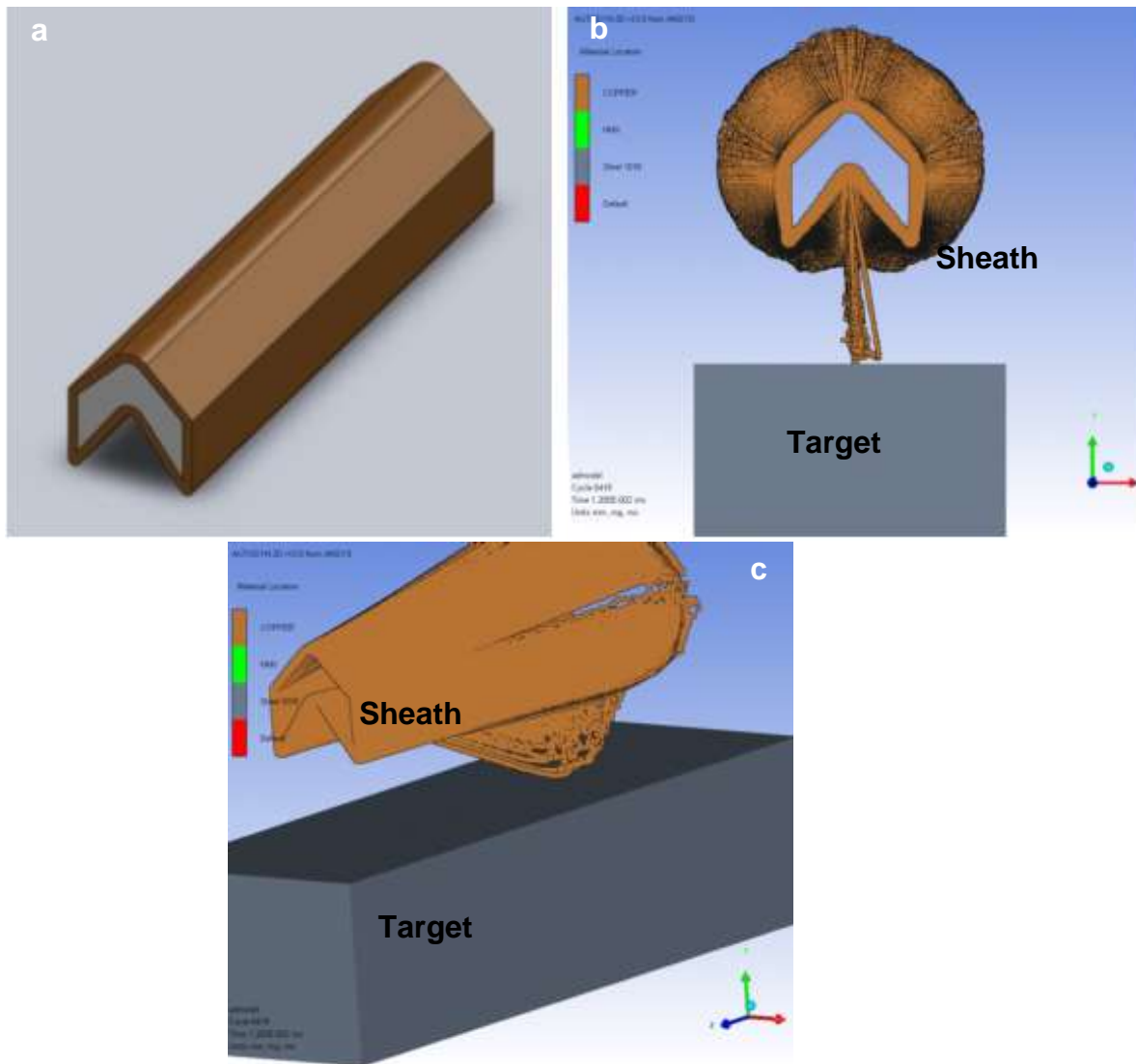


Figure 2.11 Configurational evolution of a 1200 gr/ft LSC after detonation in the time moment of (a) 0 and (b, c) 12  $\mu$ s [37].

In a typical LSC detonation (single end-initiated), the LSC jet projects in an angled fashion creating an oblique projection from the initial LSC configuration [40, 41]. This oblique projection is originated from the sweeping detonation along the explosive core of the LSC, and it causes the LSC jet to move slightly forward against the initiation point. It is noted that the oblique projection of the LSC jet can be prevented by initiating the entire LSC at the same time; that is, initiated by a wave shaper [40]. The oblique projection of the LSC jet is clearly visible when an LSC detonation is under an X-ray exposure, as shown in Figure 2.12.

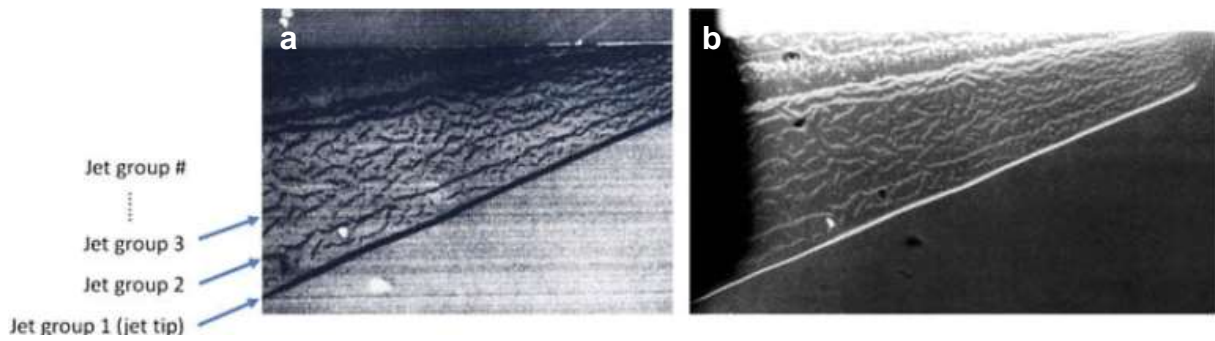


Figure 2.12 Detonation and sheath collapsing process of a (a) 600 gr/ft, and (b) 900 gr/ft copper-sheathed linear shaped charge [40].

From Figure 2.12, the jet segments can be grouped in multiple jet groups depending on the angle of the jet projection and the linear jet distribution. For instance, only three groups of jets are identified in Figure 2.12a, but equally more jet particles can be grouped depending on the X-ray exposure time (Figure 2.12b). This grouping behaviour of jet segments is observable every time in different sized LSCs, and it provides very important information regarding the jet projection property of LSCs.

First, each group of jet segments is almost a straight-line fashion representing a constant detonation velocity along the explosive core of the charge under a typical sweeping detonation. Second, as results of these factors, each group of planar-particle jet segments bears a unique oblique projection angle pivoting to the near bottom of the LSC (Figure 2.12b). Third, these jet groups are not simply from the jet being torn into long strips from a solid unparticulated jet, but they form this particulated fashion from the start. From this observation, the schematic diagram and an analytical expression shown in Figure 2.13 are derived.

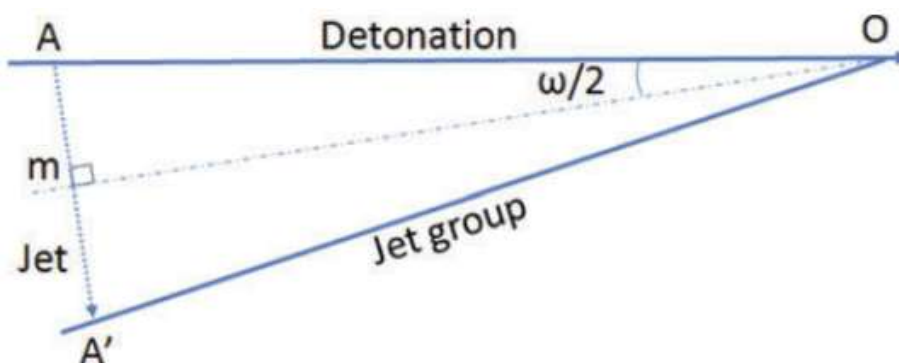


Figure 2.13 Schematic diagram of a group of jet segments projection [42].

### 2.3.3 Factors Influencing the Cutting Performance

Factor affecting the cutting performance is various and complex. A great deal of research has been carried out to explore the factors influencing the cutting efficiency of conical shaped charges, which include the effect of sheath or liner material [43, 44], geometry and thickness of liners [45, 30, 46], and stand-off distance [47]. However, very limited research on linear explosive products has been carried out. Despite the unique characteristics of the linear explosive cords in comparison with conical shaped charges, those affecting the performance of shaped charges would be reasonably regarded as the key factors determining cutting performance of the linear explosive devices. Thus, the characteristic of explosive materials, the sheath, stand-off distance, and design of cross section are crucial to the performance.

#### 2.3.3.1 Explosive Core

The desired explosive for a linear explosive cord should meet the following basic requirements: (1) the explosive core detonates after initiation without interruption throughout the entire length; (2) detonation velocity should be sufficiently high to ensure a simultaneous planar cut; (3) explosive energy output is high enough to completely defeat targets. Secondary explosives with relatively high densities (implies higher detonation pressure, velocity, energy and Gurney velocity [48]) are often desired. It is considered that explosives with a detonation velocity below 4500 m/s have a substantially lower effect and are therefore unsuitable for linear explosive cords [49]. In addition to the high detonation velocity and pressure, the explosive must be homogeneous (with no cavities, bubbles and impurities), uniformly granulated and must adhere to the housing walls.

Table 2.1 Physical properties of commonly used secondary explosives [26].

Properties	TNT	PETN	RDX	HMX	HNS
Melting point (°C)	80.4	141	205.5	277.5	316
Autoignition temp. (°C)	-	190	405	380	melts
Detonation rate (m/s)	6900	8400	8750	9100	7000
Density (g/cm <sup>3</sup> )	1.65	1.77	1.82	1.91	1.70
RE factor*	1.00	1.66	1.60	1.7	1.05

\*: The relative effectiveness factor (RE factor) relates an explosive's demolition power to that of TNT.

Based on these fundamental requirements, four explosives including PETN, RDX, HMX, and HNS are in common use. These explosives possess high detonation velocities and pressure [44]. The physical properties of these explosives are concluded in Table 2.1 in comparison with the physical data of TNT. Different explosives exhibit distinct properties such as melting points, density, explosive energy, and detonation velocities. For specific military applications those with higher melting point and a faster detonation velocity are preferred options. A larger energy output may be optimal for those solid and high strength targets.

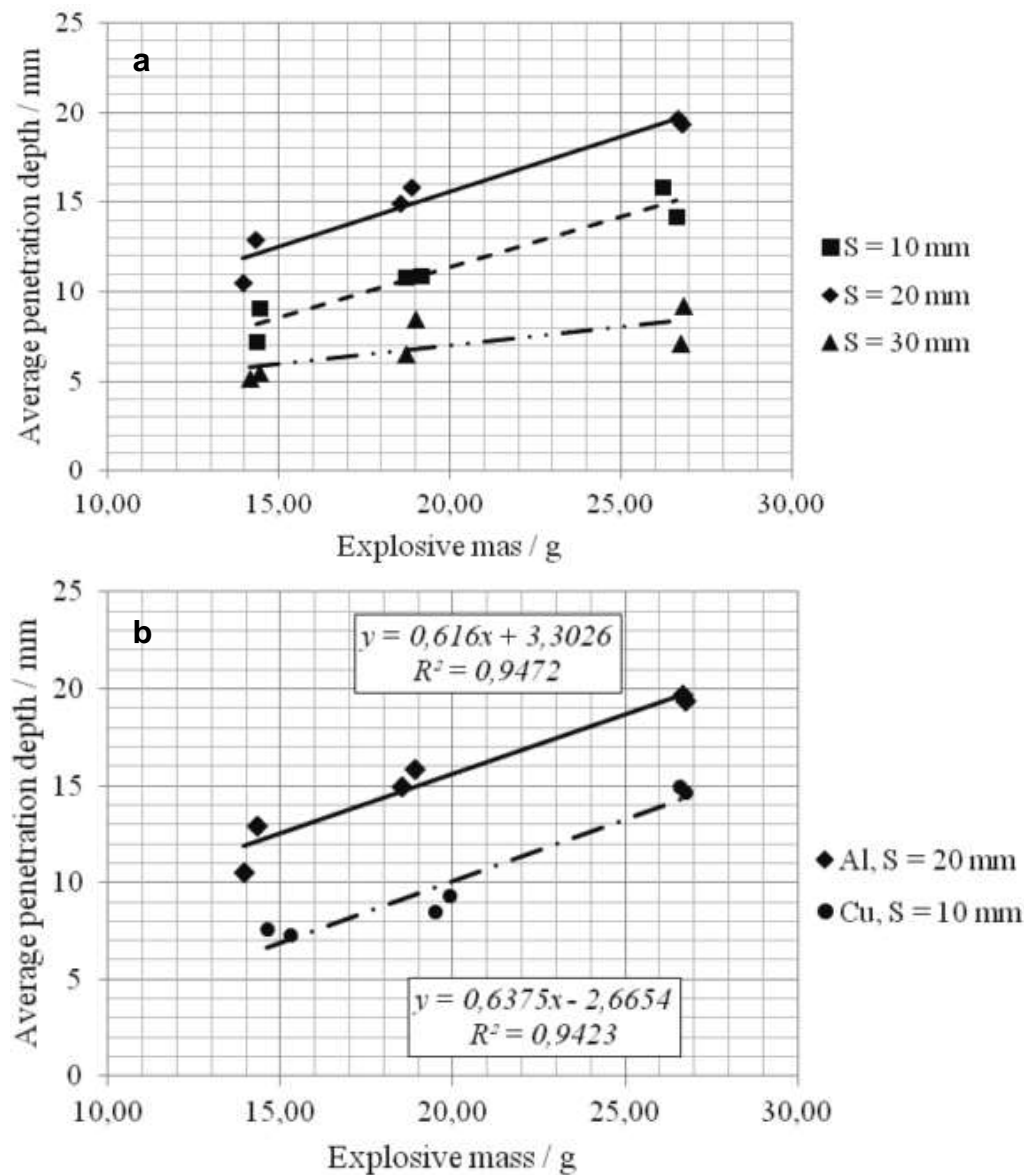


Figure 2.14 The effect of the explosive mass on the penetration depth (a) at different stand-off distance for aluminium liners and (b) for different liner materials [50].

For a similar explosive material, explosive loading is the dominant factor determining the depth of penetration. The effect of the quantity of an explosive on the cut depth of the cords can be expressed based on the explosive mass. Figure 2.14 shows the average penetration depth of a shaped charge which is caved by the copper and aluminium liner as a function of the explosive mass under various stand-off distance. It is observed from Figure 2.14a that at the same stand-off distances of 10, 20, and 30 mm, larger explosive mass gave rise to larger penetration depth. For both copper and aluminium caved explosive charges, the penetration depth exhibited a near linear relationship to the explosive mass (Figure 2.14b). Thus, it is undoubtable that the explosive core is the essential component of the cords which operates predominantly.

### 2.3.4.2 Stand-off Distance

The stand-off donates the distance between the lateral surface of the linear explosive cords/charges and the target. By moving the explosive charges away from the targets, an optimal stand-off distance can be achieved. If the stand-off distance is larger than the optimal value, the efficiency decreases due to the weakened axial or planar knife-shaped jet, i.e. the decreased concentration of kinetic energy towards the end of the jet.

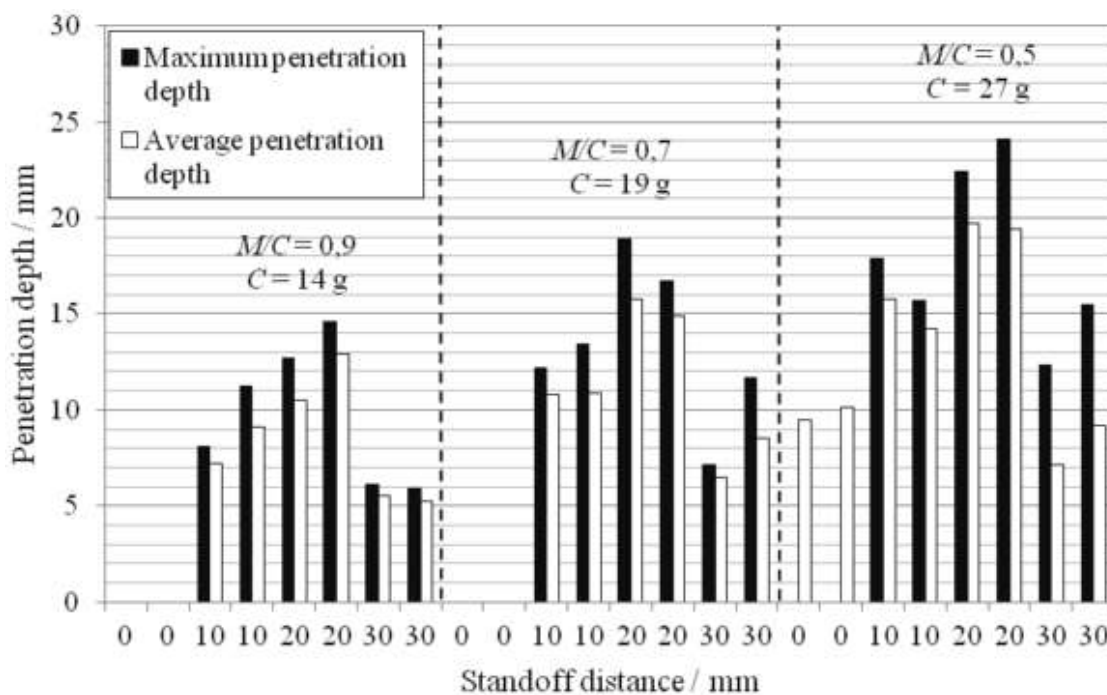


Figure 2.15 The largest and average penetration depth, the linear shaped charges with the aluminium liners [50].

The optimal stand-off distance is determined by the geometric properties of the cross section, apex angle and width of the cord with the constant properties of the target material, constant explosive filling and liner properties. Figure 2.15 shows the variation of penetration depth with the stand-off distance for an aluminium-lined explosive charge with different explosive mass ( $C$ ) or ratio of explosive mass to liner mass ( $M$ ). It is observed that under different  $M/C$  ratios, there exists an optimal stand-off distance where the penetration depth reaches the maximum values.

#### **2.3.4.3 Geometry**

The geometry or cross-sectional configuration of a linear explosive device is mainly divided into two categories: round-shaped and chevron-shaped. As for round cords, the explosive energy output is evenly distributed along the lateral plane, causing relatively small portion of shattering energy or force that interacts with the target. On the contrary, a chevron-shaped structured configuration of a linear detonation shaped charge can result in shock wave collapsing the sheath on either side of the apex to create a jet of high velocity metal directed towards the target to be severed. This focusing of the detonation products due to the chevron shape is commonly referred to as the Munroe Effect [44].

The configuration of the linear explosive devices including the apex height, apex angle, apex thickness, apex radius, charge height, charge width, and charge outer angle were demonstrated to influencing the cutting performance [51]. Also, the imperfect symmetric of the charge might result in undesired issues, for examples, this may lead to missing the target when the stand-off is significantly large, and a reduction of the penetration capability due to the angled attack rather than perpendicular attack to the target surface [42].

#### **2.4 Importance of Sheath**

The sheath of linear explosive devices is an essential part and plays important roles when the devices are in use. For example, when the device is to be used in close proximity to a charge of explosive or sensitive materials it is important that the detonation energy interior the sheath is strictly contained. The metal sheath, to a large extent, provides containment of detonation energy to prevent contamination or undesired energy leakage which cause detrimental effects on surrounding structures or members. In some cases, to overcome the containment problem a further high strength outer sheath, such as stainless steel, is employed for encasing the inner sheath to ensure that the inner sheath does not undergo plastic deformation [52]. But the

inflexibility and the relatively large size introduced by the two-layer metal sheath is a major disadvantage in some weapon systems where a small-time delay is required between detonating events, as the delay cannot be achieved by coiling an appropriate length of cord into a confined space.

The above-mentioned type of function provided by the sheath is closely associated with physical protections of the detonation from water contamination and possible damages from surroundings. As this is not the scope of the present study, no comprehensive details will be provided. In this study, the primary function of the sheath is to assist severing targets. Unfortunately, limited research with respect to the effect of the sheath of linear explosive devices on the cutting performance has been carried out, but various researchers have investigated the shaped charges that were mentioned in the previous paragraphs. Shaped charges are a very powerful penetration device and are extensively used in military and aerospace applications.

Prior to introducing the significance of the sheath to linear explosive cords in aspects of penetration, the liner and/or sheath material of the conical and linear shaped charges can offer appropriate references, as the liners/sheath in these explosive devices, in theory, provide similar penetration principles. In the domain of severing the targets, the liner or sheath materials are primarily used for providing large momentum that enhances the cutting performance. The perforation performance is highly dependent on the physical properties of the liner or the sheath. Among these properties, the density and ductility are the two critical factors dominating the perforation depth when the other characteristics such as explosive core, targets, geometric of liners, and stand-off are considered identical. Overall, optimal cutting performance of a shaped charge liner occurs when the jet formed by the liner is long, coherent, and highly dense [53].

The liner material of an axisymmetric shaped charge is accelerated along the axis of symmetry by the extremely high pressure of the high explosive detonation. During the collapsing process, the jet is squeezed out with possible tip velocities of thousands of meters per second, depending on the shaped charge geometry and the liner material, and the slug is formed with much less velocities of hundreds of meters per second [43]. The jetting process was schematically illustrated in Figure 2.9. Due to the velocity gradient between the jet tip and the slug, the jet begins with an extremely high strain rate and late the jet rearward tail displays a relatively lower strain rate, leading to a particulation or break-up of the jet into the discrete jet particles

or segments. For a particulated jet the penetration depth is related to the following simple equation [54]:

$$D = (v_{jt} - v_{js}) t \sqrt{\rho_j / \rho_t} \quad (2.1)$$

Where  $D$  is the maximum penetration depth,  $v_{jt}$  and  $v_{js}$  are the velocity of jet tip and jet rearward tail or the slug, respectively,  $t$  is the particulation time,  $\rho_j$  and  $\rho_t$  represents the density of the jet and the target, respectively.

#### 2.4.1 Density of Sheath Materials

According to the Eq. (2.1), the maximum penetration depth is directly proportional to the ratio of the jet density to the target density. Increasing the liner density can be an effective way to increase the penetration depth. Besides, the maximum length of the jet, which is given by the component of  $(v_{jt} - v_{js}) t$ , is another deciding parameter contributing to the final penetration depth. Here, the jet tip velocity,  $v_{jt}$ , is dictated by the bulk sound speed of the liner material, which is the theoretical maximum speed that the liner of a shaped charge can travel and still form a coherent jet. Rather increasing indefinitely, the maximum jet tip velocities for the different liners are limited by a factor of the bulk sound speed of the liner material. As a basic rule, the maximum achievable jet tip velocity is 2.34 times the bulk sound speed of the liner material, but unfortunately, under this condition the resulting jet will be non-coherent [43].

Accordingly, to maximize penetration depth, it is desired to operate shaped charge liners close to the bulk sound speed and it is preferable to use a liner material with high bulk sound speed to maximize the corresponding jet tip velocity. However, a contradictory fact is that some metals of high bulk sound speeds have corresponding lower densities, such as Al, and some metals with high density may possess a relatively small bulk sound speed, such as Ta. Held [43] analysed several specific metals used for the liner of shaped charges according to the density, bulk sound speed, maximum theoretical velocity of a primary jet, and the product of jet tip velocity and material density. Based on the results, and in relation to the possibility of use as the liner material for the shaped charges, the metals are ranked from best (tungsten) to worst (aluminium), as presented in the Table 2.2.

Table 2.2 Possibility of application of different liner materials for shaped charges [43]. The maximum velocity of the jet is 2.34 times of the bulk sound speed.

Physical properties	Al	Ni	Cu	Mo	Ta	U	W
Density (g/cm <sup>3</sup> )	2.7	8.8	8.9	10	16.6	18.5	19.4
Bulk sound speed (km/s)	5.4	4.4	4.3	4.9	2.4	2.5	4
$v_{jt, \max}$ (km/s)	12.3	10.1	9.8	11.3	5.4	5.7	9.2
$v_{jt, \max} \sqrt{\rho_j}$	20.2	30	29.2	35.7	22	22	40.4
Rank	7	3	4	2	6	5	1

#### 2.4.2 Ductility of Sheath Materials

As stated, it is recognized that if the liner collapses at a velocity that exceeds the bulk sound speed of the liner material the resulting jet will not be coherent. In this way, the particulation process produces tumbling and transverse moving particles. The tumbling particles are easy to break up under shear failure instead of ductile necking. This can easily generate multiple streams of large jet particles. These large and multiple-streamed jet particles are not ideal cutting jets and will not produce a focused and localized shattering force, consequently, this may drastically decrease the penetration depth. In contrast, a coherent jet is a jet that consists of a continuous stream of small particles or it is based on the straightness of the jet. This straight-lined and focused cutting jet will effectively facilitate penetration.

Generally, a coherent, long, and continuous stream of jet particles can ensure deep penetration of the targets. The jet possesses a velocity gradient from tip to tail, and it continues to stretch after the liner walls have collapsed, giving a jet length greater than the slant height of the cone. The stretching of the jet and time for initiation of jet particulation are greatly dependant on the ductility of the liner materials.

If the jet is formed from a brittle material, a stream of jet particles would form which will separate in a very short time after detonation. A jet formed from a ductile material can, however, elongate to a considerable extent as a continuous stream before the jet finally separates into a stream of particles. In other words, a ductile liner material gives rise to a ductile jet that will be able to stretch extensively without breaking up, that is, a larger particulation time,  $t$ , can be applied to Eq. (2.1). This is contributing to a larger maximum penetration depth.

## 2.5 Selection and Criteria of Sheath Materials

### 2.5.1 Materials for Shaped Charge Liners

To select the sheath materials for linear explosive cords, the materials used as liners in conical and/or linear shaped charges may be the preferred options. As interpreted above, the selection of proper liner materials in shaped charges are mainly based on data information of material density and ductility. The density of the liner jet can be increased by utilizing high density liner materials, such as heavy metals or alloys including tungsten [55], copper-tungsten [56], copper-bismuth [57], copper-lead [58], tantalum [59], and molybdenum [60, 61]. It is known that the higher the jet tip velocity and jet velocity gradient the longer the jet. In solid liners, a ductile material is desired since the solid liner can stretch into a longer jet before the velocity gradient causes the liner to particulate. Based on this idea, the relatively ductile alloys like copper [62], aluminum [63], and steel [64] are designed as the liners of shaped charges.

In specific, to achieve the required cut depth during explosion, a great deal of metals/alloys have been developed as liners of linear shaped charges [65]. The materials include Cu, Ni, Al, Ag and Au to form ductile jets, and Pb to form fluid jets. Ta, Mo and W [66, 67] can form coherent and ductile jets when properly designed [68, 69]. The copper based alloys such as Cu-(5, 10, 30)Zn, Cu-10Sn, Cu-(10, 30, 50, 70)Ni, Cu-72Ag, and other Cu-(28, 35, 50, 60)Ni-(0, 5, 6, 8, 12)W, Cu-80W are also reported in literatures [10, 70]. These materials provide excellent mechanical properties and can deeply penetrate the target due to their good ductility [71].

However, an obvious disadvantage of these W, Ta, Ni, Mo, or Cu-based alloys is that they have high melt temperatures, which causes inconvenience and even non-feasibility for casting. On the other hand, those materials possess high strength and display strong work-hardening performance during mechanical processing, which increases the complexity and difficulty in the manufacture of linear explosive cords with high-energy explosive materials contained [72], as the manufacture of the miniature detonating cords is accomplished by processing such as rolling, drawing, and swaging. Additionally, even though it is capable to draw these high strength materials into final products, the large stiffness and poor formability of these materials pose great difficulty in installation of the cords in the canopy systems. so, those liner materials for shaped charges may be reliable in theory but not applicable in real circumstances.

### 2.5.2 Tin Alloys for the Sheath Materials of Linear Explosive Cords

The standard explosive linear sheath material in use for decades has included a high proportion of lead (90-96wt.%) together with antimony (4-10wt.%) [70, 45]. The antimonial lead alloys are economical and provide the ease of manufacturing and the reliability of performance in terms of low melt temperature, high density, efficient heat transfer of the encased explosive, and sufficient hoop strength to contain the explosive before function. The physical and mechanical properties of pure Pb and Pb-(1-12) wt.%Sb alloys are summarized in Table 2.3 [73, 74, 75, 76].

Because of the significant difference in the mechanical properties shown in Table 2.3 [77, 78, 79, 80], the tensile properties of pure Pb and Pb-5Sb (4.9wt.%Sb) alloys were measured in the present study and the results are also shown in Table 2.3 (marked as \*). The measured yield strength (YS), ultimate tensile strength (UTS) and elongation is 12 MPa, 17 MPa and 76% for pure Pb, and 17 MPa, 27 MPa and 90% for the Pb-4.9wt.%Sb alloy, respectively. Even though these lead-containing materials are required to be replaced due to health and environmental concerns, the results offer the good references for the development of Pb-free alloys.

The application of lead-free tin (Sn)-based alloys to replace Pb based alloys have been the topics of numerous studies as soldering and electronic assemblies for years [81]. For example, Sn-Ag [82], Sn-Cu [83], and Sn-Ag-Cu systems [84] have been often used as solder materials. The microstructure of Sn-Ag, Sn-Cu, and Sn-Ag-Cu soldering alloys in the hypoeutectic compositions generally comprises primary  $\beta$ -Sn dendrites and Cu and/or Ag- rich intermetallic phases. For example, Figure 2.16 shows the typical microstructure of Sn-1.0Ag-0.5Cu alloy, in which Figure 2.16a presents the microstructure of the primary  $\beta$ -Sn phase with globular morphology and eutectic between the  $\beta$ -Sn cells. On closer inspection of the structure (Figure 2.16b), it is seen that the eutectic comprises  $\text{Ag}_3\text{Sn}$  and  $\text{Cu}_6\text{Sn}_5$  intermetallic phases [85].

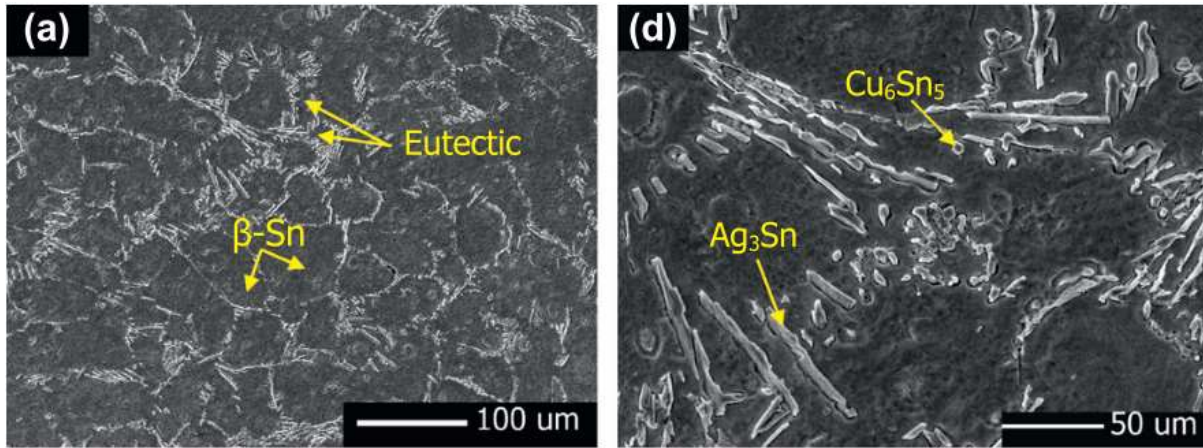


Figure 2.16 BSE-SEM micrographs showing the microstructure of Sn-1.0Ag-0.5Cu alloy under the cooling rate of 6-8 °C/s [85].

Table 2.3 The mechanical properties of lead and lead-antimony alloys collected from literatures and lab measurement.

Alloys	Stress exponent (n)	YS (MPa)	UTS (MPa)	Elongation (%)
Pb (99.9%)		12.5*, 15.5-24.8 [80]	17.0*, 17.3 [73]	76.4*
Pb-1.0wt.%Sb			23.5 [73]	
Pb-1.25wt.%Sb	10.2-10.5 [74, 75] 8.3-10.9 [78]	15.5-19.8 [74, 75]	17.5-24.8 [74, 75]	55-75 [74, 75]
Pb-2.0wt.%Sb			29 [73]	
Pb-3.0wt.%Sb		1.2-6 [79]		
Pb-4.0wt.%Sb			39.1 [74, 75]	
Pb-4.5wt.%Sb	5.4-5.6 [74, 75] 5.6-5.7 [78]	12.5-20.1 [74, 75]	14.0-25.9	52-60 [74, 75]
Pb-4.9wt.%Sb		17.3*	27.2*	90.6*
Pb-6.0wt.%Sb			47.2 [73]	
Pb-8.0wt.%Sb			51.2 [73]	
Pb-10.0wt.%Sb			52.9 [73]	
Pb-11.2wt.%Sb	2.5-3.9 [76]		52.6 [73]	

\* measured by the present study.

However, in addition to applications in soldering and electronic industry, Sn-based alloys have also been considered as sheath materials for linear explosive products due to its good workability, relatively high density, and small thermal neutrons absorption in high radiation environments [86]. Specifically, Rodney et al. [87] have reported that Sn-Sb-Cu, and Sn-Bi-Cu-Ag can be used as the outer sheath materials in ignition cords, mild detonating cords, and linear shaped charges. The Sn-2.5Cu-0.5Sb possessed the strength about 50 MPa and elongation of 39% [87]. Graham et al. [86] have suggested Sn-(0.5-4) wt.%Ag to be the sheathing of mild detonating cords due to the proper strength and good ductility, approximately 30 MPa and ~88% in elongation. Recently, Huang et al. [88] have claimed the use of Sn- (0-20) wt.% Cu/Sb as linear initiating explosive devices. These researches have certainly confirmed the capability of Sn-based alloys for their application as sheath materials in linear explosive devices.

Hitherto there have been steady developments in the field of linear explosive cords, but little has been published concerning the underlying scientific basis for the specification of improved sheath materials. As mentioned, Sn-Sb-Cu and Sn-Ag based lead-free alloys were proposed as the proper sheath of linear detonating products, but these Cu or Ag containing Sn-based alloys unfortunately have some drawbacks. For instance, Ag is a high cost element and it should be avoided in industrial manufacturing for massive applications. Plus, the big difference of the melting points between Sn (232 °C) and Ag/Cu (961/1085 °C) elements to a large extent hinders ease of casting.

More significantly, the mechanisms behind the relationship between the alloy performance associated with microstructural evolution and chemical compositions and processing is rarely investigated. There is still a lack of comprehensive understanding regarding the quantitative relationship between the processing method, microstructure and mechanical properties from casting to plastic deformation on the Sn-based alloys, which are essential to the application of the linear explosive cords. For examples, the microstructure characteristics of the sheath materials including microstructure homogeneity, grain orientations, and textural features pose a significant influence on the jetting and particulation process of the sheath. A uniform metallurgical microstructure is beneficial to the formation of smooth and late particulated jet particles stream, resulting in precision and effective cut [89]. In this sense, whether there is a randomly distributed grain structure or textured/orientated grain distribution that are very likely to form under high strain deformation during the manufacturing routes of the cords should be carefully considered in the selection and design of the sheath materials.

Furthermore, a high risk of corrosion which can occur preferably in the interface between the explosive core and inner sheath is another potential cause that will reduce the life-term and reliability of the MDCs. Hannagan et al. [9] proposed a lower melting point Sn-Zn binary alloys to be the sheath of mild detonating cords, which overcame the downsides of Ag-containing Sn-based alloys, such as high costs and high melting points. But mechanical measurements and microstructure information was provided. Besides, the corrosion performance of the Sn-Zn sheath material has not been investigated. Particularly under the condition that Zn is believed to be a corrosion vulnerable element and it will very likely cause to corrosion failure of the cords.

As such, the present study aims to assess the criteria of materials selection and the development of new materials. According to the potential candidates reviewed above, Sn-based alloys including Sn-Cu and Sn-Zn-Bi alloys were selected for investigation. Main efforts are put on the microstructure characterizations, mechanical behaviors measurement, corrosion performances assessment, and performance simulations. Moreover, the verification of the cutting performance of the cords in the aluminum targets and acrylic target plate is performed in the industrial manufacturing sites.

### *2.5.3 Selection Criteria*

In summary, as the metallic sheath of linear explosive cords, the sheath material generally provides two functions, one is to hold the explosive materials, and the other is to release momentum/energy in the form of shattering forces to break the canopy transparency when it is needed. The efficiency of explosion in the cords depends on the detonation properties of the explosive materials and the response of surrounding mass [90]. This is because the processes of fracture and fragmentation of the cord are strongly dependent on the parameters of the detonation and the dynamic response of cladding materials [91]. The detonation properties of explosive materials consist of the explosion pressure, its time history, and the total energy delivered to the sheath materials [92]. These are not in the range of the present study. However, the response of cord mass to such time varying high-amplitude stresses and the relevant strain-rate-dependent properties of sheath cord is determined by the materials properties. It is a complex process and many external factors such as stand-off distance and cross section shape affect the performance of breaking and clearing the aircraft canopies. Emphasis is put on material properties of the sheath material itself in the present work.

Based on the understanding of processing methods, the mechanical properties of lead-based alloys and the materials for the liners of shaped charges, the physical and mechanical properties of sheath materials for miniature detonating cords should satisfy the following requirements:

1. Abundant resource. The elements for making alloys must be available at a sustainable cost, in sufficient quantities to meet current and future needs.
2. Low cost. This is essential for industrial application and the high cost elements should be avoided.
3. Non-toxicity. The materials must meet the health and environmental requirement.
4. High density, similar with lead or at least larger than  $7.0 \text{ g/cm}^3$ . The density is important to impart sufficient impulse, impact energy, and momentum during the flight of fractured and fragmented piece of sheath materials for penetrating.
5. Acceptable mechanical properties, in particularly high ductility and soft. The mechanical properties should be similar with that lead alloys. The strength (YS and UTS) is less than 80 MPa or even less and elongation is higher than 70%. It is desirable that the materials do not generate strain hardening and are capable of being deformed at room temperature. The appropriate strength guarantees the cord to be fractured under low energy level.
6. Reasonably good performance in melting, casting, extrusion, rolling and drawings.

## Chapter 3 Methodology

### 3.1 Materials Preparation

#### 3.1.1 Alloy Casting

In the present study, Sn-Cu, Sn-Zn, and Sn-Zn-Bi alloys were manufactured from commercial purity (99.9%) metals or master alloys. The specific compositions of the raw metals/alloys are shown in Table 3.1. Commercial pure Sn pellets, Zn ingots, and Bi lumps were supplied by William Rowland Limited. In each experiment, about 1-2 kg of melt was prepared in an A5 clay-graphite crucible with a dimension of 124×152×86 mm, and an electric resistance furnace was used to heat up the crucible and metals during melting, as shown in Figure 3.1a. The clay-graphite crucible was coated with brine-nitride to prevent contamination during the melting.

Table 3.1 Compositions of raw materials used in this study (wt.%).

Materials	Sn	Cu	Zn	Bi	Fe	Ni	Sb	As	Cd
Sn-1Cu	Rem	0.92	0.03	0.015	0.01	0.01	0.02	0.012	0.006
Sn	Rem	<0.01	0.02	0.015	<0.01	0.01	0.015	0.013	0.006
Zn	0.01	0.01	Rem	0.012	<0.01	<0.01	0.011	0.016	0.005
Bi	0.01	0.01	0.015	Rem	<0.01	<0.01	0.012	0.014	0.005

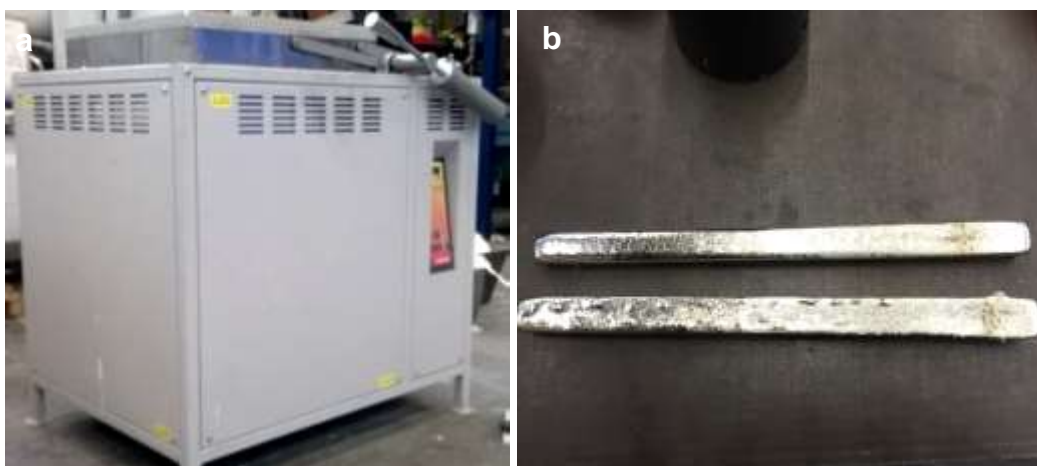


Figure 3.1 (a) The photo of electric resistance furnace used for preparing the melts, and (b) the photo of casting bars.

During the experiments, each element was weighed to a specific ratio with 5wt.% extra amounts for burning loss compensation during melting. In the case of preparation for Sn-Cu alloys, Sn and Sn-1Cu master alloy were added into the crucible and heated up to 400°C. After the elements were melted, the melt was held at 400°C for 1 hour for homogenisation. When preparing the Sn-Zn and Sn-Zn-Bi alloys, Sn element was added into the crucible, the melt was then heated up to 360°C and held at 360°C for 1 hour. The Zn and/or Bi elements were preheated at 200°C. Then the Zn and/or Bi elements were added to the melts. After that, the melt was held at 360°C for 90 mins to achieve a uniform composition distribution, before casting.

The casting process was primarily involved transferring the melt from the crucible into the stainless-steel mould to produce casting ingots. The channel of the mould was coated with boron nitride and preheated at 200°C, ready for use. Debris and oxides floating on the surface of the melt were removed using a boron nitride coated steel ladle, prior to pouring. When the melt temperature reached a pre-set temperature (360°C), the melt was poured into the mould, forming a casting bar with a length of 300 mm. The cross section of the casting bar exhibited a trapezoidal shape with a dimension of 20×16×16 mm (Figure 3.1b). The actual chemical compositions of the alloys were measured using inductively coupled plasma atomic emission spectroscopy (ICP-AES, ARCOS, Simultaneous ICP Spectrometer, SPECTRO Analytical Instruments GmbH, Germany).

### 3.1.2 Alloy Processing

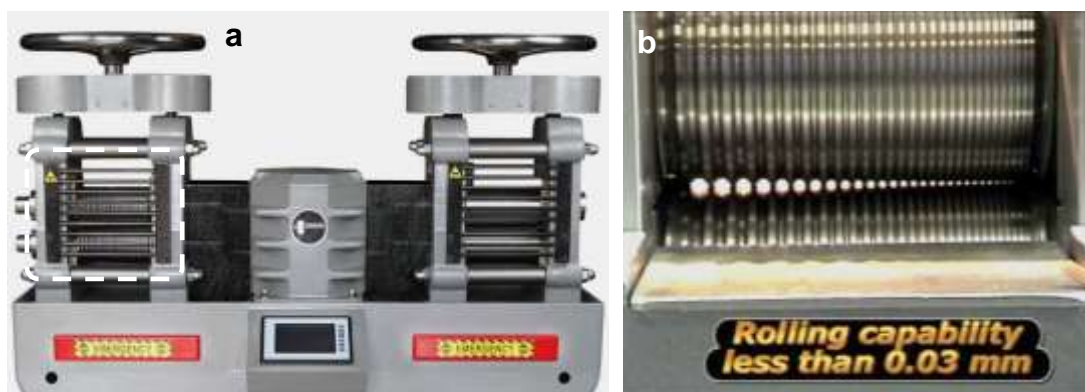


Figure 3.2 (a) The rolling machine (Durston FSM200 Rolling Mill, UK) used for rolling the casting bars, (b) the enlargement of the highlighted component in (a).

The casting bars were placed at room temperature for several weeks to allow homogenization before rolling. Then, the bars were rolled at room temperature using a rolling machine (Durstons FSM200 Rolling Mill, UK), as shown in Figure 3.2. The nominal diameter of roller is 110 mm. There are 24 square grooves on the roller surface to form square bars. The machine was operated at a rolling speed of 5 rev min<sup>-1</sup>, corresponding to the rolling velocity of 3.1×10<sup>-2</sup> ms<sup>-1</sup>. All the casting bars were rolled sequentially from 1 to 8 rolling passes. The cross sections and the rolling ratios of as-cast products to final products are presented in Figure 3.3. The casting bar after rolling was defined as rolling direction (RD), transverse direction (TD), and normal direction (ND), respectively.

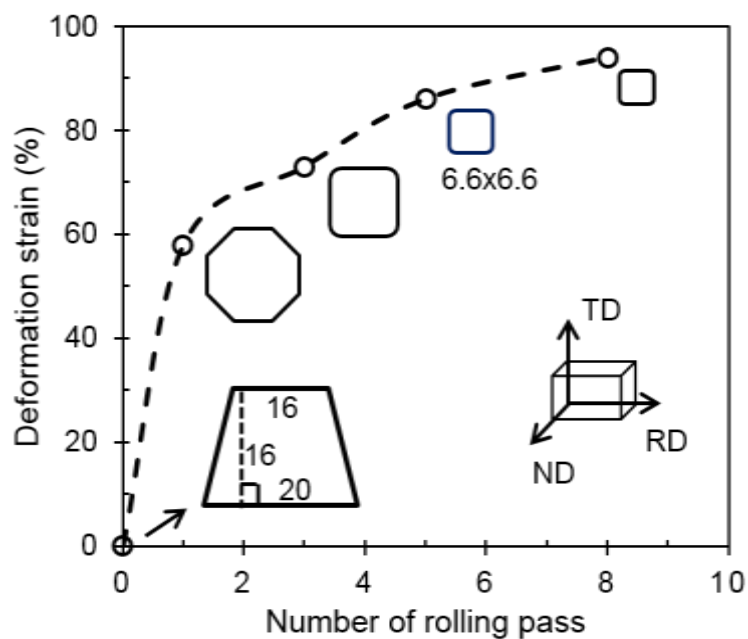


Figure 3.3 Schematic diagram showing the variation of cross section and the deformation strain ratios with increasing rolling passes (TD: transverse direction, ND: normal direction, RD: rolling direction).

## 3.2 Microstructure Characterization

### 3.2.1 Metallographic Surface Preparation

Metallographic microstructural examinations were conducted on the surfaces of cross sections of casting bars and on the surfaces of transverse (RD) and longitudinal (TD) cross sections of rolled samples. The casting bars or rolled specimen were sectioned with an abrasive cut-off wheel cutting machine. The sectioned specimens were then cold mounted at room temperature. The mounted specimens were ground and polished using a Buehler Automet ® 250 machine. Varied

grits of SiC abrasive papers (120#, 600#, 800#, 1200#, and 2400#) were used to grind the mounted samples. Silica suspension (OPS, 0.05 $\mu$ m water based SiO<sub>2</sub> suspension) was used to polish the samples for 10-15 min with a load of 5-10N depending on different samples. After polishing, specimens were cleaned in an ultrasonic bath (Engisonic B220) for 1-2 minutes to remove dirt from the surface. Figure 3.4 shows the mounted sample surfaces after polishing.



Figure 3.4 The photo of mounted specimens after polishing.

### 3.2.2 Optical Microscopy

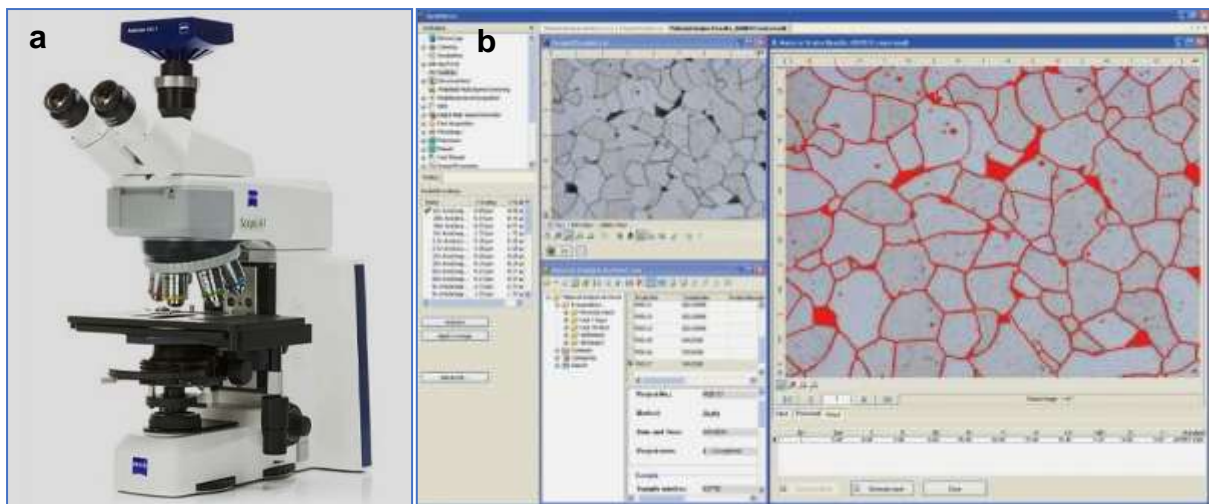


Figure 3.5 (a) Carl Zeiss AxioScope A1 optical microscope, and (b) the interface of AxioVision 4.9 image processing software.

A preliminary microstructure observation on the specimen surface including the morphology, dimension, and distribution of the primary phase and eutectics was conducted using a Carl Zeiss AxioScope A1 optical microscope (OM), equipped with an AxioCam MRm digital camera and an image processing software AxioVision 4.9, as shown in Figure 3.5. Various objective lenses of 2.5×, 5×, 10×, 20×, 50× and 100× were available with bright field and polarization field mode. The grain size, shape factor, and volume fraction could be measured by using the automatic measurement program in the AxioVision software. Manual adjustments for contrast, phase selection, and phase segregation were required during the automatic measurement. Five to ten different fields on the cross section of the sample were analysed from each specimen, and the average was taken as the actual measurement value.

### *3.2.3 Electron Microscopy*

#### **Scanning Electron Microscope**

A detailed microstructure examination including the morphology, size, and distribution of the secondary phases was performed using a Zeiss Supra 35 field-emission scanning electron microscope (SEM), equipped with energy dispersive X-ray spectroscopy (EDS) (Oxford Instruments, Oxfordshire, UK), as shown in Figure 3.6. The TEAM 4.3 software was used for processing EDS point analysis, line scan, and mapping. An accelerating voltage of 20 kV and working distance at 10-20 mm were used for the microstructure observation and element mapping.



Figure 3.6 The photo of Zeiss Supra 35VP field-emission SEM equipped with EDS and EBSD detectors.

## Electron Backscattered Diffraction

Detailed information of the microstructure of the rolled samples including grain sizes, boundary characteristics, and grain or phase orientations were obtained using the electron backscattered diffraction (EBSD) technique. The EBSD characterization was carried out on the Zeiss Supra 35VP SEM instrument equipped with a high speed and high sensitivity Hikari EBSD camera. TEAM 4.3 software was used for mapping operation and TSL Orientation Imaging Microscopy (OIM) 7.3 software (EDAX, NJ, USA) was used to acquire information on grain orientation and to identify grains with internal misorientation smaller than  $2^\circ$ .

The accelerated voltage used was 15 kV and working distance was 14-16 mm for both low magnification global mapping and local mapping at high magnification. The step size of EBSD mapping was in the range of 0.09-3.0 $\mu\text{m}$ , depending on the dimension of mapping area and the size of the target phases. The surface preparation for EBSD was conducted by SiC paper grinding and mechanical polishing using 0.05 $\mu\text{m}$  colloidal silica suspension. No electrochemical polishing was used. The samples were held in  $70^\circ$  pre-tilt sample holder. The clean-up method to orientation maps was performed using Grain CI Standardization (Grain Tolerance Angle: 3, and Minimum Grain Size: 2), giving very limited modification on original or actual results.

### 3.2.4 X-Ray Diffraction

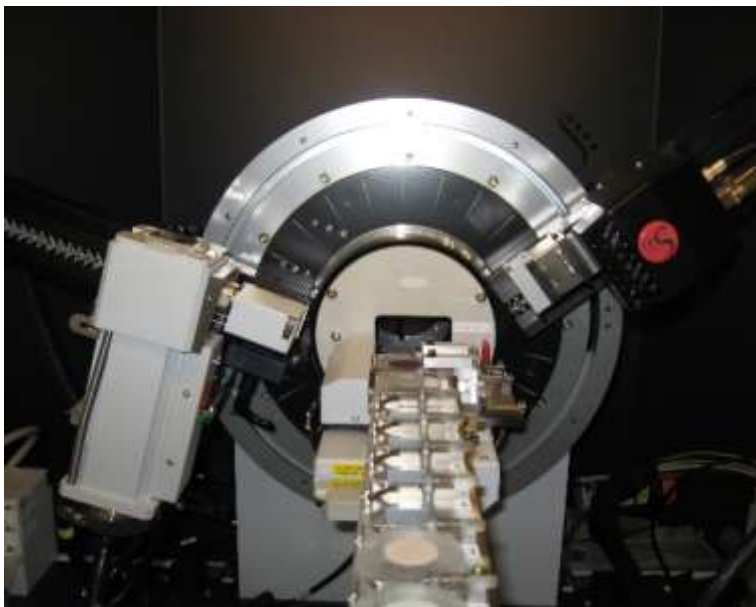


Figure 3.7 The photo of Bragg-Brentano geometry in Bruker X Ray diffractometer.

Phase identifications were carried out using X-ray diffraction (XRD) analysis on a Bruker D8 Advance (Figure 3.7) Cu-K $\alpha$  source on grinded sample surfaces. The 2 $\theta$  angle of XRD analysis was set between 20° to 90° with the step size of 0.01°/s and an overall scan time for each sample of approximately 115 min. The Bruker D8 Advance XRD was equipped with LYNXEYE high resolution energy-dispersive 1-D detector and DIFFRAC.SUITE software package for operation (Bruker, Coventry, UK).

### 3.3 Mechanical Property Measurements

#### 3.3.1 Tensile Tests

Tensile testing was conducted following the ASTM B577 standard using an Instron 5500 Universal Electromechanical Testing System equipped with Bluehill software and a  $\pm 50$  KN load cell, as shown in Figure 3.8. The samples for tensile tests were machined from the rolled bars (after rolling for 5 passes). The schematic of the samples for tensile tests is shown in Figure 3.9. The tensile results including yield stress, ultimate tensile strength, Young's modulus, and elongation were attained by the Bluehill software. All the tests were performed at ambient temperature (20°C) with a strain rate of  $2.0 \times 10^{-3} \text{ s}^{-1}$ . Each data reported was based on the average measurement obtained from 5 to 7 samples.

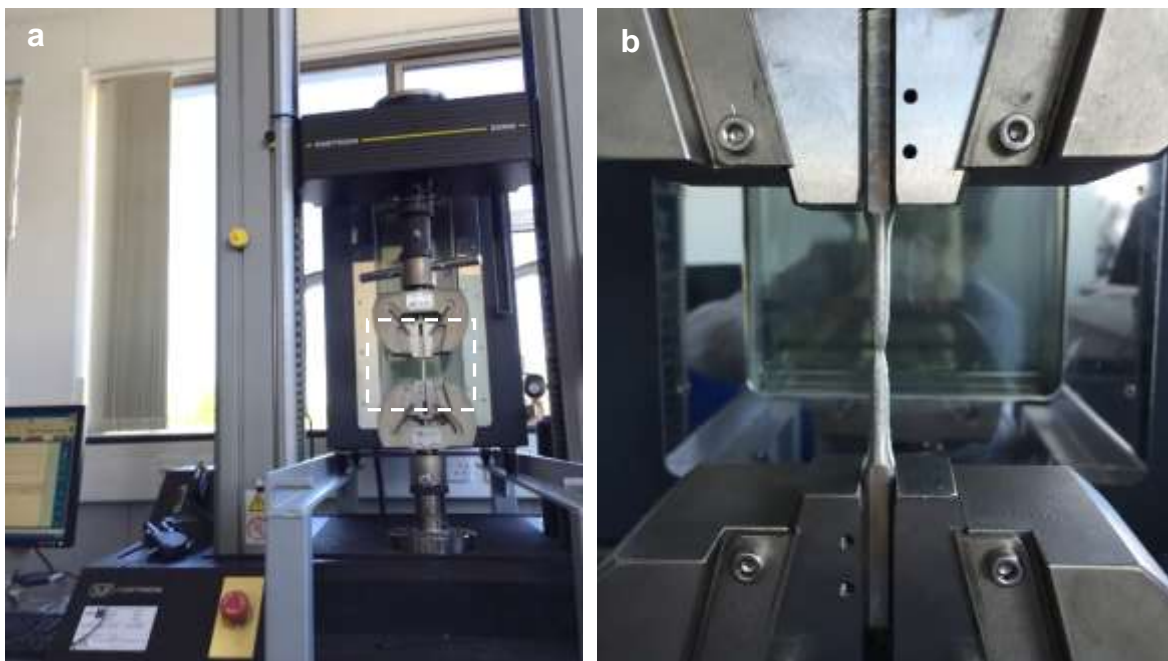


Figure 3.8 The photo of Instron® 5500 universal materials testing machine, (b) is corresponding to the rectangle area in (a).

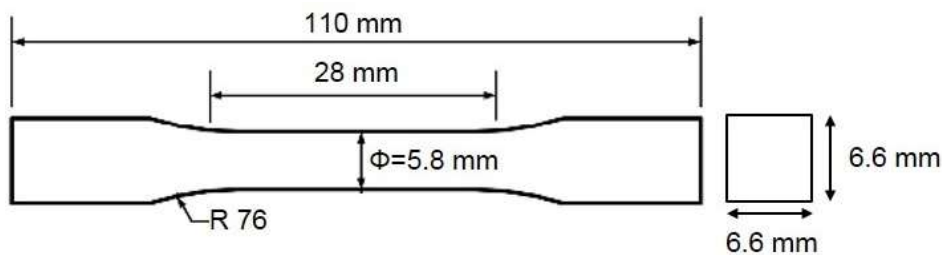


Figure 3.9 Schematic of the tensile testing samples according to the specification defined in the ASTM B557.

### 3.3.2 Vickers Harness

Vickers hardness tests were conducted on a Wilson 432 SVD digital auto turret macro Vickers Hardness Tester with a load of 10 N and for a dwell time of 10 s. Samples for Vickers hardness test were taken from the transverse cross section of both as-cast and as-rolled specimens following standard polishing procedures. All the hardness tests were performed at ambient temperature (20°C). All reported hardness values were based on average measurement from 8-10 indentations.

## 3.4 Electrochemical Measurements

Sn-3Zn and Sn-3Zn- $x$ Bi ( $x=1, 3, 5, \text{ and } 7$  wt.%) alloys were prepared for electrochemical corrosion tests. The specimens for electrochemical measurements were cut along the transverse cross section of casting bars, with a thickness of 8 mm. The working surface was mechanically ground with successive SiC paper from 400 to 4000 grits. The ground surface was then ultrasonically cleaned with distilled water and dried with high pressure air for corrosion tests.

### 3.4.1 Potentiodynamic Polarization

Electrochemical measurements were performed using EZstat NuVant Systems Inc. in 0.5 M NaCl solution at room temperature (20±2°C). The NaCl solution was prepared using analytical grade chemicals and distilled water, and was aerated by direct contact with the laboratory atmosphere. A conventional three-electrode cell configuration was employed to conduct the electrochemical measurements with the Sn-Zn-Bi alloy as working electrode, as shown in Figure 3.10. A Pt spiral wire was used as the counter electrode, and the reference electrode used in this study was saturated calomel electrode (SCE, saturated KCl). Working surface of the electrode exposed to the solution was approximately 1.0 cm<sup>2</sup>. Potentiodynamic polarization

curves were acquired by stepping the potential at a scan rate of 0.166 mV/s, from  $-250$  mV to  $+1000$  mV with respect to the OCP.

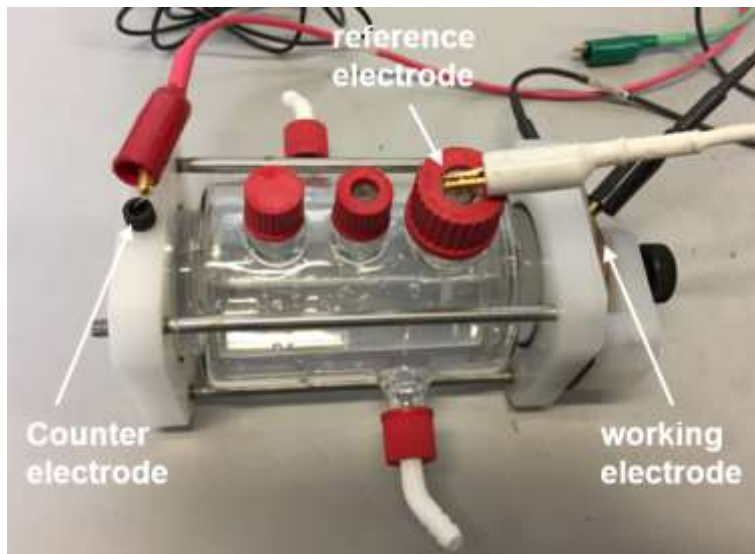


Figure 3.10 The three-electrode cell configuration.

### 3.4.2 Electrochemical Impedance Spectroscopy

Electrochemical impedance spectroscopy (EIS) curves were obtained at the open circuit potential over a frequency range from 10 mHz -100 kHz with an applied sinusoidal perturbation of 10 mV RMS (root-mean-square) potential. Prior to potentiodynamic polarization and the EIS tests, a 60-min OCP test was conducted to ensure that the working surface has reached a relatively stable state. The experimental EIS spectra were interpreted on the basis of equivalent electrical circuit using the program Zview to obtain the fitting parameters.

### 3.5 Numerical Simulation and Proof Test

Numerical simulations were conducted using Ansys 19.0 AUTODYN 2D to examine the cutting performance of the MDCs against aluminium and acrylic targets. The effects of explosives, sheath materials, stand-off distance, and target material on the cut depths were investigated. Four components including the explosive, sheath, air, and target were modelled in the simulation. As the entire elements in the model have the characteristics of axial and planar symmetry, a two-dimensional model was used in simulations to improve the computational efficiency.

To verify the successful development of Sn-based cords, the final Sn-Zn-Bi sheathed miniature detonating cords against acrylic and aluminium targets were proofed in the manufacturing sites.

## **Chapter 4 Microstructure and Mechanical Properties of Sn-Cu Alloys for Miniature Detonating Cords**

### **4.1 Introduction**

In consideration of the potential candidates reviewed in literatures (Chapter 2), and similar mechanical properties of Sn-Cu eutectic solders with lead-based soldering alloys, Sn-Cu alloys were selected for the first trial, aiming to assess the feasibility of developing Sn-Cu as the sheath or cladding material of the miniature detonating cords (MDCs). It notes that although Sn-Cu alloys have been extensively used as soldering and electronic packaging materials, majority of the research on the Sn alloys were focused on the soldering properties, such as wettability and melting properties. There was limited work on the quantitative analysis among the composition, processing, microstructure and mechanical properties, which is particularly important in the applications as the sheath materials for MDCs in aerospace industry.

As such, four alloys including Sn-0.3wt.%Cu, Sn-0.5wt.%Cu, Sn-0.7wt.%Cu, and Sn-1.0wt.%Cu were prepared by casting, followed by rolling at room temperature. The experimental exercise in the present chapter investigated the microstructure and the mechanical properties of Sn-Cu alloys with different compositions and different processes from casting to rolling, in efforts to replicate current designs and manufacturing techniques with lead-free alloys for economical solution. The examination and understanding of the relationship between the composition, processing, microstructure and mechanical properties will pioneer the research in new applications. Emphasis is put on the microstructural evolution, and the strain softening of Sn-Cu alloys and the relationship between microstructure and mechanical properties.

### **4.2 Microstructure and Hardness of As-cast Sn-Cu Alloys**

#### *4.2.1 Solidification Microstructure*

Table 4.1 shows the actual compositions of the experimental Sn-Cu alloys. It is observed that the actual compositions of the castings are close to the nomination compositions. The Sn-1.0wt.%Cu alloy is obtained directly from sectioning the master alloy bar.

Table 4.1 Chemical compositions of the experimental Sn-Cu alloys analysed by inductively coupled plasma atomic emission spectroscopy (ICP-AES).

Alloys	Sn	Cu	Zn	Ni	Bi	Fe	Sb	As	Cd
Sn-0.3wt.%Cu	Rem	0.29	0.03	0.01	0.014	0.01	0.03	0.011	0.005
Sn-0.5wt.%Cu	Rem	0.49	0.03	0.01	0.015	0.01	0.02	0.014	0.006
Sn-0.7wt.%Cu	Rem	0.74	0.02	0.01	0.015	0.01	0.02	0.015	0.007
Sn-1.0wt.%Cu	Rem	0.99	0.03	0.01	0.01	0.01	0.03	0.009	0.006

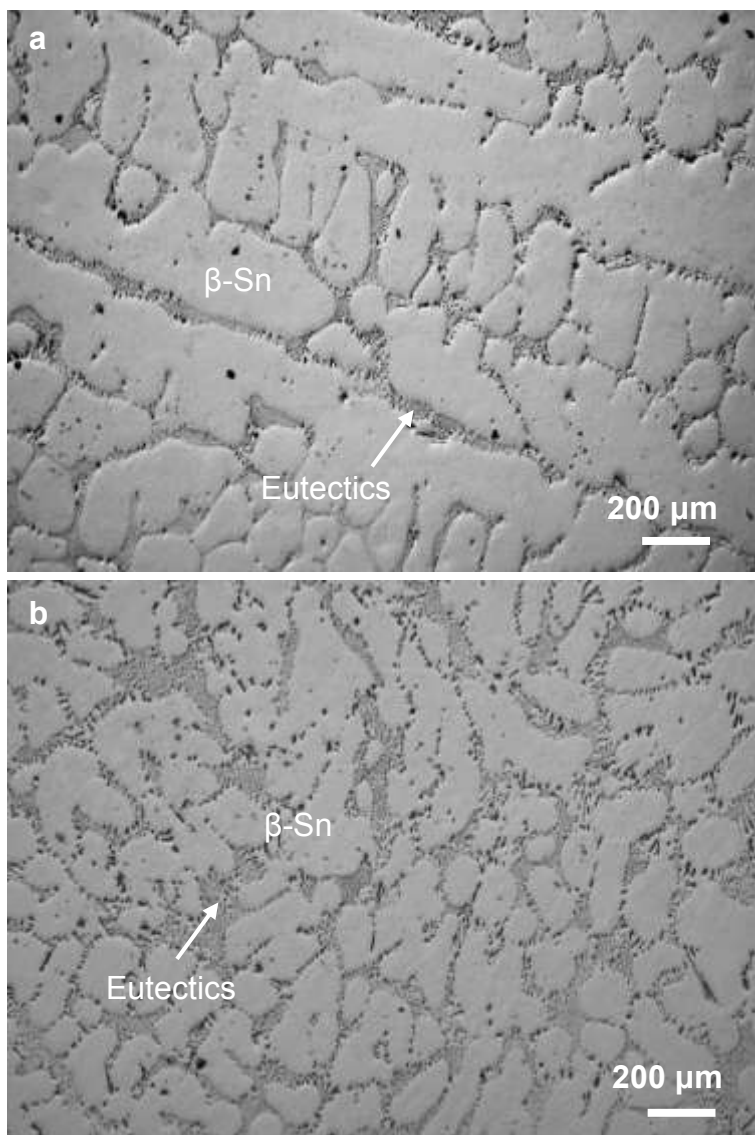


Figure 4.1 Optical micrographs showing the as-cast microstructure of (a) Sn-0.3wt.%Cu, and (b) Sn-0.5wt.%Cu alloys.

Figure 4.1 presents the optical micrographs, showing the size, morphology and distribution of the primary  $\beta$ -Sn phase in the as-cast microstructure of the Sn-0.3wt.%Cu and Sn-0.5wt.%Cu alloys. It was observed that the  $\beta$ -Sn phase was the primary phase with dendritic morphology in Sn-Cu hypoeutectic alloys when Cu was added at 0.3 and 0.5 wt.%. The primary  $\beta$ -Sn phase showed a morphology of long and narrow dendrites when the Cu contents was at 0.3wt.% (Figure 4.1a). With increasing the Cu contents, the primary Sn phase of Sn-0.5wt.%Cu showed a morphology of finer equiaxial grains (Figure 4.1b).

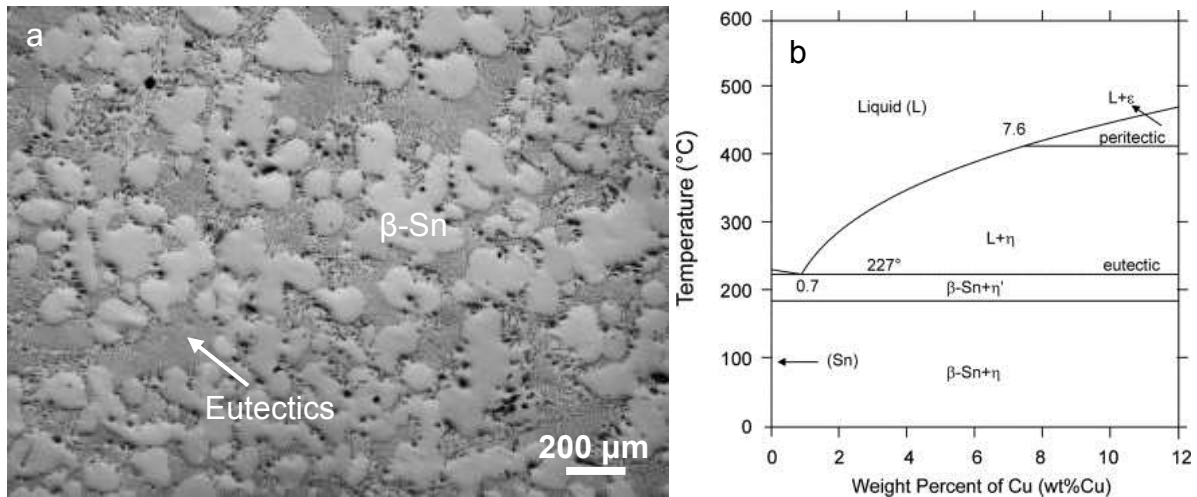


Figure 4.2 (a) Optical micrographs showing the as-cast microstructure of Sn-0.7wt.%Cu alloy, (b) partial phase diagram of the Sn-Cu binary system [93].

Figure 4.2a presents the optical micrographs, showing the size, morphology and distribution of the primary  $\beta$ -Sn phase in the as-cast microstructure of the Sn-0.7wt.%Cu alloy, which was at eutectic composition according to the equilibrium phase diagram [93], as shown in Figure 4.2b. In addition to the conventional lamellae eutectic microstructure, it was found the existence of primary Sn phase in the morphology of globular rosettes with sizes of 100-150 $\mu\text{m}$ . It is noted that the primary Sn dendrites display in the form of  $\beta$ -Sn phase which has a body centred tetragonal (BCT) crystal structure. In the case of Sn based alloys such as the Sn-Cu alloy, the  $\beta$ -Sn phase is not fully (100%) made of Sn atoms, instead, there are small amounts of solutes atoms (Cu atoms in the Sn-Cu alloy) which are incorporated in the Sn crystal lattice, despite the tiny amount. On top of the BCT-structured  $\beta$ -Sn phase, Sn has another phase structure which displays in the form of  $\alpha$ -Sn. The  $\alpha$ -Sn has the crystal structure of face centred diamond cubic (FCDC). Normally, when the temperature is below 13  $^{\circ}\text{C}$ , the BCT-structured Sn ( $\beta$ -Sn) can be transformed into FCDC-structured Sn ( $\alpha$ -Sn) [93]. However, this is only the case for extremely high purity Sn. If the impurities like Cu, Zn etc was included, the transformation

temperature could be largely reduced to below 0 °C. This is the reason that no  $\alpha$ -Sn phase was recognised in the Sn-Cu phase diagram (Figure 4.2b). Also, it is worthy to note that in the present study no  $\alpha$ -Sn phase will be mentioned because this phase will be hardly formed in the investigated Sn alloys.

When the Cu concentration was further increased to 1.0 wt.% (Figure 4.3), the alloys were at hypereutectic composition according to the equilibrium phase diagram [93], and the primary  $\text{Cu}_6\text{Sn}_5$  phase was expected to be the primary phase. However, there was no primary  $\text{Cu}_6\text{Sn}_5$  phase being observed in the matrix except the fact that the microstructure became finer than the hypoeutectic Sn-Cu compositions. This similar phenomenon was also observed by Shen et al. [94], which might be associated with the high cooling rate during solidification. The further interpretation will be given next.

Figure 4.4 illustrates the relationship between the Cu contents and the grain size of primary  $\beta$ -Sn phase for the as-cast structures of Sn-Cu alloys. It is obvious that the grain size was decreased with increasing the Cu contents. The grain size in the Sn-0.3wt.% Cu alloy was 250 $\mu\text{m}$ . It was 146 $\mu\text{m}$  and 126 $\mu\text{m}$ , respectively, when Cu was at 0.5 and 0.7 wt.%, respectively. The grain size was further decreased to 63 $\mu\text{m}$  in the alloy with 1.0 wt.% Cu.

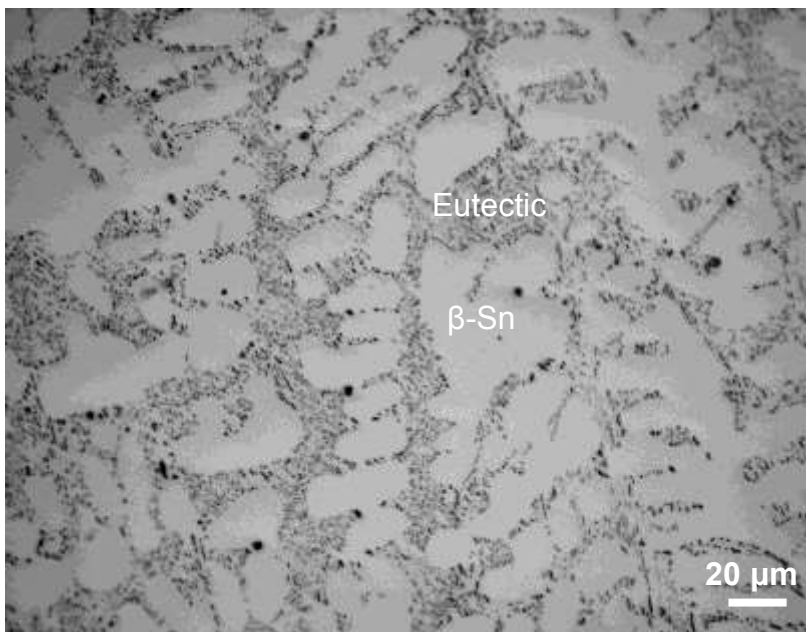


Figure 4.3 Optical micrographs showing the as-cast microstructure of Sn-1.0wt.%Cu alloy.

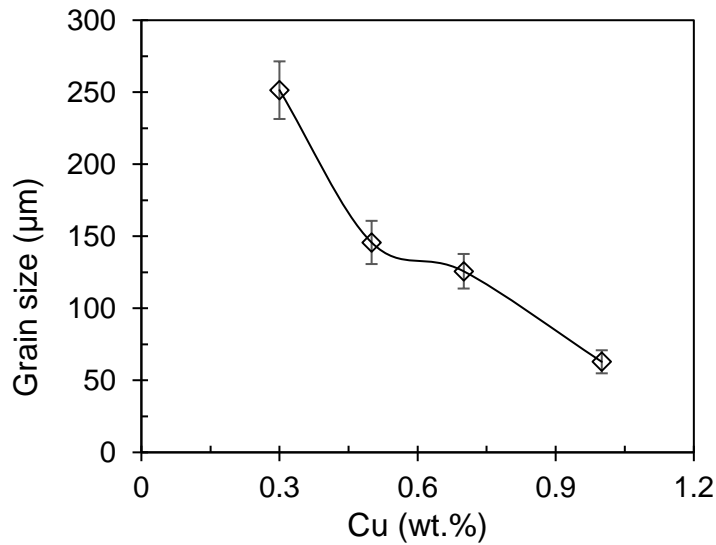


Figure 4.4 Effect of Cu contents on the grain size of primary  $\beta$ -Sn phase for the as-cast Sn-Cu alloys.

Figure 4.5 shows the XRD profiles of the as-cast Sn-Cu alloys with different Cu contents. Two types of peaks corresponding to primary  $\beta$ -Sn phase and  $\text{Cu}_6\text{Sn}_5$  phase were recognized. The eutectic intermetallic phase was identified as  $\text{Cu}_6\text{Sn}_5$  (JCPDS No.04-0673).

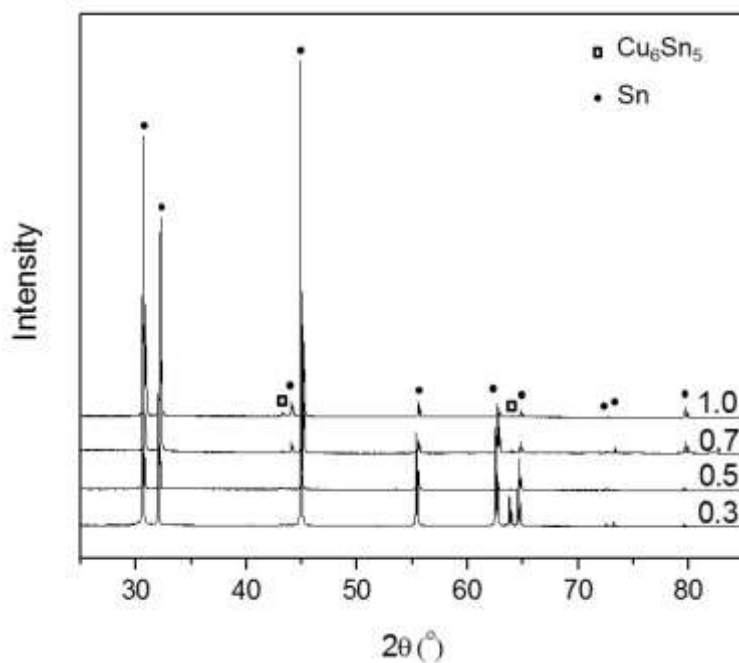


Figure 4.5 XRD patterns for the as-cast Sn-Cu alloys with 0.3, 0.5, 0.7, and 1.0 Cu (wt.%). The JCPDS No for  $\text{Cu}_6\text{Sn}_5$  is 04-0673.

Figure 4.6 shows the backscattered SEM micrographs for the morphology and size of the intermetallic phase in the Sn-0.3wt.%Cu alloy, in which Figure 4.6b and c is the enlargement of the rectangular regions in Figure 4.6a. The intermetallic phase was identified as  $\text{Cu}_6\text{Sn}_5$  compound, displaying a needle-like morphology with the diameter of approximately  $2\mu\text{m}$  and the length of  $10\text{-}20\mu\text{m}$ . The eutectic spacing was measured as  $3\text{ to }5\mu\text{m}$ , and the eutectic region took up a small volume proportion of the structure.

Figure 4.7 shows the backscattered SEM micrographs for the morphology and size of the intermetallic phase in the Sn-0.7wt.%Cu alloy, in which Figure 4.7b and c is the enlargement of the rectangular regions in Figure 4.7. In comparison with Sn-0.3wt.%Cu alloy, the volume fraction of the  $\text{Cu}_6\text{Sn}_5$  intermetallic phase was increased. However, the morphology and the size of the intermetallic phase in both Sn-Cu alloys were similar, resulting in the intermetallic phase showing a needle-like morphology with the diameter of approximately  $2\mu\text{m}$  and the length of  $10\text{-}30\mu\text{m}$ . The eutectic spacing was measured as  $2\text{ to }5\mu\text{m}$ .

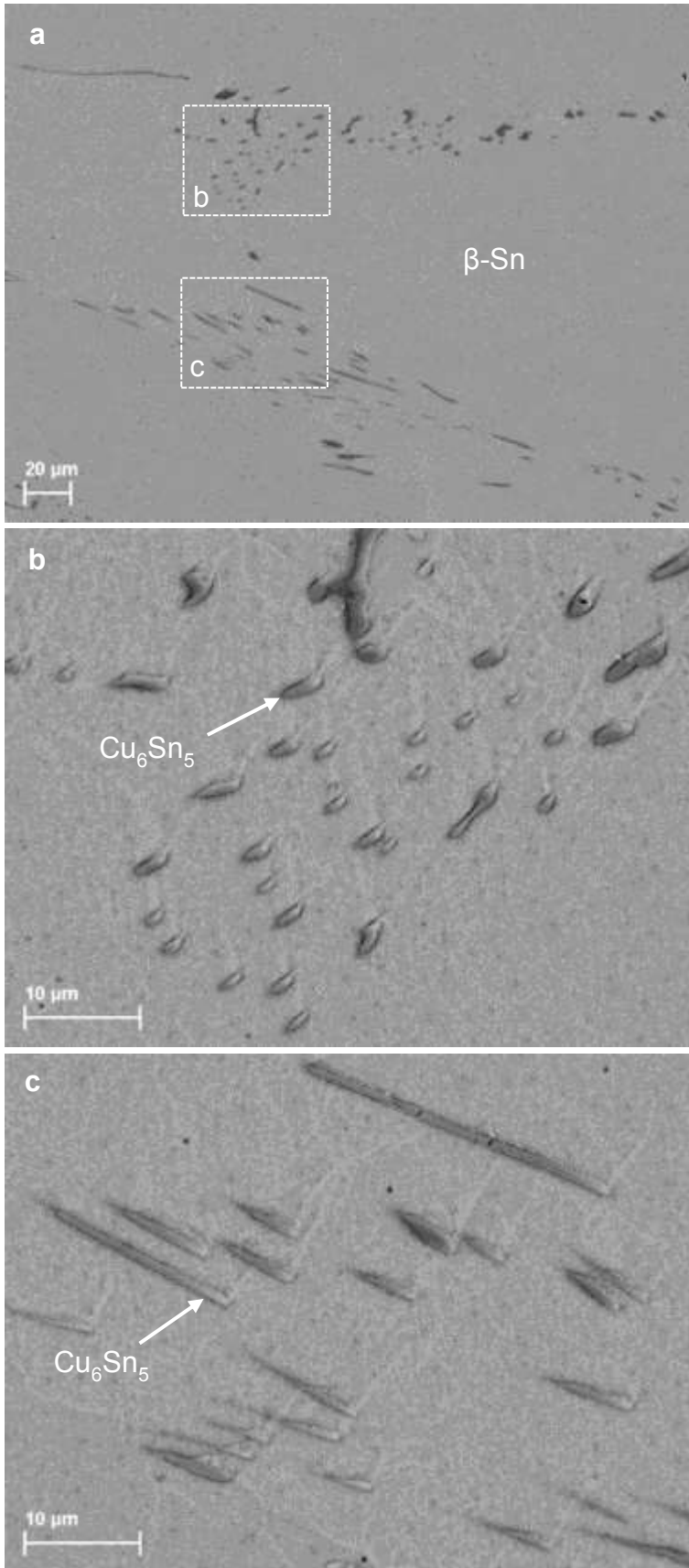


Figure 4.6 Backscattered SEM micrographs showing the morphology of eutectic and intermetallic phases in the as-cast Sn-0.3wt.%Cu alloy.

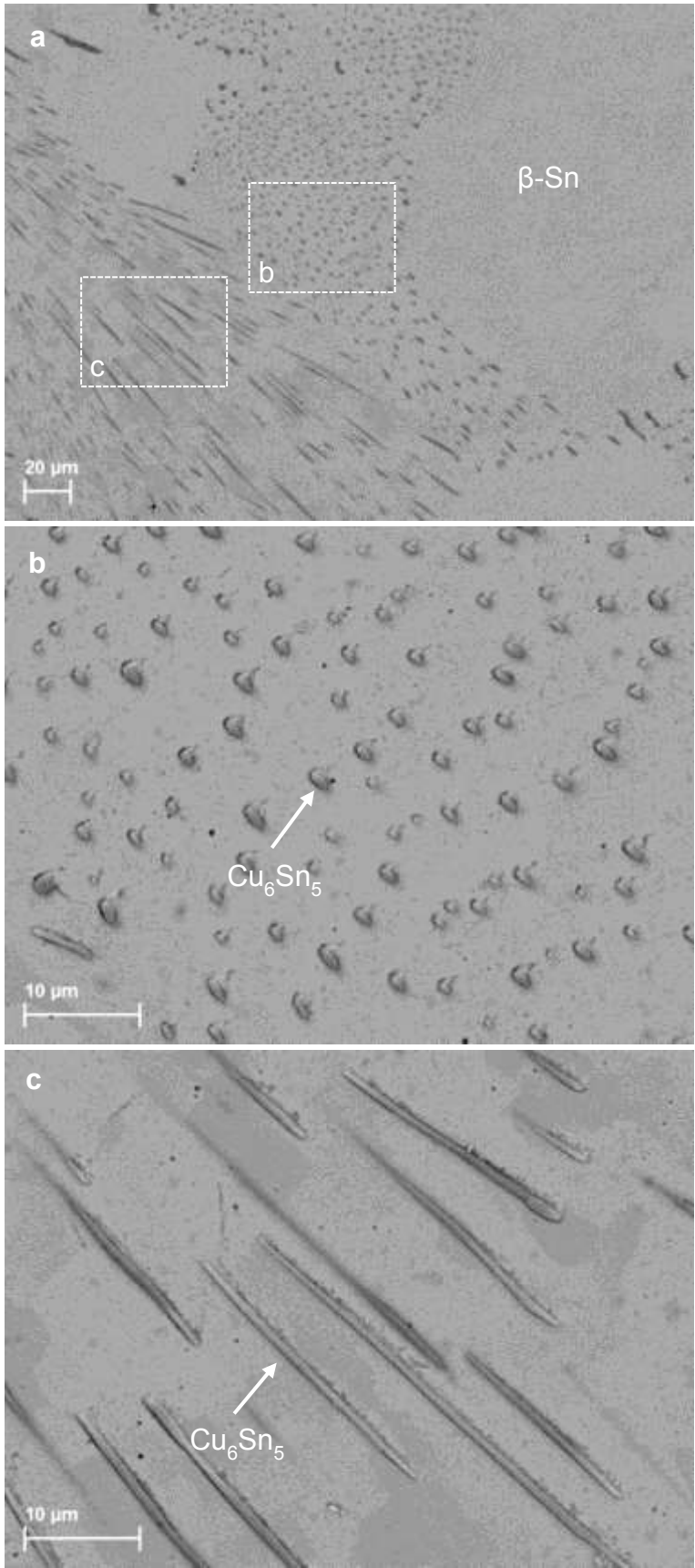


Figure 4.7 Backscattered SEM micrographs showing the morphology of eutectic and intermetallic phases in the as-cast Sn-0.7wt.%Cu alloy.

The solidification path and microstructural evolution can be understood through the equilibrium phase diagram of Sn-Cu system [95], as shown in Figure 4.2b. When the Cu contents are 0.3 wt.% and 0.5 wt.%, Sn-Cu alloys are solidified as hypoeutectic alloys, following the phase transformation:  $L \rightarrow L + \text{primary } \beta\text{-Sn} \rightarrow \text{primary } \beta\text{-Sn} + \text{Eutectic (Sn+Cu}_6\text{Sn}_5)$ . When Cu is 0.7 wt.%, the solidification follows the phase transformation:  $L \rightarrow \text{Eutectic (Sn+Cu}_6\text{Sn}_5)$ . When Cu is increased to 1.0 wt.%, the hypereutectic reaction is  $L \rightarrow L + \text{primary Cu}_6\text{Sn}_5 \rightarrow \text{primary Cu}_6\text{Sn}_5 + \text{Eutectic (Sn+Cu}_6\text{Sn}_5)$ . Therefore, the different solidification paths form different as-cast microstructures. The eutectic  $\text{Cu}_6\text{Sn}_5$  is formed in all the experimental alloys. However, the different Cu contents can form different amounts of eutectics [96, 97]. In the present research, the volume fraction of Sn- $\text{Cu}_6\text{Sn}_5$  eutectic is proximately 31% for Sn-0.3 wt.% Cu alloy, 33% for Sn-0.5wt.%Cu, 36% for Sn-0.7wt.%Cu alloy, and 51% for Sn-1.0wt.%Cu alloy. The eutectic spacing is similar in the different experimental alloys, which implies that the cooling rate during solidification is at a similar level according to the Jackson-Hunt models [98].

It is interesting to note that the microstructure in the eutectic Sn-0.7wt.%Cu alloy shows a large volume fraction of primary  $\beta\text{-Sn}$  phase (around 64%). Generally, under equilibrium condition, the solidification microstructure of eutectic Sn-0.7wt.%Cu alloy should show the regular Sn- $\text{Cu}_6\text{Sn}_5$  eutectic while the microstructure of the experimental Sn-0.7wt.%Cu alloy is characterized by mainly primary  $\beta\text{-Sn}$  phase. This phenomenon was also observed in high speed solidification of Sn-Cu and other binary systems [99, 100]. At a high cooling rate, ‘off-eutectic’ structure (primary dendrites and eutectics) are likely to be observed, although the alloy is at eutectic composition. This could be interpreted by a coupled zone theory [101, 102]. The coupled zone is defined as a region (in a phase diagram) of alloy compositions and interface temperatures, inside which the microstructure is wholly composed of eutectics, i.e. without primary dendrites. In the coupled zone theory, the principle of competitive growth between primary dendrites and eutectics has been widely used to describe the special structure (with eutectic only or eutectic and a primary phase). The affecting factors during solidification include the growth rate, melt composition, and temperature gradient [103].

#### 4.2.2 Vickers Hardness

Figure 4.8 shows the Vickers hardness of the as-cast Sn-Cu alloys with different Cu contents. Hardness was measured with load=1.0 kg, dwell time=10 s, at 15 indentations and the average value was applied. The actual indentation sizes were in the range of 300-500  $\mu\text{m}$ , depending

on the hardness at different locations and samples. 2 to 5 grains were covered by the indentation, depending on testing position and sample grain size. The hardness was at a similar level of HV8.5 ( $HV_{1/10}=8.5$ , load=1.0 kg, dwell time=10 s) for the alloys with 0.3, 0.5 and 0.7wt.%Cu, but it was increased to HV9.6 when Cu was at 1.0wt.%. By considering the microstructures discussed in previous, the microstructure with more eutectics and finer microstructure provided higher hardness.

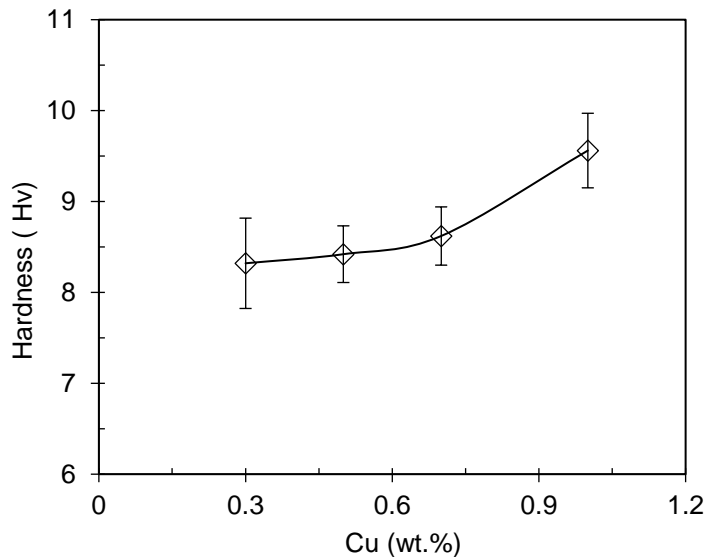


Figure 4.8 Effect of Cu contents on the Vickers hardness of as-cast Sn-Cu alloys.

### 4.3 Microstructure and Mechanical Properties of Sn-Cu Alloys after Rolling

#### 4.3.1 Microstructural Evolution of Sn-1.0wt.%Cu during Rolling

Figure 4.9 presents the microstructural evolution of Sn-1.0wt.%Cu alloy during rolling after 1, 5 and 8 passes, in which the microstructures across the transverse direction are shown in Figure 4.9a, c and e, and the microstructures across the rolling direction are shown in Figure 4.9b, d and f. After rolling one pass (Figure 4.9a and b), the primary  $\beta$ -Sn phase and the Sn-Cu<sub>6</sub>Sn<sub>5</sub> eutectic were deformed along the rolling direction, resulting in the formation of elongated  $\beta$ -Sn phase. However, the outline/interfaces of the primary  $\beta$ -Sn phase and eutectic cells were clearly visible.

After rolling 5 passes (Figure 4.9c and d), the size of primary  $\beta$ -Sn dendrites was dramatically decreased and the microstructure became much finer, although the elongated grains were still visible. The Cu<sub>6</sub>Sn<sub>5</sub> intermetallic was re-distributed and became less heterogeneity in the matrix. The thickness of  $\beta$ -Sn grains and eutectic cells were reduced, but the laminar structure

distribution was still clear. Further rolling 8 passes (Figure 4.9e and f), a severely deformed microstructure was observed and the  $\beta$ -Sn grains were much refined. The  $\text{Cu}_6\text{Sn}_5$  intermetallic was mixed with the primary  $\beta$ -Sn phase and the laminar feature disappeared.

After analytical measurements by using polarized optical micrographs, the size of grain can be obtained for different rolling passes. After rolling one pass, the  $\beta$ -Sn grains size was at a level of  $45\mu\text{m}$ . The grain sizes become  $25\mu\text{m}$  and  $10\mu\text{m}$  when rolling 5 passes and 8 passes, respectively. In comparison with the as-cast microstructure, it is significant in the grain refinement by rolling.

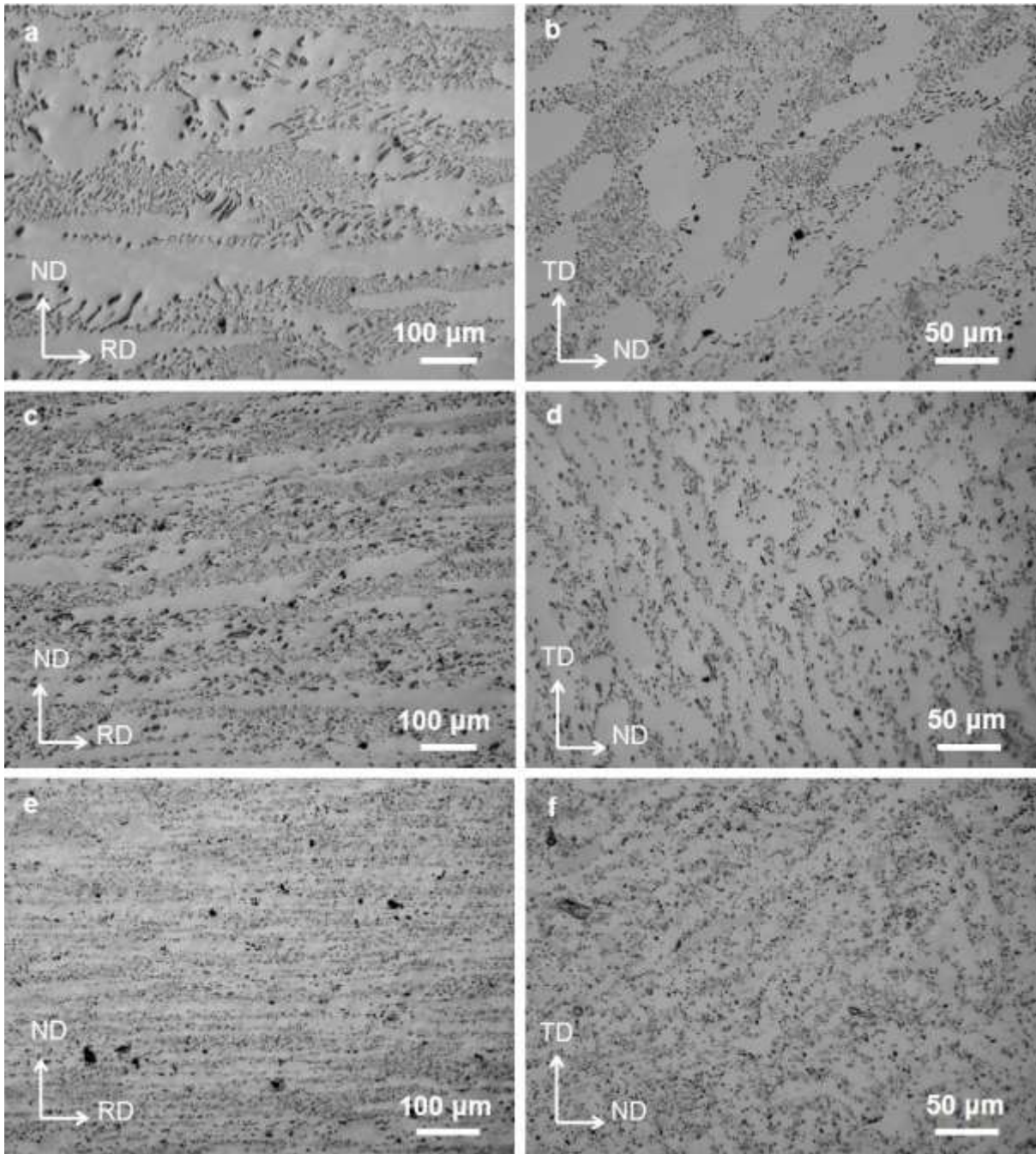


Figure 4.9 Optical micrographs showing the microstructure on the cross section of TD and RD of the as-rolled Sn-1.0wt.%Cu alloy after rolling for different passes: (a, b) 1 pass, (c, d) 5 passes, (e, f) 8 passes.

Figure 4.10 presents the backscattered SEM micrographs, showing the detailed morphological evolution of the  $\text{Cu}_6\text{Sn}_5$  intermetallic phase in the Sn-1.0wt.%Cu alloy after rolling for 1 and 5 pass(es). After rolling one pass, the cracks were seen in the needle-like  $\text{Cu}_6\text{Sn}_5$  intermetallic phase. However, the broken needles were still stacked together as short rods, as marked by the arrows in Figure 4.10a. After rolling 5 passes (Figure 4.10b), the short  $\text{Cu}_6\text{Sn}_5$  intermetallic

rods were further broken into smaller segments and separated each other in the matrix. The size of  $\text{Cu}_6\text{Sn}_5$  intermetallic was ranged from 1 to  $6\mu\text{m}$  with an average of  $3\mu\text{m}$ . It was noted that the segmented intermetallic were not refined after further rolling. The size was maintained stable after rolling 5 passes.

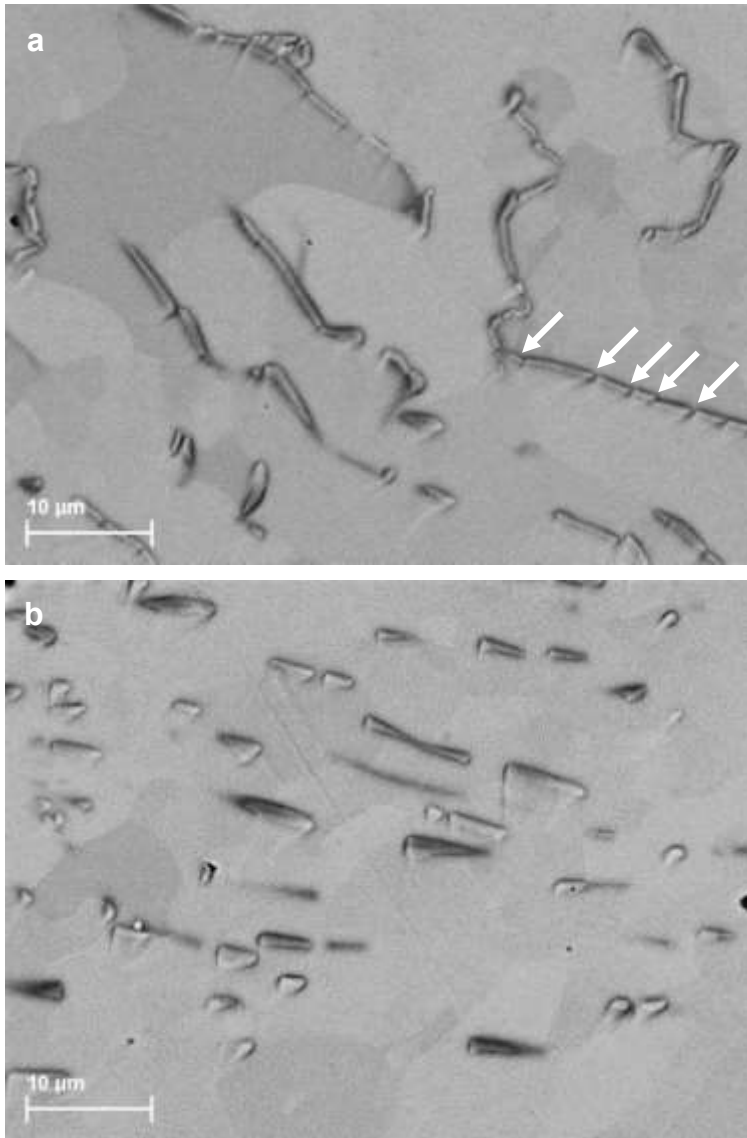


Figure 4.10 Backscattered SEM micrographs showing  $\text{Cu}_6\text{Sn}_5$  intermetallic morphology on the cross section of ND of the Sn-1.0wt.%Cu alloy after rolling for (a) 1 pass, and (b) 5 passes.

#### 4.3.2 Mechanical Properties of the Sn-Cu Alloys after Rolling

Figure 4.11 shows the Vickers hardness of Sn-1.0wt.%Cu alloy after rolling for 1, 3, 5, and 8 passes. The hardness is observed to experience a constant increase with increasing the rolling pass. In brief, the hardness was increased by 10.4% from HV9.6 after one rolling pass to HV10.6 after 8 rolling passes. The significant change in the microstructure of the rolled alloy

might alter the mechanical properties. Figure 4.12 presents the measured Vickers hardness against the grain scale,  $d^{-1/2}$ ,  $d$  refers to primary  $\beta$ -Sn grain size. for the experimental Sn-Cu alloys under as-rolled condition. The grain sizes and the hardness of as-rolled Sn-Cu alloys with different Cu contents can be well fitted with linear lines. Clearly, the increased solute contents and the finer grain sizes offer higher hardness.

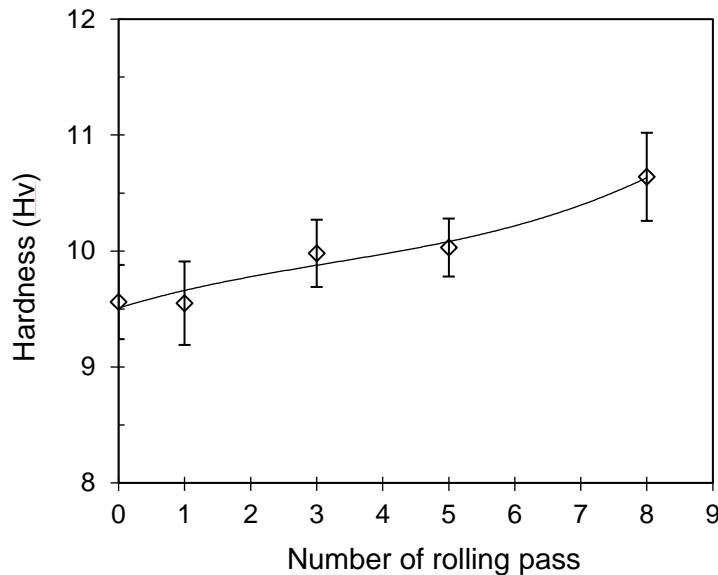


Figure 4.11 Effect of rolling on the Vickers hardness of Sn-1.0wt.%Cu alloy.

The tensile properties of Sn-Cu alloys after rolling 5 passes was measured and the stress-strain curves are shown Figure 4.13. The increased Cu contents led to significant increase of strength and significant decrease of elongation in the Sn-Cu alloys. The detailed tensile results are summarised in Figure 4.14. The UTS of Sn-0.3wt.%Cu alloy was 30.1MPa, which was increased to 34.0MPa and 51.5MPa when Cu was 0.5 wt.% and 1.0wt.%. Similarly, the yield strength of 26.1MPa for the Sn-0.3wt.%Cu alloy was increased to 31.9MPa for the Sn-0.5wt.%Cu alloy and 50.8MPa for the Sn-1.0wt.%Cu alloy. However, the elongation was decreased from 87.5% for the Sn-0.3wt.%Cu alloy to 86.4% for the Sn-0.5wt.%Cu alloy and further to 56.0% for the Sn-1.0wt.%Cu alloy.

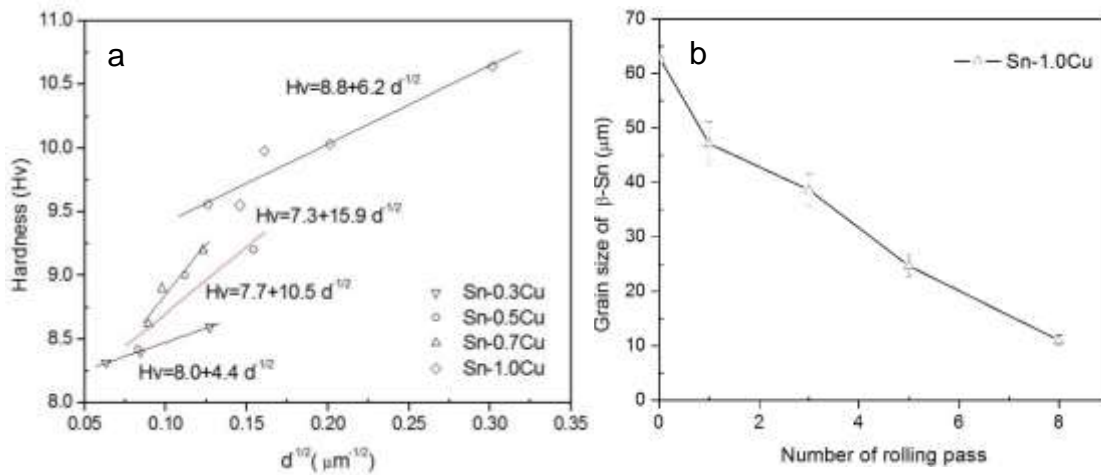


Figure 4.12 (a) The relationship between the Vickers hardness and grain scale,  $d^{1/2}$ , of the Sn-Cu alloys with Cu contents of 0.3, 0.5, 0.7, and 1.0wt.%. (b) Variation of grain scale,  $d$ , with the rolling passes for the Sn-1.0Cu alloy.

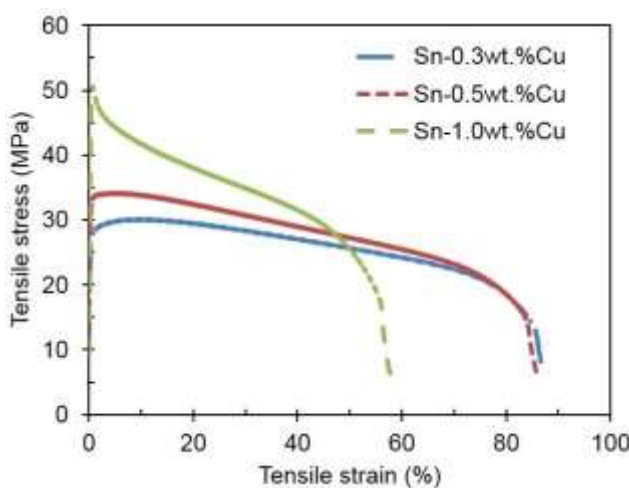


Figure 4.13 Tensile stress-strain curves for different Sn-Cu alloys after rolling 5 passes.

More interestingly, it was found that strain softening instead of strain hardening has occurred for all specimens during tensile process (Figure 4.13). This is consistent with the results obtained by others for directionally solidified Sn-1.0wt.%Cu alloy [104, 105]. It should be emphasized that strain softening is particularly important for the specific application as miniature detonating cords because the further processing is essentially required after assembly with high-energy explosive materials. The strain hardening can prevent the material deformation to the final gauge and extra annealing is avoided, which is one of the most dangerous operation because of the explosive materials are very unstable at high temperature of heat treatment. Therefore, the strain softening is desirable characteristics for the processing of detonating cords.

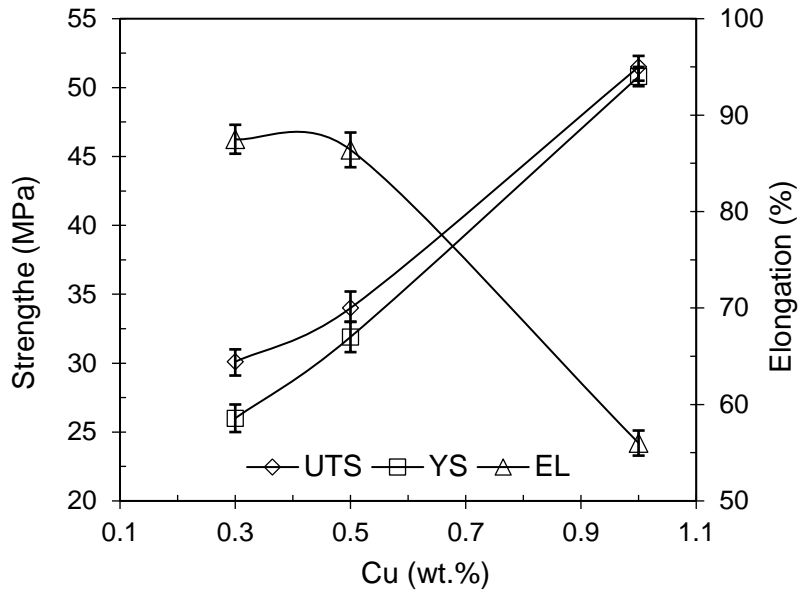


Figure 4.14 Effect of Cu contents on the tensile properties of Sn-Cu alloys after rolling 5 passes.

#### 4.3.3 Fractrograph Characterization

Figure 4.15 shows the SEM fractrographs of the Sn-0.3wt.%Cu, Sn-0.5wt.%Cu, and Sn-1.0wt.%Cu alloys after rolling 5 passes. Numerous dimples were observed on the fractured surfaces of the three alloys, confirming the ductile fracture mechanism. The dimples in the Sn-0.3wt.%Cu alloy were large and deep, showing an average dimple size  $> 28\mu\text{m}$  (Figure 4.15a and b). With increasing the Cu content to 0.5 wt.% (Figure 4.15c and d) and 1.0 wt.% (Figure 4.15e and f), dimples became smaller. The average dimple size in the Sn-1.0wt.%Cu alloy was at a level of  $20\mu\text{m}$ . As shown in Figure 4.14, the strength was higher and the ductility was lower for the Sn-Cu alloys with higher Cu contents. Therefore, the finer dimples could enhance the tensile strength.

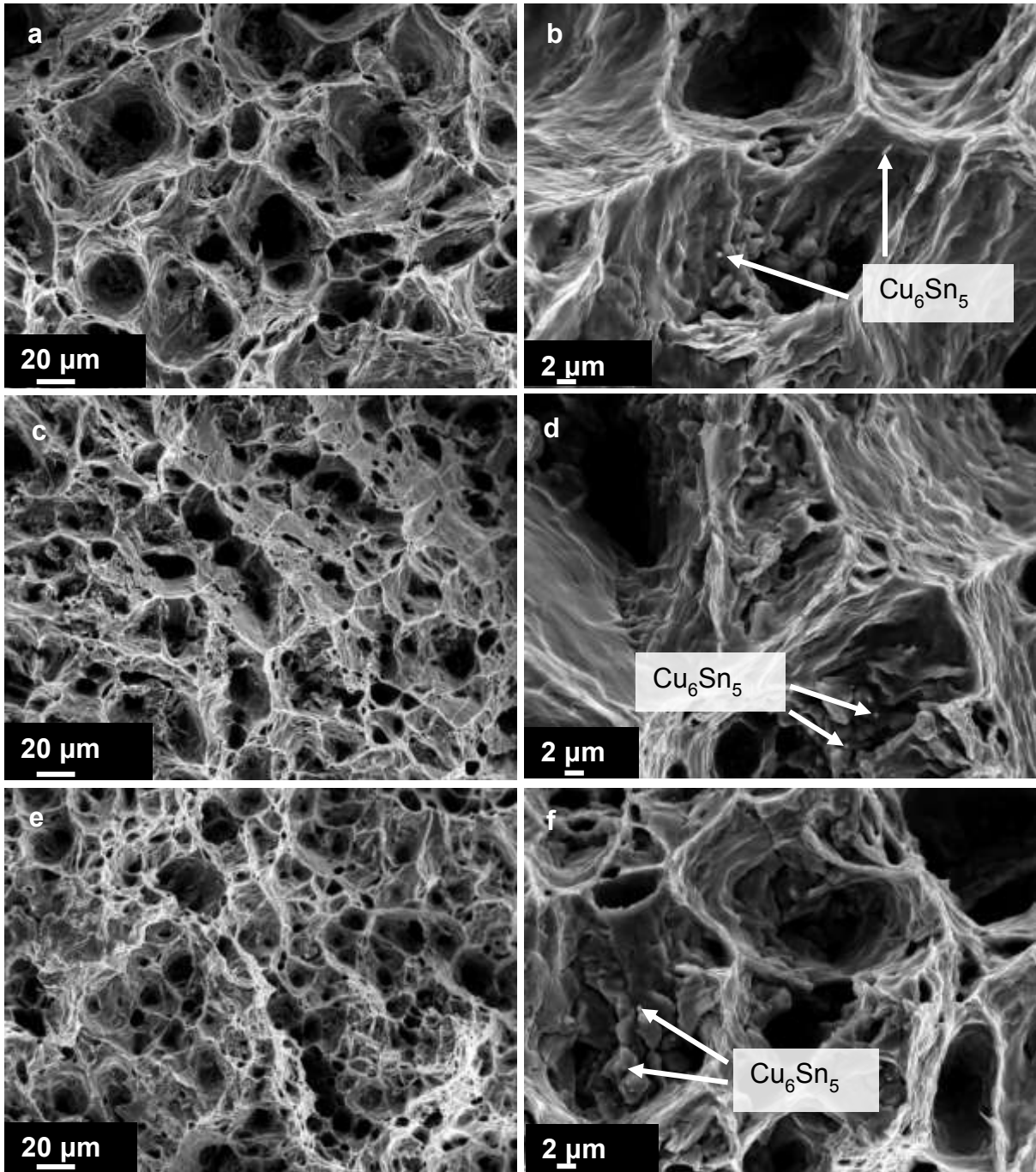


Figure 4.15 SEM fractographs for Sn-Cu alloys after rolling 5 passes, (a, b) Sn-0.3wt.%Cu, (c, d) Sn-0.5wt.%Cu, and (e, f) Sn-1.0wt.%Cu.

## 4.4 Relation between Microstructure and Mechanical Properties

### 4.4.1 Strengthening in Sn-Cu Alloys

The experimental results have confirmed that (1) the increased Cu contents can increase the strength, but reduce the ductility of Sn-Cu alloys, and (2) the rolling can increase the strength. These are associated with the strengthening mechanisms in the Sn-Cu alloys processed under different conditions.

The strengthening can be roughly described as solution strengthening, second phase strengthening, and grain size strengthening. Under equilibrium conditions, the solid solubility of Cu in Sn is very limited with the value of 0.0063 wt.% for Cu at the eutectic temperature [106]. During casting, the increased cooling rates for non-equilibrium solidification can promote the extension of solid solubility for higher values [107]. The increased solute contents in the solid solution can increase the solution strengthening, which can increase the alloy strength. On the other hand, the increased Cu contents will cause to form more  $\text{Sn}_6\text{Cu}_5$  intermetallic phase. The strengthening from the second phase can be enhanced. Therefore, the strength of Sn-Cu alloys is increased when increasing the Cu contents.

The strengthening of grain size results from the refinement through plastic deformation. When applying rolling on the Sn-Cu alloys, the plastic deformation has refined the primary  $\beta$ -Sn grains and eutectics (Figures 4.9 and 4.10). The refined primary  $\beta$ -Sn grains can increase the strength according to the Hall-Petch relationship [108, 109]. The experimental data fits the Hall-Petch model in Figure 4.12, confirming the finer grain sizes can effectively increase the mechanical properties of Sn-Cu alloys. Moreover, the strengthening from the refined  $\text{Cu}_6\text{Sn}_5$  is also positive as the rolling has refined the intermetallic phase and has improved the uniformity of distribution in the matrix.

### 4.4.2 Strain Softening

It has experimentally confirmed the strain softening in the as-rolled Sn-Cu alloys during tensile process (Figure 4.13). Strain softening has been observed by previous studies in different metals with different mechanisms. Yu et al. [110] attributed the strain softening in their tensile tests to an early onset of necking. However, Haouaoui et al. [111] observed strain softening in their fractured tension samples without showing significant necking, which is similar to the results observed in this study. Jia et al. [112] suggested that a strain softening mechanism is

associated with the formation of shear bands promoted by reorientation of grains during plastic deformation, which is different to results observed here as no shear bands were found in the Sn based alloys. Other suggestions include the coarsening of dislocation structure [113], reduction in dislocation density [114], annihilation of dislocations at grain boundaries [115], or dynamic recovery [116], dislocation creation and absorption at grain boundaries [117].

It has established that the  $\beta$ -Sn crystal has a tetragonal distortion of the diamond crystal structure with two atoms per primitive cell. Due to such a complex tetragonal crystal structure, slip deformations in  $\beta$ -Sn have not been fully clarified yet. But it has been confirmed that there are about 32 different slip systems in  $\beta$ -Sn [118], and at least five slip systems: (110)[-111]/2, (101)[010], (101)[11-1]/2, (121)[-101], and (121)[1-11]/2 are energetically preferable [119]. Understandably, the mechanism of plastic deformation of Sn-based alloys mainly consists of dislocation slip and climb, twinning behaviours and grain boundary sliding. The experimental results are likely to support the mechanism associated with dislocation activities and dynamic or post-dynamic recrystallization.

When Sn-Cu alloys are deformed under tensile stress, dislocation activities including dislocation multiplication and annihilation (recovery) will predominate the deformation, a competition of the dislocation multiplication which resulting in hardening and the dislocation annihilation contributing to softening will occur. If the rate of dislocation multiplication is higher than that of dislocation annihilation, the strain hardening will be attained. Inversely, the strain softening will operate. The strain softening occurred under tensile stress is ascribed to the higher rate of dislocation annihilation based on the two aspects: (1) the melting temperature of the Sn-1.0wt.%Cu alloy is very low, about 503 K [95], the rolling under ambient condition may be considered as a hot working processing since the rolling temperature at 293K is larger than  $0.5T_m$  [120]. As such, the dynamic recovery rate during the rolling is sufficiently high to counteract the hardening effect caused by dislocation accumulation; (2) the tensile or the strain rate is relatively low ( $2 \times 10^{-3}/s$ ) during experiments and in the reality of applications. The recovery will occur more easily at the slower deformation speed [121]. On the other hand, dynamic or post-dynamic recrystallization is believed to be a significant factor affecting the softening phenomenon. Since the temperature will be increased during tensile, the dynamic crystallization is very likely to occur. However, profound details on the dynamic recrystallization behaviour in the Sn-based material under deformation need to further study for supportive evidences.

## 4.5 Summary

In the present chapter, the Sn-Cu alloys were prepared by casting and rolling. Experimental Sn-Cu alloys with Cu contents in the range of 0.3-1.0wt.% provided good mechanical properties (UTS: 30.1-51.5MPa, yield strength: 26.1-50.8MPa, and elongation: 56.0-87.5%). Microstructures of as-cast Sn-(0.3-1.0) wt.% Cu alloys consists of Sn solution phase and  $\text{Cu}_6\text{Sn}_5$  intermetallic phase in the matrix. The rolling does not alter the phase constituent of the alloys, but significantly refine the microstructure and enhance the mechanical properties.

The rolled hypoeutectic Sn-(0.3-0.5) wt.% Cu alloys offer the yield strength from 26.1 to 31.9MPa, UTS from 30.1 to 34MPa and elongation from 86.4 to 87.5%, which is at a similar level of tensile properties in comparison with the Pb-based alloys with the UTS from 17 to 27MPa and elongation from 76 to 90%. Plus, Sn-Cu alloys exhibit strain softening during tensile tests, which benefits the cladding manufacture and subsequent processing in rolling and drawing after assembly with high-energy explosive materials. Strain softening is desirable for the sheath/cladding materials in miniature detonating cords.

The advantages of Sn-Cu alloys include resource abundance, low materials cost, non-toxicity for the health and environmental requirement, relatively high density for supplying sufficient impulse energy and momentum for penetration, acceptable mechanical properties, and easy in melting, casting, extrusion, rolling, and drawing.

## **Chapter 5 Microstructure, Dynamic Restoration and Recrystallization Texture of Sn-0.5wt.%Cu Processed by Rolling**

### **5.1 Introduction**

The feasibility and reliability of the alloys for the sheath of miniature detonating cords are highly dependent on the mechanical behaviour and microstructural evolution that occur interactively during the manufacturing process and its service lifetime. In Chapter 4, Sn-(0.3-1.0) wt.%Cu alloys have been studied and proposed as the sheath materials for MDCs, ascribed to good mechanical properties, particularly nonwork-hardening under tensile straining which will largely facilitate easy-manufacturing through rolling, extrusion, and drawing [122]. Despite the investigation on mechanical performances of Sn-Cu alloys, very limited work has been done for the exploration of detailed deformation mechanisms during processing, which is particularly important in the manufacturing of the cords when the Sn-Cu sheath is simultaneously drawn with an explosive core in the strict conditions for aerospace applications.

Furthermore, the interaction between the explosive core and the metal sheath is critical as well in the manufacturing process, especially under the condition that intense deformation heat may be generated. All this is closely associated with the deformation mechanisms of the sheath material. Although the macrostructural evolution of Sn-Cu alloys involving the  $\text{Cu}_6\text{Sn}_5$  intermetallic phase and grain refinements were investigated in the previous chapter, a comprehensive examination of fundamental micro-scaled deformation mechanisms with references to the evolutionary process of the dislocations, grain boundaries, and grain orientations information is still highly desirable.

This chapter thus aims to explore the microstructural features and thorough deformation mechanisms of the Sn-0.5wt.%Cu alloy processed by rolling (5 rolling passes) under the moderate strain rate at room temperature. The microstructure, grain boundaries, dynamic restorations, twinning, and recrystallization texture has been characterized through the electron backscattered diffraction (EBSD) technique. The emphasis has been focused on the dynamic recrystallization (DRX) phenomenon and the effect of  $\text{Cu}_6\text{Sn}_5$  particles on the microstructural characteristics. The results provide the deformation database as the reference for the Sn-based alloys, especially for those comprising the Sn matrix and the second phase particles in the similar applications.

## 5.2 Microstructure prior to Rolling

The metallography examinations of the as-cast Sn-0.5wt.%Cu alloys have been conducted using OM and SEM, and the associated results have been presented in Chapter 4. For quick grasp of the microstructure features prior to rolling, a brief interpretation of the solidification process is provided. Figure 5.1 shows the morphology, size and distribution of the primary  $\beta$ -Sn phase and the intermetallic phase in the as-cast microstructure of the Sn-0.5wt.%Cu alloy. The microstructure comprised the primary  $\beta$ -Sn phase with dendritic morphology and eutectic (Figure 5.1a, b and c). The grain size of the  $\beta$ -Sn phase was measured in the range of 100-300 $\mu\text{m}$ . It was observed from Figure 5.1c and d that the intermetallic phase was characterized as  $\text{Cu}_6\text{Sn}_5$ , showing a needle-like morphology with the diameter of 1-3 $\mu\text{m}$  and the length of 10-20 $\mu\text{m}$  [122]. The volume fraction of Sn- $\text{Cu}_6\text{Sn}_5$  eutectic was proximately 33%. Note that no other intermetallic phases such as  $\text{Cu}_3\text{Sn}$  were observed in the structure. The solidification path and microstructural evolution can be understood through the equilibrium phase diagram of Sn-Cu system [99]. The Sn-0.5wt.%Cu alloy is solidified as a hypoeutectic alloy, following the phase transformation:  $L \rightarrow L + \text{primary } \beta\text{-Sn} \rightarrow \text{primary } \beta\text{-Sn} + \text{Eutectic (Sn} + \text{Cu}_6\text{Sn}_5)$ .

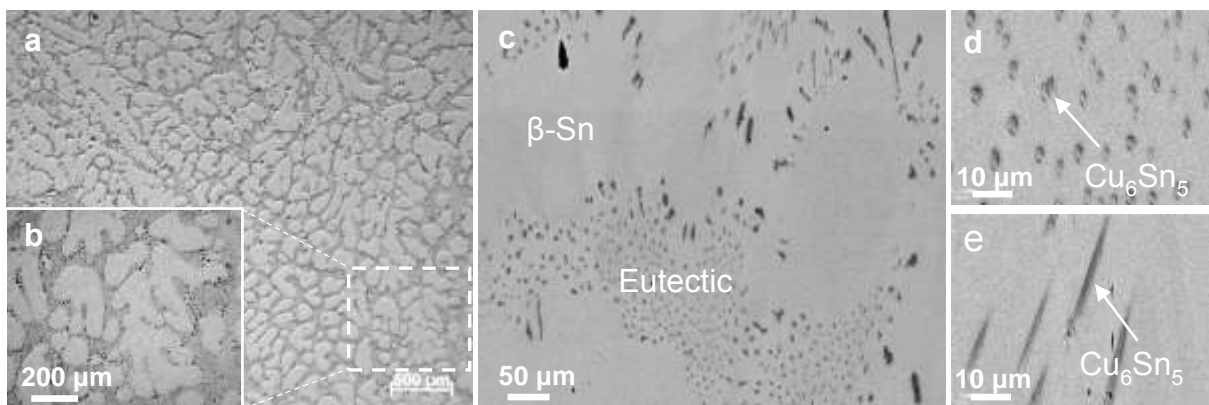


Figure 5.1 (a, b) Optical micrographs and (c, d, e) backscattered SEM micrographs showing the morphology and size of the primary  $\beta$ -Sn dendrites, eutectic, and intermetallic phase in the as-cast Sn-0.5wt.%Cu alloy.

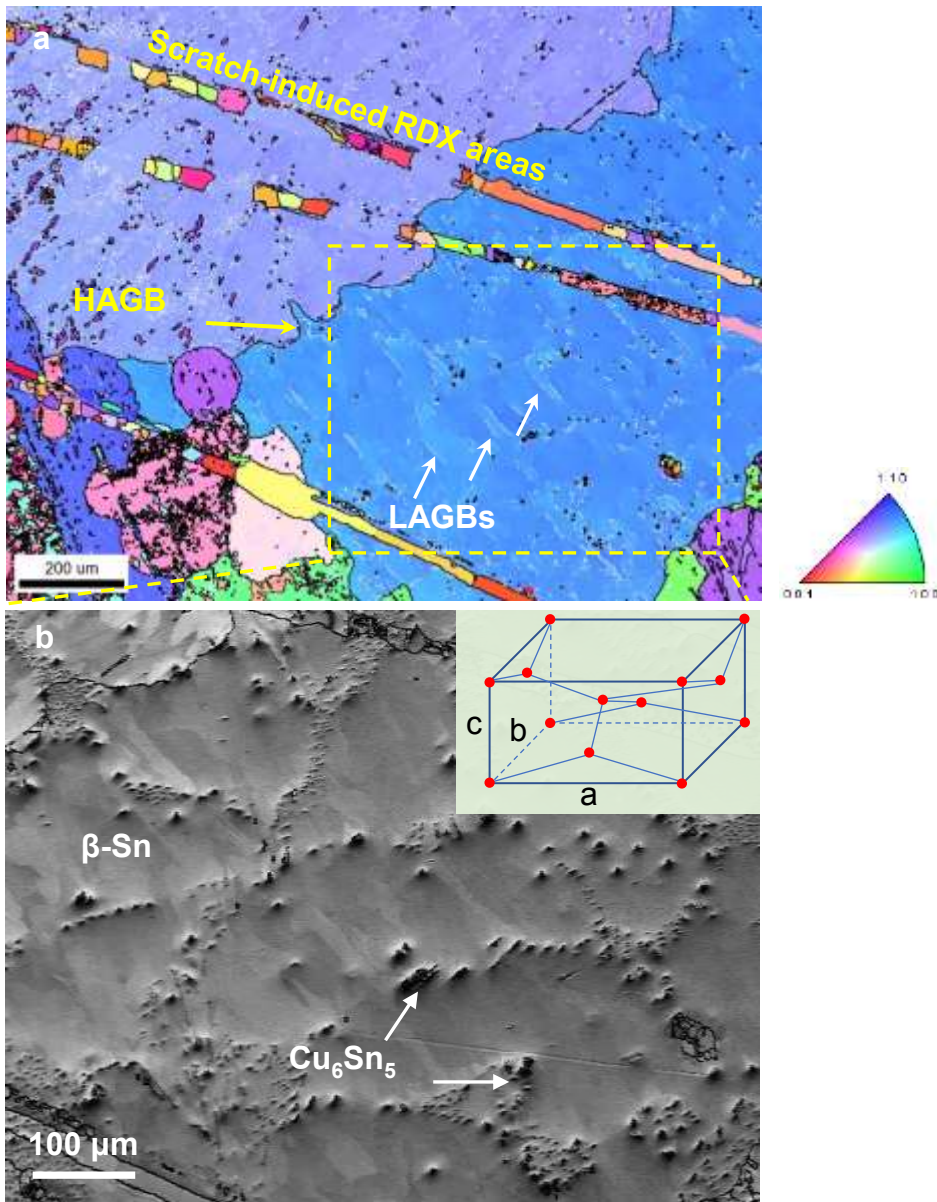


Figure 5.2 Inverse pole figure (IPF) map of the as-cast Sn-0.5wt.%Cu alloy with its corresponding IPF referring to the axis of the casting bar, (b) image quality (IQ) map of the highlighted region in (a). Inset showing the crystal cell of  $\beta$ -Sn with body centred tetragonal (BCT) structure. The high-angle grain boundaries (HAGBs,  $>15^\circ$ ) signified by thick black lines, and the light white lines presenting the low-angle grain boundaries (LAGBs,  $2-5^\circ$ ).

Figure 5.2 shows the inverse pole figure (IPF) map and image quality (IQ) map of the as-cast Sn-0.5wt.%Cu alloy with the corresponding IPF along the axis of casting bar. Clearly, a trace of high-angle grain boundary (HAGB), marked by the yellow-colour arrow, with a great length was extended from the top right corner to the bottom left corner of the image, separating the two neighbouring  $\beta$ -Sn grains (Figure 5.2a). Numerous low-angle grain boundaries (LAGBs)

or sub-grain boundaries were observed interior the  $\beta$ -Sn grains, such as those highlighted by the white-colour arrows in Figure 5.2a. These LAGBs had the misorientations less than  $5^\circ$ , indicating the existence of slight lattice distortion in the as-cast microstructure. Close inspection on the highlighted region, numerous coarse intermetallic particles of  $\text{Cu}_6\text{Sn}_5$  were embedded into the individual  $\beta$ -Sn grain (Figure 5.2b). These embedded  $\text{Cu}_6\text{Sn}_5$  particles were deemed to cause lattice distortions of the  $\beta$ -Sn matrix surrounding them.

The lattice distortion in the Sn matrix at the vicinity of the  $\text{Cu}_6\text{Sn}_5$  particles are very likely in association with the difference in coefficient of thermal expansion of the two phases ( $\text{Cu}_6\text{Sn}_5$  and surrounding Sn phases). After the two individual phases solidified, they continued to cool down to the room temperature. In this process, the slight volume variation of the two phases occurred in a difference pace, which might cause the formation of mismatch or defects such as voids and dislocations in the interface between  $\text{Cu}_6\text{Sn}_5$  and surrounding Sn matrix. In this way, the micro-strain energy resulted from the different extent of bulk volume variation can be relieved. In those areas near large-sized  $\text{Cu}_6\text{Sn}_5$  particles or near  $\text{Cu}_6\text{Sn}_5$  clusters, the defects in the interface might not sufficiently high in energy to release the distortion energy, consequently, severer lattice distortions in the Sn matrix further away from the  $\text{Cu}_6\text{Sn}_5$  particles were likely formed to compromise the increased distortion energy.

It is worthy to note that the readily perceived regions with fine grains (Figure 5.2a) were likely the recrystallized areas. These fine grains were formed in straight lines, which were most likely introduced by scratching during surface grinding. This indicates that the Sn-0.5wt.%Cu alloy is highly susceptible to dynamic recrystallization under deformation. Accordingly, the dynamic recrystallization behaviour will be discussed next. Inset in Figure 5.2b illustrates the  $\beta$ -Sn crystal structure.  $\beta$ -Sn has a body-centred tetragonal (BCT) structure with lattice parameters:  $a=5.8194\text{\AA}$ , and  $c=3.1753\text{\AA}$ . It has four atoms per unit cell at the points  $000$ ,  $\frac{1}{2}0\frac{1}{4}$ ,  $0\frac{1}{2}\frac{3}{4}$ , and  $\frac{1}{2}\frac{1}{2}\frac{1}{2}$  [123].

### 5.3 Microstructure after Rolling

Figure 5.3 presents the microstructure on the transverse and longitudinal cross sections of the Sn-0.5wt.%Cu alloy after rolling. The size of primary  $\beta$ -Sn dendrites was dramatically decreased and the microstructure became much finer (Figure 5.3a). The primary  $\beta$ -Sn phase and the Sn- $\text{Cu}_6\text{Sn}_5$  eutectic region were severely deformed along the rolling direction, resulting in the formation of elongated  $\beta$ -Sn phase and eutectic regions (Figure 5.3b). Inset in Figure 5.3

shows the size and morphology of  $\text{Cu}_6\text{Sn}_5$  intermetallic phase after rolling. The original  $\text{Cu}_6\text{Sn}_5$  intermetallic rods were broken into smaller segments and separated each other in the  $\beta$ -Sn matrix. The size of  $\text{Cu}_6\text{Sn}_5$  intermetallic phase was ranged from 1 to  $6\mu\text{m}$  with an average of  $3\mu\text{m}$ . More details of the structural evolution of the  $\text{Cu}_6\text{Sn}_5$  intermetallic phase can be referred to our published work [122].

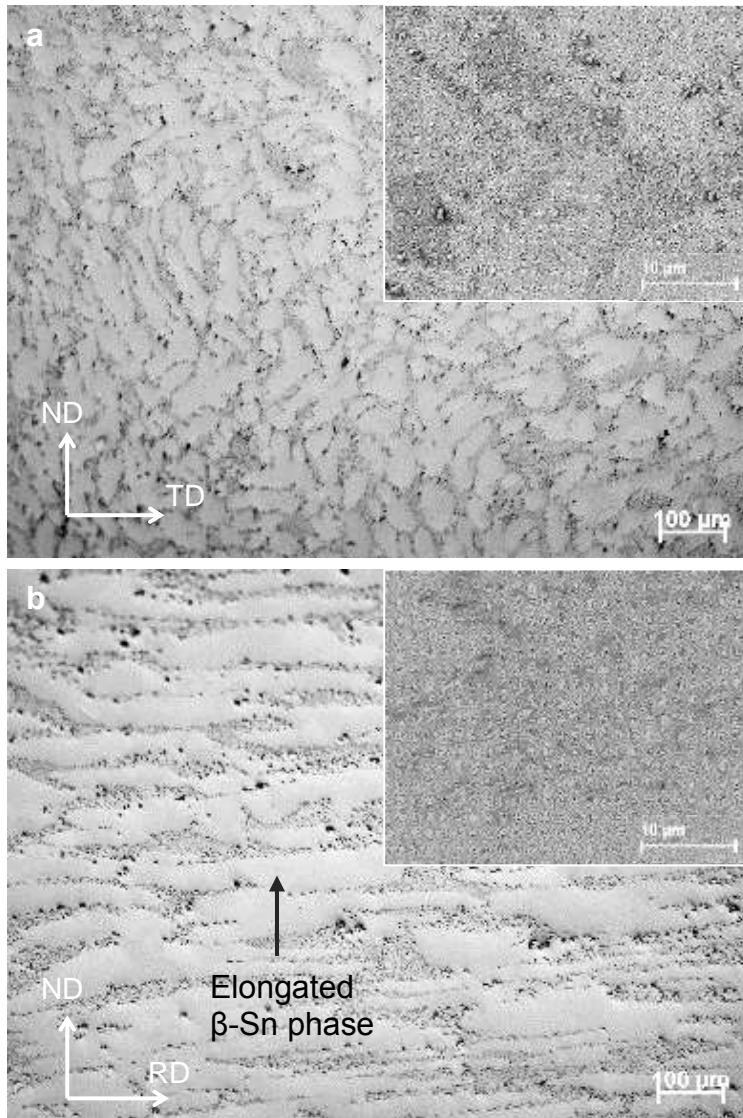


Figure 5.3 Optical micrographs showing the microstructure of the rolled Sn-0.5wt.%Cu alloy, (a) transverse cross section, and (b) longitudinal cross section. Insets are the SEM micrographs showing the corresponding morphology and size of the  $\text{Cu}_6\text{Sn}_5$  particles. Note that the black and white dots in inset are noises.

### 5.3.1 Bimodal Grain Structure

Figure 5.4 shows the IPF map on the ND+TD plane of the Sn-0.5wt.%Cu alloy after rolling. A considerable change in the microstructure was observed in comparison with the as-cast structure. It was clearly seen from Figure 5.4 that a predominant bimodal grain structure was well established, with an alternatively distributed fine grains and coarse grains. The fine grains were less than 30 $\mu\text{m}$  with near-equiaxed grain structures, while the coarse ones were in the range of 50-150 $\mu\text{m}$  and displayed irregular-shaped grain structures instead.

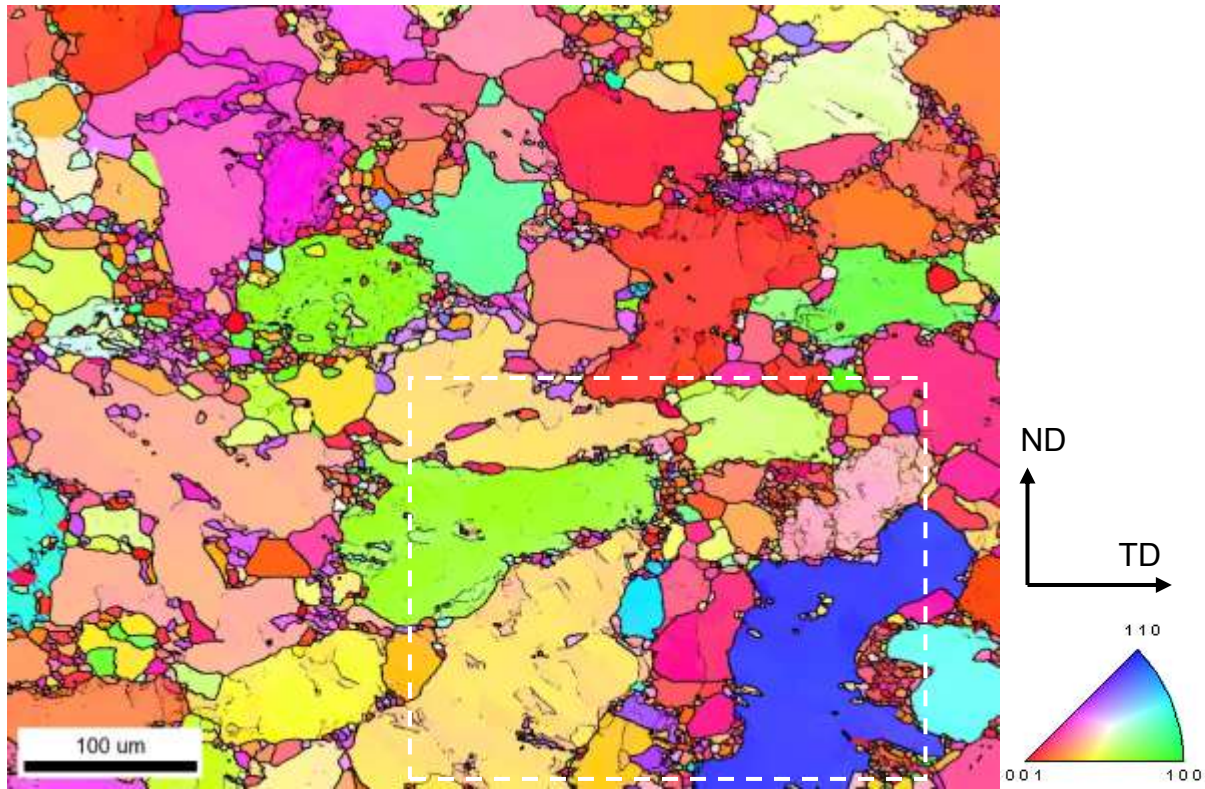


Figure 5.4 Inverse pole figure (IPF) map of the rolled Sn-0.5wt.%Cu alloy with its corresponding IPF referring to RD direction, The HAGBs ( $> 15^\circ$ ) andLAGBs ( $2-15^\circ$ ) presented by thick and thin black lines, respectively.

Figure 5.5 shows the statistical measurements of the grain size distribution and grain boundary misorientations distribution of the rolled Sn-0.5wt.%Cu alloy, extracted from the orientation data of Figure 5.4. The fine grains accounted for greater than 97% of total number of grains (Figure 5.5a) and the coarse grains represented extremely limited numbers ( $< 3\%$ ). It was seen from Figure 5.5b that the high-angle grain boundaries (HAGBs) with misorientations higher than  $15^\circ$  were evenly distributed in the whole misorientations range except the fact that a group of near- $60^\circ$  misorientation angles constituted an exceptional increased fraction. The HAGBs took up more than 78% of total grain boundaries. The near- $60^\circ$  misorientation angles were associated with the twinning configurations in the  $\beta$ -Sn structure,  $\{301\}$  and  $\{101\}$  type twins,

rotation about a common  $\langle 100 \rangle$  axis [124]. The  $\{301\}$  twinning system has been usually observed in the  $\{301\}$  twin plane with  $\langle \bar{1}03 \rangle$  twinning shear direction but the  $\{101\}$  twinning system was rarely seen in the  $\{101\}$  twin plane with  $\langle \bar{1}01 \rangle$  twinning shear direction [123].

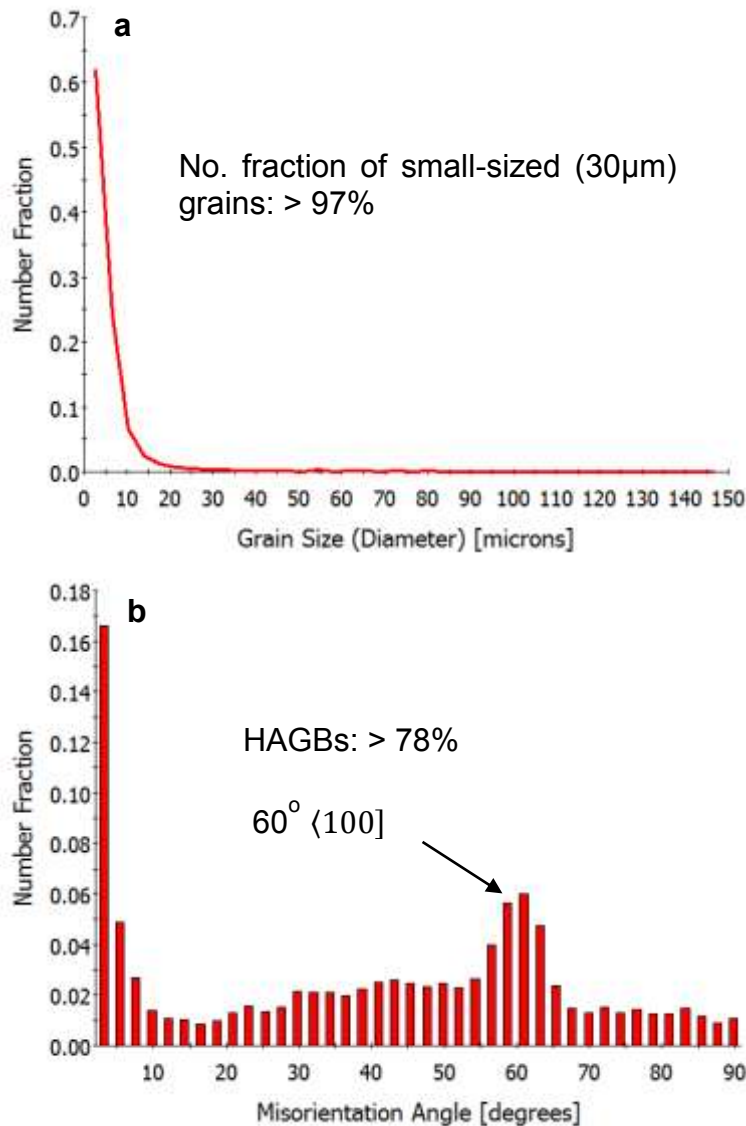


Figure 5.5 (a) Grain size distribution, and (b) grain boundary misorientations distribution of the rolled Sn-0.5wt.%Cu alloy.

Based on the perceived characteristics of the structure in the as-rolled Sn-0.5wt.%Cu alloy including the bimodal grain structure, high-fractioned HAGBs and the equiaxed-shape grains, it was suggested that the microstructure after rolling exhibited a typical hot-processing structure with the grains being partially or fully recrystallized. It has been well documented that conventional dynamic recrystallization (often referred as discontinuous dynamic recrystallization, DDRX) takes place during straining as long as the working temperature is

above  $0.5T_m$  [125, 126, 127]. In the Sn-0.5wt.%Cu alloy, the rolling at ambient temperature was considered as hot working because the processing temperature at 293K was higher than  $0.5T_m$  [122]. Dynamic recrystallization was thus one of the dominant features during deformation and could play an essential role in final microstructure establishment.

### 5.3.2 Dynamic Restoration

Figure 5.6 shows the image quality (IQ) combined with the grain orientation spread (GOS) map of an enlargement of the highlighted region in Figure 5.4. GOS map is deemed a useful tool to evaluate the in-grain misorientation. The GOS value is the average deviation between the orientation of each individual measuring point within a grain and the average grain orientation calculated for the specific grain [128]. It provides a quantitative description of the crystallographic orientation gradients in individual grains. As deformed grains possess internal orientation gradients, they give rise to relatively high GOS values. However, the recrystallized grains possess no or very limited in-grain orientation gradients, and thus produce low GOS values. Here the grains with GOS values smaller than  $1.5^\circ$  (colour scaled in Figure 5.6) can be reasonably considered as the recrystallized grains, and those with no colour scale represent the GOS values larger than  $1.5^\circ$ , which can be treated as non-recrystallized grains.

The LAGBs at  $2-15^\circ$  and the formation of sub-grains were seen interior the non-recrystallized grains, as represented by the black-colour arrows in Figure 5.6. This indicates that the dynamic recovery (DRV) has occurred under rolling. The basic mechanisms of DRV involve dislocation climbing and gliding, which result in the formation of LAGBs [129]. DRV is greatly dependent on the deformation conditions, such as strain rate and temperature. Stacking fault energy (SFE) also plays critical roles in dislocation generation and recovery. In high-SFE alloys, such as aluminium alloys, dislocation climbing and cross-slip can occur readily, DRV is thus rapid and extensive at high temperatures. In the present study,  $\beta$ -Sn processes multiple preferred slip systems at room temperature, which has been identified as  $\{100\} \langle 001 \rangle$ ,  $\{110\} \langle 001 \rangle$ , and  $\{100\} \langle 010 \rangle$  [130, 131]. On top of the preferred slip systems, depending on the crystal orientation, Sn can access up to 10 different slip systems [132]. Therefore, multiple slip systems can offer great potential for dislocation generation under strain. During the initial stage of rolling, an increase in the flow stress results from the dislocations interaction and multiplication. The dislocation density and the stored energy increase with further straining, leading to the increase of the driving force for the recovery. Consequently, the microstructure of low-angle grain boundaries or sub-grains develops.

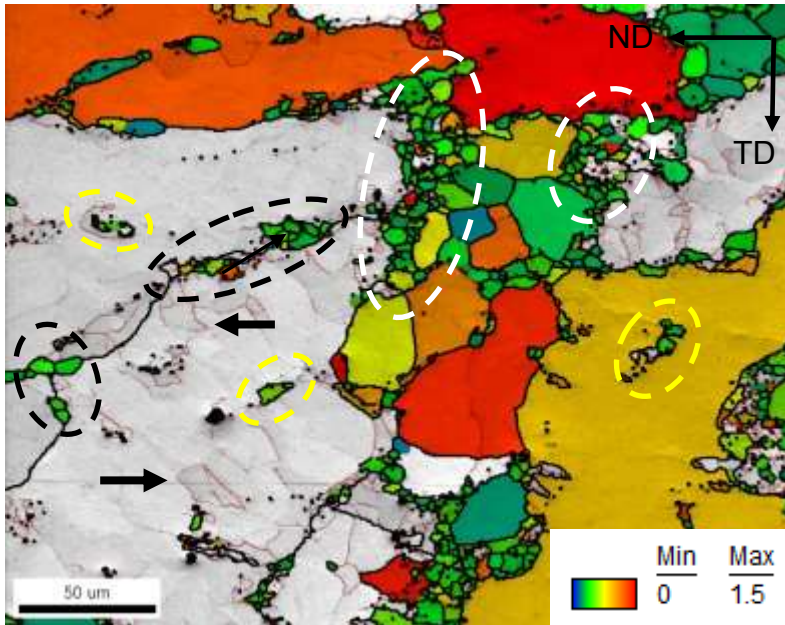


Figure 5.6 Superposed image quality (IQ) and grain orientation spread (GOS) maps of the rolled Sn-0.5wt.%Cu alloy, showing the recrystallized grains differentiated by selecting GOS values smaller than  $1.5^\circ$ . The HAGBs ( $>15^\circ$ ) and LAGBs ( $2-15^\circ$ ) presented by thick and thin black lines, respectively.

On the other hand, the hot deformation and the relatively low strain rates facilitate DRV. At high temperatures, slip systems which are not activated at low temperatures may become active and cause the increase in the number of operating slip system and the deformation therefore becomes homogeneous. In this case, DRV occurs more easily than DRX does. The relatively low strain rates further increase the time for dislocations motion, interaction and annihilation, which can benefit the formation of DRV as well.

Given that the DRV was largely observed, DRX was still the noticeable restoration phenomenon since the large regions of inhomogeneity from  $\text{Cu}_6\text{Sn}_5$  particles and original grain boundaries in association with the severely strain-accumulated areas could be the sites for initiating the DRX. Moreover, from Figure 5.6, it is worthy pointing out that the recrystallized fine grains can be generally classified into three categories: (1) those with aggregated distribution highlighted by white-colour ellipse, (2) those sparsely distributed in the grain interior, as marked by yellow-colour ellipse, and (3) those formed at the vicinities of the grain boundaries (marked by black-colour ellipse). This is ascribed to the different recrystallization mechanisms mainly involving the particle-stimulated nucleation (PSN) and the boundary associated nucleation, which will be interpreted individually in the following sections.

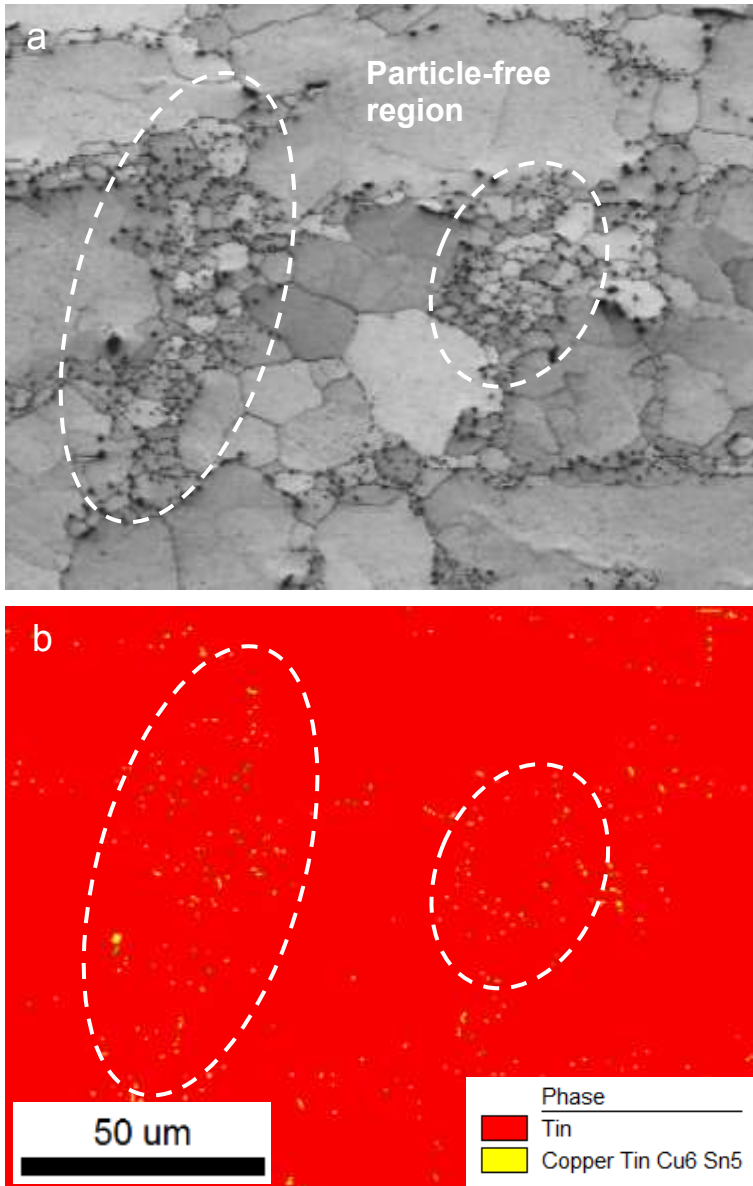


Figure 5.7 (a) Image quality (IQ) map and (b) phase map of the rolled Sn-0.5wt.%Cu alloy with its corresponding IPF referring to RD direction, showing the small-sized grains and large-sized grains in the particle-dominant region and particle-free region, respectively.

Figure 5.7 shows the image quality (IQ) map and the phase map of a region extracted from Figure 5.6. Clearly, the fine grains tended to form in the regions where  $\text{Cu}_6\text{Sn}_5$  intermetallic particles were densely spaced, as highlighted by the ellipses in Figure 5.7. However, particles were scarcely observed in the interior of coarse grains, which could be represented as the particle-free regions. This phenomenon is the clear indication of the particle-stimulated nucleation (PSN). It has been well documented that the coarse ( $> 1\mu\text{m}$ ) second-phase particles, especially those widely spaced particles, can promote dynamic recrystallization via the mechanism of particle-stimulated nucleation [133, 134, 135]. In the present study of Sn-

0.5wt.%Cu alloy, the  $\text{Cu}_6\text{Sn}_5$  particles with the sizes over  $1\mu\text{m}$  in diameter [122] meet the criteria of nucleation initiation in terms of the particle dimensions. Moreover, PSN has been proposed on the basis of that the enforced strain gradient at the vicinity of a less- or non-deformable particle can create a region of high-density dislocations and large orientation gradients, namely particle deformation zone or PDZ. The PDZ can be the site for nucleation of recrystallization. Therefore, PSN is generally regarded as an effective approach to accelerate recrystallization and to obtain fine grains in the microstructure.

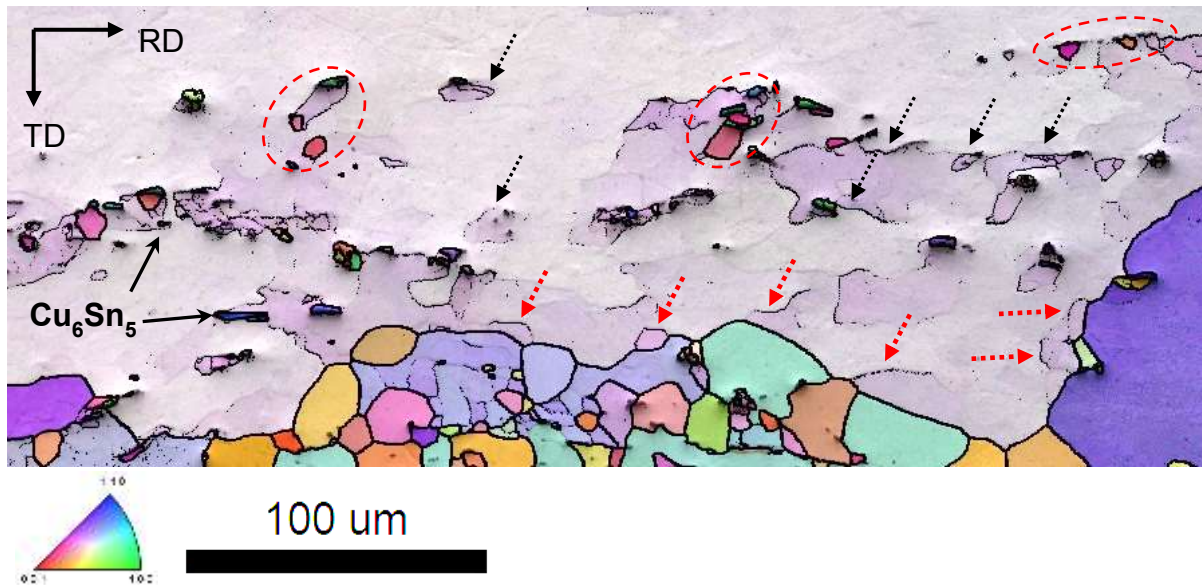


Figure 5.8 IPF+IQ map on the RD+TD plane of the rolled Sn-0.5wt.%Cu alloy, showing the PSN phenomenon and boundary-induced nucleation. The HAGBs ( $>15^\circ$ ) and LAGBs ( $2-15^\circ$ ) presented by thick and thin black lines, respectively.

Figure 5.8 and Figure 5.9 show the typical EBSD orientation maps of the Sn-0.5wt.%Cu alloy after rolling, presenting the IQ+IPF map on the RD+TD plane and the IPF map on the TD+ND plane, respectively. The grain was elongated along the RD, into which numerous sparsely spaced  $\text{Cu}_6\text{Sn}_5$  particles were embedded (Figure 5.8). The PSN nuclei/grains were clearly perceived near these  $\text{Cu}_6\text{Sn}_5$  particles, as demonstrated by the large lattice orientation differences between the nuclei and the surrounding matrix (highlighted by the red-colour ellipses in both Figure 5.8 and Figure 5.9). In brief, the particle-stimulated nucleation could be summarised as the following successive process: first, the dislocation multiplication or accumulation developed near the  $\text{Cu}_6\text{Sn}_5$  particles; then, LAGBs or sub-grains formed owing to highly accumulated dislocations; finally, new nuclei with HAGBs were established.

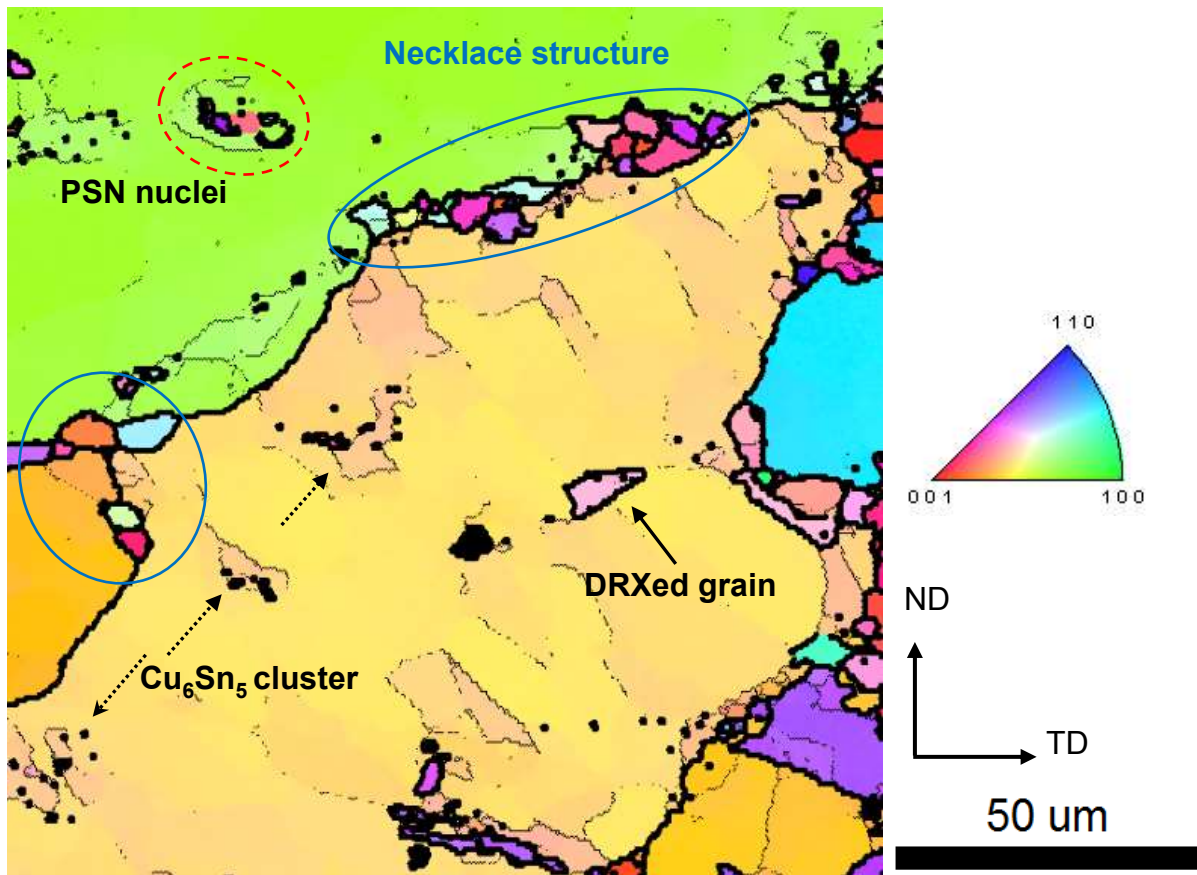


Figure 5.9 IPF map on the ND+TD plane of the rolled Sn-0.5wt.%Cu alloy, showing the PSN phenomenon and boundary-induced nucleation. The HAGBs ( $>15^\circ$ ) and LAGBs ( $2-15^\circ$ ) presented by thick and thin black lines, respectively.

Under strain, the hard  $\text{Cu}_6\text{Sn}_5$  particles were considered as the deformation heterogeneities which could act as the barriers for the motion of the active dislocations. Therefore, the high density mobile dislocations were pinned and accumulated to enforce the strain gradient. With further progress of straining, the highly accumulated dislocations interact each other through dislocation tangling or rearrangement, leading to the formation of LAGBs or sub-grains. Examples of the resulting LAGBs/sub-grains near the  $\text{Cu}_6\text{Sn}_5$  particles can be found on both the longitudinal plane and the transverse plane, as shown by the dotted black-colour arrows in Figure 5.8 and Figure 5.9. Subsequently, these sub-grain boundaries were retarded by the  $\text{Cu}_6\text{Sn}_5$  particles after a specific deformation level, and dislocations were continuously trapped into these boundaries, eventually resulting in the possible transformation of LAGBs into HAGBs, namely the formation of new recrystallized nuclei/grains. It should be noted that, besides the single  $\text{Cu}_6\text{Sn}_5$  particle, the  $\text{Cu}_6\text{Sn}_5$  clusters could also act as the heterogeneous sites for initiating nuclei. Those particle clusters were deemed to introduce severer lattice distortion

in the surrounding matrix and to enhance the dislocations accumulation [136]. Thus, the  $\text{Cu}_6\text{Sn}_5$  clusters can serve as effective nucleation sites, as shown in Figure 5.9.

After the formation of the recrystallized nuclei, grain growth might subsequently occur. For the  $\text{Cu}_6\text{Sn}_5$  particles which were sparsely spaced into the interior of Sn grains, once the energy conditions for growth were met, the nuclei by PSN would grow by consuming the neighbouring deformed structure, leading to the boundary motion (growth) of the DRX grains. As a result, relatively large DRX grain could be formed. Note that the “energy conditions” referred to the combined effects caused by the driving forces and the retarding forces. The driving forces which dominated the boundary growth was the interface energy of the DRX grain boundaries, while the retarding forces were mainly resulted from the dispersed fine particles and solute atoms. However, if the criteria for nuclei growth was not met, the new nuclei would be maintained steady at small sizes. On the contrary, for the regions dominated by densely spaced  $\text{Cu}_6\text{Sn}_5$  particles such as the original eutectic regions (highlighted in Figure 5.7), numerous recrystallized nuclei might form simultaneously under a specific strain, resulting in a narrow distribution of fine grains. Also, the high number density of  $\text{Cu}_6\text{Sn}_5$  particles acted as the obstacles to hinder the growth of the nuclei. Consequently, numerous closely packed fine recrystallized grains were established in the  $\text{Cu}_6\text{Sn}_5$  particles dominant regions.

Figure 5.8 and Figure 5.9 provides the detailed microstructural features, which suggests another typical nucleation mechanism of DRX. Bunches of small DRX grains formed along the existing high-angle grain boundary and at the tri-junction of the boundaries, resulting in the formation of the necklace structures, as shown by the blue-colour ellipses in Figure 5.9. Necklace structures were the typical microstructures observed in DRX of other alloy systems like face-centred cubic and hexagonal close-packed metals and alloys [137, 138, 139], indicative of DRX from boundary-induced nucleation. Usually, the initiation of DRX at grain boundaries has been explained based on the bulging mechanism which in brief offers the idea that the DRX is set off by strain induced bulging of prior grain boundaries [140, 141]. That is, grain boundary shearing and/or sliding takes place at serrated grain boundaries developed at the early stage of deformation [137] and leads to the development of inhomogeneous or structure fluctuations near grain boundaries. The fluctuations prevent the boundary sliding or shearing under further deformation, dislocations then accumulate to increase the dislocation density gradients followed by sub-grains formation, and subsequently form HAGBs. The noticeable characteristic of this bulging mechanism is the appearance of the bulging boundaries, as well perceived by others [142]. However, this appears not the dominant mechanism in the present

study of Sn-0.5wt.%Cu alloy since grain boundary bulging was barely detected in the structure after deformation.

It is also observed in Figure 5.8 that LAGBs and sub-grains were formed at the vicinities of the high-angle grain boundaries, as indicated by the dotted red-colour arrows. It is reminiscent of continuous dynamic recrystallization (CDRX) mechanism [129]. Although CDRX is defined as the global recovery of dislocations, higher dislocation density at mantle regions very likely lead to formation of necklace structure at grain boundaries. The condition of plastic deformation in the present work involved relatively high temperatures and low strain rate, a homogeneous microstructure usually developed. CDRX occurs by the progressive accumulation of dislocations into LAGBs which may increase their misorientations, and eventually HAGBs are formed. This mechanism has been reported in Al alloys [143] and micro-duplex stainless steel [144]. Here, the CDRX is considered as the reason for the formation of necklace structure along the boundaries.

### 5.3.3 *Twinning*

In addition to the dislocation activities with respect to the formation, motion, and accumulation of LAGBs, twinning was observed as a readily existing deformation mechanism of the Sn-0.5wt.%Cu alloy under rolling. As aforementioned, a relative portion of boundaries with near-60° misorientation angles were identified and those boundaries were considered as twin boundaries associated with the {101} and {301} type twins. For accuracy, confirmation of the twin relationship was performed through analysis of the pole figures from the two neighbouring grains separated by a 60° boundary. The plot of the shared orientation relationship components, ie. (101) or (301) planes in BCT  $\beta$ -Sn structure, reveals a shared point between the pole figures from twin and parent. Figure 5.10 presents an example of a type of {101} instead of {301} twin relationship between the grain 1 and grain 2 on the ND+TD plane of the as-rolled Sn-0.5wt.%Cu alloy, evidenced by the shared point of {101}, rather than {301} in the corresponding pole figures (Figure 5.10b). This twin possessed the twin plane along {101} and the misorientation angle associated with this is 57.2° about  $\langle 100 \rangle$  axis. Moreover, the trace normal of the {101} twin plane (dotted arrow in Figure 5.10b) appeared not perpendicular to the trace of the highlighted twin boundary (Figure 5.10a), indicating the twin boundary an incoherent twin boundary (ITB).

Figure 5.11 shows an example of another type of twin on the RD+TD plane of the as-rolled Sn-0.5wt.%Cu alloy. The twin boundaries signified by ITB1-ITB5 were proved associated with

the {301} twin planes, evidenced by the pole figures in Figure 5.11b. Significantly, it is worthy pointing out that the five pairs of twins formed interior a same large deformed grain (the blue-colour elongated grain). The formation of these twins was very likely triggered by the strong local stress concentration. Also, these twins were, without exception, the {301} type twins but {101} type twins, might be indicative of the orientation-related formation of deformation twinning.

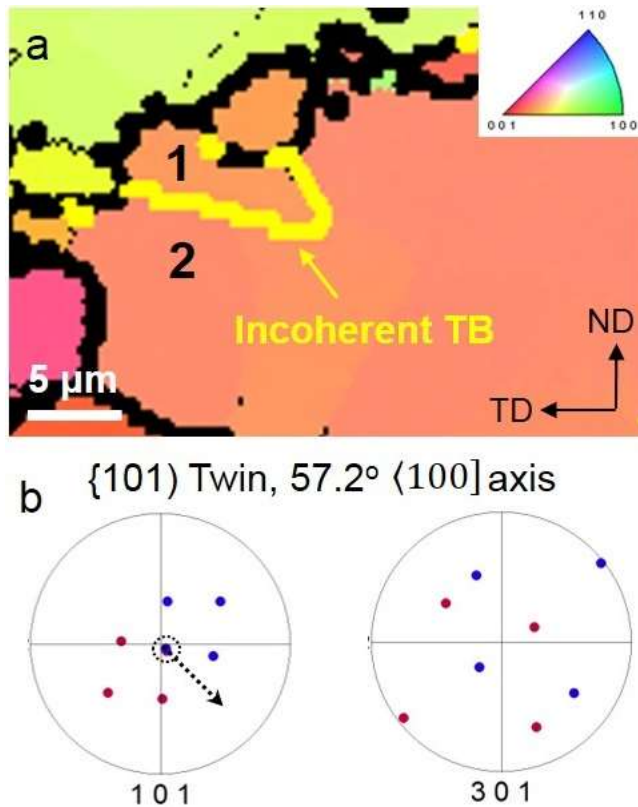


Figure 5.10 (a) IPF map showing a typical {101} type twin on the ND+TD plane of the rolled Sn-0.5wt.%Cu alloy, and (b) the (101) and (301) pole figures from grain 1 and grain 2, demonstrating a {101} twin relationship between the two grains. The HAGBs ( $>15^\circ$ ) and LAGBs ( $2-15^\circ$ ) presented by thick and thin black lines, respectively. Yellow-coloured thick line showing the a  $57.2^\circ$  incoherent twin boundary (ITB).

It has been well established that deformation twinning is considerably dependent on the strain rate, deformation temperature, and the stacking fault energy (SFE) [145]. In the  $\beta$ -Sn system, owing to its multiple slip systems, dislocation-mediated slips such as dislocation climbing and cross-slip generally play essential roles in the deformation at moderate strain rates and room temperature [146]. However, deformation twinning has still been extensively observed and studied in the BCT Sn [146, 147, 148]. It is seen from Figure 5.11a that a great deal of  $\text{Cu}_6\text{Sn}_5$

particles and numerous particle-induced highly accumulated dislocations or sub-grain boundaries/LAGBs formed interior the deformed grain (the blue-colour elongated one). The strongly concentrated stress and the highly stored localized strain energy introduced by these LAGBs were prone to be released either through formation of HAGBs or twinning. Usually, formation of HAGBs is the common way to reduce the system energy at moderate strain rates. But on occasions that the external stress and the twinning planes established a preferred geometrical orientation relationship, twinning could be initiated easily [147]. It might be for this reason that all the twins formed interior the same deformed grain were exclusively in association with the  $\{301\}$  type twins. That is, the orientation-related formation of deformation twinning operates.

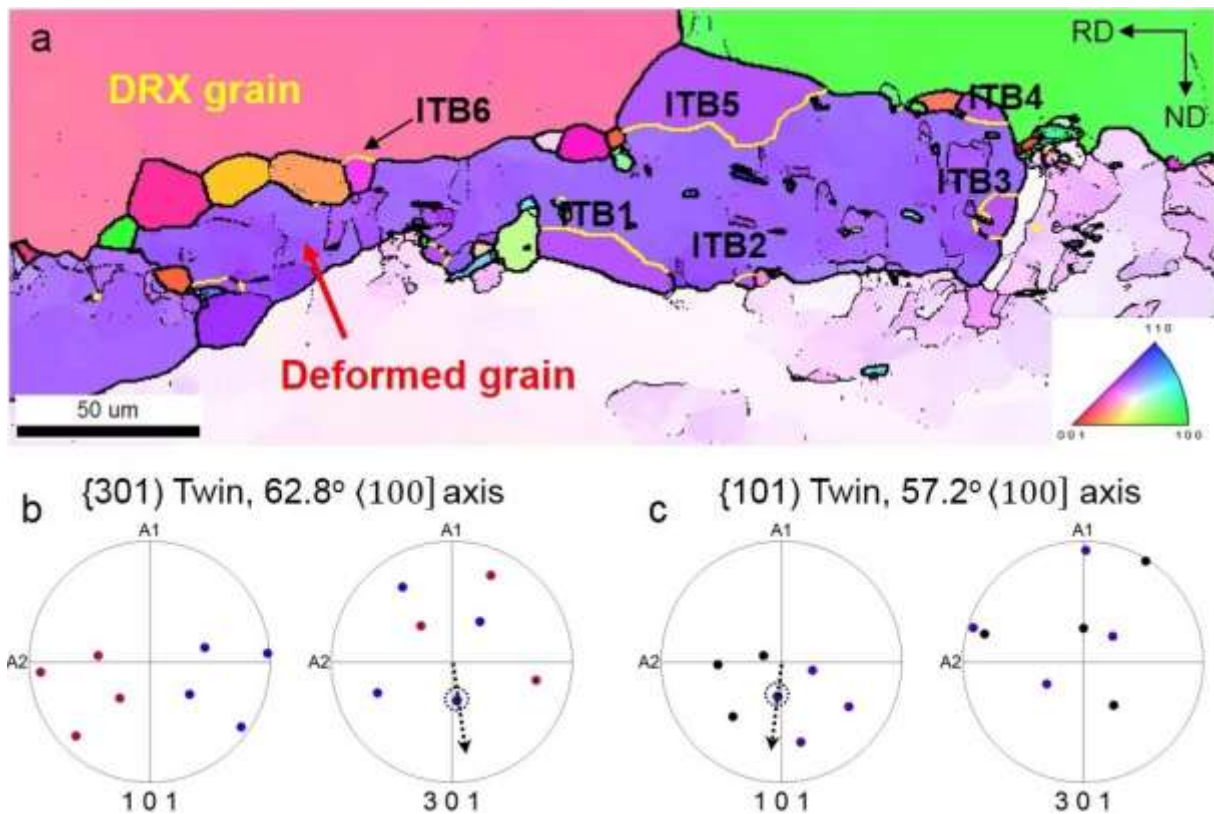


Figure 5.11 (a) IPF map on the RD+ND plane of the rolled Sn-0.5wt.%Cu alloy, showing the two types of  $\{301\}$  and  $\{101\}$  twins, with the corresponding incoherent twin boundaries ITB1-5 and ITB6, respectively, (b)  $\{101\}$  and  $\{301\}$  pole figures from grain-pairs isolated by ITB1-5, (c)  $\{101\}$  and  $\{301\}$  pole figures from grain-pair separated by ITB1.

In addition to the  $\{301\}$  twin related ITB1-5 on the RD+ND plane, the ITB6 was proved related to the  $\{101\}$  twin plane, evidenced by the pole figures in Figure 5.11c. This  $\{101\}$  twin boundary (ITB6) was observed in a fully recrystallized grain instead of interior the deformed

grain which was the case for the formation of ITB1-5. This phenomenon was associated with the nuclei nucleation process occurring near the high-angle grain boundaries, which was reported in other metals/alloys under dynamic recrystallization [149]. It was based on the idea that DRX nuclei could be nucleated by bulging of some portions of serrated grain boundaries accompanied by the formation of twinning. The boundaries of the DRX grains move outwards into the neighbouring deformed grain, leaving a twinning boundary in the back of the newly developed DRX grains. Thus, fine DRX grains could normally be found at the vicinity of the HAGBs. This is in line with the structure characterized in Figure 5.11a in which a series of fine DRX grains formed at the boundary region between the highlighted DRX grain and the large elongated grain.

### 5.3.4 Recrystallization Texture

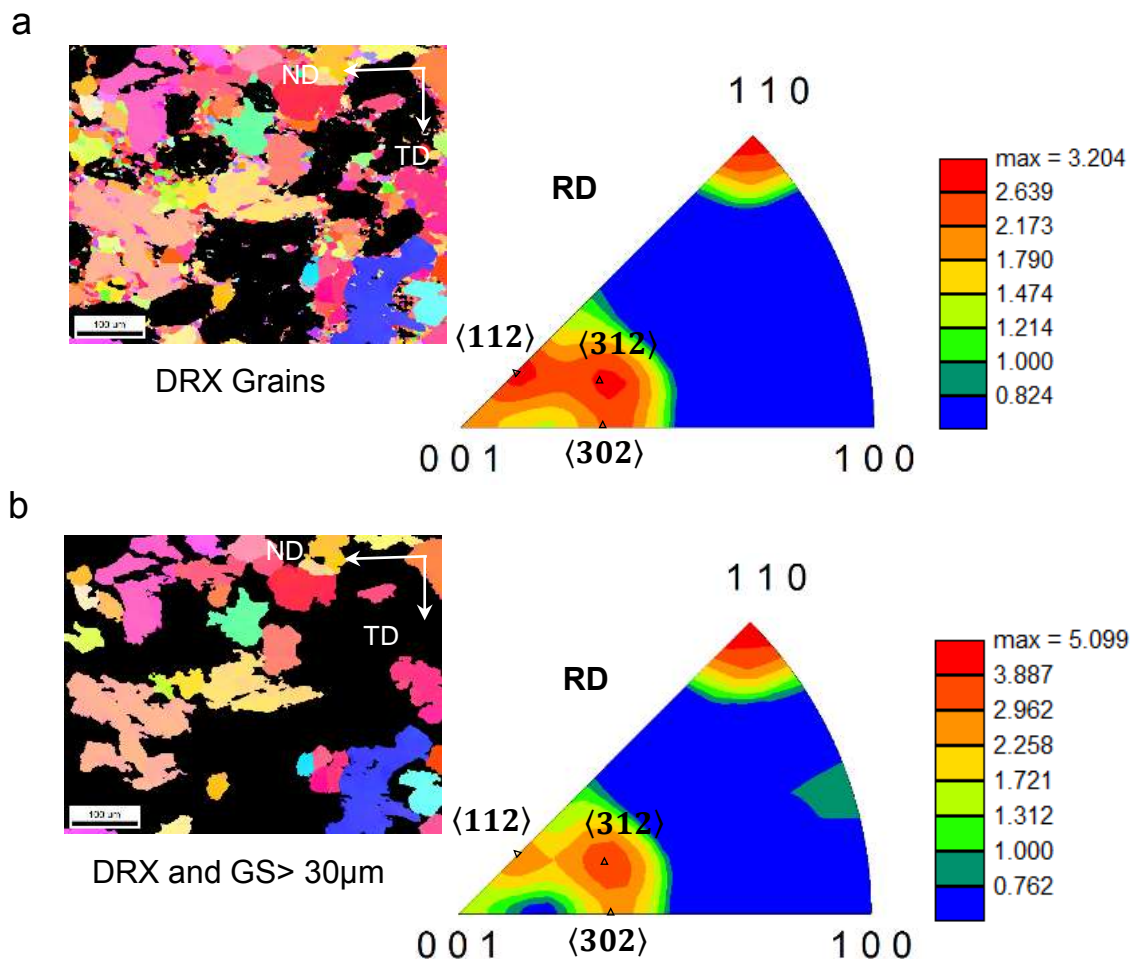


Figure 5.12 Inverse pole figures (IPF) maps of on the ND+TD plane of the rolled Sn-0.5wt.%Cu alloy, showing (a) the recrystallized (DRX) grains and (b) DRX grain larger than 30μm.

Figure 5.12 shows the inverse pole figures along the RD, extracted from all the recrystallized grains and the coarse recrystallized grains with grain sizes greater than  $30\mu\text{m}$ . It was seen from Figure 5.12a that in all recrystallized grains a clear  $\langle 110 \rangle // \text{RD}$  fibre texture was established, with the texture intensity of 3.2 times random (3.2TR), and an asymmetrical arc spanning from  $\langle 112 \rangle$  passing through  $\langle 312 \rangle$ , and then reaching  $\langle 302 \rangle$  was formed, with the corresponding texture intensities of 2.8, 2.8, and 2.3TR, respectively. The coarse recrystallized grains ( $> 30\mu\text{m}$ ) displayed a slightly different textural feature in comparison with the whole recrystallized grains, presenting a stronger  $\langle 110 \rangle // \text{RD}$  (5.0TR) and  $\langle 312 \rangle // \text{RD}$  (3.5TR) texture but a weaker  $\langle 112 \rangle // \text{RD}$  (2.7) texture and the same intensity (2.3TR) of the  $\langle 302 \rangle // \text{RD}$  texture (Figure 5.12b).

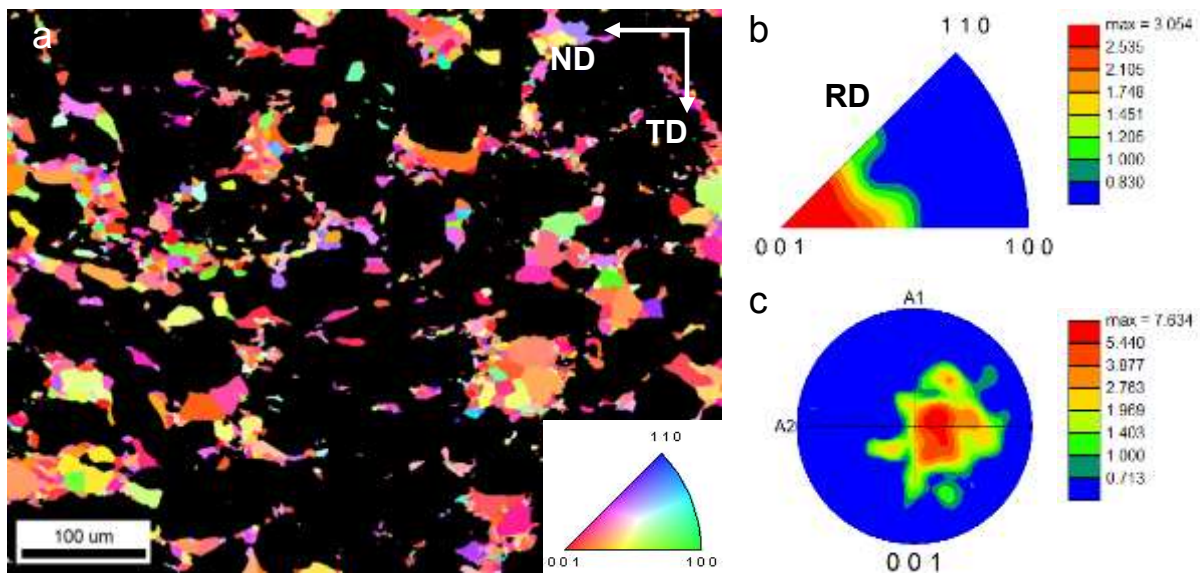


Figure 5.13 (a) Inverse pole figure (IPF) map on the ND+TD plane of the rolled Sn-0.5wt.%Cu alloy, showing the recrystallized grains with grain size smaller than  $30\mu\text{m}$ , (b) corresponding IPF and (c) (001) pole figure.

To further analysis the initial texture of the recrystallized nuclei, the texture features from the fine grains ( $< 30\mu\text{m}$ ) was investigated solely. Figure 5.13a shows the IPF map differentiated from Figure 5.4, illustrating the orientations and distribution of the fine recrystallized grains with the grain size smaller than  $30\mu\text{m}$ . Figure 5.13b and c present the corresponding inverse pole figure and (001) pole figure along the RD, respectively, suggesting a manifest textural figure for the fine DRX nuclei/grains. It was found that a near- $\langle 001 \rangle // \text{RD}$  fibre texture was established for the fine DRX grains, which was evidenced by the fact that most of the fine grains/nuclei had the  $c$ -axes closely aligned to the RD, as indicated by the IPF (texture intensity:

2.7TR) and PF (texture intensity: 7.5TR) (Figure 5.13b and c). Therefore, it was generally established that the nuclei possessed a  $\langle 001 \rangle // \text{RD}$  fibre texture, while the overall recrystallized grain had a co-existence of the arc  $\langle 112 \rangle // \text{RD}$ - $\langle 312 \rangle // \text{RD}$ - $\langle 302 \rangle // \text{RD}$  and the  $\langle 110 \rangle // \text{RD}$  fibre, indicating the occurrence of transformation of the orientation from the  $\langle 001 \rangle // \text{RD}$  texture to others such as the  $\langle 110 \rangle // \text{RD}$  texture after grain growth.

As stated, the fine recrystallized grains/nuclei were mainly originated from PSN despite of the occasional existence of small portion of nucleation along the initial grain boundaries, it is thus reasonably deduced that the  $\text{Cu}_6\text{Sn}_5$  particles could be closely related to the formation of strongly oriented nuclei ( $\langle 001 \rangle // \text{RD}$ ). This was also observed in nickel alloys where the nuclei formed near the silica particles were found to be oriented as well [150].

It was reported in our previous work that the  $\text{Cu}_6\text{Sn}_5$  particles tended to be distorted in such a way that the axes of  $\text{Cu}_6\text{Sn}_5$  particle rods were aligned to the rolling direction [122]. This might provide preferential orientation configurations between the stresses and the  $\text{Cu}_6\text{Sn}_5/\beta\text{-Sn}$  interfaces, which could facilitate the formation of  $\langle 001 \rangle // \text{RD}$  nuclei. Those oriented nuclei might not necessarily grow into coarse grains with the  $\langle 001 \rangle // \text{RD}$  orientation remained, as on one hand, the motion of nuclei boundaries could be hindered or pinned by the densely distributed  $\text{Cu}_6\text{Sn}_5$  particles. On the other hand, even if there were no obstacles retarding the nuclei growth, such as the nuclei formed in the interior of grains, the specific strong orientation ( $\langle 001 \rangle // \text{RD}$ ) of the nuclei could still be weakened by the oriented growth of other nuclei such as those with orientations of  $\langle 110 \rangle // \text{RD}$ . This relies on the growth advantages of the specific PSN orientations mostly due to their close to a certain relationship with the deformed  $\beta\text{-Sn}$  matrix. For example, a growth advantage of a near  $40^\circ$   $\langle 111 \rangle$  orientation relationship in Al-1.8wt.%Cu [151], and a  $24^\circ$   $\langle 150 \rangle$  orientation relationship in aluminium crystals [152] were observed. Although the preferential orientation relationship in the present alloy is still unclear, the oriented growth was very likely the reason for the transformation of oriented texture from  $\langle 001 \rangle // \text{RD}$  into  $\langle 110 \rangle // \text{RD}$ . However, further works with references to the preferential growth orientation in the present Sn-Cu alloy under the specified processing configurations need to be performed for profound understanding in this respect.

## 5.4 Summary

In this chapter, the Sn-0.5wt.%Cu alloy was investigated after rolling at moderate strain rates. The microstructure features including grain boundaries, dynamic restoration of DRV and DRX, twinning, and recrystallization texture were extensively characterized through EBSD technique. Main findings could be listed as following:

- (1) The Sn-0.5wt.%Cu alloy after rolling at room temperature showed a manifest bimodal grain structure containing over 97% (frequency) of fine grains less than 30 $\mu$ m and small portion of coarse grains in the range of 50-150 $\mu$ m.
- (2) DRX played a dominant role in the deformation. Particle-induced nucleation (PSN) phenomenon by the Cu<sub>6</sub>Sn<sub>5</sub> particles/clusters were the dominant DRX mechanism. And, the boundary-induced nucleation was detected as another DRX mechanism, which was associated with the continuous dynamic recrystallization (CDRX).
- (3) {301} and {101} type twins were extensively observed as an effective deformation mechanism during rolling. The formation of the {301} twin might be closely related to the orientation, which resulted from a specific orientation relation between the stress and the orientation of the deformed grains.
- (4) The fine DRX nuclei/grains displayed the  $\langle 001 \rangle // RD$  fibre texture, which was associated with the specific orientation relationship between the external stress and the Cu<sub>6</sub>Sn<sub>5</sub>/ $\beta$ -Sn interface. The  $\langle 001 \rangle // RD$  fibre texture in fine DRX nuclei was weakened and  $\langle 110 \rangle // RD$  fibre texture became strengthened with grain growth, which could be ascribed to the growth advantages of the specific orientation relationships.

## **Chapter 6 Microstructure and Mechanical Properties of Sn-Zn-Bi Alloys Processed by Rolling**

### **6.1 Introduction**

In Chapter 4, it has been reported that the Sn-Cu alloys displayed appropriate mechanical properties and non-hardening behaviour, which to large extent suggested the great potential of Sn-Cu for use as the sheath material of miniature detonating cords. While, a further comprehensive examination of microstructures of Sn-0.5wt.%Cu after rolling has confirmed the microstructural inhomogeneity, evidenced by the existence of texture or crystallographic orientation inhomogeneity and bimodal grain structures (Chapter 5). This could cause a failure concern in practical manufacturing process. The sheath tube will be filled with explosive materials (powders) and then the explosive-loaded tube is drawn and extruded continually. The tube loaded with explosive has an original external diameter of 13 mm and the wall thickness of 2 mm. After extrusion, the external diameter will be decreased to 1 mm and the sheath thickness dropped to less than 0.5 mm for the final products. This can easily pose a risk of failure of the cord sheath, particularly when the sheath material exhibits inhomogeneous microstructural characteristics under straining. In this sense, the resulting texture introduced by processing is somehow undesired from perspectives of manufacturing, as the textural structure can enhance inhomogeneous plastic deformation during drawing or swaging, which poses an increased risk of failure of the cords, consequently, increasing the difficulty in manufacturing.

In addition, as aforementioned in literature review (Chapter 2), the crystal structure and/or grain statistical distribution play significant roles in the perforation performance of the linear explosive devices. Fine grain structures with homogeneous grain size distribution and the structure with uniformly distributed grain orientations of each grains will be beneficial to cutting or penetration performance. This is because a uniform microstructure with non-texture and evenly distributed grain sizes can allow a uniform flow of the sheath elements into the collapse zone, thus, produce greater jet length [153].

Also, when it comes to practical penetration performance, the inhomogeneity in structure (bimodal grain structure and inhomogeneous grain orientations) introduce unsmooth jet particles during jetting process of the sheath, which is deemed detrimental to the cutting

performance. In addition to this, Sn-Cu alloys unfortunately have other disadvantages, for example, the big difference of the melting points between Sn (232°C) and Cu (1085°C) elements somehow brings inconvenience for ease of casting.

It is thus essential to consider other more proper lead-free Sn-based alloys that are expected to be cost-effective and easy-to-manufacture, and certainly with no or least deterioration in mechanical performance. Besides, there is a great expectation of non-existence of inhomogeneous structure introduced by processing. In comparison with other Sn-based alloys, Sn-Zn and Sn-Zn-Bi alloys have unique characteristics, which include low melting temperature [154, 155], low cost [156], and proper mechanical properties (UTS: ~50-90MPa, elongation:10-25%) [157, 158]. Bi was reported to improve the reliability of Sn-Zn alloys by optimization of mechanical properties based on the solid solution effects of Bi atoms and precipitation strengthening by Bi particles [159].

As such, the present chapter aims to investigate the feasibility of developing a cost-effective and easy-manufacturing Sn-Zn-Bi alloys, which can be used as the sheath for MDCs. For the first time, the microstructure and mechanical properties of Sn-Zn and Sn-Zn-Bi alloys were studied after mechanical deformation. Sn-3Zn, Sn-3Zn-1Bi, and Sn-3Zn-5Bi were prepared by casting and rolling. Significantly, Bi was found to enhance both the strength and ductility of the rolled Sn-Zn-Bi alloys. The relationship between the microstructure and tensile properties of rolled specimens were discussed in association with the influence of Bi solutes and second phases on refinement of dynamic crystallized microstructure.

## 6.2 Solidification Microstructure

The actual compositions of the experimental alloys were analysed by the inductively coupled plasma atomic emission spectroscopy (ICP-AES, ARCOS, Simultaneous ICP Spectrometer, SPECTRO Analytical Instruments GmbH, Germany, as shown in Table 6.1.

Table 6.1 Chemical composition of the experimental Sn-Zn-Bi alloys analysed by inductively coupled plasma atomic emission spectroscopy (ICP-AES), wt.%.

Alloys	Zn	Bi	Ni	Cu	Fe	Sb	As	Cd	Sn
Sn-3Zn	3.11	0.03	0.01	0.015	0.01	0.02	0.014	0.006	Rem.
Sn-3Zn-1Bi	2.89	0.98	0.01	0.012	0.01	0.02	0.008	0.006	Rem.

### 6.2.1 Solidification Microstructure of Cast Sn-3Zn

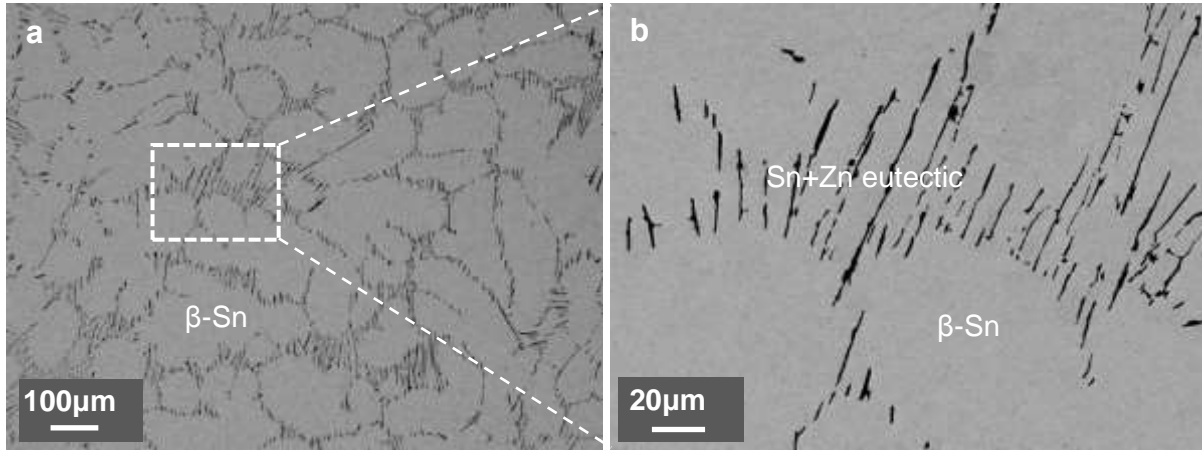


Figure 6.1 Backscattered SEM micrographs showing the solidification microstructure of Sn-3Zn alloy, (b) is the enlargement of the rectangle region in (a).

Figure 6.1 shows the backscattered SEM micrographs for the solidification microstructure of the Sn-3Zn alloy. It was clearly observed that the  $\beta$ -Sn phase was the primary phase. The microstructure of Sn-3Zn mainly consisted of the light grey primary  $\beta$ -Sn phase and Sn-Zn eutectics (Figure 6.1a). The primary  $\beta$ -Sn phase exhibited dendrites morphology with the size being approximately 100-150 $\mu$ m. The Sn-Zn eutectic was in the form of alternate distribution of Sn phase and dark needle-like Zn-rich phase [160], possessing well-aligned acicular Zn-rich precipitates with relatively small spacing being 10-20 $\mu$ m (Figure 6.1b).

### 6.2.2 Solidification Microstructure of Cast Sn-3Zn-xBi

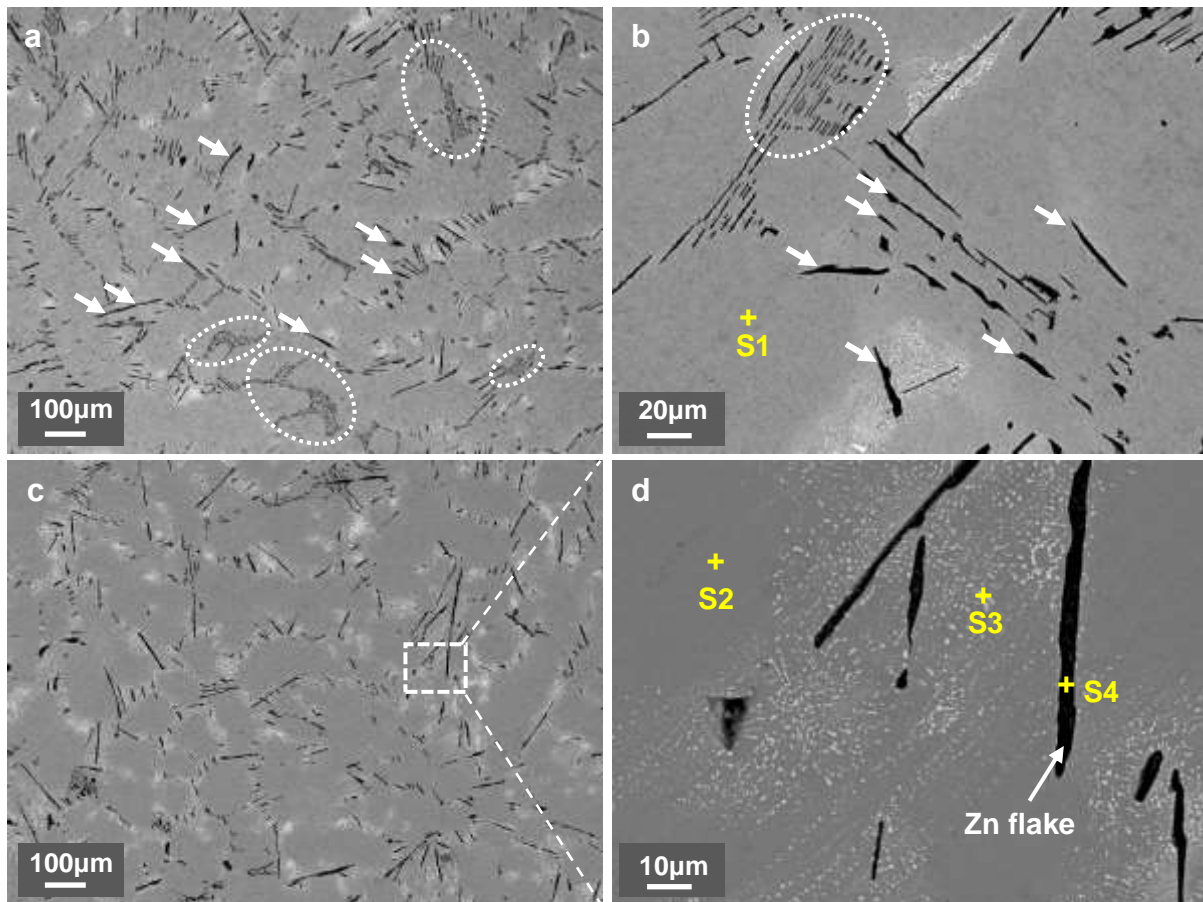


Figure 6.2 Backscattered SEM micrographs showing the solidification microstructure of (a, b) Sn-3Zn-1Bi, and (c, d) Sn-3Zn-5Bi alloy.

Figure 6.2 shows the backscattered SEM micrographs for the solidification microstructure of the Sn-3Zn-1Bi and Sn-3Zn-5Bi alloys. With addition of Bi, the microstructure was greatly changed in terms of the morphology, size, and distribution of both primary  $\beta$ -Sn phase and eutectics, in comparison with the microstructure of the Sn-3Zn alloy. The matrix phase, white phase, and black phase were analysed by EDS, corresponding phases information was illustrated in Figure 6.3. It was observed from Figure 6.2 that the microstructure in the Sn-Zn-Bi alloys mainly comprised  $\beta$ -Sn phase, Zn-rich precipitates, and white Bi particles.

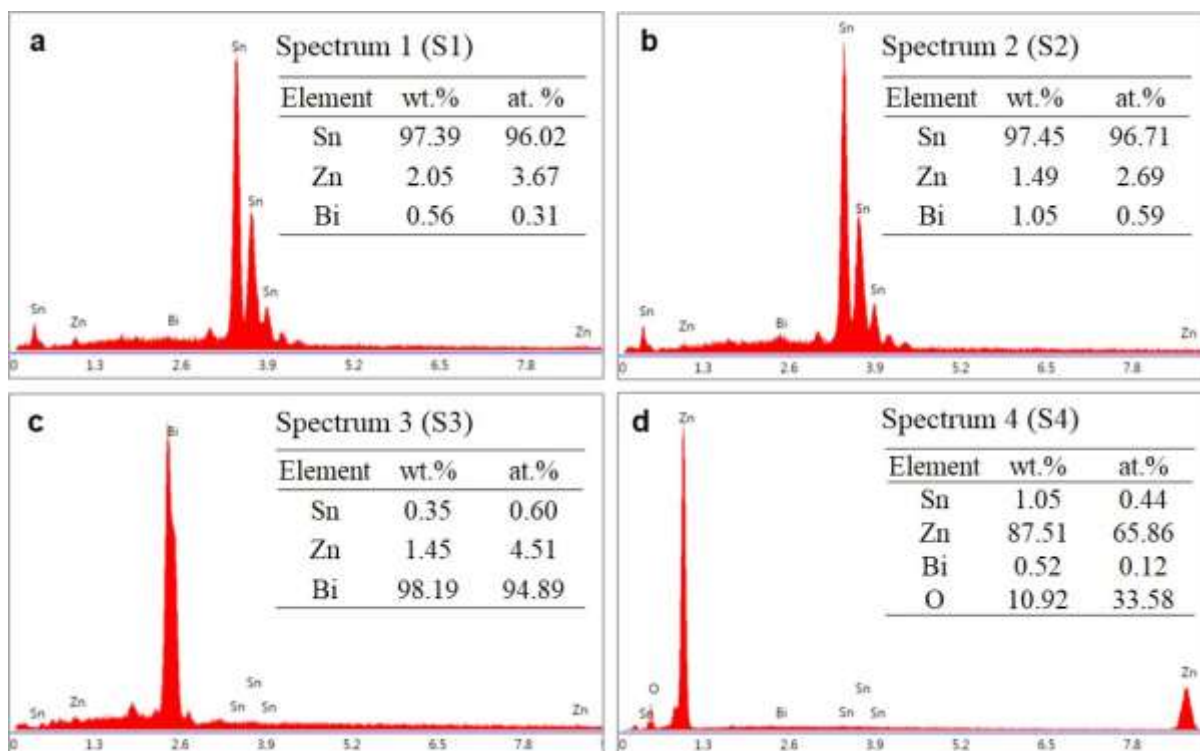


Figure 6.3 EDS point analysis on (a, b) matrix phase, (c) white phase, and (d) black phase of the Sn-Zn-Bi alloys, corresponding to the spectrums in Figure 6.2.

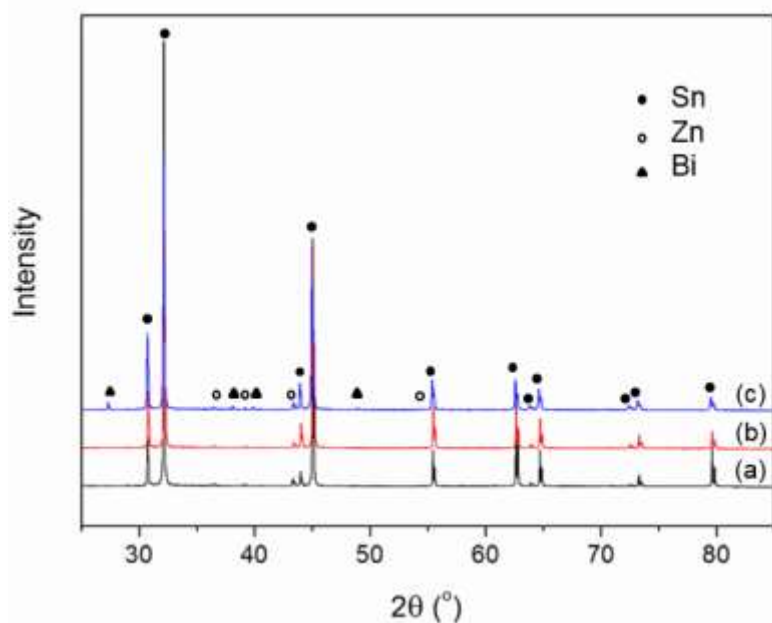


Figure 6.4 XRD patterns for the as-cast (a) Sn-3Zn, (b) Sn-3Zn-1Bi, and (c) Sn-3Zn-5Bi alloys.

Specifically, for Sn-3Zn-1Bi, clearly visible outlines of globular  $\beta$ -Sn dendrites were not easily observed any more. Normal eutectic cells made of alternately distributed Sn and Zn-rich precipitates highlighted with dotted ellipses were rarely seen, whereas the misaligned Zn-rich precipitates in the form of relatively coarse flakes with sizes of approximately 3-5 $\mu$ m were largely dispersed in the Sn matrix (shown by arrows in Figure 6.2a and b). Aggregates of the white Bi particles tended to be randomly distributed at the vicinity of coarse Zn-rich precipitates. When Bi content was increased to 5 wt.%, normal Sn-Zn eutectic cells nearly disappeared and the Zn-rich precipitates became more homogenous (Figure 6.2c). Much more regions of Bi aggregates formed, with individual Bi particle size being less than 1 $\mu$ m.

Figure 6.3 shows the XRD profiles of the as-cast Sn-3Zn, Sn-3Zn-1Bi, and Sn-3Zn-5Bi alloys. It was further confirmed that the Sn-3Zn alloy comprised two phases: a body centred tetragonal  $\beta$ -Sn matrix phase and a second phase of hexagonal Zn. The Sn-3Zn-5Bi alloy was signified as  $\beta$ -Sn phase, hexagonal Zn-rich phase, and Bi precipitates. Due to less Bi phase in Sn-3Zn-1Bi, no Bi peaks were identified through XRD.

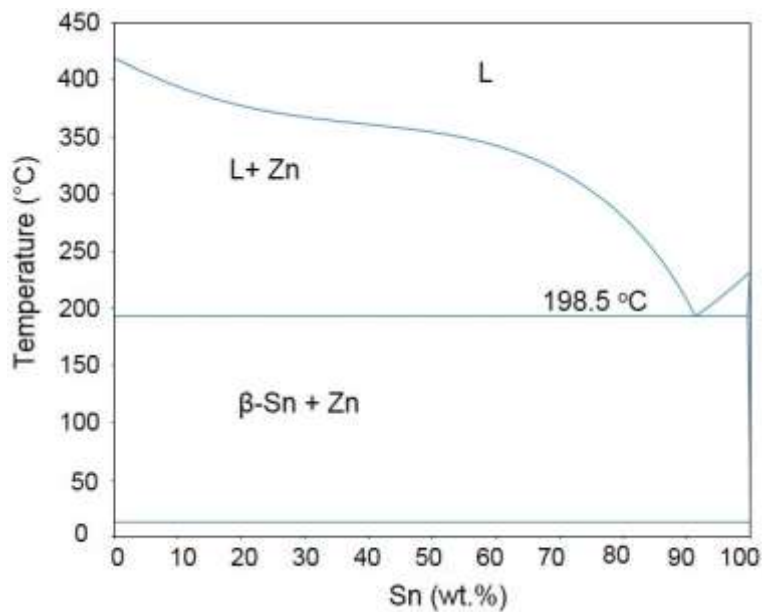


Figure 6.5 Equilibrium phase diagram of Sn-Zn alloy calculated using Panda.

The solidification microstructure of the Sn-Zn alloy can be understood through the solidification path from the equilibrium phase diagrams, as shown in Figure 6.5. The Sn-3Zn alloy was solidified as a hypoeutectic alloy, following the phase transformation:  $L \rightarrow L + \text{primary } \beta\text{-Sn} \rightarrow \text{primary } \beta\text{-Sn} + \text{Eutectic (Sn+Zn)}$ . The microstructure comprised globular

primary  $\beta$ -Sn phase and normal Sn-Zn eutectics, appearing in the form of well aligned fine needle-like Zn-rich precipitates being alternatively distributed in the Sn matrix.

Modification of Bi on the solidification microstructure of Sn-3Zn can be understood through the solidification path from the equilibrium phase diagrams, as shown in Figure 6.6. When 1 and 5wt.% Bi were added, the practical solidification follows phase transformation:  $L \rightarrow L + \text{primary } \beta\text{-Sn} \rightarrow \text{primary } \beta\text{-Sn} + \text{Eutectic (Sn+ Zn)} \rightarrow \text{primary } \beta\text{-Sn} + \text{Eutectic (Sn+ Zn)} + \text{Bi precipitates}$ . Both fine needle-like Zn-rich precipitates and coarse Zn-rich flakes were observed, whereas the fraction of fine Zn-rich needles appeared to be less in the Sn-3Zn-5Bi alloy than that in the Sn-3Zn-1Bi alloy. Similar phenomena were reported in previous research [160], in which the Sn-Zn eutectic turned out to exhibit two kinds of morphologies: the normal Sn-Zn eutectic with fine Zn-rich needles formed alternatively; and the irregular Sn-Zn eutectic with misaligned coarse thick Zn-rich flakes.

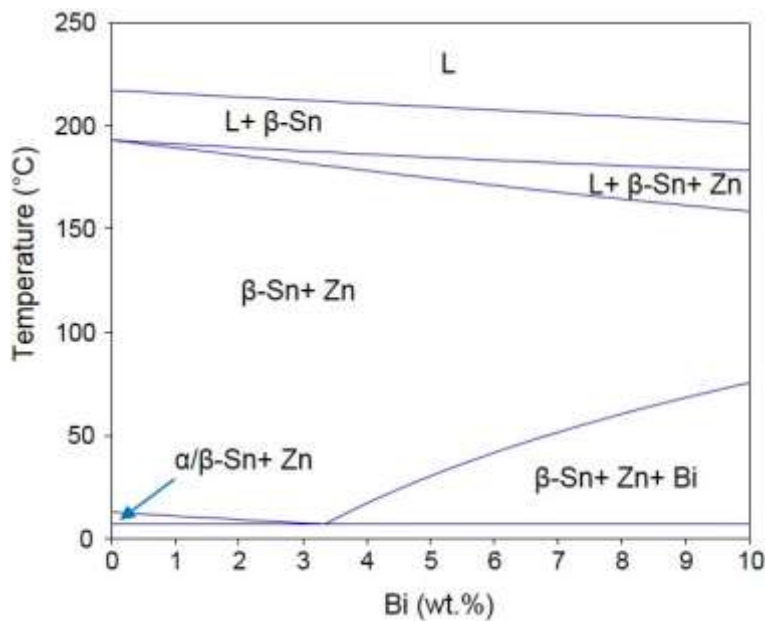


Figure 6.6 Equilibrium phase diagram of Sn-3Zn-xBi alloy calculated using Panda.

Difference between the morphology, distribution, and size of Zn-rich phase in hypoeutectic Sn-3Zn alloy and Sn-Zn-Bi alloy was ascribed to the Bi addition which is a kind of surface-active elements [161]. On one hand, EDS point analysis on Sn matrix (spectrum 1 and 2 in Figure 6.2) confirmed the Bi solution into the Sn matrix. Bi alloying element could dissolve into the eutectic structure and thus probably cause change in the lattice parameters of Sn and Zn, and subsequently an increase in entropy of solution, which may result in the morphological

change of the Sn-Zn eutectic from well aligned Zn-rich needles to irregular coarse Zn-rich flakes [160].

During the solidification process, the initially solidified Sn-Zn eutectic regions with low Bi solute concentrations formed a normal morphology and then the residual liquid with a greater Bi solute content solidified to become the irregular eutectic structure with coarse Zn-rich flake at lower temperature. This was then followed by Bi precipitation in the form of Bi particles at the vicinity of Zn-rich phase (Figure 6.2b and d). 5wt.% Bi alloying was abundant enough in the liquids, the front liquid of the primary solidified Sn had a large quantity of Bi solutes, which consequently generated more irregular Sn-Zn eutectic regions with coarse Zn-rich flakes, resulting in the absence of the normal Sn-Zn eutectic structure in the Sn-3Zn-5Bi alloy. On the other hand, Bi addition further lowered the melting temperature [162]. When solidified, the higher melting point element, Zn, was solidified first, that is, the Zn-rich phase formed earlier, which offered longer time for Zn-rich phase to grow thicker to minimize the surface free energy, resulting in large Zn-rich phase.

### **6.3 Microstructural Evolution under Rolling**

#### *6.3.1 Evolution of Primary $\beta$ -Sn Phase, Eutectics and Precipitates*

Figure 6.7 shows the backscattered SEM micrographs for the microstructure across the longitudinal (RD+ND) and the transverse (ND+TD) sections of the Sn-3Zn alloy. It can be observed that the primary  $\beta$ -Sn phase and the Sn-Zn eutectic regions were severely deformed and elongated along RD. The Zn-rich precipitates were well aligned to RD (Figure 6.7a). The intersection dimensions obtained on ND+TD section of primary  $\beta$ -Sn cells and eutectic regions were remarkably decreased in comparison with the solidification microstructure. The deformed microstructure became much finer. Zn-rich precipitates were observed to be distorted and some were fractured (Figure 6.7b). By applying plastic deformation on the samples, the soft Sn matrix flows plastically while the non/less-deformable Zn-rich phase experience a brittle fracture in elastic region. In fact, as results of the rolling processes, some of the brittle Zn-rich phase are mechanically fractured and changed to finer phase.

Figure 6.8 shows the backscattered SEM micrographs for the microstructure across the longitudinal (RD+ND) and the transverse (ND+TD) sections of the Sn-3Zn-1Bi and Sn-3Zn-5Bi alloy. Similarly, the primary  $\beta$ -Sn phase and the eutectic regions were severely deformed and elongated along RD. The Zn-rich precipitates and/or Bi aggregates were well aligned to

RD (Figure 6.8a and c). EDS point analysis on the Sn matrix was provided, and the morphology and size of individual Bi particles were presented in the insets.

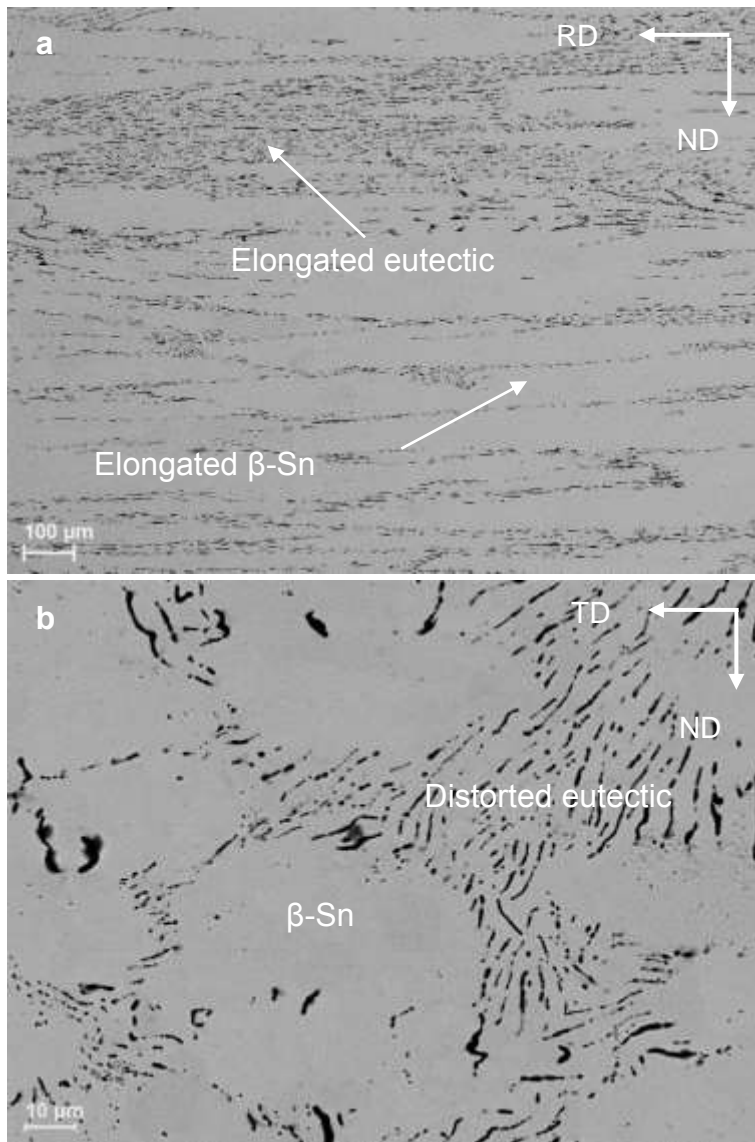


Figure 6.7 Backscattered SEM micrographs showing the microstructure on the cross section of TD and RD of as-rolled Sn-3Zn alloy.

It is well known that fibre-like phases play a main role as stress concentration and crack initiation sites, and therefore noticeably reduce the mechanical properties of the alloys. So, it can be said that modifying the Zn-rich phase is a potential benefit of the rolling process as a secondary mechanical process on cast Sn-Zn-Bi alloys. The Zn-rich precipitates in the Sn-3Zn-1Bi and Sn-3Zn-5Bi alloys were more homogeneous than that in the Sn-3Zn alloy, which was ascribed to more uniform distribution of the Zn-rich precipitates in the corresponding solidification microstructure. The improved uniformity of cast alloys during rolling is due to

the flow of the alloy under the applied shear and compressive forces, resulting in de-clustering of the Zn-rich phase.

It is noted that, after rolling, the distribution of Bi aggregates appeared to be sparser, whereas the size of the individual Bi particles became larger (Figure 6.8c&d vs. Figure 6.2c&d). This phenomenon was believed to be associated with the dissolution of Bi into Sn matrix and reassembling of the small Bi particles into a bigger one under the rolling stress [163, 164, 165]. In fact, the dissolution of Bi during rolling was evidenced by the EDS analysis on rolled Sn-3Zn-1Bi and Sn-3Zn-5Bi: the contents of Bi alloying were measured to be largely increased from 0.56wt.% (as-cast) to 0.96wt.% (as-rolled) for Sn-3Zn-1Bi and from 1.05wt.% (as-cast) to 2.43wt.% (as-rolled) for Sn-3Zn-5Bi, as shown in Figure 6.3 and Figure 6.8a&c.

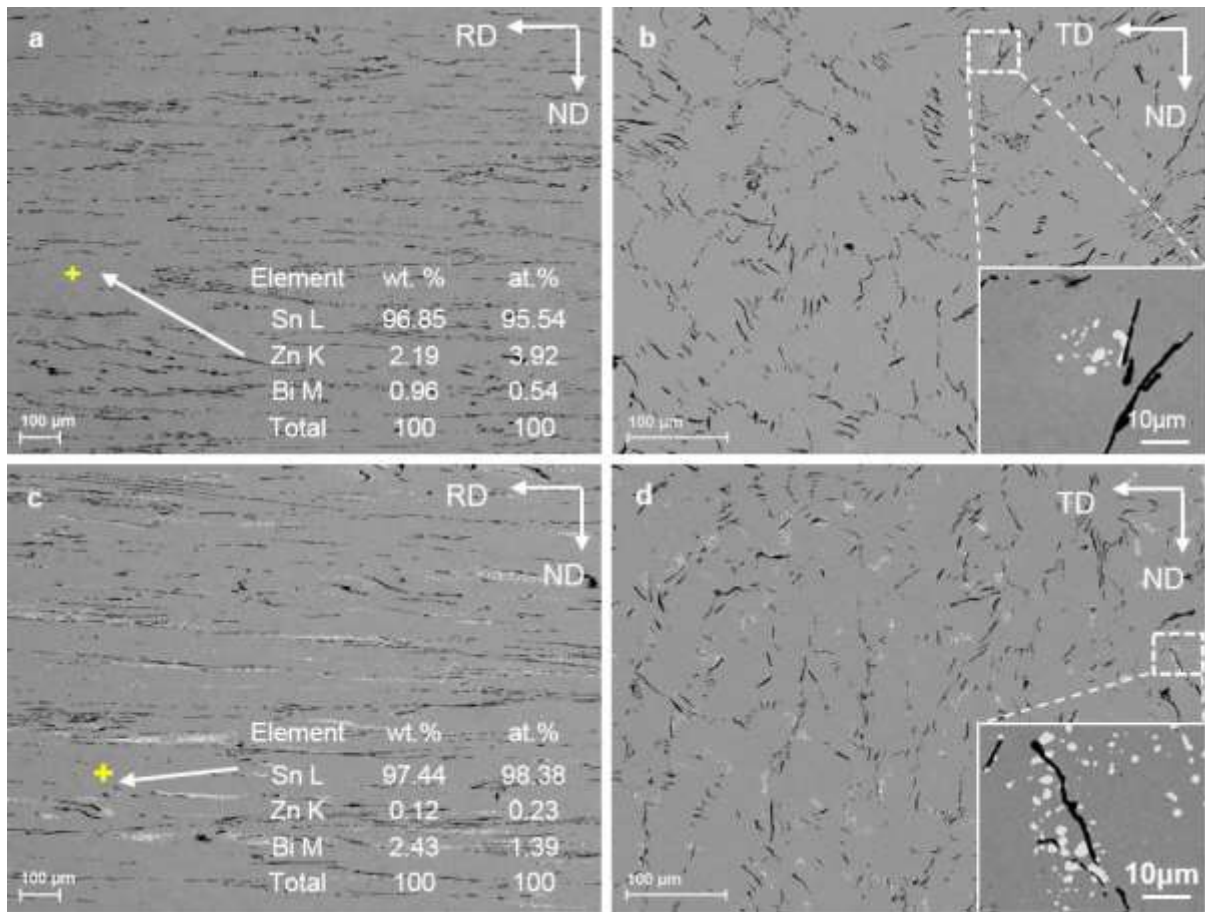


Figure 6.8 Backscattered SEM micrographs showing the microstructure on the cross section of TD and RD of as-rolled (a, b) Sn-3Zn-1Bi, and (c, d) Sn-3Zn-5Bi alloys.

### 6.3.2 Grain Refinement

Figure 6.9 presents the EBSD IQ+IPF map showing the microstructure grain orientations on the RD-ND section of the rolled Sn-3Zn specimen. High-angle grain boundaries (HAGBs) with misorientation angles being larger than  $15^\circ$  are presented with black solid lines. Low-angle grain boundaries (LAGBs) with misorientation angles being in the range of  $2-15^\circ$  are illustrated with light-blue solid lines. It was seen that the structure showed partially recrystallized grain morphology. Inhomogeneous grains with a wide grain size range presented, possessing large grain sizes being in the range of  $50-120\mu\text{m}$  and small ones being several microns. The large grains were originated from the pre-rolled primary Sn phase regions, whereas the small grains were found to be located at the eutectic regions and/or at the vicinity of the Zn-rich precipitates, as highlighted with yellow lines, for instance.

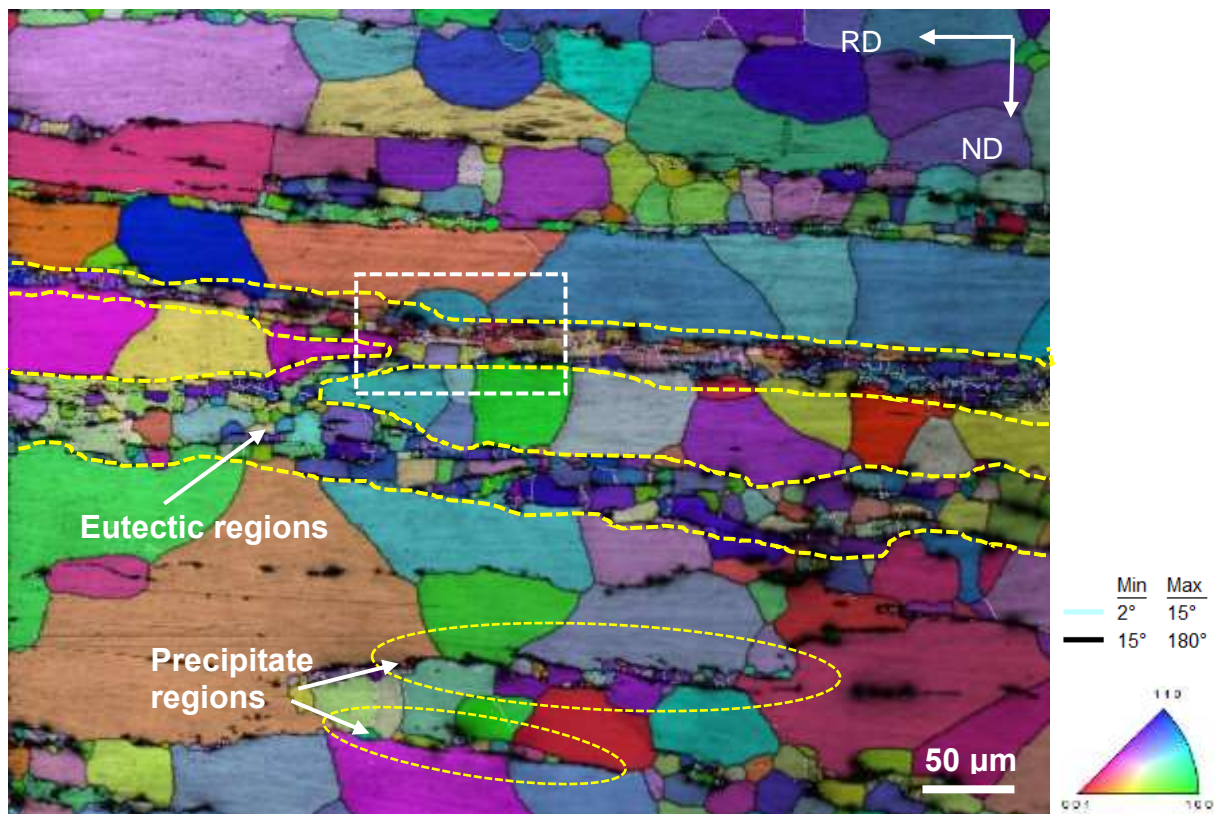


Figure 6.9 EBSD IQ+IPF map for the rolled Sn-3Zn alloy extracted on the RD-ND section. LAGBs: low-angle grain boundaries ( $2-15^\circ$ ).

Figure 6.10a presents the EBSD phase map corresponding to the highlighted rectangular region in Figure 6.9, and Figure 6.10b illustrates the grain boundary misorientations distribution diagram extracted from Figure 6.9. Full inspection of the Sn-Zn eutectic area marked with rectangular (Figure 6.9) revealed that majority of the grains within the region exhibited small-

sized equiaxed morphologies with grains size being less than 10 $\mu\text{m}$  and a large fraction of low-angle grain boundaries formed, as shown in Figure 6.10. This indicated that the Sn-Zn eutectic sites or Zn-rich precipitate sites were beneficial to accumulation of strains or dislocations and consequently facilitated the formation of smaller grains. It is observed from Figure 6.10b that the distribution of grain boundary misorientations suggested a relatively uniform misorientations distribution. Low-angle grain boundaries (2-15 $^\circ$ ) took up about 12% of the total grain boundaries. The average misorientation angle was measured to be approximately 50.3 $^\circ$ .

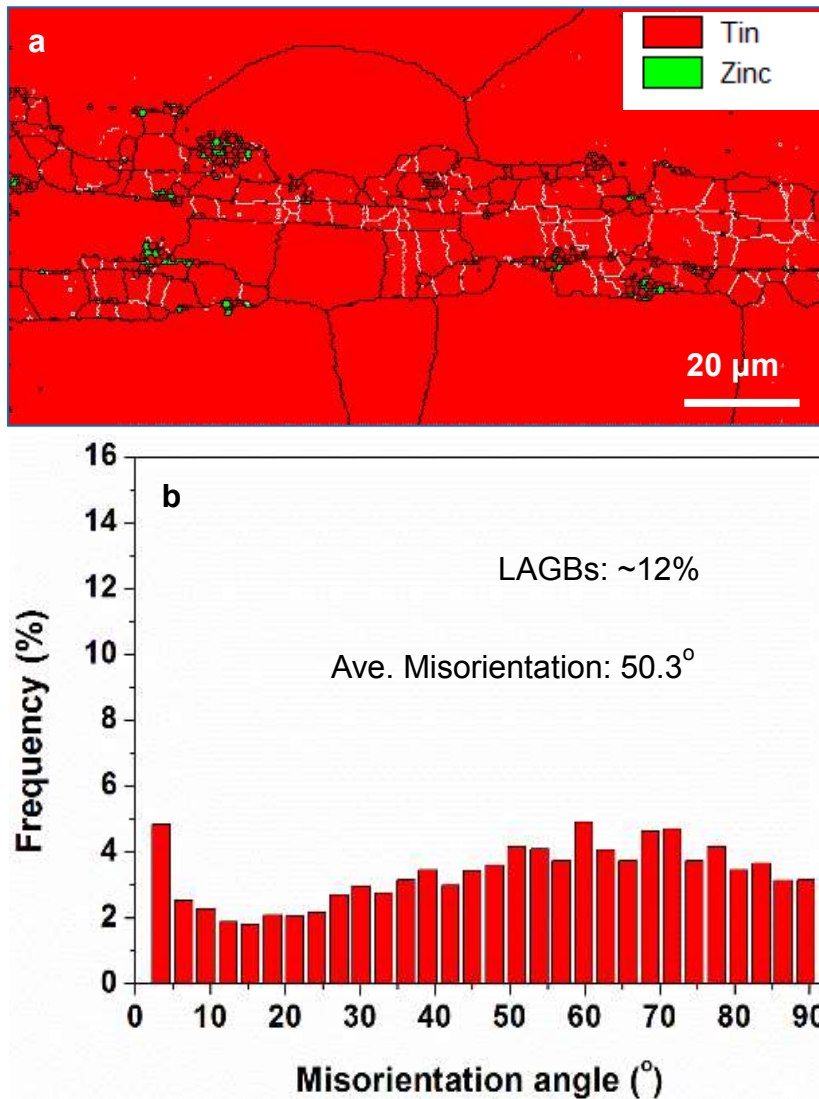


Figure 6.10 (a) EBSD IQ+IPF, (b) EBSD phase map, and (c) distribution of grain boundary misorientations for the rolled Sn-3Zn alloy extracted on the RD-ND section. LAGBs: low-angle grain boundaries (2-15 $^\circ$ ).

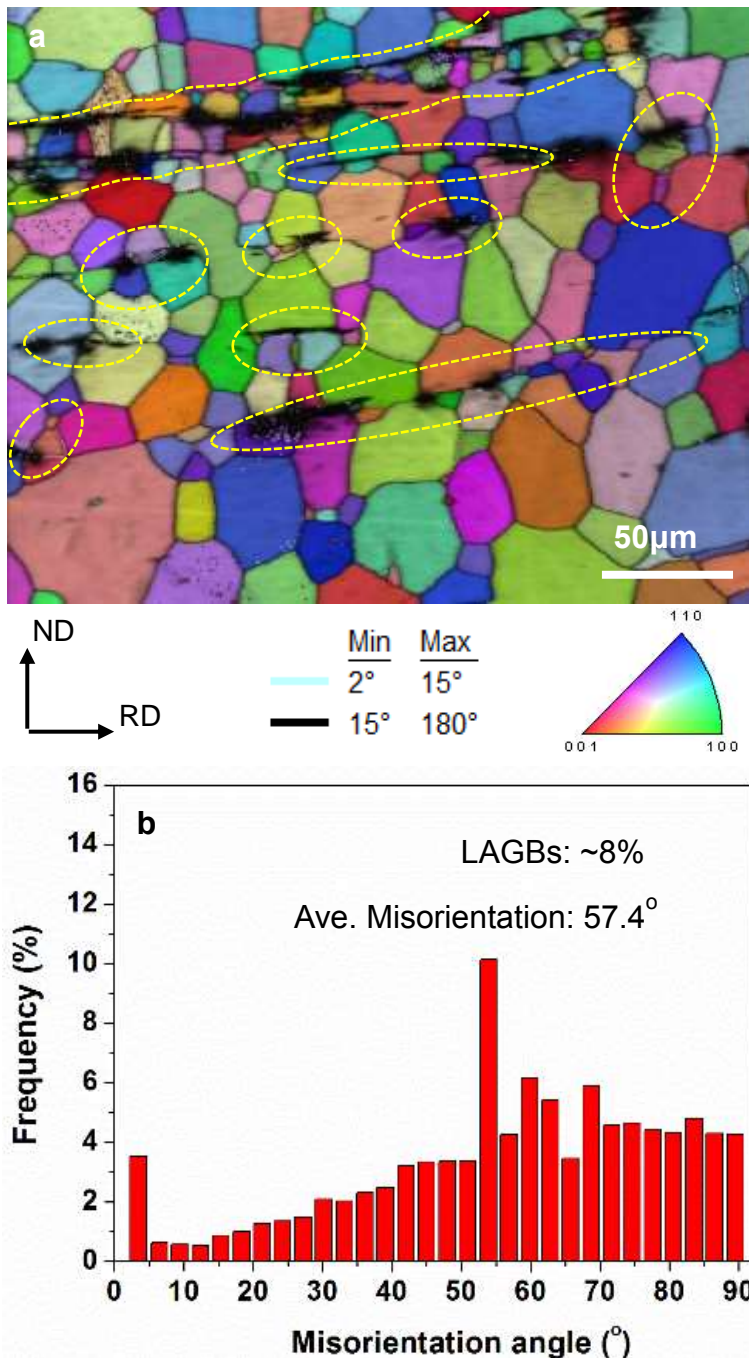


Figure 6.11 (a) IQ+IPF maps and (b) grain boundary misorientations distribution on the ND+RD plane of the rolled Sn-3Zn-1Bi alloy. LAGBs: low-angle grain boundaries (2-15°).

Figure 6.11 shows the EBSD maps and grain boundary misorientations distribution on the RD-ND section of the rolled Sn-3Zn-1Bi alloy. The microstructure was characterized as relatively homogeneous grains (Figure 6.11a). Equiaxed grains, defined as those with grain shape aspect ratio larger than 0.6, rather than elongated grains largely presented. The grain sizes covered a relatively small range from several microns to ~50µm. Still, small grains tended to form at the vicinity of Sn-Zn eutectic regions or Zn precipitate sites (circled areas), further indicating that

these sites favoured the formation of smaller grains. It was measured that low-angle grain boundaries accounted for ~8% of total grain boundaries, which was lower than that in rolled Sn-3Zn alloy, suggesting a more complete recrystallization (Figure 6.11b).

Figure 6.12 shows the EBSD maps and grain boundary misorientations distribution on the RD-ND section of the rolled Sn-3Zn-5Bi alloy. It was obvious that with further increasing Bi content to 5wt.%, the microstructure became much finer with highly homogeneous equiaxed grains, being approximately 10-20 $\mu\text{m}$  in grain size (Figure 6.12a). Additionally, it is noted that extremely small grains (< 5 $\mu\text{m}$ ) appeared in the region highlighted with white lines. This region contained large amounts of Bi particles (Figure 6.12b), further indicating that Bi particle-enriched area could benefit the formation of small grains. Also, the fraction of low-angle grain boundaries (2-15 $^\circ$ ) further decreased to ~4% (Figure 6.12c).

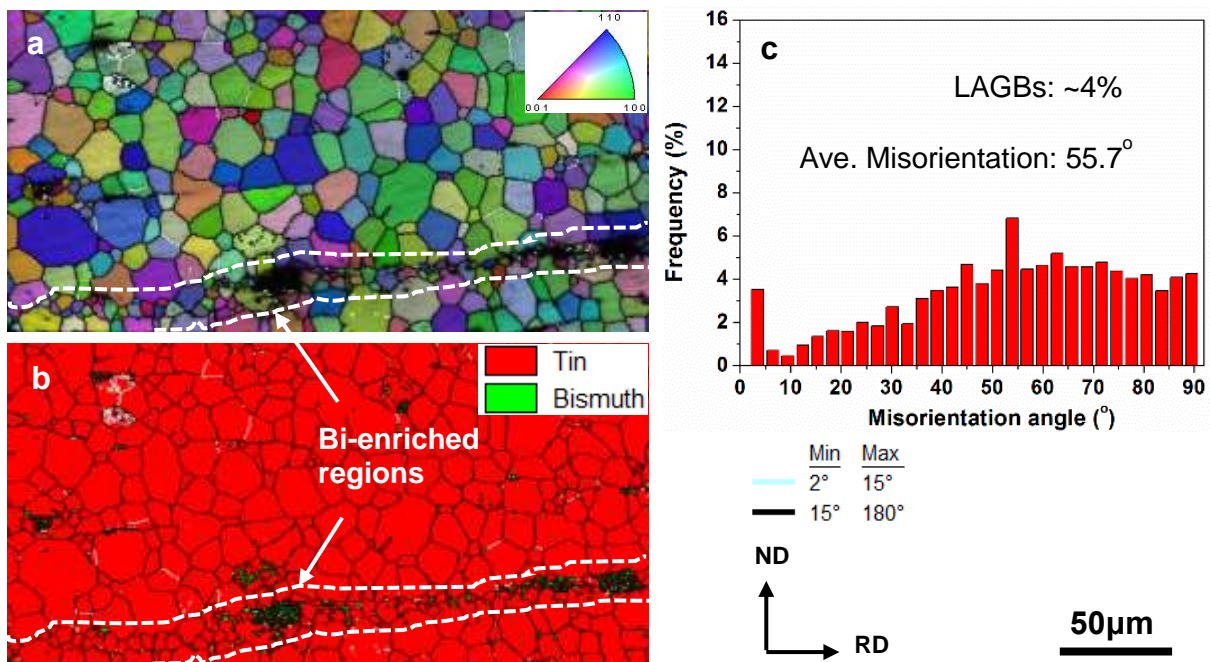


Figure 6.12 (a) IQ+IPF maps, (b) phase map, and (c) grain boundary misorientations distribution on the ND+RD plane of the rolled Sn-3Zn-5Bi alloy. LAGBs: low-angle grain boundaries (2-15 $^\circ$ ).

Figure 6.13 shows the EBSD boundary maps and grain distribution attained on the ND-TD section of the Sn-3Zn alloy. Grains with different sizes were highlighted with different colours (blue: 3-10 $\mu\text{m}$ ; white: 10-30 $\mu\text{m}$ ; and red: > 30 $\mu\text{m}$ ). The misorientations angle from 2-180 $^\circ$  were illustrated in the legend. The grains with grain size being larger than 3 $\mu\text{m}$  were taken into consideration for statistically grain size measurements. The structure of rolled Sn-3Zn

exhibited bimodal grain distribution (Figure 6.13a). It was measured that in the Sn-3Zn alloy the grains with grain size being larger than 30 $\mu\text{m}$  took up most of the area, 66.9% in area fraction, and the area fraction of small grains with grain size being less than 10 $\mu\text{m}$  just accounted for 4.9%. In average, the grain size was measured to be around 44.3 $\mu\text{m}$  (Figure 6.13b)

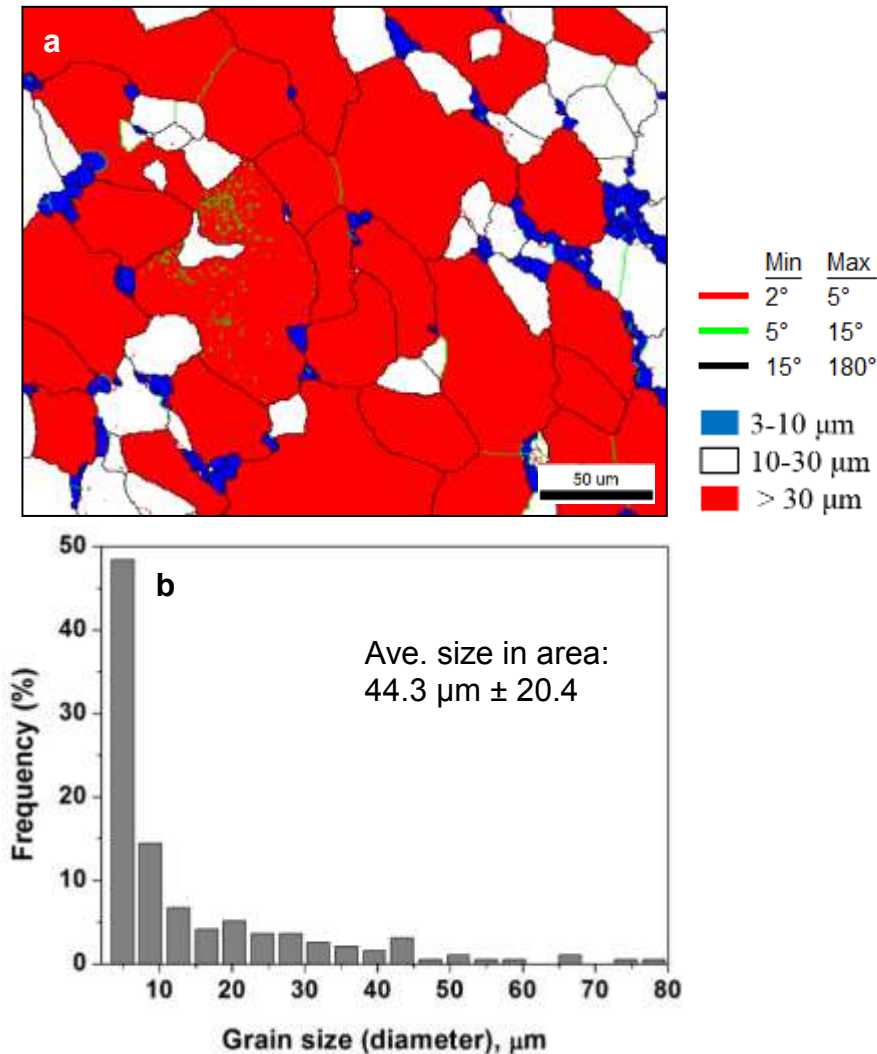


Figure 6.13 The EBSD (a) boundary maps and (b) grain distribution diagrams obtained on ND+TD section of the rolled Sn-3Zn alloy. LAGBs: low-angle grain boundaries (2-15°).

Figure 6.14 shows the EBSD boundary maps and grain distribution attained on the ND-TD section of the Sn-3Zn-1Bi alloy. Grains with different sizes were highlighted with different colours (blue: 3-10 $\mu\text{m}$ ; white: 10-30 $\mu\text{m}$ ; and red: > 30 $\mu\text{m}$ ). In comparison with the rolled Sn-3Zn alloy, the microstructure for the rolled Sn-3Zn-1Bi had relative uniform grains. It was measured that the number of small grains with grain size being less than 10 $\mu\text{m}$  was increased, with the area fraction twice of that for Sn-3Zn, 11.4%, whereas the number of large grains with

grain size being larger than 30 $\mu\text{m}$  was dramatically decreased, with area fraction dropping to 24.7%. In average, the grain size was measured to be around 22.8 $\mu\text{m}$  (Figure 6.14b).

Figure 6.15 shows the EBSD boundary maps and grain distribution attained on the ND-TD section of the Sn-3Zn-6Bi alloy. Grains with different sizes were highlighted with different colours (blue: 3-10 $\mu\text{m}$ ; white: 10-30 $\mu\text{m}$ ; and red: > 30 $\mu\text{m}$ ). It was suggested that further adding 5wt.% Bi led to majority of smaller equiaxed and homogeneous grains, no more grains being larger than 30 $\mu\text{m}$  was observed. The small grains being less than 10 $\mu\text{m}$  took up 20.1% of the whole area. In average, the grain size was measured to be around 15.3 $\mu\text{m}$  (Figure 6.15b).

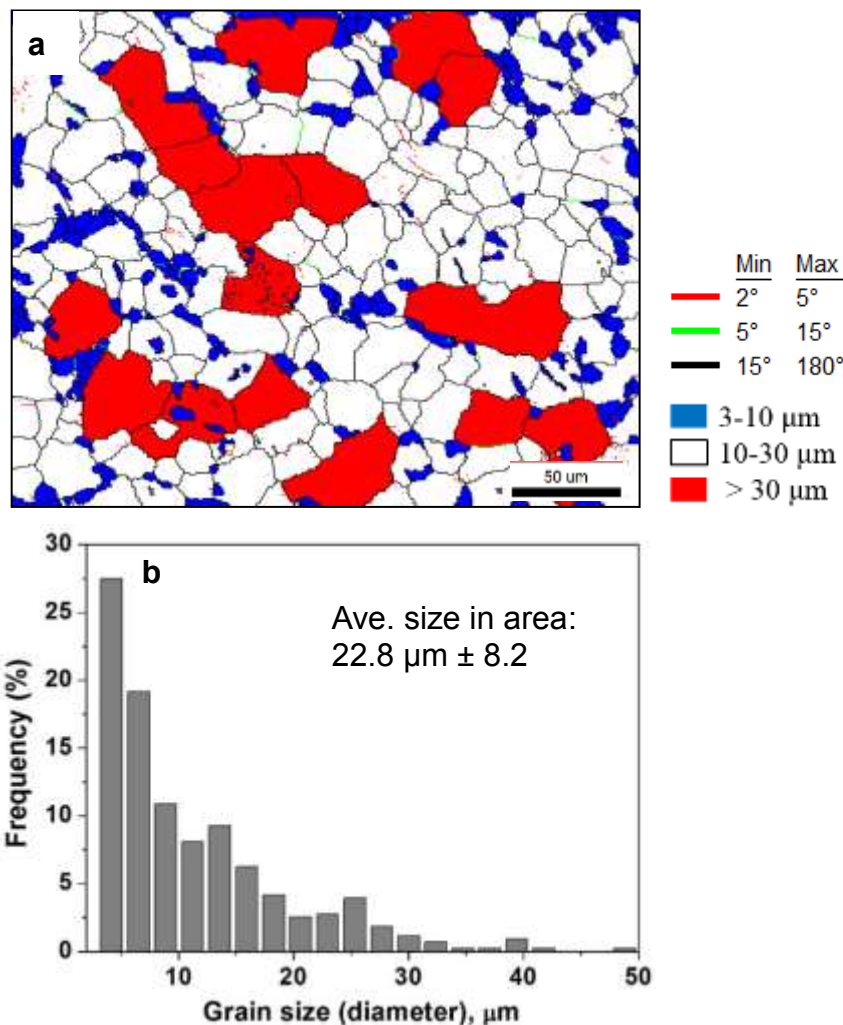


Figure 6.14 The EBSD (a) boundary maps and (b) grain distribution diagrams obtained on ND+TD section of the rolled Sn-3Zn-1Bi alloy. LAGBs: low-angle grain boundaries (2-15°).

The grain refinement and the grain boundaries evolution during rolling could be closely related to dislocation activities and dynamic recrystallization (DRX) behaviour. DRX refers to the occurrence of recrystallization during deformation. In the process of DRX, accumulation of

dislocations by straining is often accompanied by nucleation and growth of the newly formed dislocation-free grains. Same as static recrystallization (SRX) that usually takes place during annealing, DRX is a process of energy-releasing, which counteracts the energy-storing process associated with multiplication of dislocations and sub-boundaries produced during straining.

It has been well documented that conventional dynamic recrystallization (often referred to as discontinuous dynamic recrystallization, DDRX) takes place during straining as long as the working temperature is above  $0.5T_m$  [125, 166, 127]. In our case, the ambient rolling was considered as hot working because the processing temperature, 293K, is larger than  $0.5T_m$  [157], in addition to the dislocations accumulation and formation of sub-grains, the DRX was thus the most common feature during deformation. This was, in fact, well supported by the fact that the microstructure after rolling presented typical hot-processing structures with the grains being partially or fully recrystallized.

In general, DDRX is considered as a two-step process: first the nucleation of new grains, and then the growth. In these materials subjected to DDRX, the dislocation density increases to a high level and eventually some of the local difference in density reach a high enough level to permit the nucleation of new grains. Then, this followed by the long-range migration of high angle grain boundaries. Factors affecting the process of nucleation and/or growth will influence the final grain configuration. Second phases including Zn-rich precipitates and Bi particles, combined with Bi solutes were believed to affect the two processes (nucleation and growth) of DRX and to be responsible for the different grain configurations in terms of the grain size and homogeneity.

It has been suggested that large ( $> 1\mu m$ ) second phase particles, especially those widely spaced particles could promote dynamic recrystallization via the mechanism of particle-stimulated nucleation (PSN) [167, 134, 168]. This was based on the explanation that the enforced strain gradient at the vicinity of a less-deformable particle creates a region of high-density dislocations and large orientation gradient (particle deformation zone, or PDZ), which is an ideal site for the development of a recrystallization nucleus. In the Sn-3Zn alloy, the Zn-rich precipitates acting as nucleation sites, can lead to large amounts of recrystallized nuclei in the Sn-Zn eutectic regions. This facilitates the initiation of recrystallization. On the other hand, when recrystallized nuclei grow the Zn-rich precipitates can act as the obstacles to hinder the growth of the recrystallized grains. Many small-sized recrystallized grains consequently formed in the regions of Sn-Zn eutectics. On the contrary, the original primary  $\beta$ -Sn regions

lack nucleation sites such as particles and/or high density of dislocations, thus, impeding the initiation of recrystallization. Moreover, mobility of boundaries (growth) of the recrystallized grains forward cross the primary  $\beta$ -Sn regions can easily occur as no particles acting as barriers will prevent the boundaries from moving, which as a result causes relatively large grains in the particle-free areas.

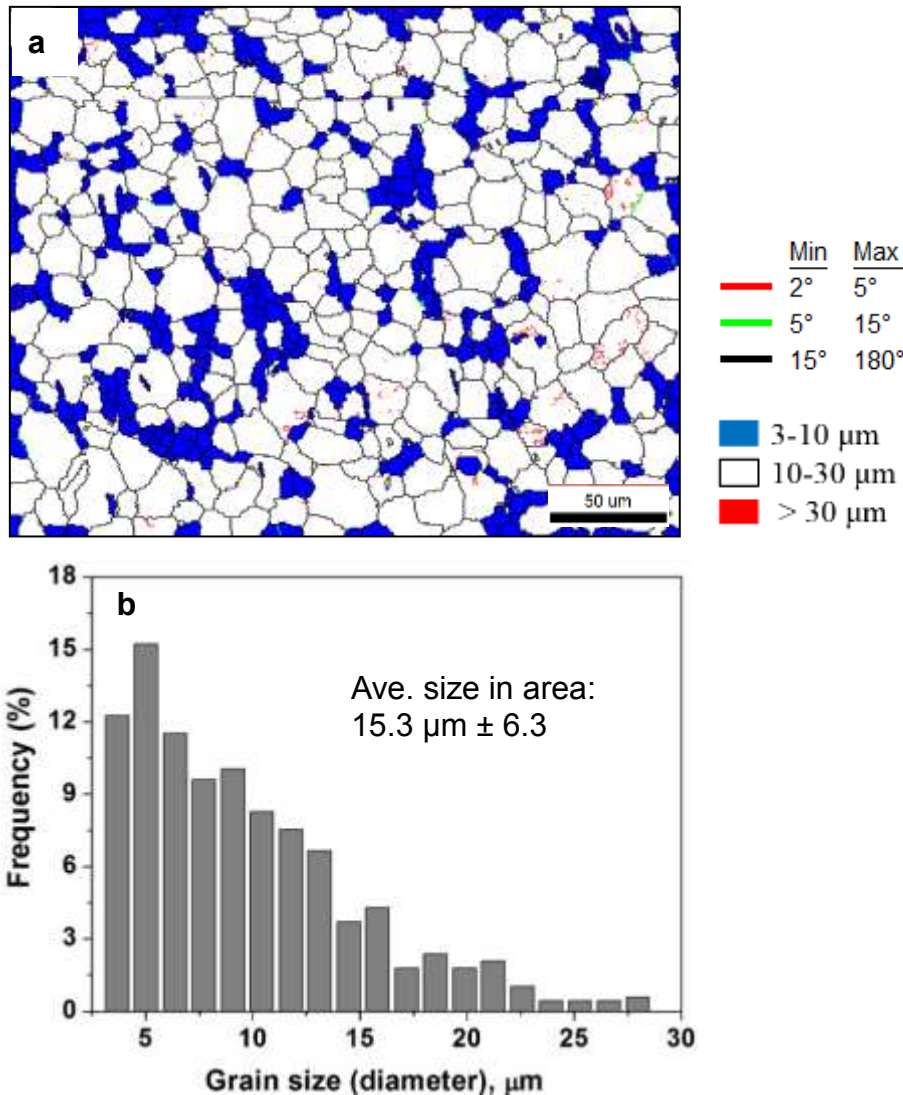


Figure 6.15 The EBSD (a) boundary maps and (b) grain distribution diagrams obtained on ND+TD section of the rolled Sn-3Zn-5Bi alloy. LAGBs: low-angle grain boundaries (2-15°).

When Bi was added, as discussed before, Bi solutes in one aspect cause homogeneously distributed Zn-rich precipitates and Bi second phase particles, which on one hand offers more sites for nucleation, and on the other hand, provides more barriers to hinder the growth of recrystallized grains. This boosts the effect of the second phase particles on reduction of recrystallized grain size. In other aspects, Bi has relative amount of solubility in Sn at room

temperature [162, 169], which was also evidenced by the EDS results (Figure 6.8). The role of solutes in decreasing the rate of grain boundary motion through solute drag has been largely discussed in previous research [170, 171, 172, 173], which is based on the idea that a moving boundary drags an atmosphere of solute atoms that exerts a retarding force on it. The retardation of grain boundary mobility in return impedes the growth process, decreasing the recrystallized grain size. Moreover, the effect of solutes on the nucleation of DRX was introduced by Cram et al [174], which further enriched the understanding of retardation effect of DRX. This is based on the consideration that solute atoms may segregate to the dislocations in the sub-grain boundary and their binding with the vacancies that mediate the sub-grain motion retards the kinetics of DRX. Based on these, it is understandable that with Bi addition the grain size of rolled Sn-Zn-Bi alloys became much finer, reaching the smallest value in the case of Sn-3Zn-5Bi alloy.

### 6.3.3 Correlation between the Microstructure and Mechanical Properties

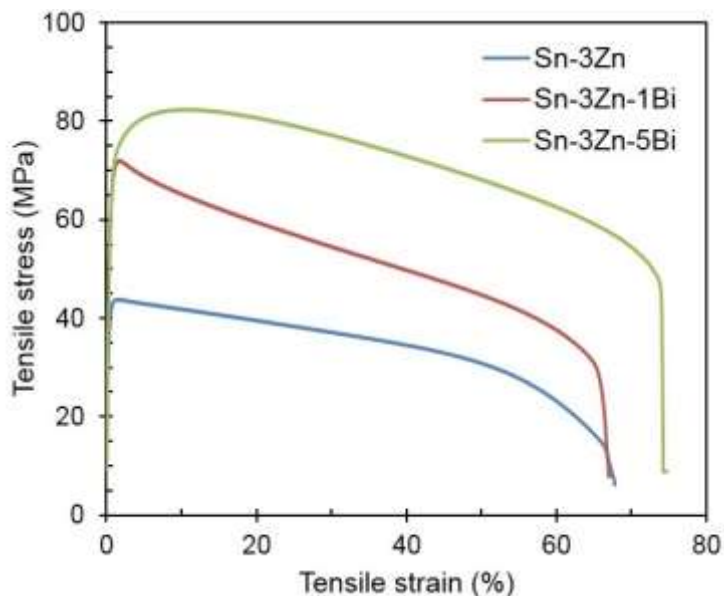


Figure 6.16 Tensile stress-strain curves for the rolled Sn-3Zn, Sn-3Zn-1Bi, and Sn-3Zn-5Bi alloys.

Figure 6.16 presents the tensile stress-strain curves of the rolled Sn-3Zn, Sn-3Zn-1Bi, and Sn-3Zn-5Bi alloys. It indicated that strain softening occurred in all cases when the alloys were subjected to tensile stress. This was ascribed to the high-rate annihilation (recovery) of dislocations and dynamic recrystallization under tensile stress. The  $\beta$ -Sn crystal is known to have a tetragonal distortion of the diamond crystal structure with two atoms per primitive cell. There are about 32 different slip systems in  $\beta$ -Sn and at least five slip systems:  $(110)[\bar{1}11]/2$ ,

(101)[010], (101)[11-1]/2, (121)[-101], and (121)[1-11]/2 are energetically preferable [118, 175]. When the alloys are deformed under tensile stress, dislocation activities including dislocation multiplication and annihilation will predominate the deformation, a competition of the dislocation multiplication which resulting in hardening and the dislocation annihilation contributing to softening will take place. If the rate of dislocation annihilation is higher than that of dislocation multiplication, the strain softening will be attained. Inversely, the strain hardening will exhibit. As mentioned before, the tensile test which was carried out at 293K was a hot working processing. The dynamic recovery rate is sufficiently high to counteract the hardening effect caused by dislocation accumulation. Moreover, the newly formed recrystallized grains appearing during straining could produce softening, decreasing the work hardening rate, as a result contribute to the softening phenomenon.

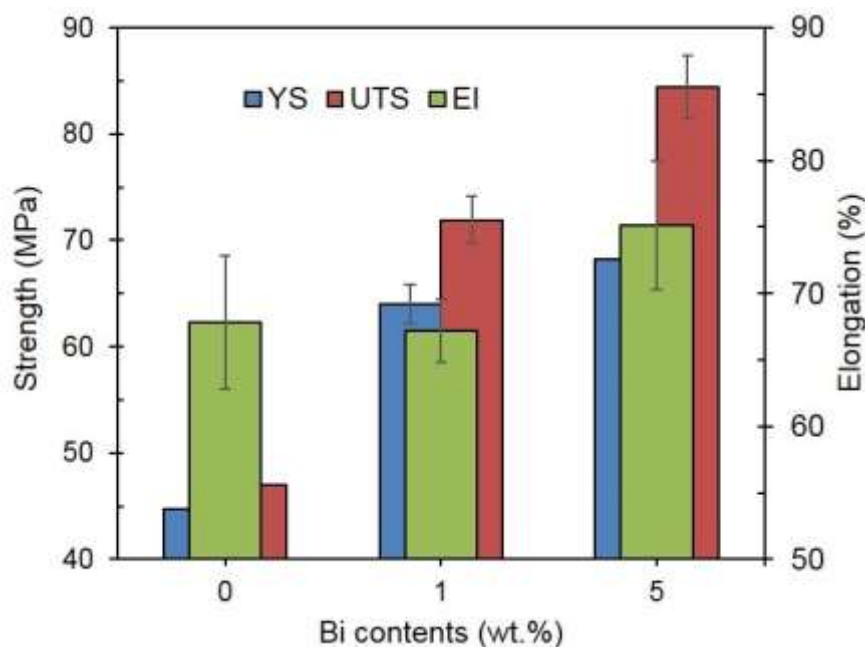


Figure 6.17 The effect of Bi contents on the tensile properties of the rolled Sn-3Zn alloy.

Figure 6.17 compares the tensile results including the yield strength, UTS, and elongation of the rolled Sn-3Zn, Sn-3Zn-1Bi, and Sn-3Zn-5Bi alloys extracted from Figure 6.16. It was obvious that Bi not only caused a significant increase in the strength but also improved the elongation of Sn-3Zn alloys. Specifically, the UTS and yield strength of the Sn-3Zn alloy was 47.0MPa and 44.8MPa, respectively. With 1wt.% Bi addition, the UTS and yield strength was dramatically increased to 71.9MPa and 64.0MPa, respectively. When Bi was further increased to 5wt.%, the UTS and yield strength was further increased to 84.4MPa and 68.3MPa, respectively. The elongation of Sn-3Zn and Sn-3Zn-1Bi showed a similar value around 67.5%,

whereas 5wt.% Bi addition increased the elongation to 75.2%. The improvement in both strength and ductility was closely dependent on the microstructure variation, mainly involving the solutes, second phases, and grain boundaries.

Elements in solid solution usually strengthen crystals. This effect is mainly attributable to interaction of the solute atoms with the dilatational stress field around dislocations, which makes dislocation motion more difficult. As a result, the strength, especially, the yield strength of alloys is enhanced. The maximum solubility of Zn in Sn is around 0.33wt.% at 198.5°C and at room temperature it is around 0.14wt.% [161], suggesting that the solubility is very limited. The solid solution strengthening from Zn solutes is thus believed to be very minimal. However, Bi has relative solubility in Sn (~1.5wt.% at room temperature [162, 170]). In fact, EDS analysis on rolled Sn-Zn-Bi (Figure 6.8) has confirmed the increased Bi solubility in Sn, from 0.96wt.% to 2.43wt.% with Bi content increasing from 1wt.% to 5wt.%. Therefore, Bi solid solution strengthening could be an important factor improving strength of the Bi-containing alloys.

Besides, second phase strengthening mechanism operate effectively. The non-deformable Zn-rich phase and brittle Bi particles are stronger than the soft Sn matrix. These second phases act as barriers for dislocation movement, causing an enhancement of initial strength. The experimental results have confirmed that Bi addition changed the Sn-Zn eutectic morphology, leading to essential microstructural refinement with highly dispersed Zn-rich precipitates [176]. Consequently, more uniformly distributed Zn-rich precipitates enhanced the effectiveness of second phase strengthening. Therefore, the strength of the alloys was increased with increasing Bi content.

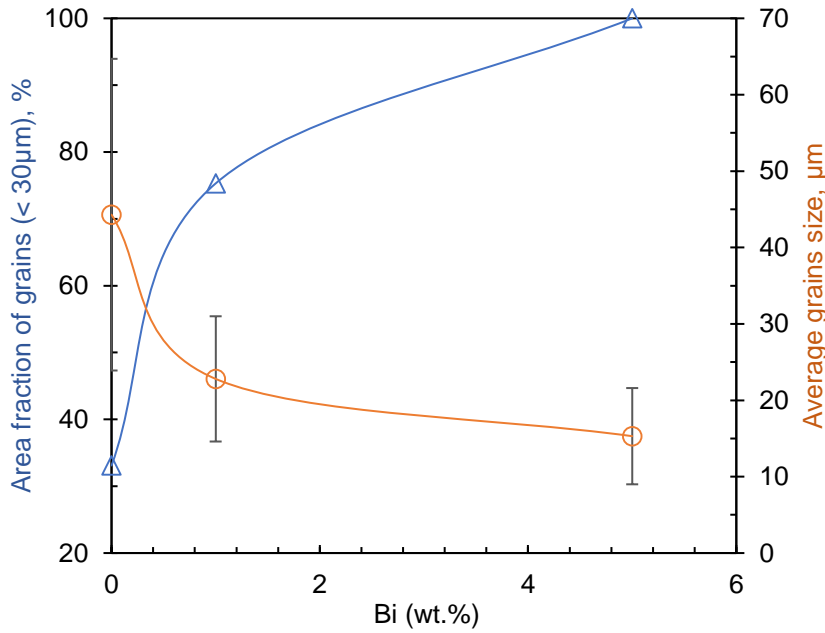


Figure 6.18 The effect of Bi contents on the grain size evolution of the rolled Sn-Zn-Bi alloys.

Grain boundaries are important obstacles to slip, with finer grain sizes there are more grain boundaries to impede dislocation motion. Therefore, materials with fine grains are stronger than those with large grains. The relationship between yield strength and grain size are often expressed by the Hall-Petch equation [177, 178]:  $\sigma = \sigma_0 + kd^{1/2}$ , where  $\sigma_0$  and  $k$  are constants, and  $d$  is the grain size. The grain size was proved to be decreased with increasing Bi content (Figure 6.13-6.15). For clarity, the relation between the grain size and Bi content was plotted, as shown in Figure 6.18. With increasing Bi content, the mean grain size experienced a dramatic decrease (from 44.3µm dropping to 15.3µm). The fraction of smaller grains (< 30µm) increased considerably. So, the decreased grain size contributes to the increased strength in the Bi-containing alloys.

It should be noted that the brittle Bi phase was reported to harm the ductility [179]. However, this is not in agreement with the present results. In our case, 5wt.% Bi addition possesses a highest elongation (~75%). The superior ductility of rolled Sn-3Zn-5Bi was attributable to the ductility-boosting factors: (1) smaller grain size; (2) larger fraction of equiaxed grains; and (3) larger proportion of HAGBs. Figure 6.19 shows variation of fraction of equiaxed grains, and grain boundary misorientation angles with Bi contents. The number fraction of the equiaxed grains was increased notably with increasing Bi, from 20.2% to 37.1% (Figure 6.19a). Also, higher number proportion of HAGBs was obtained in higher Bi-containing alloys (Figure

6.19b). Based on these, it is induced that the good ductility of Sn-3Zn-5Bi is a result of high proportion of small equiaxed grains and HAGBs.

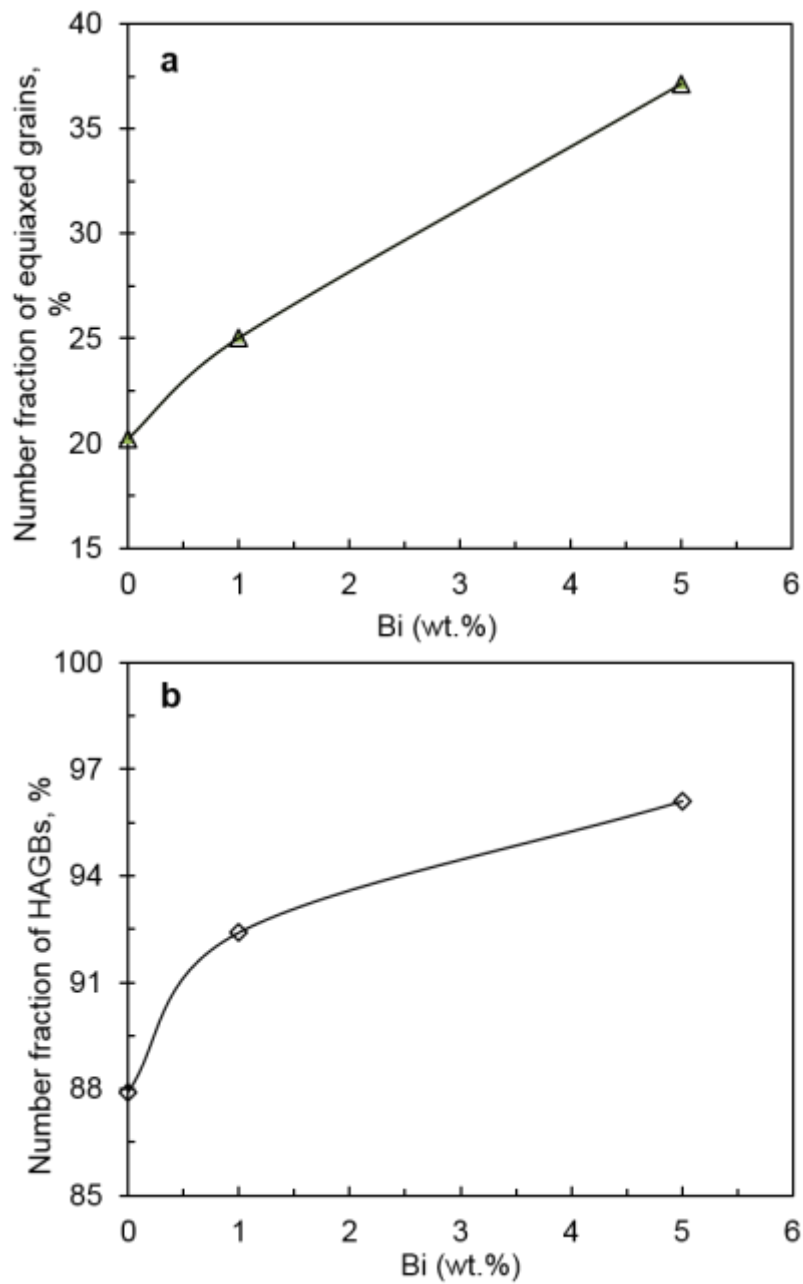


Figure 6.19 The effect of Bi contents on the fraction of (a) equiaxed grains, and (b) high angle grain boundaries (HAGBs) of the rolled Sn-Zn-Bi alloys.

## 6.4 Summary

In the present chapter, effects of Bi on the microstructure and mechanical properties of the Sn-3Zn alloys were investigated under as-cast and as-rolled conditions. Bi can effectively refine the solidification microstructure. It shows that Bi enhances both the strength and ductility of the rolled Sn-3Zn-Bi alloys. The structure displays equiaxed grain distributions.

Adding Bi can modify the Sn-Zn eutectic morphology from well-aligned Zn-rich needles to irregular coarse Zn-rich flakes and result in effective refinement of the microstructure. Zn-rich phase, Bi precipitates, and Bi solutes have significant effects on dynamic recrystallization (DRX) occurring during plastic deformation. This is because second phases on one hand provide more nucleation sites, on the other hand, offer relative obstacles to growth of new crystallized grains. Also, Bi solutes can hinder motion of the new grain boundaries.

Higher Bi content enhances the strength and elongation of the rolled Sn-Zn-Bi alloys. The Sn-3Zn-5Bi alloy achieved superior mechanical properties, with the UTS, yield strength, and elongation of 84.4MPa, 68.3MPa, and 75.2%, respectively, because it possessed most homogenous smallest equiaxed grains combined with largest proportion of HAGBs.

From perspective of decent mechanical properties and ease of casting, Sn-Zn-Bi alloys are very likely to be prospective substitute for currently used Pb-based materials for the application as cladding materials in miniature detonating cords. Significantly, the homogeneous microstructure which evidenced by the uniformly distributed equiaxed grains is considerably beneficial to the cutting performance of the cords in practical applications.

## Chapter 7 Electrochemical Corrosion Performance of Sn-Zn-Bi Alloys

### 7.1 Introduction

It was reported in Chapter 6 that the Sn-Zn-Bi alloys possess an excellent combination of strength and ductility, and display homogeneous recrystallized structure after rolling at room temperature, suggesting a great potential for the sheath material of linear explosive cords [180]. Nevertheless, despite the advantages in aspects of mechanical performance and structural homogeneity, the corrosion performance of the sheath material needs to be assessed because the corrosion resistance is thought of as another crucial cause of failure and shortening life-time of the cords. In practice, the sheath is directly in contact with the explosive material, posing a risk of corrosion between the explosive and the sheath. Furthermore, the manufacturing process often involves drawing and swaging of the sheath together with the explosive core [8], the deformation thus increases the potential of corrosion that initiates at the interface of the explosive core and the sheath, due to the temperature rise resulted from plastic deformation.

Significantly, metal corrosion is the deterioration of the metal by chemical or electrochemical attack. This type of damage can take place internally as well as on the surface. In practical, the environmental conditions under which an aircraft is maintained and operated greatly affect corrosion characteristics. Aircraft operating in a marine environment, i.e. exposure to sea water and salt air, or in areas where the atmosphere contains industrial fumes that are corrosive, are particularly susceptible to corrosive attacks. In a predominately marine environment, moisture-laden air is considerably more detrimental to an aircraft than it would be if all operations were conducted in a dry climate. Water vapour containing salt combines with oxygen in the atmosphere will produce the main source of corrosion for the products in aircraft.

The data information of corrosion performance of currently used lead/lead-antimony cords will be used as the reference, with the 3.5wt.% NaCl water solution as a representative marine environment. A comparison of the corrosion resistance between newly developed Sn based alloys and the previously used Pb based alloys will be performed to evaluate the qualifications for the application.

Therefore, in this chapter the objective is to study the reliability of developing Sn-Zn-Bi alloys as the sheath material of the cords from the perspective of corrosion properties. Bi addition (1-5wt.%) has been reported to enhance both strength and ductility of Sn-3Zn [180]. However, to the best of our knowledge, very limited study has reported the influence of Bi on the corrosion properties of Sn-Zn alloys, despite that Ahmido et al. [181, 182] have mentioned Bi addition had essential effects on the corrosion performance of Sn-9Zn, but limited explanation for the corrosion mechanism was provided.

Hereby, Sn-3Zn- $x$ Bi ( $x=0, 1, 3, 5, 7$  wt.%) alloys were prepared by casting and rolling, and the electrochemical corrosion behaviour was investigated using potentiodynamic polarization and electrochemical impedance spectroscopy (EIS) techniques, to assess the corrosion performance and the effect of Bi on the corrosion properties of the Sn-Zn alloy. A comparison of the corrosion resistance for Sn-Zn-Bi and current Pb/Pb-5Sb was made to provide references. The corrosion mechanism of the Sn-Zn-Bi alloys was studied through microstructure examination on the surface and cross section of the alloys after corrosion measurements, using X-ray diffraction and scanning electron microscopy (SEM) equipped with energy dispersive X-ray analyser (EDS). Focus is on the effect of Bi on the corrosion performance of Sn-Zn-Bi system.

## 7.2 Microstructure of Sn-3Zn-xBi Prior to Corrosion Measurements

The microstructure of the Sn-3Zn, Sn-3Zn-1Bi, and Sn-3Zn-5Bi was examined and interpreted in detail in the last chapter. Here, a complimentary interpretation of microstructure of Sn-3Zn-3Bi and Sn-3Zn-7Bi was provided for a full understanding of the microstructural evolution as Bi contents was increased from 1 to 7wt.%. Figure 7.1 shows the typical microstructure of as-prepared Sn-3Zn alloy prior to electrochemical measurements. The microstructure of the hypoeutectic Sn-3Zn mainly consisted of light grey  $\beta$ -Sn phase exhibiting dendrites morphology and Sn-Zn eutectic in the form of alternate distribution of Sn phase and dark Zn-rich needles with very small spacing (inset).

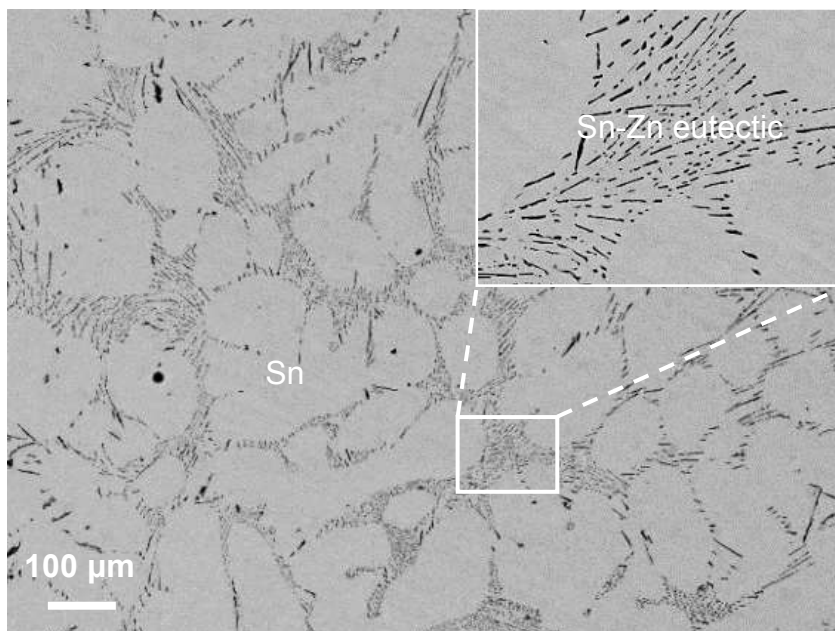


Figure 7.1 Backscattered SEM micrographs showing the microstructure of Sn-3Zn alloy prior to electrochemical measurements.

Figure 7.2 shows the typical microstructure of Sn-3Zn-3Bi and Sn-3Zn-7Bi alloy prior to electrochemical measurements. When 3wt.% of Bi were added, the microstructure was largely changed in terms of the morphology, size, and distribution of both primary  $\beta$ -Sn phase and eutectics, comprising  $\beta$ -Sn phase, Zn-rich phase and white Bi particles, as shown in Figure 7.2a. Notably, misaligned Zn-rich phase in the form of relatively coarse flakes instead of well-aligned small Zn-rich needles was largely observed in both Sn-3Zn-3Bi and Sn-3Zn-7Bi (Figure 7.2b and c). Higher Bi contents led to more Bi aggregates and those were located close to Zn-rich precipitates, with individual particle at a size of approximate 1 $\mu$ m (Figure 7.2c).

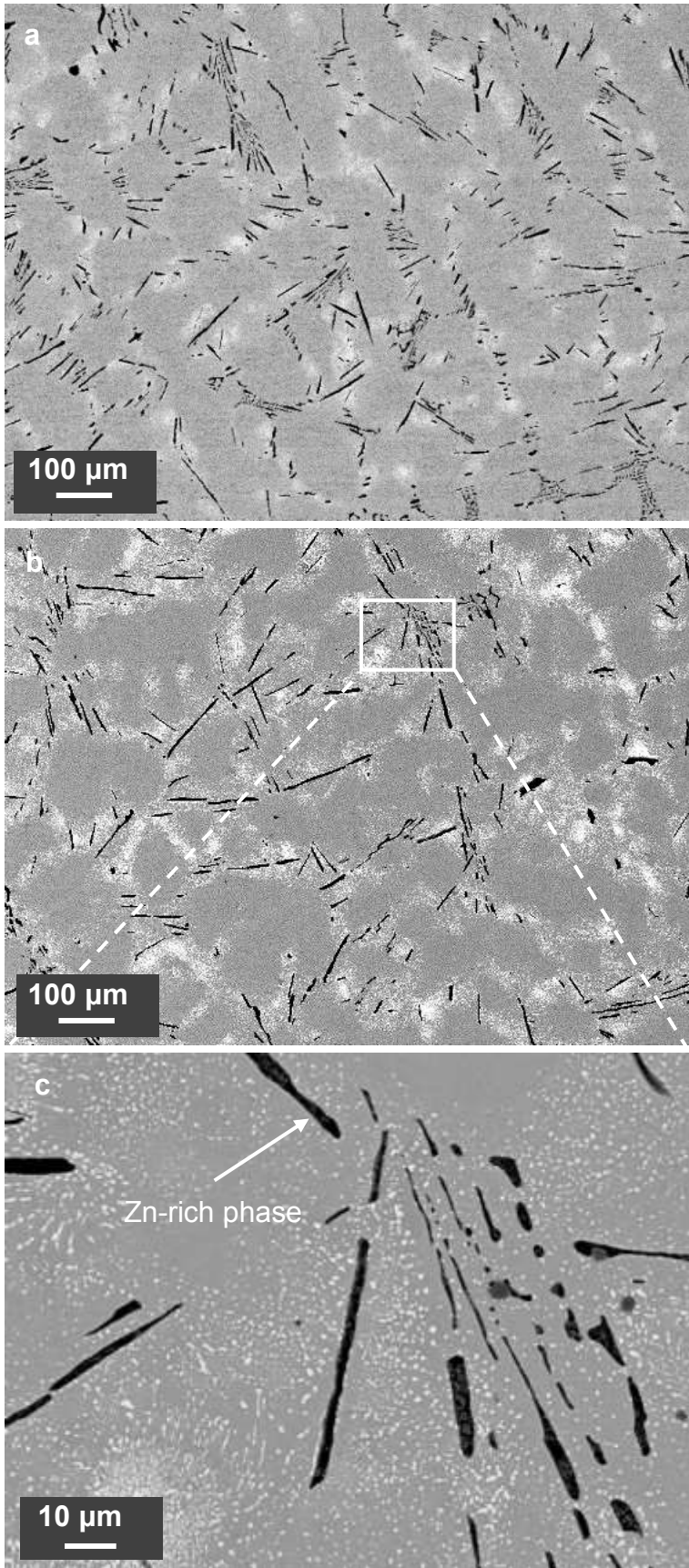


Figure 7.2 Backscattered SEM micrographs showing the microstructure of (a) Sn-3Zn-3Bi, and (b, c) Sn-3Zn-7Bi alloys prior to electrochemical measurements.

## 7.3 Electrochemical Measurements of Sn-3Zn-xBi

### 7.3.1 Potentiodynamic Polarization Curves

Figure 7.3 shows the potentiodynamic polarization curves of Sn-3Zn and Sn-3Zn-xBi ( $x=1, 3, 5,$  and  $7$  wt.%) alloys in  $0.5$  M NaCl solution. It was seen that all the Sn-3Zn-xBi alloys exhibited similar corrosion behaviours, evidenced by similar polarization curves. Since polarization measurements were conducted in a stagnant and naturally aerated NaCl solution at room temperature, the cathodic branch ( $AB$ ) of polarization could be ascribed to the reaction with the dissolved oxygen [183]:  $O_2 + 2H_2O + 4e^- \rightarrow 4OH^-$ . On scanning in the anodic direction to  $BC$  stage, all the alloys exhibited sharp increases in anodic current density attributable mainly to the active dissolution of Zn phase [184]:  $Zn + 2OH^- \rightarrow Zn(OH)_2 + 2e^- \rightarrow ZnO + H_2O$ .  $OH^-$  would react with Zn near the interface to produce porous  $Zn(OH)_2$ , covering the interface. For all the experimental alloys, active dissolution of zinc continued with increasing potential until zincate concentration reached a critical value (point  $C$ ).

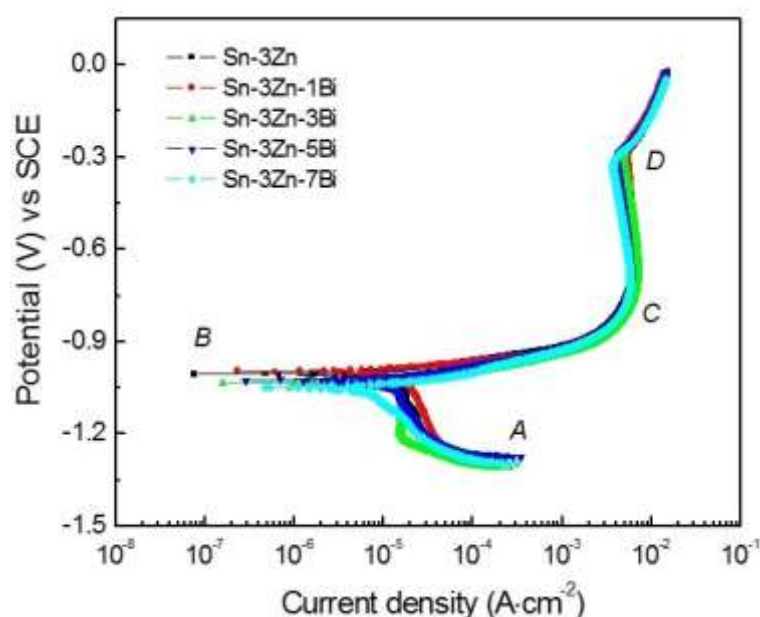


Figure 7.3 Potentiodynamic polarization curves of Sn-3Zn-xBi ( $x=0, 1, 3, 5,$  and  $7$ wt.%) alloys after 60-min immersion in  $0.5$ M NaCl solution.

Afterwards, in the range of  $CD$ , the insoluble zincate salts covered the surface of the corroded samples and formed a plateau region. At this stage, the current density was found to be independent of potential over a range of  $450$  mV. This could be attributed to the formation of Zn and/or Sn oxide or hydroxides [185, 186]. The film formation began with precipitation of

Zn(OH)<sub>2</sub> on the surface, which might transform into ZnO with further corrosion. It should be noted that the film formed in the *CD* region was not a protective film as the current density was high. Abayarthna et al. [187] reported that the zinc oxidation film formed in the *CD* region was not a passivation film but could protect the solder from further corrosion. After point *D*, a sharp increase in the current density was observed, corresponding to the breakdown of the non-protective film. This could be caused by the existence of Cl<sup>-</sup> absorbed by corrosion products and by the oxygen evolution reactions.

Detailed electrochemical parameters are summarised in Table 7.1. The corrosion current density ( $i_{\text{corr}}$ ) was obtained by extrapolating the cathodic Tafel region back to the corrosion potential ( $E_{\text{corr}}$ ) [188]. It was seen that the Sn-3Zn-1Bi alloy possessed higher value of  $i_{\text{corr}}$  compared with that of the Sn-3Zn alloy, suggesting a tendency to lower the corrosion resistance after a small amount (1 wt.%) of Bi addition. However, in the Bi-containing Sn-3Zn-*x*Bi alloys, the corrosion resistance increased with increasing the Bi contents, which was evidenced by the fact that the value of  $i_{\text{corr}}$  decreased constantly from 17.4  $\mu\text{A}\cdot\text{cm}^{-2}$  to 8.7  $\mu\text{A}\cdot\text{cm}^{-2}$  as Bi contents was increased from 1 wt.% to 7 wt.%. The Sn-3Zn-7Bi alloy showed the lowest  $i_{\text{corr}}$  which indicates the highest corrosion resistivity among these alloys. It is noted that the Sn-3Zn-5Bi exhibited nearly same level of value (13.4  $\mu\text{A}\cdot\text{cm}^{-2}$ ) of  $i_{\text{corr}}$  with that of Sn-3Zn alloy (13.5  $\mu\text{A}\cdot\text{cm}^{-2}$ ), indicating the similar capability of corrosion resistance. Hence, according to the potentiodynamic polarization results, it could be concluded that the trend of corrosion resistance decreased in the order of Sn-3Zn-7Bi > Sn-3Zn-5Bi  $\geq$  Sn-3Zn > Sn-3Zn-3Bi > Sn-3Zn-1Bi.

Table 7.1 Electrochemical parameters for the Sn-3Zn-*x*Bi (*x*= 0, 1, 3, 5, and 7 wt.%) alloys measured in 0.5 M NaCl solution.  $E_{\text{corr}}$ : corrosion potential,  $i_{\text{corr}}$ : corrosion current density,  $i_{\text{cc}}$ : critical current density.

Alloys	$E_{\text{corr}}$ (mV vs SCE)	$i_{\text{corr}}$ ( $\mu\text{A}\cdot\text{cm}^{-2}$ )	$i_{\text{cc}}$ ( $\mu\text{A}\cdot\text{cm}^{-2}$ )
Sn-3Zn	-1003 $\pm$ 14	13.5 $\pm$ 0.5	5954 $\pm$ 87
Sn-3Zn-1Bi	-995 $\pm$ 9	17.4 $\pm$ 0.9	6575 $\pm$ 72
Sn-3Zn-3Bi	-1034 $\pm$ 12	15.8 $\pm$ 1.3	7138 $\pm$ 85
Sn-3Zn-5Bi	-1025 $\pm$ 16	13.4 $\pm$ 1.1	6009 $\pm$ 84
Sn-3Zn-7Bi	-1048 $\pm$ 13	8.7 $\pm$ 1.5	5821 $\pm$ 78

### 7.3.2 Electrochemical Impedance Spectroscopy

Figure 7.4 shows the Nyquist plots of Sn-3Zn- $x$ Bi ( $x=0, 1, 3, 5$  and 7 wt.%) alloys in 0.5 M NaCl solution at their open circuit potential, in which Figure 7.4b is corresponding to the rectangular area in Figure 7.4a. It was observed that each Nyquist plot was composed of two depressed capacitive semi-arcs (Figure 7.4a). The Sn-3Zn-1Bi alloy displayed a smallest arc radius, indicating the lowest corrosion resistance among these alloys, as shown in Figure 7.4b. Also, larger capacitive arc radius appeared in the Bi-containing Sn-3Zn- $x$ Bi alloy with higher Bi contents.

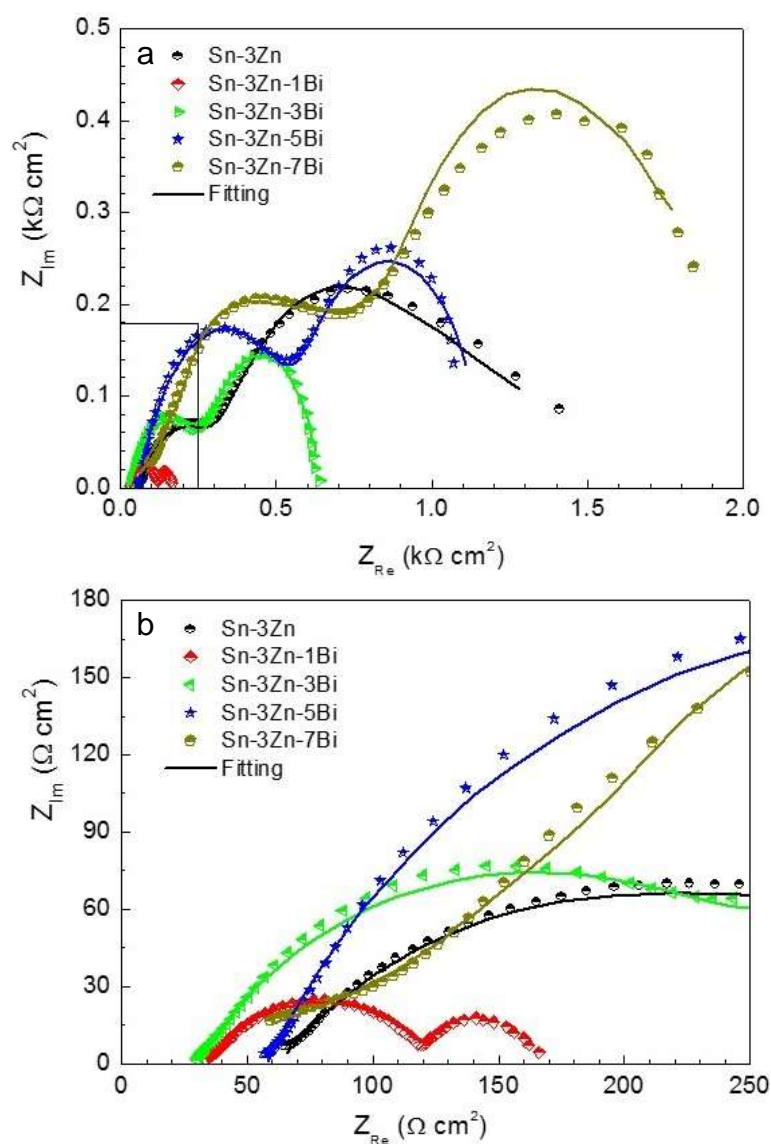


Figure 7.4 Nyquist plots of Sn-3Zn- $x$ Bi ( $x=0, 1, 3, 5,$  and 7 wt.%) alloys under the open circuit potential after 60 min immersion in 0.5 M NaCl solution, (b) is the enlargement of the rectangle region in (a).

Figure 7.5 shows the Bode plots of Sn-3Zn- $x$ Bi ( $x=0, 1, 3, 5$  and  $7$  wt.%) alloys in  $0.5$  M NaCl solution at their open circuit potential. The Bode plots of  $|Z|$  vs. frequency (Figure 7.5a) revealed that higher Bi contents resulted in higher values of impedance in the Bi-containing alloys, suggesting that Bi addition (in the range of  $1-7$  wt.%) could decrease the corrosion susceptibility of the Bi-containing Sn-3Zn- $x$ Bi alloys.  $|Z|/f$  Bode curves at low frequency range illustrate that Sn-3Zn-7Bi shows the biggest  $|Z|$  value, agreement with the largest capacitive semi-circle of it. It is noted that these phenomena were in line with the results shown by polarization measurements.

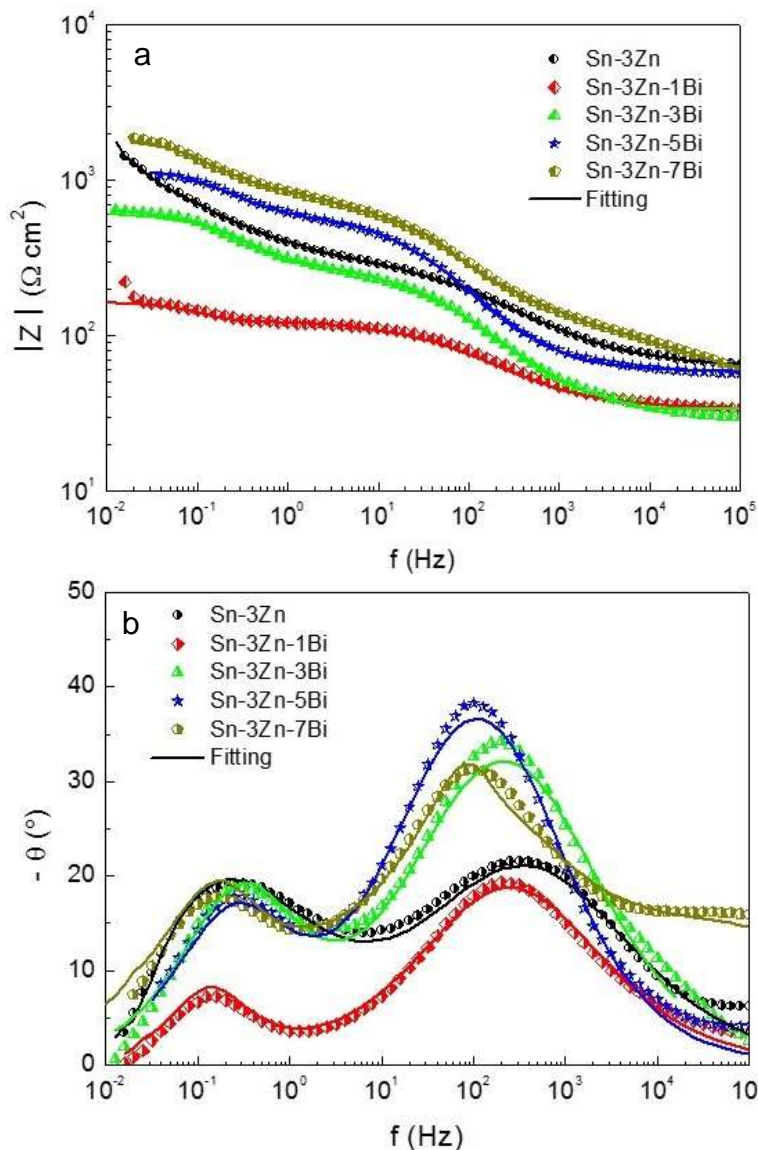


Figure 7.5 (a) Bode  $Z$  plots (modulus vs  $f$ ), (b) Bode phase plots (phase angle vs  $f$ ) of Sn-3Zn- $x$ Bi ( $x= 0, 1, 3, 5,$  and  $7$  wt.%) alloys under the open circuit potential after  $60$  min immersion in  $0.5$  M NaCl solution.

Focusing on the phase angle plots in Figure 7.5b, clearly, two peaks present near 100 Hz and 0.1 Hz, respectively, which indicates the existence of two time constant, corresponding to two capacitive loops in Figure 7.4a. The time constant at low frequencies (0.1-0.3 Hz) can be attributed to the electrical double layer formed at the interface between the alloy and the corrosion product. The capacitive semi-circle at high frequency (80-400 Hz) is related to the formation of corrosion products [189].

Figure 7.6 shows two different equivalent circuits (ECs) which were used in this study to fit the experimental points. The fitted EIS results are summarised in Table 7.2. The goodness of fit was evaluated with the chi-squared ( $\chi^2$ ) values, which in all cases was in the order of  $10^{-4}$ - $10^{-3}$ . Also, a good agreement was observed between the experimental points and the fitting curves, denoted as scattered symbols and solid lines, respectively (Figure 7.4 and Figure 7.5). In the ECs,  $R_s$  represents the uncompensated electrolyte resistance. As can be seen in Figure 7.5, real systems do not behave as an ideal capacitor, therefore, a constant phase element (CPE) instead of a pure capacitor in the equivalent circuit was used to fit the impedance behaviour more accurately. In general, the constant phase element (CPE) is associated with the distributed surface reactivity, inhomogeneity, roughness, adsorption of species and electrode porosity [190].  $R_1$  and  $CPE_1$  represents the resistance and capacitance of the corrosion product layer, respectively.  $R_{ct}$  and  $CPE_{dl}$  represents the resistance and capacitance of the electrical double layer between the interface of alloy and corrosion products.  $W$  represents the Warburg impedance describing the interface diffusion of charge species.

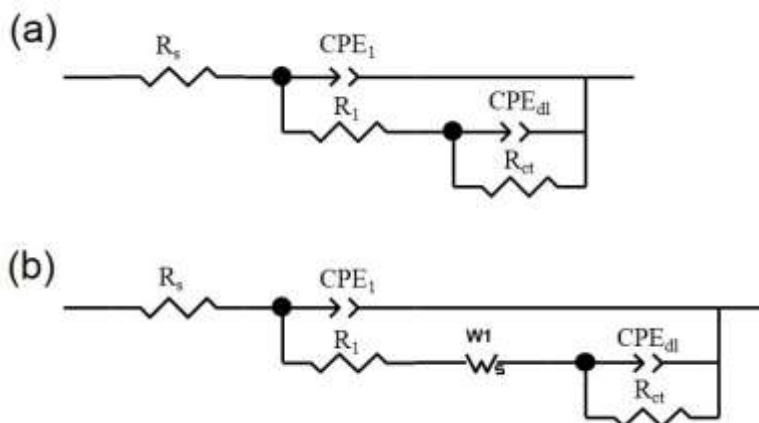


Figure 7.6 Equivalent circuits (ECs) for EIS data fitting of Sn-Zn-Bi alloys in 0.5 M NaCl solution: (a) Sn-3Zn- $x$ Bi ( $x=0, 1, 3,$  and  $5$  wt.%), and (b) Sn-3Zn-7Bi.

The evidence in Figure 7.4, Figure 7.5, and Table 7.2 confirmed that the charge transfer resistance ( $R_{ct}$ ) of Sn-3Zn-1Bi was much lower than that of Sn-3Zn. Smaller capacitive arc radius means lower corrosion resistance. However, the pronounced increases of  $R_{ct}$  was observed in Bi-containing alloys with increasing the Bi contents from 1 wt.% to 7 wt.%, indicating that the charge transfer process occurred in higher difficulty by adding more Bi. Interestingly, adding 7 wt.% Bi resulted in the presence of diffusion-controlled impedance, which might indicate that the corrosion mechanism of the modified alloy was controlled by both charge transfer and diffusion process. Note that, the existence of transport or diffusion resistance ( $R_w$ ) showed that the transport process of charge species occurred much more difficult in the Sn-3Zn-7Bi alloy.

According to the ECs (neglect the solution resistance), total impedance ( $R_t$ ) can be extracted from  $R_l$ ,  $R_{ct}$  and  $R_w$ , to evaluate the overall corrosion resistance. The Sn-3Zn exhibited a large value of  $R_t$ , 969.5  $\Omega \cdot \text{cm}^2$ . When small amount of Bi was added, the total impedance of Sn-3Zn-1Bi and Sn-3Zn-3Bi alloys showed lower values of  $R_t$ , indicating a worse corrosion resistance. However, the  $R_t$  value for Sn-3Zn-5Bi and Sn-3Zn-7Bi was relatively large, approximately 1178.5 and 2265  $\Omega \cdot \text{cm}^2$ , respectively, suggesting an enhanced corrosion resistance with a higher amount of Bi addition. It was clear that the Sn-3Zn-7Bi exhibited the highest corrosion resistance among these alloys. Thus, based on the EIS results, it was further confirmed that the corrosion resistance increased in the sequence of Sn-3Zn-1Bi, Sn-3Zn-3Bi, Sn-3Zn, Sn-3Zn-5Bi, and Sn-3Zn-7Bi. This was in agreements with the results proved by polarization measurements.

Table 7.2 Equivalent circuit parameters obtained by fitting the experimental EIS results of Sn-3Zn- $x$ Bi ( $x=0, 1, 3, 5,$  and  $7$  wt.%) alloys in  $0.5$  M NaCl solution, (Unit of  $R$ :  $\Omega \text{ cm}^2$ , unit of CPE:  $10^{-4} \Omega^{-1} \text{ cm}^{-2} \text{ s}^n$ )

Alloy	$R_s$	$R_l$	$\text{CPE}_1$	$n_1$	$R_{ct}$	$\text{CPE}_{dl}$	$n_2$	$R_w$	$\chi^2$ ( $10^{-3}$ )	$R_t$
Sn-3Zn	62	284.5	1.28	0.55	685	18.9	0.7	-	0.6	969.5
Sn-3Zn-1Bi	33	92	2.37	0.61	91.5	386	0.9	-	0.6	183.5
Sn-3Zn-3Bi	30	260.5	1.13	0.64	380.4	26.1	0.78	-	1.1	640.6
Sn-3Zn-5Bi	58	540	55.6	0.72	638.5	16.2	0.83	-	1.3	1178
Sn-3Zn-7Bi	18.9	174	2.90	0.31	911	12.5	0.93	1180	0.3	2265

## 7.4 Corrosion Products Characterization

### 7.4.1 Surface Characterization

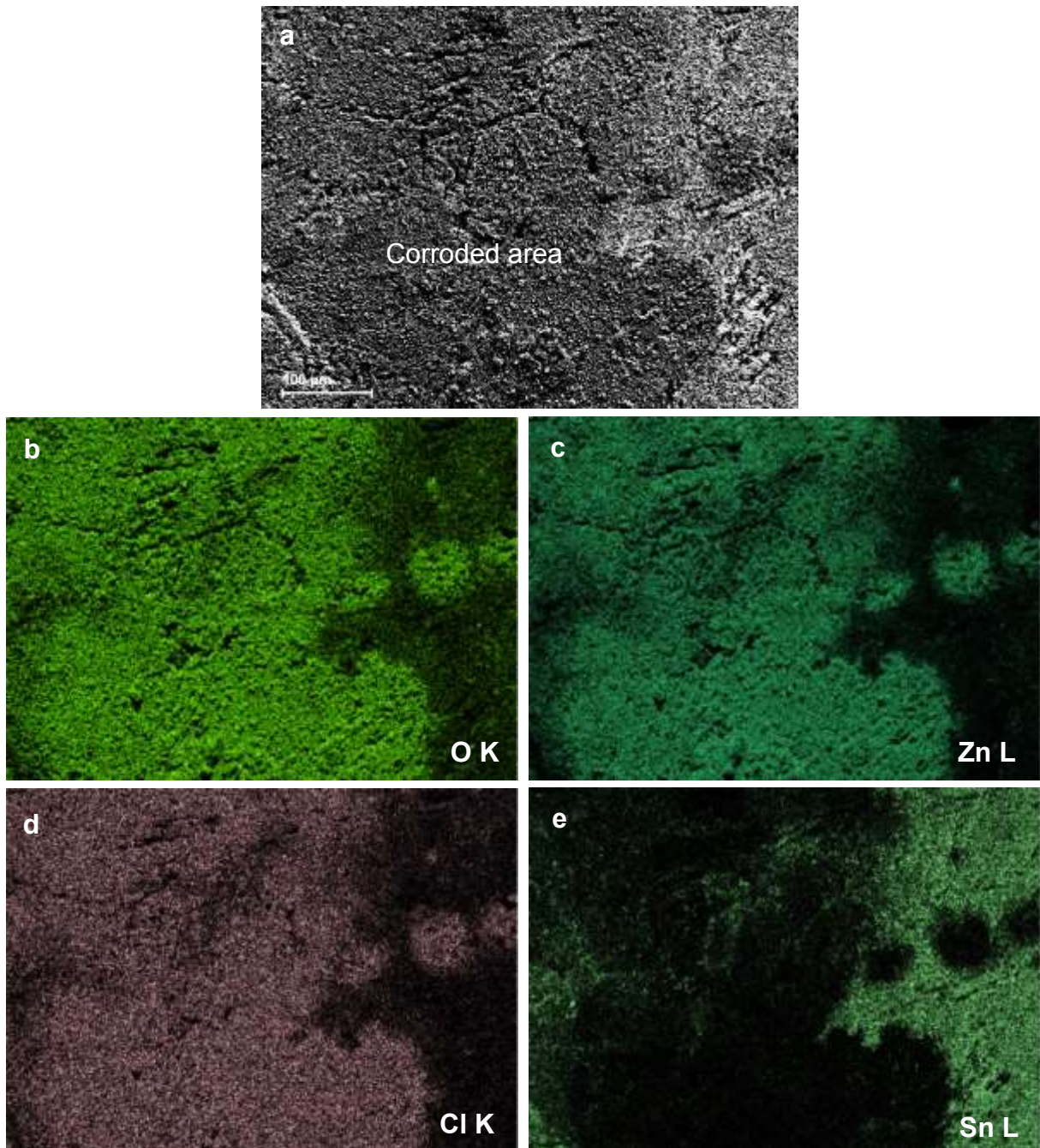


Figure 7.7 SEM-BSE micrograph of the surface and element mapping for the Sn-3Zn alloy after polarization measurements in 0.5 M NaCl solution.

Figure 7.7 shows the typical SEM micrographs and element mappings of the surface of Sn-3Zn after the polarization measurement. The severely corroded area denoted by the dark contrast (Figure 7.7a) was mainly composed of Cl, O, and Zn elements, indicating that corrosion

products were predominantly made of Cl, O, and Zn. The slightly-/non- corroded area represented by the light contrast in Figure 7.7a was covered with numerous Sn and a small amount of O. It was thus deduced that Zn phase instead of Sn was selectively and preferentially corroded under the engagement of  $\text{Cl}^-$  and  $\text{OH}^-$  anions.

Figure 7.8 presents the XRD patterns of the surface of Sn-3Zn- $x$ Bi ( $x=0, 1, 3, 5,$  and  $7$  wt.%) alloys after polarization measurements, for the purposes of confirming the phase composition of corrosion products. It was seen that there was still  $\beta$ -Sn phase remained after polarization measurements in all cases, while Zn phase was scarcely detected, further revealing that Zn-rich phase was heavily consumed. Bi phase was extensively detected in the Bi-containing alloys with Bi contents being more than 1 wt.%, confirming the difficulty of Bi in being corroded in 0.5 M NaCl solution due to its relatively higher corrosion potential compared with Sn and Zn [191]. The main corrosion product for all Sn-3Zn- $x$ Bi alloys was identified as a complexed Zn hydroxyl chloride hydrates, namely simonkolleite  $\text{Zn}_5(\text{OH})_8\text{Cl}_2 \cdot \text{H}_2\text{O}$ . Plus, a trace amount of ZnO was discovered as well.

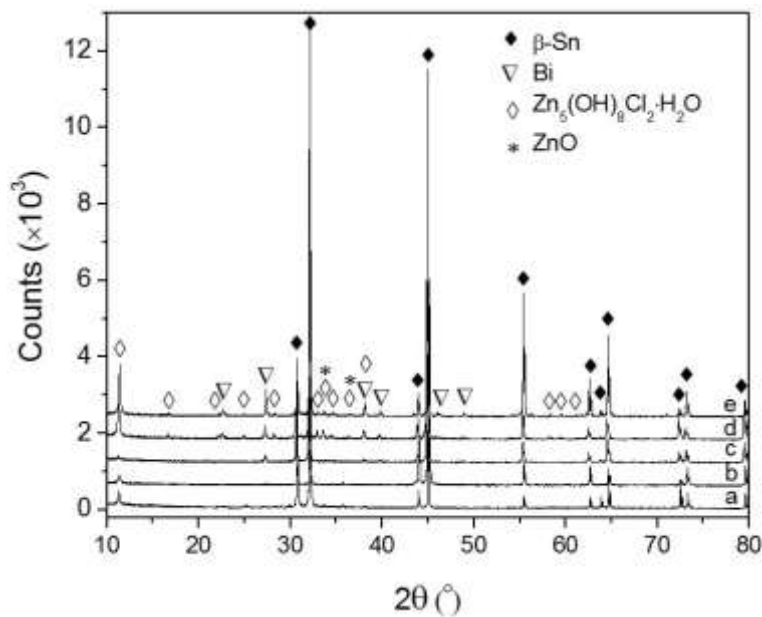


Figure 7.8 XRD patterns for the (a) Sn-3Zn, (b) Sn-3Zn-1Bi, (c) Sn-3Zn-3Bi, (d) Sn-3Zn-5Bi, and (e) Sn-3Zn-7Bi alloys after polarization measurements in 0.5 M NaCl solution.

Figure 7.9 presents the typical SEM micrographs and EDS analysis illustrating the surface morphology and corresponding chemical composition of the corrosion products of Sn-3Zn after polarization measurement. From Figure 7.9a and b, the corroded region was covered with sparsely aggregated plate-like structures, which were confirmed simonkolleite

$\text{Zn}_5(\text{OH})_8\text{Cl}_2 \cdot \text{H}_2\text{O}$  by EDS analysis on spectrum S1. This was in agreement with the XRD results.

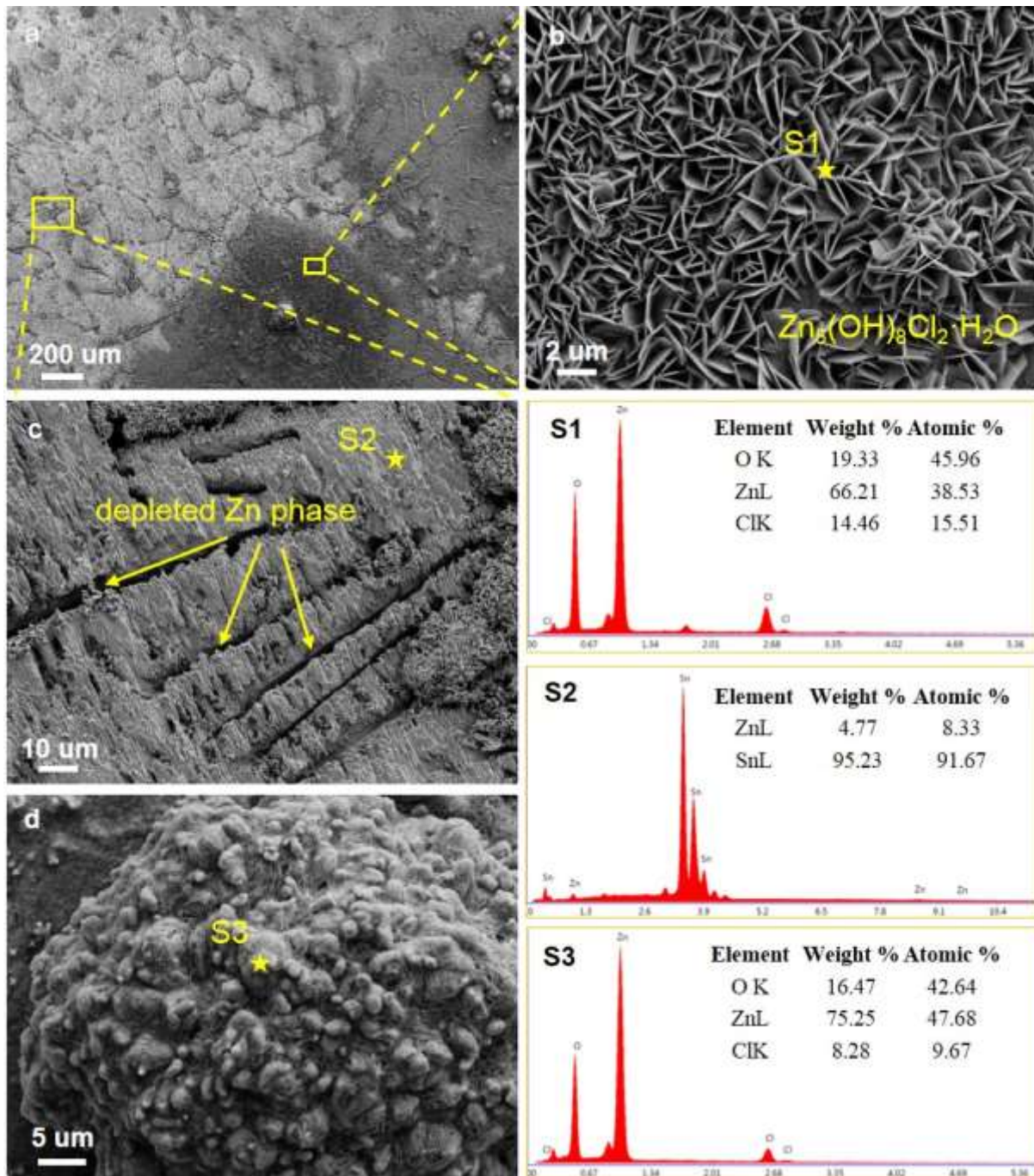


Figure 7.9 SEM micrographs with different magnification of the Sn-3Zn alloy after polarization measurements in 0.5 M NaCl solution. The EDS result is corresponding to the spectrums in b, c, and d (S1, S2, and S3).

Enlarging the initial eutectic region (Figure 7.9c), it was seen that the initial Zn-rich needles were dissolved and depleted, leaving narrow channels on the surface, whereas the initial  $\beta$ -Sn

phase in the eutectic region remained, as demonstrated by EDS analysis on spectrum S2, further indicating the easier destruction of Zn-rich phase compared to  $\beta$ -Sn phase. Furthermore, the corrosion product exhibiting a sphere-shaped morphology was observed, which was found the aggregate of the ZnO plates (EDS analysis on S3). These sphere-like ZnO products have been previously reported by other researchers on the study of Sn-Zn alloys after immersion corrosion [192].

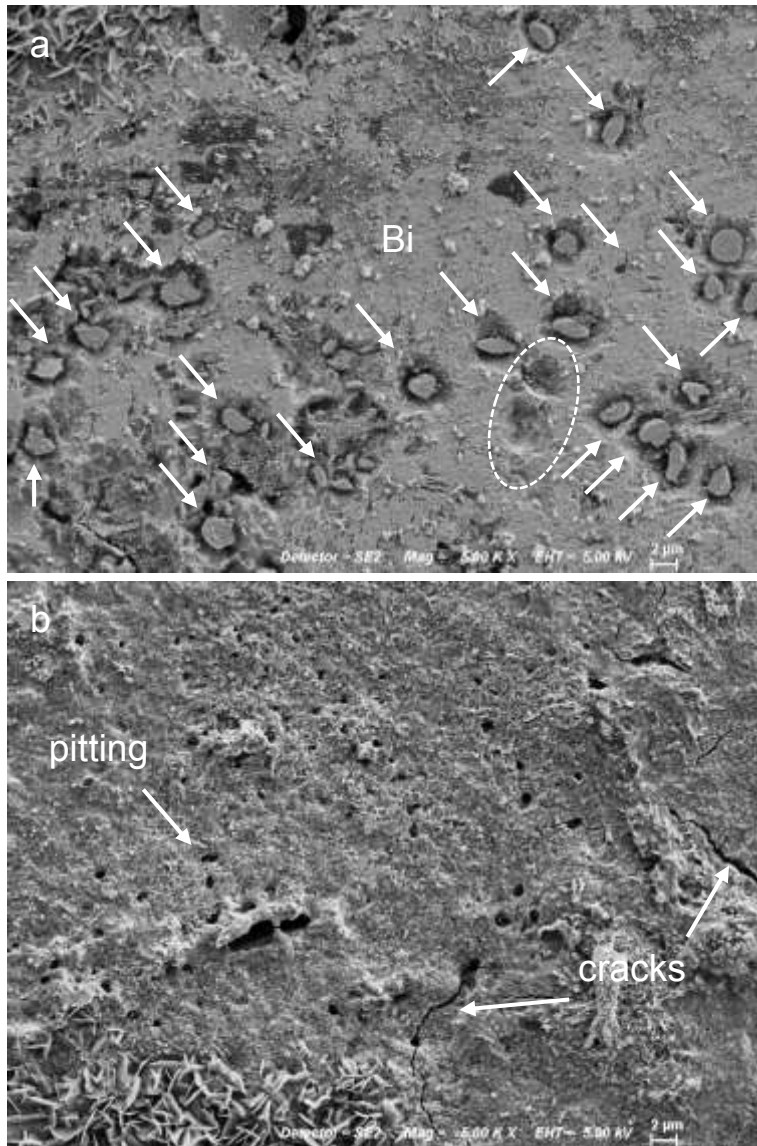


Figure 7.10 SEM micrographs of (a) Sn-3Zn-1Bi alloy and (b) Sn-3Zn-5Bi after polarization measurement in 0.5 M NaCl solution, showing the  $\beta$ -Sn/Bi micro-galvanic couples, pits, and micro-cracks on the surfaces.

Figures 7.10a and b presents the SEM micrographs of the surface of the Bi-containing Sn-3Zn-1Bi and Sn-3Zn-5Bi alloys after polarization measurements in 0.5 M NaCl solution,

respectively. From Figure 7.10a, many Bi particles were seen to remain on the surface, as shown by arrows. These particles were confirmed Bi particles by EDS analysis (not present here). Surrounding the Bi particle, Sn phase was selectively corroded, suggesting appearance of micro-galvanic couples between the  $\beta$ -Sn phase and the Bi phase. For certain sites (dashed circle), Bi particles were depleted because the neighbouring  $\beta$ -Sn matrix was severely consumed and thus the interface bonding was consequently damaged. Also, pits and micro-cracks were observed in the corroded surface of Sn-3Zn-5Bi alloy, which might indicate weak protection of the corrosion product layers (Figure 7.10b). Note that, pits and micro-cracks were observed not only in the case of Sn-3Zn-5Bi but also in all Sn-3Zn- $x$ Bi ( $x=0, 1, 3, 5,$  and  $7$  wt.%) alloys.

#### 7.4.2 Cross Section Characterization

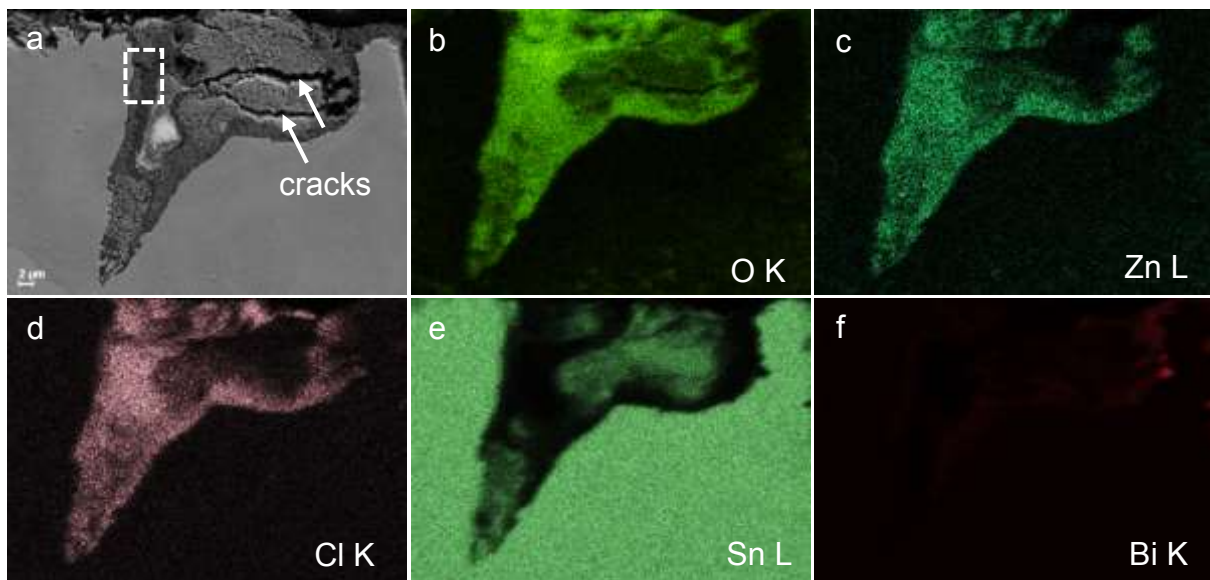


Figure 7.11 SEM-BSE micrograph of the cross section and element mapping for Sn-3Zn-5Bi alloy after polarization measurements in 0.5 M NaCl solution, showing the pitting near Zn-rich precipitates.

For a better understanding of pitting corrosion process, cross section characterization was further carried out after the corrosion measurements. Figure 7.11 shows the cross-section SEM micrographs and the element mappings of a typical pit of the Sn-3Zn-5Bi alloy after the polarization measurement. The result of element mapping confirmed the strong presence of Cl, O, and Zn in the pit, suggesting that anions including  $\text{Cl}^-$  and  $\text{OH}^-$  had migrated inwards the alloy along the initial Zn-rich precipitates. It was thus concluded that Zn-rich precipitates could provide preferential transport paths for  $\text{Cl}^-$  and  $\text{OH}^-$  penetration. Notably, Bi phase was scarcely

identified by the element mapping (Figure 7.11f), indicating that this individual pit initiated and propagated without the participation of Bi particles.

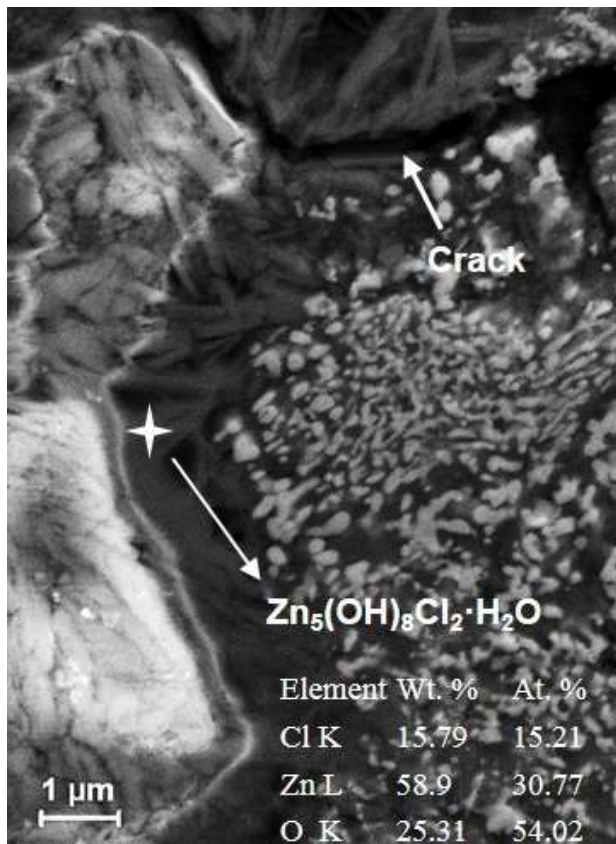


Figure 7.12 High magnification SEM micrograph of Sn-3Zn-5Bi alloy after polarization measurements in 0.5 M NaCl solution, corresponding to the highlighted region in Figure 7.11.

Closer inspection of the pit (Figure 7.12), the major pitting product was found  $Zn_5(OH)_8Cl_2 \cdot H_2O$ , which was confirmed by the EDS results. Interestingly, the pitting product,  $Zn_5(OH)_8Cl_2 \cdot H_2O$ , exhibited a porous interlinked network structure. A similar porous network-structured corrosion product was also reported on the study of Sn-Zn [192]. The pores could provide ease of transport of  $Cl^-$  and  $OH^-$  from solution inwards the interior of the alloys. In this way, a continuous complement of poisonous anions (e.g.  $Cl^-$ ) was delivered, thus, promoting the pitting propagation. In the meantime, localized cracks/breakdown appeared as well. The crack on one hand provided the channel for the penetration of corrosive medium ( $Cl^-$  and  $OH^-$ ); on the other hand, the crack could increase the chances of removal of pitting products away from the surface, increasing the possibility of anions in the solution diffusing towards the alloy, which promoted the pitting rate kinetically.

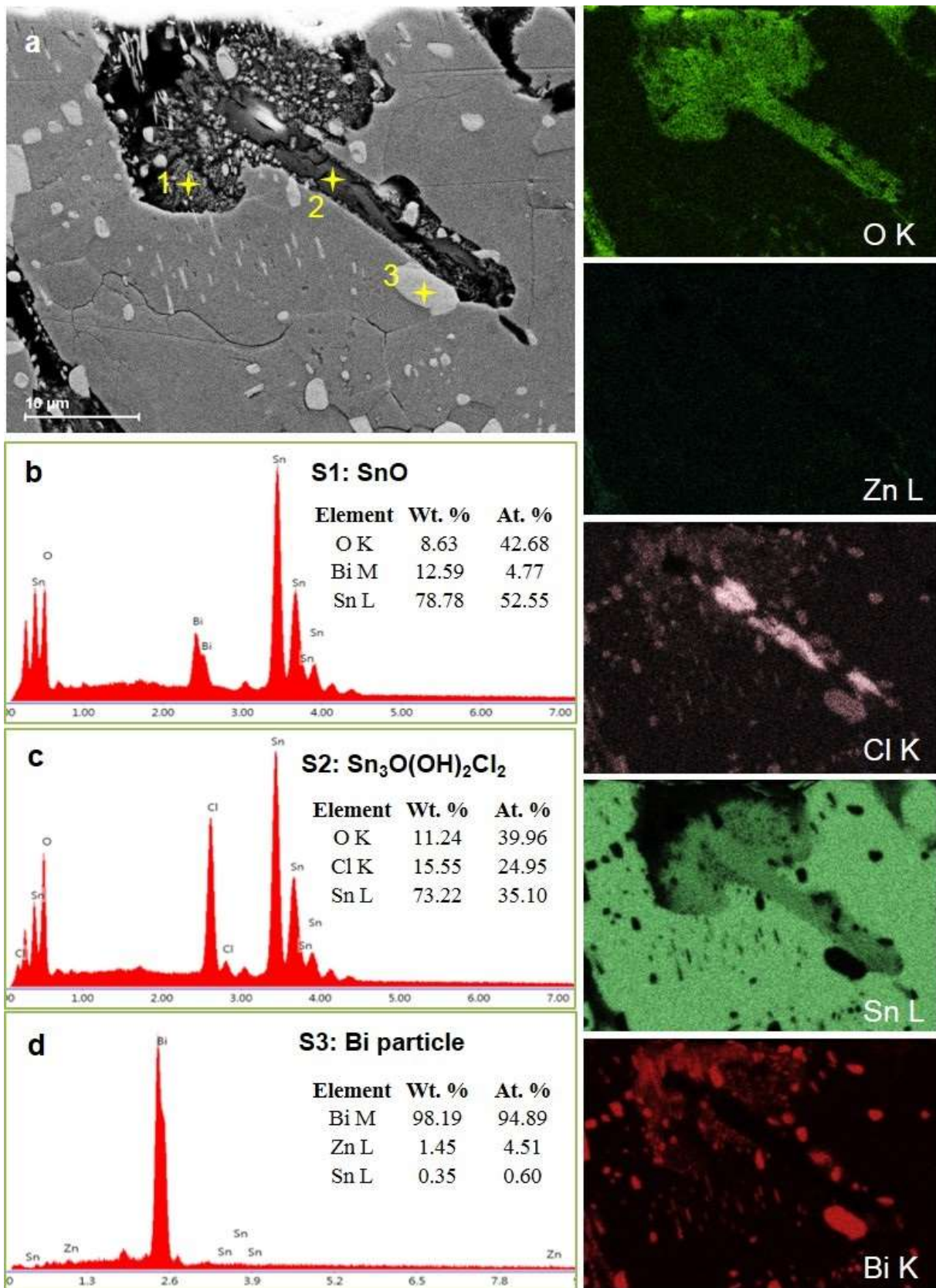


Figure 7.13 SEM-BSE micrograph of the cross section and element mapping for Sn-3Zn-5Bi alloy after polarization measurements in 0.5 M NaCl solution, showing the pitting near the Bi particles.

Figure 7.13 shows the cross-section SEM micrographs and the element mappings of another typical type of pits in Sn-3Zn-5Bi after the polarization measurement. It was observed that the pit was covered with Cl, O, Sn, and Bi elements. A similar conclusion could be drawn that the pitting initiation and subsequent propagation were resulted from the migration of attacking Cl<sup>-</sup> and OH<sup>-</sup> anions inwards the alloy. EDS results (Figure 7.13b and c) confirmed that pitting products contained SnO and the Sn hydroxyl chloride hydrate compounds, Sn<sub>3</sub>O(OH)<sub>2</sub>Cl<sub>2</sub>. Different from the previously mentioned pit, the Zn-rich precipitate was barely identified here, while numerous Bi particles were considerably detected in this pit (Figure 7.13d). Thus, the pitting susceptibility could be enhanced in the sites where large amounts of Bi particles were assembled. This could be related to the formation of the β-Sn/Bi galvanic couples which will be discussed next.

### 7.5 Effects of Bi on the Corrosion Resistance of Sn-Zn

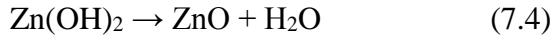
Based on the polarization and EIS results, it has been confirmed that a small amount (1 and 3 wt.%) of Bi addition to the Sn-3Zn alloy could cause decreased corrosion resistance. However, when Bi contents was further increased to 5 and 7 wt.%, the Sn-3Zn-*x*Bi (*x*=5, and 7 wt.%) alloys exhibited higher corrosion resistance than that of Sn-3Zn. Furthermore, for Bi-containing Sn-3Zn-*x*Bi alloys the corrosion resistance increased with increasing Bi contents from 1 wt.% to 7 wt.% and the Sn-3Zn-7Bi alloy showed the best corrosion resistance among them. This could be associated with: (1) the microstructure modification through addition of Bi with respect to the morphology, size, and distribution of the Zn-rich precipitates; (2) the additional micro-galvanic effect caused by Bi particles; and (3) the barrier effect of Bi phase.

In the Sn-Zn system since Zn exhibits more negative electrode potential (-0.763 V vs. SHE) than Sn (-0.136 V vs. SHE) the Zn-rich precipitates act as active anodes and can be preferentially corroded under corrosive circumstances [193]. The corrosion process begins with the dissolution of Zn at anodic sites:



In this way, the initial Zn-rich precipitates could be selectively consumed, leaving the β-Sn phase (cathode) remained (Figure 7.9c). With the participation of water and oxygen further electrochemical reactions take place, forming zinc hydroxide and/or zinc oxide:





In the presence of  $\text{Cl}^-$ , especially when the chloride concentration is higher than 0.1 M,  $\text{Cl}^-$  will move towards Zn dissolution sites, causing gradual formation of insoluble zinc hydroxychloride,  $\text{Zn}_5(\text{OH})_8\text{Cl}_2 \cdot \text{H}_2\text{O}$  [194]:



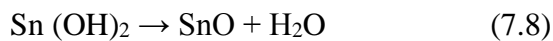
These corrosion products, ZnO and  $\text{Zn}_5(\text{OH})_8\text{Cl}_2 \cdot \text{H}_2\text{O}$ , were readily recognised by the XRD results (Figure 7.8) and EDS composition analysis (Figure 7.9b). In this sense,  $\text{Zn}_5(\text{OH})_8\text{Cl}_2 \cdot \text{H}_2\text{O}$  is thus expected to precipitate close to the anodic sites, i.e., Zn-rich precipitates, which was in deed the case denoted by the pit shown in Figure 7.11.

In the case of Sn-3Zn, the Zn-rich precipitates displayed as small-sized needle-shaped morphologies and these Zn-rich needles were located at the Sn-Zn eutectic cells/regions. Accordingly, the eutectic regions could be reasonably regarded as the corrosion-vulnerable sites at which anodic Zn-rich phase was dissolved and depleted, while the primary  $\beta$ -Sn cells could be considered as the cathodic noble locations where corrosion could rarely occur. This was supported by the surface examination and composition analysis of Sn-3Zn after the polarization measurement (Figure 7.9c).

When Bi was added, i.e., in the case of Sn-3Zn- $x$ Bi ( $x=1, 3, 5, \text{ and } 7$  wt.%) alloys, Zn-rich precipitates were dramatically increased in dimensions, and its distribution became more uniform. Those in larger size could lead to degradation of corrosion performance due to the weak bond between the coarse Zn-rich precipitates and  $\beta$ -Sn matrix. This was based on the idea that defects (e.g. dislocations or voids) could be easily accumulated near the interface between the coarse Zn-rich precipitate and the Sn phase [195, 196]. The defects-accumulated sites could thus benefit transport of  $\text{Cl}^-$  or  $\text{OH}^-$  inwards and promote chemical reaction between anions and the Zn-rich phase, increasing the corrosion rates. Meanwhile, the pitting can be highly prone to initiation and propagation along the vulnerable Zn/Sn interface, which was reflected from the pit microstructure shown in Figure 7.11. A similar phenomenon was reported by Liu *et al.* [197] who has demonstrated that the corrosion resistance is enhanced after addition of trace amount of Ti to the Sn-9Zn alloy attributed to elimination of large Zn-rich precipitates.

Also, in the Sn-3Zn alloy the corrosion-vulnerable sites, i.e., Sn-Zn eutectic “islands”, were geographically and largely isolated by a large proportion of primary  $\beta$ -Sn dendrites serving as noble cathodes (Figure 7.1). This means that noble  $\beta$ -Sn phase can act as the barrier, causing obstruction of corrosion [198]. On the contrary, in the Bi-containing Sn-3Zn- $x$ Bi alloys, a much more uniform distribution of the Zn-rich precipitates appeared, which means that more proportions of corrosion-vulnerable sites presented and fewer fractions of effective anodic barriers exhibited. Consequently, the Sn-3Zn- $x$ Bi ( $x=1$ , and 3 wt.%) alloys presented higher corrosion susceptibility in comparison with the Sn-3Zn alloy.

It is worthy of note that in addition to the effect attributable to the change of the Zn-rich precipitate with respect to its size and distribution, the Bi particle itself played a crucial role in affecting the corrosion resistance of the alloys. The effect caused by Bi particles may involve two aspects: galvanic effect and anodic barrier. When a small amount of Bi (1 wt.%) was added to Sn-3Zn, Bi particles were randomly aggregated and discretely dispersed in the  $\beta$ -Sn matrix and majority of those were located near Zn-rich precipitates. Extra micro-galvanic couples, i.e.,  $\beta$ -Sn phase/Bi phase and Zn-rich phase/Bi phase, may form, due to Bi phase possessing the highest electrode potential (0.293 V vs. SHE) compared with Sn (-0.136 V vs. SHE) and Zn (-0.763 V vs. SHE). Therefore, in the  $\beta$ -Sn/Bi micro-galvanic couples the  $\beta$ -Sn could be selectively resolved as the anodes, leaving Bi remained (Figure 7.10a), causing formation of corrosion products, SnO and  $\text{Sn}_3\text{O}(\text{OH})_2\text{Cl}_2$  (Figure 7.13). Possible chemical reactions involve [199, 200]:



In this way, the additional galvanic effect could have a negative effect on the corrosion resistance of Sn-Zn alloys. However, it worthy noted that the detrimental galvanic effect caused by  $\beta$ -Sn/Bi micro-galvanic couple was believed to be minimal because the corrosion potential difference between Bi and Sn is not large [191]. This was also reflected by the fact that no clear peaks corresponding to the corrosion products, SnO and/or  $\text{Sn}_3\text{O}(\text{OH})_2\text{Cl}_2$ , were identified in the XRD results of the corroded surface of the Bi-containing Sn-3Zn- $x$ Bi alloys. Therefore, the galvanic corrosion theory which gives the idea that larger ratio of cathodic to anodic would

lead to a severer corrosion of the anode alloy, resulting more damage during electrochemical measurement, might be not the dominant mechanism operating in the present case of Bi-containing Sn-3Zn-xBi alloys.

On the contrary, the noble barrier effect of cathodic Bi phase operates more significantly than the galvanic cathode, leading to the increased corrosion resistance with more Bi particles. Similar phenomenon was reported in the Mg alloys where the Mg<sub>17</sub>Al<sub>12</sub> ( $\beta$  phase) has two influences on corrosion, as a galvanic cathode and as a barrier, depending on the volume fraction of Mg<sub>17</sub>Al<sub>12</sub> in the Mg matrix [201, 202]. The Mg<sub>17</sub>Al<sub>12</sub> phase mainly serves as a galvanic cathode and accelerates the corrosion process of matrix if the volume fraction of Mg<sub>17</sub>Al<sub>12</sub> phase was small. However, for a higher volume fraction, the Mg<sub>17</sub>Al<sub>12</sub> phase acts as an anodic barrier to inhibit the overall corrosion of the alloy. Also, Osorio *et al.* [203] reported that in the Al-1.5 wt.% Fe alloy more extensive distribution of Al<sub>6</sub>Fe particles provides a better protective effect with the nobler intermetallic Al<sub>6</sub>Fe particles “enveloping” the anodic Al-rich phase, resulting in better corrosion resistance. Notably, with increasing the Bi contents from 1 wt.% to 7 wt.%, the volume fraction of Bi particles was observed to be largely increased and those became better connected from each other, forming the noble barriers or “enveloping” against corrosion. Based on these, it was deduced that a larger proportion of Bi networks acting as anodic barriers in Sn-3Zn-xBi alloys with higher Bi contents was the reason for the correspondingly increased corrosion resistance.

## 7.6 Electrochemical Measurements of Pb/Pb-5Sb

Figure 7.14 shows the potentiodynamic polarization curves for pure Pb and the Pb-5Pb (4.9wt.% Sb) alloy, polarized up to +500 mV in 3.5wt.% NaCl solution. The corresponding polarization parameters including corrosion potential ( $E_{\text{corr}}$ ), corrosion current density ( $i_{\text{corr}}$ ) values obtained from the polarization curves are listed in Table 7.3.

At the initial stage (*AB*), the cathodic reduction reaction occurs, corresponding to the dissolved oxygen reduction reaction. The potential at point *B* was referred to as the corrosion potential ( $E_{\text{corr}}$ ). The corrosion current density ( $i_{\text{corr}}$ ) which represented the corrosion rate of the system was determined by Tafel extrapolation. From Table 7.3, it was seen that the pure Pb exhibited a corrosion potential of -646 mV/SCE which changes to -638 mV/SCE for Pb-5Sb. The corrosion current density of pure Pb was 17.8  $\mu\text{A}\cdot\text{cm}^{-2}$  which was decreased to 15.2  $\mu\text{A}\cdot\text{cm}^{-2}$  for the Pb-5Sb alloy. Both Pb and Pb-5Sb exhibited relatively small corrosion current densities

and accordingly revealed slow corrosion rates. The Pb-5Sb alloy processed a bit higher corrosion potential and lower corrosion current density compared with pure Pb, indicating that 5wt.% Sb addition could moderately improve the corrosion resistance of Pb.

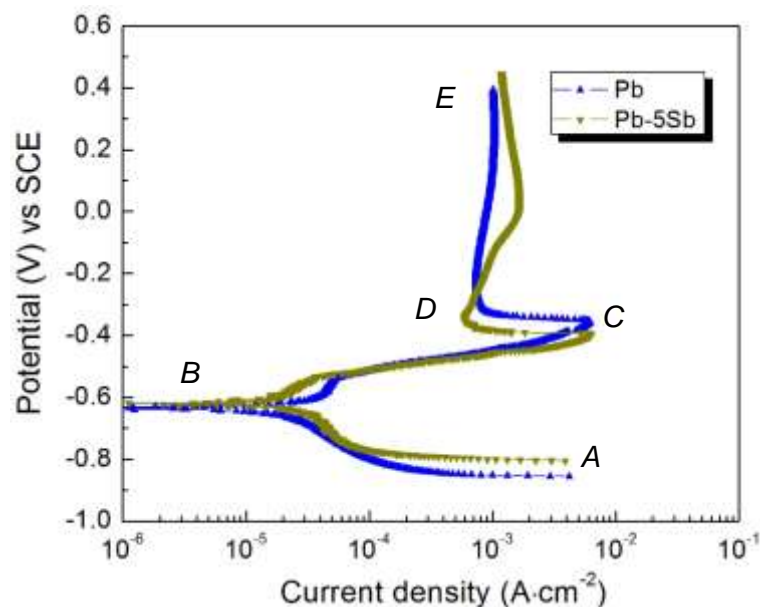


Figure 7.14 Potentiodynamic polarization curves of pure Pb and Pb-5Sb alloy after 60-min immersion in 0.5M NaCl solution

On scanning in the anodic direction from point *B*, the current density increased rapidly due to active dissolution of Pb. The active dissolution of Pb continued with an increase of current density to a maximum current density up to point *C* until the hydroxide or oxide concentration reached to this maximum value. Solid oxide precipitated on the electrode surface when solubility product of the Pb oxide was exceeded at the anode surface. This phenomenon suggested the formation of a passive film through a dissolution precipitation mechanism. The potential and current density at point *C* were referred to as the passivation potential and critical current density ( $i_c$ ), respectively. It was seen from Figure 7.14 and Table 7.3 that Pb and Pb-5Sb had the critical current density of  $6456 \mu\text{A}\cdot\text{cm}^{-2}$  and  $6695 \mu\text{A}\cdot\text{cm}^{-2}$ , respectively. The relatively large critical current densities revealed that the protection performance of initial passive films for Pb and Pb-5Sb were not effective.

The current density decreased sharply from point *C* to *D* and it was almost independent of potential from point *D* to *E*. The region of *CD* was regarded as active/passive transition stage, corresponding to formation of passive layer. From point *D*, the current density remained independent and almost constant to potential up to point *E*. At point *D*, the current density was

referred to as the passivation current density ( $i_{\text{pass}}$ ) and the potential range where the current density remained almost constant was the passivation range. Pb had the passive current density of  $692 \mu\text{A}\cdot\text{cm}^{-2}$  and Pb-5Sb had the passive current density of  $575 \mu\text{A}\cdot\text{cm}^{-2}$ . It was noted that Pb had a more stable passivation current density during passivation stage, indicating a more stable passive film to prevent further corrosion attack.

Table 7.3 Electrochemical parameters for pure Pb and Pb-5Sb alloys measured in 3.5wt.% NaCl solution.

Alloys	$E_{\text{corr}}$ (mV vs SCE)	$i_{\text{corr}}$ ( $\mu\text{A}\cdot\text{cm}^{-2}$ )	$i_c$ ( $\mu\text{A}\cdot\text{cm}^{-2}$ )	$i_{\text{pass}}$ ( $\mu\text{A}\cdot\text{cm}^{-2}$ )
Pb	$-646 \pm 11$	$17.8 \pm 0.8$	$6456 \pm 370$	$692 \pm 42$
Pb-5Sb	$-638 \pm 18$	$15.2 \pm 1.0$	$6695 \pm 385$	$575 \pm 31$

## 7.6 Summary

In this chapter, the corrosion properties of Sn-3Zn- $x$ Bi alloys were investigated using potentiodynamic polarization and electrochemical impedance spectra (EIS) techniques. The polarization measurements and EIS results proved that the corrosion resistance increases in the order of Sn-3Zn-1Bi, Sn-3Zn-3Bi, Sn-3Zn, Sn-3Zn-5Bi, Sn-3Zn-7Bi. The Zn-rich phase possessing the lowest corrosion potential among all phases serves as the anodic and thus is selectively and preferentially corroded, accompanied by the formation of major corrosion products,  $\text{Zn}_5(\text{OH})_8\text{Cl}_2\cdot\text{H}_2\text{O}$ .

Bi addition (1-7 wt.%) can cause dramatic increases in the sizes of corrosion-vulnerable Zn-rich precipitates and lead to more uniform distribution of these precipitates. This is the reason that addition of 1 wt.% and 3 wt.% Bi increased the corrosion susceptibility of the Sn-3Zn alloy. In Bi-containing Sn-3Zn- $x$ Bi alloys, the corrosion resistance is constantly increased with increasing the Bi contents from 1 wt.% to 7 wt.%, due to the enhanced barrier effect of Bi particles. When Bi concentration reaches 5 wt.% and 7 wt.%, the barrier effect of Bi phase can counteract the detrimental effect resulted from the coarsened Zn-rich precipitates, resulting in the increased corrosion resistance of Sn-3Zn-5Bi and Sn-3Zn-7Bi in comparison with Sn-3Zn.

The corrosion current density of pure Pb and Pb-5Sb which are current sheath materials for the MDCs was  $17.8 \mu\text{A}\cdot\text{cm}^{-2}$  and  $15.2 \mu\text{A}\cdot\text{cm}^{-2}$ , respectively. The values were proved at similar

levels of Sn-3Zn-xBi alloys (in the range of 8-18  $\mu\text{A}\cdot\text{cm}^{-2}$ ). This, from the perspective of corrosion resistance, strongly support the reliability of Sn-Zn-Bi alloys as the sheath materials of the cords for the specific application.

## Chapter 8 Performance Simulations and Proof of Sn-Zn-Bi MDCs

### 8.1 Introduction

After investigating the mechanical performances, corrosion properties, and microstructural characteristics of potential candidates for the sheath of miniature detonating cords, it is reasonably said that the investigated Sn-Zn-Bi alloys are prospective materials for the application, due to their decent mechanical properties and good corrosion resistance in comparison with currently used antimonial or non-antimonial Pb materials. Prior to large-scale production of final products in industries, live proof firings are required for determining if the identified Sn alloys are suitable replacement of antimonial or non-antimonial lead. Before proof tests, performance simulations are performed to offer reference information and provide a pre-selection of potential cords.

In the present chapter, numerical simulations were conducted to model the cutting process of different MDCs against aluminium and acrylic targets. The simulations were applied using varied sheath materials (Pb, Pb-Sb, Sn, Sn-Cu, Sn-Zn-Bi, Al, Cu, and Ta), two target materials including Al7039 and PMMA (poly(methyl methacrylate)), and different stand-off distances (0, 0.5, 1.0, and 3.0mm), for the purpose of studying the effects of these factors on penetration. Also, four types of explosives incorporating HNS1.65, PETN1.5, PETN1.77, and HMX were modelled to study the effects of explosives on the cutting performance.

Proof firings were conducted for Sn-Zn-Bi sheathed cords against aluminium and acrylic materials to verify the development, with stand-off distances of 0 mm.

### 8.2 Performance Simulations

#### 8.2.1 Geometrical Setup

Numerical simulations were carried out using Ansys 19.0 AUTODYN 2D. The geometrical setup is illustrated in Figure 8.1. The model comprised the explosive core, sheath material, target, and surrounding air. As the entire elements in the model have the characteristics of axial and planar symmetry, a two-dimensional model was preferably used in the simulations for improving computational efficiency. The cords had an outer diameter of 2.0mm and an inner diameter of 1.2mm. Both targets were 5.0mm in thickness.

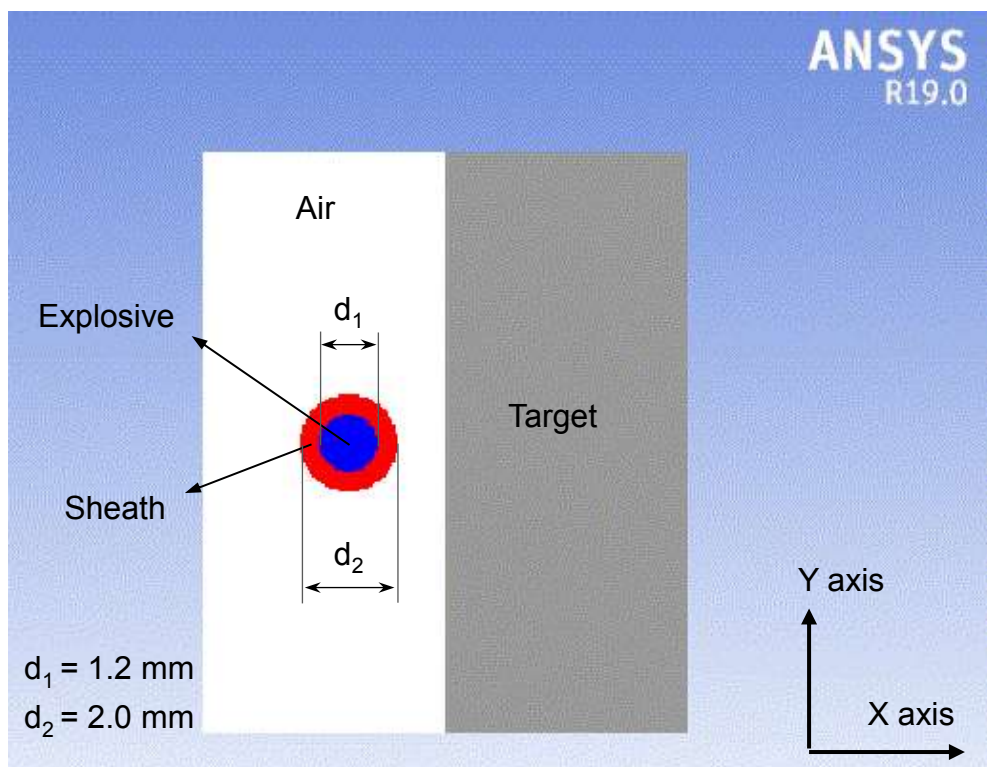


Figure 8.1 The geometrical model showing the configuration and dimension of different exponents simulated using Ansys 19.0 AUTODYN 2D.

### 8.2.2 Material Models and Parameters

The material models including the equation of state, constitutive or strength model and failure model are incorporated in Table 8.1. The respective material models will be interpreted in the following paragraphs.

Table 8.1 Material models including equation of state (EOS), strength/constitutive model, and failure model.

Component	EOS	Strength model	Failure model
Air	Ideal Gas	None	None
Explosive	JWL	None	None
Sheath	Shock	None	None
Target	Shock	Johnson-Cook or von Mises	None

## Explosive

The Jones-Wilkins-Lee equation of state (JWL EOS [204]) was chosen to describe the detonation and explosion behaviours. The JWL EOS is able to describe the pressure, volume, and energy characteristics of gaseous products in the process of detonation, which is expressed as follows:

$$P = A \left(1 - \frac{\omega}{R_1 V}\right) e^{-R_1 V} + B \left(1 - \frac{\omega}{R_2 V}\right) e^{-R_2 V} + \frac{\omega e}{V} \quad (8.1)$$

where  $P$  is the detonation pressure,  $V = \rho/\rho_0$  is the relative volume,  $e$  is the specific energy, and  $A$ ,  $B$ ,  $R_1$ ,  $R_2$ , and  $\omega$  are empirically determined constants that are dependent on different explosives. Table 8.2 lists the JWL EOS coefficients of different explosives applied in the present simulations.

Table 8.2 Material parameters in Jones-Wilkins-Lee (JWL) equation for different explosives.

Parameters	HNS1.65	PETN1.5	PETN1.77	HMX
Reference density, $\rho$ (g/cm <sup>3</sup> )	1.65	1.5	1.77	1.891
Parameter $A$ (kPa)	$4.631 \times 10^8$	$6.253 \times 10^8$	$6.171 \times 10^8$	$7.783 \times 10^8$
Parameter $B$ (kPa)	$8.873 \times 10^6$	$2.329 \times 10^7$	$1.693 \times 10^7$	$7.071 \times 10^6$
Parameter $R_1$ (none)	4.55	5.25	4.4	4.2
Parameter $R_2$ (none)	1.35	1.6	1.2	1.0
Parameter $\omega$ (none)	$3.5 \times 10^{-1}$	$2.8 \times 10^{-1}$	$2.5 \times 10^{-1}$	$3.0 \times 10^{-1}$
C-J Energy/ unit volume (kJ/cm <sup>3</sup> )	$7.45 \times 10^6$	$8.56 \times 10^6$	$1.01 \times 10^7$	$1.05 \times 10^7$
C-J Detonation velocity (m/s)	$7.03 \times 10^3$	$7.45 \times 10^3$	$8.3 \times 10^3$	$9.11 \times 10^3$
C-J Pressure (kPa)	$2.15 \times 10^7$	$2.2 \times 10^7$	$3.35 \times 10^7$	$4.2 \times 10^7$

## Air

The equation of state for air was considered as ideal gas, which is shown as follows:

$$P = \rho(\gamma - 1)e \quad (8.2)$$

$$\gamma = C_p/C_v \quad (8.3)$$

$$e = C_v T \quad (8.4)$$

Where  $P$ ,  $\rho$ ,  $\gamma$  is the pressure, density, and polytropic index, respectively.  $C_p$  and  $C_v$  are the specific heat at constant pressure and specific heat at constant volume.  $T$  is the temperature, and  $e$  is the specific energy of air. The internal energy of air at room temperature and ambient pressure is  $2.068 \times 10^5$  kJ kg<sup>-1</sup>. The specific parameters of air are shown in Table 8.3.

Table 8.3 Material properties of air extracted from the material database in Ansys AUTODYN.

$\rho$ (g/cm <sup>3</sup> )	$T$ (K)	$C_v$ (J/kg K)	$C_p$ (J/kg K)	$\gamma$ ( $C_p/C_v$ )
$1.225 \times 10^{-3}$	$2.882 \times 10^2$	$7.176 \times 10^2$	$1.005 \times 10^3$	1.400

## Sheath

The metallic sheaths were modelled as different materials, incorporating Al, Cu, Ta, Sn, Pb, Sn-Cu, and Sn-Zn-Bi alloys. With high impact pressure and great blast force resulting from explosive detonation, the sheath undergoes extremely high strain rates, it was thus modelled using the shock equation of state [205], following the equation:

$$U_s = C_0 + S U_p \quad (8.5)$$

Where  $U_s$  and  $U_p$  is the shock and particle velocity, respectively.  $C_0$  is the bulk sound speed of the material,  $S$  is the material constant that represents the slope of  $U_s$ - $U_p$  relationship. Values of  $C_0$  and  $S$  often tabulated in open literature. Based on the pioneering work conducted at Los Alamos National Laboratory on shock Hugoniot, the tabulation of shock parameters for numerous metals and relative number of alloys can be obtained in the LASL Shock Hugoniot Data Handbook [206]. For some specific alloys, parameter  $C_0$  and  $S$  cannot be collected directly in the literatures, however, there is a simple procedure that is based on the interpolation of  $C_0$  and  $S$  values in the shock EOS by mass averaging:

$$C_0 = \sum m_i C_{0i} \quad (8.6)$$

$$S = \sum m_i S_i \quad (8.7)$$

$$\text{and } \rho = \sum m_i \rho_i \quad (8.8)$$

Where  $m_i$  is the mass proportion of the element  $i$  in the specific alloy. In this approach, the values of parameter  $C_0$  and  $S$  for tin alloys including Sn-Cu and Sn-Zn-Bi can be calculated from the value of  $C_0$  and  $S$  of Sn, Cu, Zn, and Bi metals. It is noted that no strength model or constitutive model was applied to sheath materials due to the constantly large strain and strain rate of sheaths caused by high explosive detonation. The material models for different sheath materials used in the simulations are listed in Table 8.4.

Table 8.4 The material models for different sheaths.

Materials	EOS	Strength model	$\rho$ (g/cm <sup>3</sup> )	Gruneisen coefficient	$C_0$ (m/s)	$S$	Ref. $T$ (K)
Ta	shock	none	16.654	1.6	3414.0	1.201	300
Pb	shock	none	11.352	2.77	2051.0	1.640	300
Pb-5Sb	shock	none	11.181	1.94	2047.6	1.470	300
Cu	shock	none	8.931	1.99	3940.0	1.489	300
Al	shock	none	2.785	2.00	5328.0	1.338	300
Sn	shock	none	7.287	1.26	2608.0	1.486	300
Sn-0.3Cu	shock	none	7.292	1.97	2612.0	1.486	300
Sn-0.5Cu	shock	none	7.295	1.97	2614.7	1.486	300
Sn-0.7Cu	shock	none	7.299	1.97	2617.3	1.486	300
Sn-1.0Cu	shock	none	7.303	1.97	2621.3	1.486	300
Sn-0.2Zn-0.5Bi	shock	none	7.299	1.97	2604.9	1.486	300
Sn-1Zn-1Bi	shock	none	7.311	1.97	2604.2	1.487	300
Sn-1Zn-5Bi	shock	none	7.413	1.97	2572.9	1.486	300
Sn-3Zn-5Bi	shock	none	7.410	1.98	2580.8	1.488	300

## Target

The targets including Al7039 and acrylic were modelled using shock EOS, due to high strain rates introduced by the high velocity of exploded segments of the cords. Besides, strength models were applied to the targets. The Johnson-Cook strength model (J-C model) [207] that shows very good advantages in describing the strain rate effect of metallic materials was applied to Al7039 targets. The J-C model are shown as follows:

$$\sigma_y = (A + B\varepsilon_p^n) (1 + C \ln \dot{\varepsilon}^*) (1 + T^{*m}) \quad (8.9)$$

Where  $\sigma_y$  presents the yield stress,  $A$ ,  $B$ ,  $C$ ,  $n$ , and  $m$  are the Johnson-Cook material coefficients.  $\varepsilon_p$  is the equivalent plastic strain,  $\dot{\varepsilon}^*$  is the equivalent strain rate, and  $T^{*m}$  is the reduced temperature.

Table 8.5 Material models and parameters for Al7039 and acrylic (PMMA) targets

Target material	Al7039	PMMA
Equation of state	Shock	Shock
Reference density (g/cm <sup>3</sup> )	2.77	1.186
Gruneisen coefficient (none)	2.00	0.97
Parameter C <sub>0</sub> (m/s)	5.328×10 <sup>3</sup>	2.598×10 <sup>3</sup>
Parameter S (none)	1.338	1.516
Reference temperature (K)	3.00×10 <sup>2</sup>	293
Specific heat (J/kg K <sup>-1</sup> )	8.75×10 <sup>2</sup>	1.45×10 <sup>3</sup>
Strength model	Johnson-Cook	von Mises
Shear modulus (kPa)	2.76×10 <sup>7</sup>	1.7×10 <sup>6</sup>
Yield stress (kPa)	3.37×10 <sup>5</sup>	1.9×10 <sup>5</sup>
Hardening constant (kPa)	3.43×10 <sup>5</sup>	-
Hardening exponent (none)	4.1×10 <sup>-1</sup>	-
Strain rate constant (none)	1.0×10 <sup>-2</sup>	-
Failure model	None	None

A simple elastic-perfectly plastic model was used as the strength model for acrylic targets. This model requires a shear modulus and a yield stress which is the value that the material yields from being elastic into being plastic. The shear modulus can be found from the open literature. The yield stress was found by performing a parameter study in which various simulations were performed using various values of yield stress until the cut depth obtained matched the trial data that CEUK supplied. CEUK provided cut depth data from a JF17 detonating cord on a solid acrylic target. The average cut depth was 2.23mm. In the end, a value for yield stress of  $1.9 \times 10^5$  kPa matched the trial data. The material models and parameters for Al7039 and acrylic targets are listed in Table 8.5.

### *8.2.3 Solvers and Boundary Conditions*

Ansys AUTODYN provides various solvers for nonlinear problems. Lagrange and Euler solvers were adopted in the present numerical simulations. As is well known, the Lagrange element formulation solver utilizes a mesh that moves and distorts with the material it models as results of forces from neighbouring elements. This is a very efficient solution methodology for solid with accurate pressure history definition. However, if there is too much deformation of any elements, Lagrange solver results in a very slowly advancing solution and is usually terminated because the smallest dimension of an element causes a time step that is below the threshold level. Euler solver allows materials to flow from cell to cell, while the mesh is spatially fixed. And this is typically suitable for representing fluids and gases.

In the present model, the explosive, sheath, and air were meshed as Euler part to deal with great deformation, while the target was meshed as Lagrange part for fracture and fragmentation. The Euler and Lagrange interaction was also implemented to consider the interaction between fluid (explosive and air) and structures (sheath and target). This coupling technique allows complex fluid-structure interaction problems that include deformation of the structure to be solved in a single numerical analysis.

The flow-out boundary was applied for the Euler boundary to eliminate the influence of the boundary effect. A boundary condition of 'X velocity=0 and Y velocity =0' was applied to clamp the top, bottom, and right of the target, as shown in Figure 8.2. The contact between the Lagrange mesh and the Euler mesh was defined as automatic, and the initiation mode was centre point initiation. A gauge point was applied to record the displacement variation of the indent of the target surface as a function of detonation time. The exploding and cutting histories of the cords towards the target was observed.

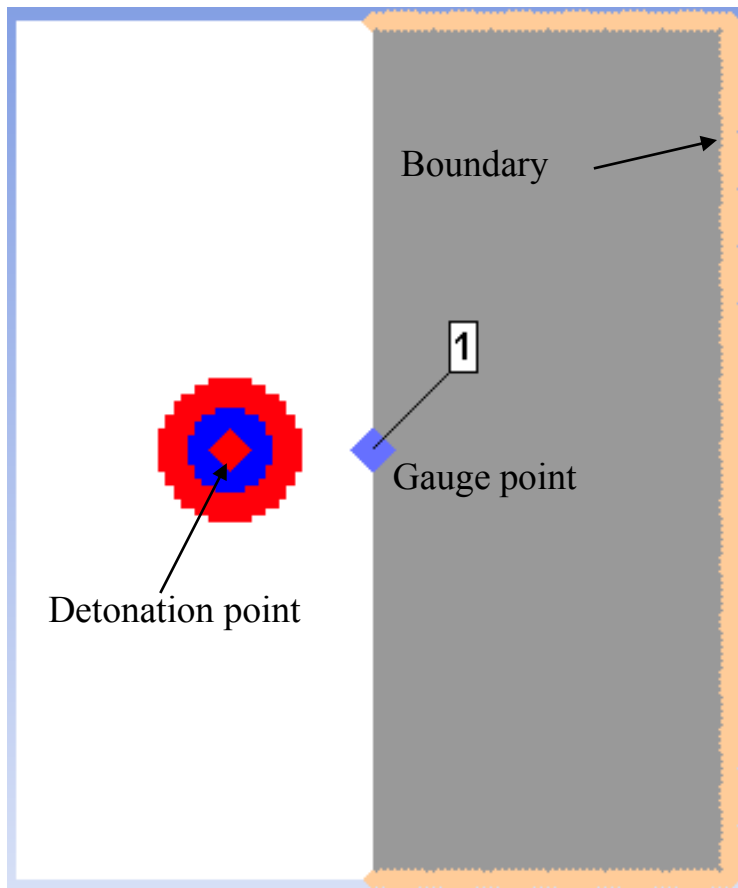


Figure 8.2 Geometrical model showing the detonation point, Gauge point, and Lagrange (the target part) boundary.

## 8.2.4 Simulation Results

### 8.2.4.1 Effects of Mesh Length on Cut Depths

The square meshes with the mesh lengths of 0.2, 0.1, and 0.05 mm were selected for both Eulerian part and Lagrangian part. Figure 8.3 shows the relation between the cut depth and detonation time for Sn sheathed miniature detonating cord against the Al7039 target. Once detonation, under explosive shock the sheath started to shatter towards the target in a short time interval of 0-0.001ms, followed by the interaction between shattering sheath and target. The displacement of gauge points increased sharply during a period of 0.001 to 0.003ms, reaching to the peak value of 0.2527, 0.1607, and 0.1598 mm for different meshes with the mesh length of 0.2, 0.1, and 0.05 mm, respectively. Then, the penetration terminated after the peak, as indicated by the plateaus of cut depths. The cutting process was captured at detonation times of  $0.5 \times 10^{-3}$ ,  $1.7 \times 10^{-3}$ ,  $3.3 \times 10^{-3}$ , and  $6.0 \times 10^{-3}$  ms, as shown in Figure 8.4.

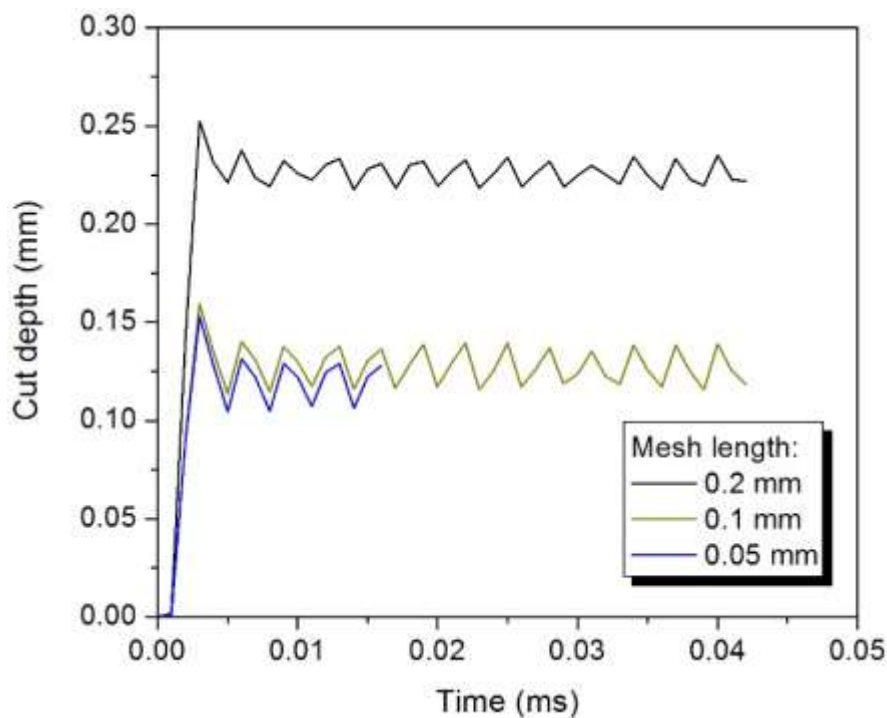


Figure 8.3 Variation of the cut depth with detonation time for the Sn sheathed miniature detonating cord against Al7039 targets, modelled under different meshes with mesh lengths of 0.2, 0.1, and 0.05 mm.

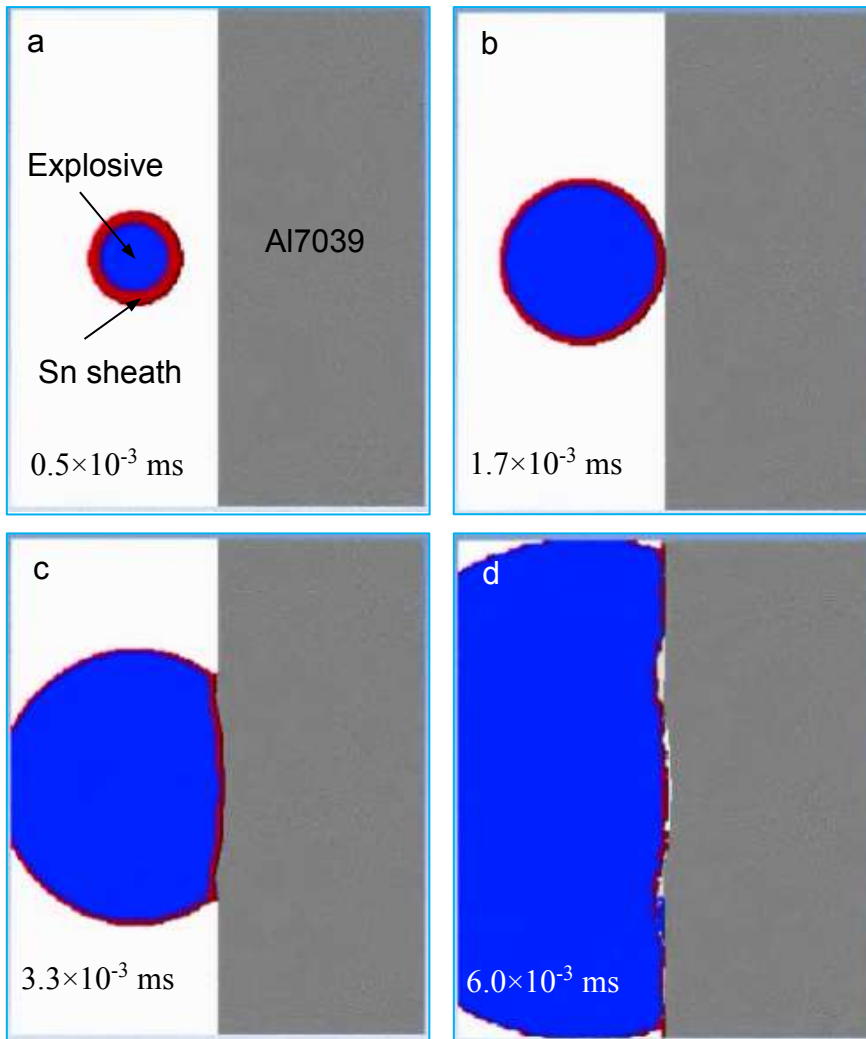


Figure 8.4 Cutting performance of Sn sheathed miniature detonating cords against the Al7039 target, captured at different detonation times: (a)  $0.5 \times 10^{-3}$  ms, (b)  $1.7 \times 10^{-3}$  ms, (c)  $3.3 \times 10^{-3}$  ms, and (d)  $6.0 \times 10^{-3}$  ms.

Figure 8.5 shows the cut depth as a function of detonation time for Pb sheathed miniature detonating cords against the Al7039 target. Similarly, the cutting process terminated quickly in a short time period of 0 to 0.003ms, and reaching at plateaus soon. In comparison with Sn sheathed cords, the Pb sheathed cords in general provided larger values of cut depths. The maximum displacement was regarded as the maximum cut depth, which was 0.319, 0.1920, and 0.1914 mm for Pb sheathed cords under the mesh length of 0.2, 0.1, and 0.05 mm, respectively.

Table 8.6 compares the cut depths of the cords sheathed by Sn and Pb, towards Al7093 targets under the three mesh schemes. It is obvious that the cut depths for both Sn and Pb sheathed cords converge to a stable value of approximately 0.16 and 0.19 mm as the mesh length

decreased from 0.2 mm to 0.05 mm. This indicates relative mesh sensitivity of cut depths. In theory, it is reasonable to decrease mesh size as small as possible to attain more accurate simulated results. However, according to the simulation results obtained from different mesh sizes it is appropriate to set the mesh size to be 0.1 mm for computation, which could improve the computational efficiency, without losing computing accuracy.

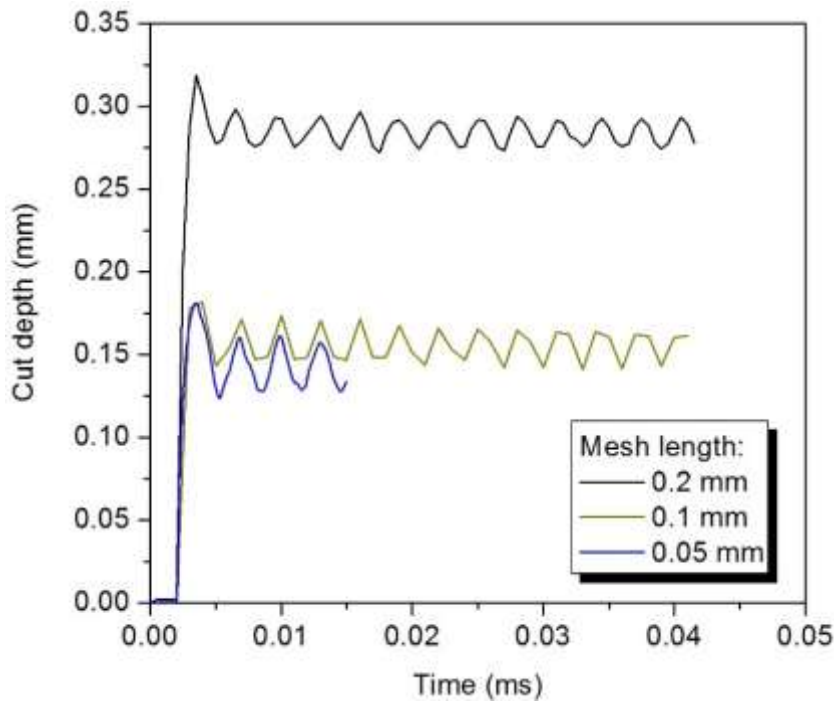


Figure 8.5 Variation of the cut depth with detonation time for the Pb sheathed miniature detonating cord against Al7039 targets, modelled under different meshes with the mesh lengths of 0.2, 0.1, and 0.05 mm.

Table 8.6 The cut depth of Sn and Pb sheathed miniature detonating cords loaded with HNS1.65, against the Al7039 targets, simulated with different mesh lengths.

Sheath material	Mesh length (mm)	Cut depth (mm)
Sn	0.2	0.2527
	0.1	0.1607
	0.05	0.1598
Pb	0.2	0.3190
	0.1	0.1920
	0.05	0.1914

### 8.2.4.2 Effects of Explosives on Cut Depths

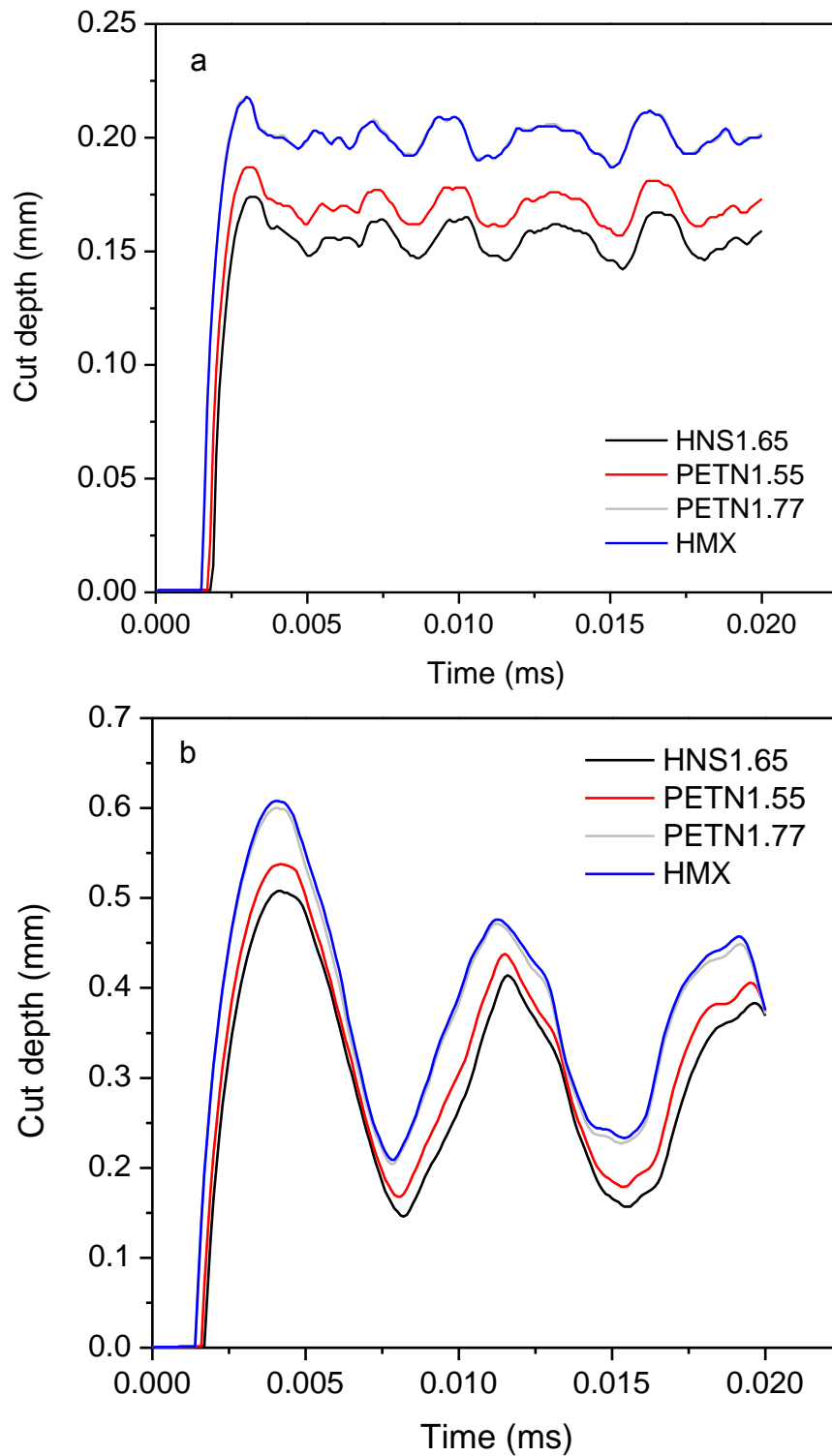


Figure 8.6 Variation of the cut depth with detonation time for the Sn sheathed miniature detonating cords loaded with different explosives, against (a) Al7039 target and (b) acrylic target. The stand-off distance is 1.0 mm.

Figure 8.6 shows the variation of cut depths as a function of detonation time for the Sn sheathed MDCs against Al7039 and acrylic targets. The cords were loaded with different explosives. The stand-off distances were fixed at the same value of 1.0 mm. For Al7039 targets, the gauge displacement first maintained at 0 mm within a short time period of 0 to 0.002ms and then increased dramatically to the pick values. Afterwards, the curve fluctuated at relatively stable statuses, as shown in Figure 8.6a. The maximum cut depth was measured to be 0.1742, 0.1868, 0.2175, and 0.0.2178 mm for the cords loaded with HNS1.65, PTEN1.5, PTEN1.77, and HMX, respectively. In the case of acrylic targets, the displacements of the gauge points experienced large fluctuations after arriving at pick values, as shown in Figure 8.6b. This is because the strength model that was applied to acrylic materials was different from that of Al7039 materials. The respective maximum cut depths for the cords loaded with HNS1.65, PTEN1.5, PTEN1.77, and HMX were 0.5079, 0.5368, 0.5999, and 0.6087 mm.

The simulated results from the cords against both Al7039 and acrylic targets suggested that the cut depths of cords with different explosives increased in the order of HNS1.65 < HNS1.65 < PTEN1.5 < PTEN1.77 < HMX. This was in line with the variation trend of the detonation energy and detonation pressure of explosive materials, which increased in the sequence of HNS1.65 < HNS1.65 < PTEN1.5 < PTEN1.77 < HMX, as indicated in Table 8.2. Based on this, it is indicated that the explosive core with higher detonation energy and pressure results in larger cut depths, ascribed to the increased kinetic energy of the sheath attained from the increased explosive energy.

#### **8.2.4.3 Effects of Stand-off Distance on Cut Depths**

Figure 8.7 shows the variation of cut depths as a function of detonation time for the Sn sheathed MDCs against the Al7039 targets. The cords were loaded with HNS1.65. The respective stand-off distances were 0, 0.5, 1.0, and 3.0 mm. After detonation, the sheath expanded and shattered towards the targets. Different times were taken for the shattered sheath to arrive at targets due to differences of stand-offs. Once occurrence of interaction between the sheath and the target, gauge displacements increased significantly and reached to the pick values in a very short time interval. Then, the curves fluctuated and the penetration terminated. The maximum cut depth was measured to be 0.2613, 0.1969, 0.1736, and 0.1316 mm, corresponding to the stand-off distance of 0, 0.5, 1.0, and 3.0 mm, respectively.

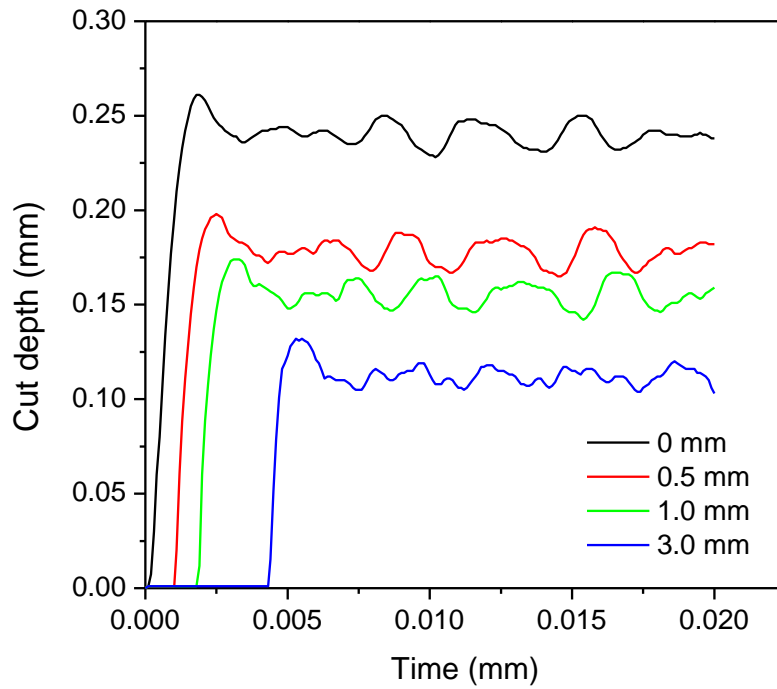


Figure 8.7 The variations of cut depths as a function of detonation time for the Sn sheathed miniature detonating cords loaded with HNS1.65, against the Al7039 targets under different stand-off distances of 0, 0.5, 1.0, and 3.0mm.

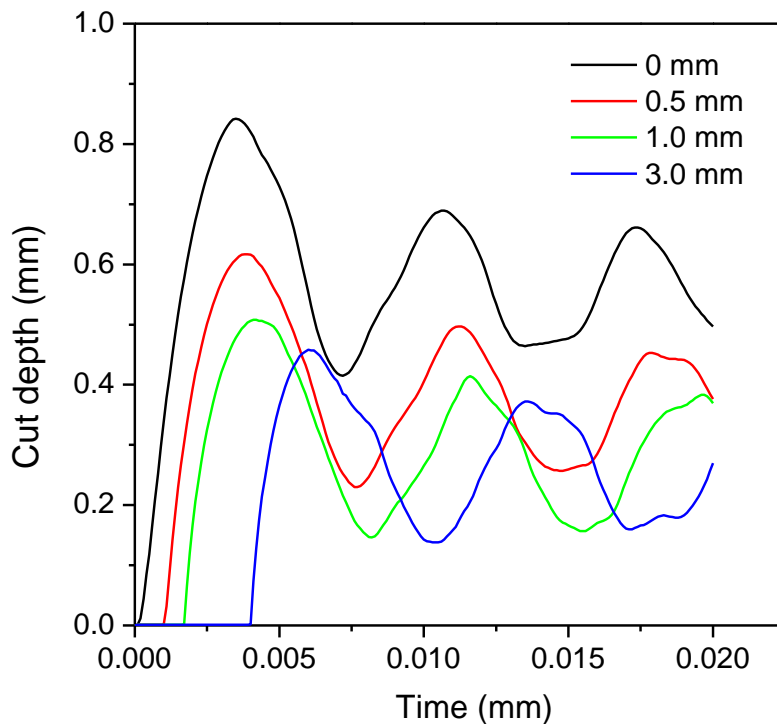


Figure 8.8 The variations of cut depths as a function of detonation time for the Sn sheathed miniature detonating cords loaded with different explosives, against the acrylic targets under different stand-off distances of 0, 0.5, 1.0, and 3.0 mm.

Figure 8.8 shows the variation of cut depths with detonation time for the Sn sheathed MDCs against the acrylic targets. The cords were loaded with HNS1.65 and simulated at the stand-offs of 0, 0.5, 1.0, and 3.0 mm. Still, the fluctuation of the curves after maximum cut depths were much more obvious in comparison with the Al7039 targets. The respective maximum cut depths for these with stand-off distances of 0, 0.5, 1.0, and 3.0 mm were 0.8411, 0.6182, 0.5064, and 0.4573 mm, indicating that the lower stand-off causes the higher cut depth.

#### 8.2.4.4 Effects of Sheath Materials on Cut Depths

Figure 8.9 and Figure 8.10 compares the cut depths as a function of detonation time for different miniature detonating cords against the Al7039 and acrylic target, respectively. Varied sheath materials including Al, Cu, Ta, Pb, Pb-5Sb, Sn, Sn-0.5Cu, Sn-0.2Zn-0.5Bi, and Sn-3Zn-5Bi were applied. These cords were loaded with the same explosive of HNS1.65 and at the same stand-off of 1.0 mm. It is observed that different sheaths led to different cut depths. For both Al7039 and acrylic targets, the cords sheathed by Sn or Sn-based alloys resulted in similar cut depths and presented similar displacement-time curves. The detailed cut depths for different cords and associated alloy densities are listed in Table 8.7.

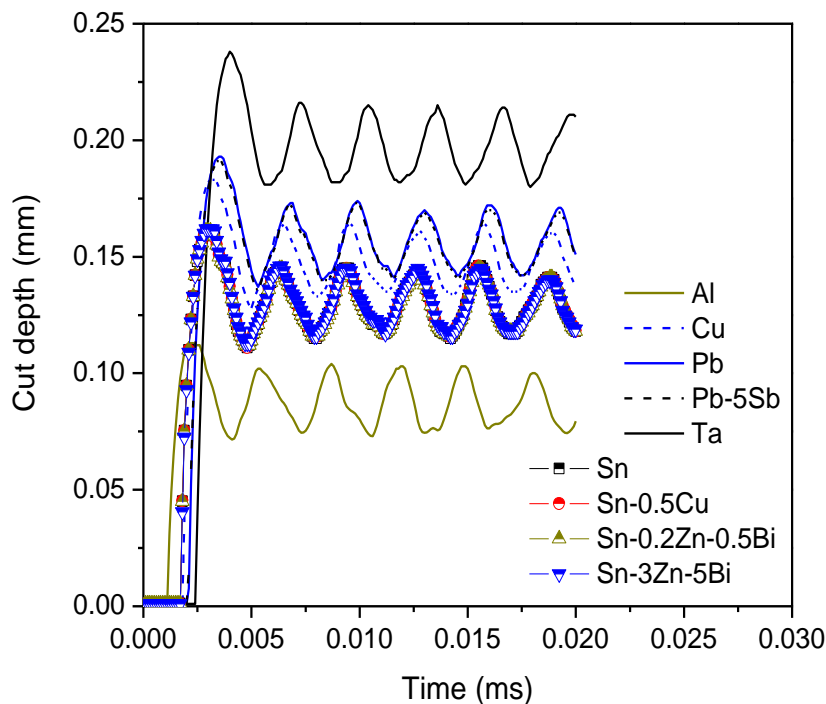


Figure 8.9 The variations of cut depths as a function of detonation time for the miniature detonating cords with different sheaths, against the Al7039 targets. The explosive core was HNS1.65 and the stand-off distance was 1.0 mm.

Inspection on the cutting performance of the cords against the Al7039 targets, the cord sheathed with Al processed smallest cut depth of 0.12 mm and the cord sheathed with Ta displayed largest cut depth of 0.24 mm. Accordingly, Al and Ta processed the lowest and highest density among the studied materials, with values of 2.785 and 16.654 g/cm<sup>3</sup>. Cu, Pb-5Sb, and Pb possessed similar values of density in the range of 8.9-11.2 g/cm<sup>3</sup>, displaying the cut depths at similar levels of 0.1838, 0.1911, 0.1920 mm, respectively. The Sn-based alloys including Sn, Sn-Cu and Sn-Zn-Bi alloys had similar cut depths, approximately 0.16 mm, which were slightly lower in comparison with currently used antimonial or non-antimonial lead cords.

In the meantime, a similar variation trend of cut depths for the cords against acrylic materials was perceived. From Table 8.7, the cord sheathed by lightest Al processed lowest cut depth of 0.37 mm, while the heaviest Ta sheathed cord displayed largest cut depth of approximately 0.74 mm. The Cu, Pb, and Pb-5Sb sheathed cords presented smaller cut depths of 0.58-0.60 mm, and the newly developed Sn-based cords displayed the cut depth of 0.50 mm.

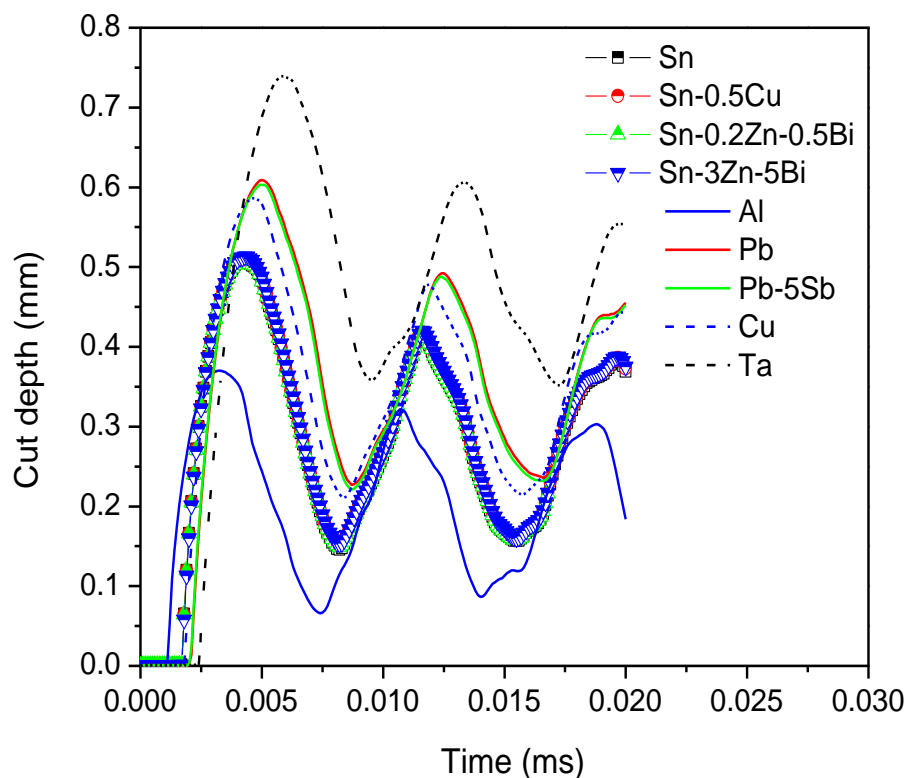


Figure 8.10 The variations of cut depths with time for the miniature detonating cords with different sheaths, against acrylic target. The explosive core is HNS1.65 and the stand-off distance was 1.0 mm.

Therefore, according to the performance simulations conducted on various cords, it is indicated that the cords with higher-density sheath can pose a higher cut depth. This is due to the larger momentum introduced by heavier sheath material. The respective maximum cut depths of Sn-based alloys against Al7039 and acrylic materials were 0.16 and 0.50 mm, which was comparable to that obtained from Pb based alloys (0.19 and 0.61 mm for Al7039 and acrylic target, respectively). Note that for the Sn-Zn-Bi alloys, the concentration of Zn and Bi appeared to have no significant influences on cutting performance, evidenced by the same cut depths of Sn-0.2Zn-0.5Bi and Sn-3Zn-5Bi.

Table 8.7 The cut depth of miniature detonating cords with different sheath materials, against Al7039 and acrylic targets. The explosives were HNS1.65 and the stand-offs were 1.0 mm.

Sheath material	Density (g/cm <sup>3</sup> )	Cut depth (mm)	
		Al7039	Acrylic-PMMA
Sn	7.287	0.1607	0.5074
Sn-0.3Cu	7.292	0.1607	0.5079
Sn-0.5Cu	7.295	0.1609	0.5081
Sn-0.7Cu	7.299	0.1611	0.5083
Sn-1.0Cu	7.303	0.1612	0.5086
Sn-0.2Zn-0.5Bi	7.300	0.1614	0.5085
Sn-3Zn-5Bi	7.410	0.1623	0.5133
Al	2.785	0.1133	0.3691
Cu	8.932	0.1838	0.5862
Pb	11.344	0.1920	0.6082
Pb-5Sb	11.181	0.1911	0.6044
Ta	16.654	0.2373	0.7396

One may notice that data in Table 8.7 shows the cut depth was similar for all Sn based alloys irrespective of alloying additions, and they may argue using pure Sn is quite straightforward for the specific application. Although the cut depth results may not prove the difference

introduced by the alloying elements, the added alloying elements such as Cu, Zn, Bi could certainly provide additional benefit. When the cord is in service in aircraft, it will bear loading, sometimes even cyclic loading. The relatively high mechanical strength is desired to ensure good resistance of external loadings and thus to improve the cord lifetime. In this aspect, addition of alloying elements to the tin base becomes highly desirable. For example, with higher Cu contents, the Sn-Cu alloys displayed higher strength (Chapter 4). In addition, as discussed in Chapter 6, Bi alloying elements turned out to have a positive effect on the mechanical properties, particularly ductility, which means that the alloying elements very likely improve the ease of processing of the cords. Besides, in Chapter 7, Zn and Bi were found to significantly affect the corrosion performance of the Sn-Zn based alloys. Higher Bi addition was found beneficial to corrosion resistance of Sn-3Zn alloys. On the other hand, alloying elements can influence the microstructural evolution when the alloy was under straining, therefore, result in different microstructure features and mechanical behaviours during processing. This was evidenced in Chapter 5 and 6, in which Sn-Zn-Bi alloy exhibited more homogenous microstructure subject to rolling, in comparison with Sn-Cu alloys. All gives the idea that the alloying elements will matter to the cords, from manufacturing to performance.

### 8.3 Proof Tests

The last stage in determining if the newly developed lead-free Sn-Zn-Bi alloys are the suitable lead replacements is to proof live miniature detonating cords sheathed by the Sn-Zn-Bi alloys. Inert and live MDCs were successfully manufactured by CEUK, using the existing manufacturing facilities located at CEUK. Both round and chevron profiled live MDCs were proofed against their current lead MDC proof target, and against a cast acrylic block and witness aluminium plate to allow for validation of MDC performance simulations.

One lot of Sn-Zn-Bi round MDC and one lot of Sn-Zn-Bi chevron MDC were manufactured using the current cord manufacturing processes as defined by CEUK Manufacturing Operating Instructions (now shown here), with the only difference being that Sn-Zn-Bi tubes were used instead of the standard antimonial lead tubes. The proof firings are detailed in Table 8.8, These were all conducted at ambient temperature. The round and chevron Sn-Zn-Bi MDC is denoted as R\_SZB-MDC and C\_SZB-MDC, respectively.

Table 8.8 Proof firings of Sn-Zn-Bi miniature detonating cords.

Proof firing	MDC	Target plate	Witness plate
#1	R_SZB-MDC	10mm thick cast acrylic plate	0.5mm thick Al plate
#2	R_SZB-MDC	Cast acrylic block	0.5mm thick Al plate
#3	C_SZB-MDC	10×0.5mm thick Al plate	0.5mm thick Al plate
#4	C_SZB-MDC	Cast acrylic block	0.5mm thick Al plate

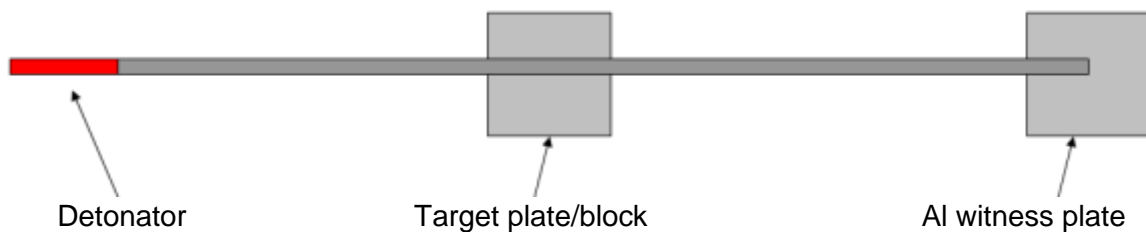


Figure 8.11 Setup of the miniature detonating cord attached to the target plate/block, with an Al witness plate bonded at the end of the cord.

Figure 8.11 shows the configuration of the four proof firings. The live MDC was stretched and bonded at the surface of the target plate or block. One end of the MDC was connected to the detonator, another end of the MDC was attached onto the aluminium witness plate to identify if the detonation could successfully propagate along the full length of the cord. Figure 8.12 shows the proof setup of a live R\_SZB-MDC attached to a 10mm thick cast acrylic plate, with an aluminium witness plate placed under the end of the cord.

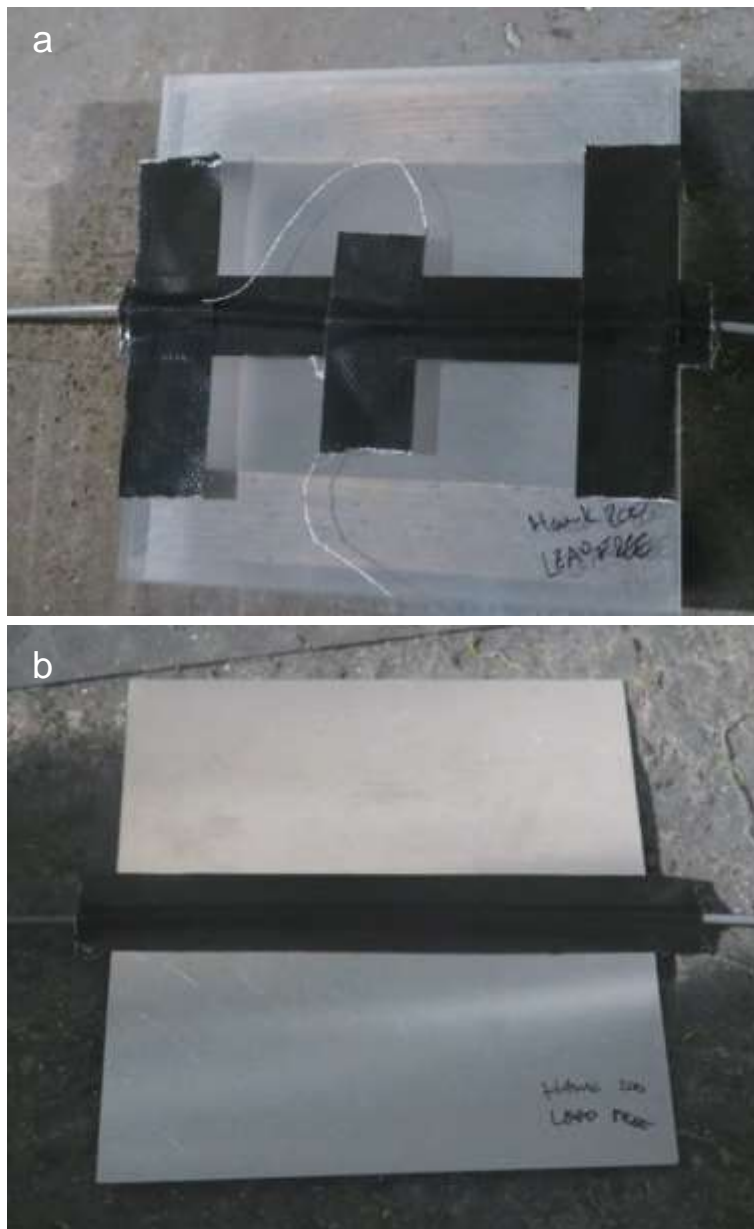


Figure 8.12 Proof setup of the R\_SZB-MDC bonded to (a) the 10mm thick cast acrylic plate and (b) aluminium witness plate.

Figure 8.13 presents the photos of the results from proofing of the Sn-Zn-Bi sheathed round MDC against its standard proof target of 10mm thick cast acrylic plate (proof firing #1). It is seen that the 10mm thick cast acrylic plate was successfully defeated (Figure 8.13a). Figure 8.13b is the aluminium witness plate that was placed under the end of the cord, showing that detonation successfully propagated throughout the full length of the cord.

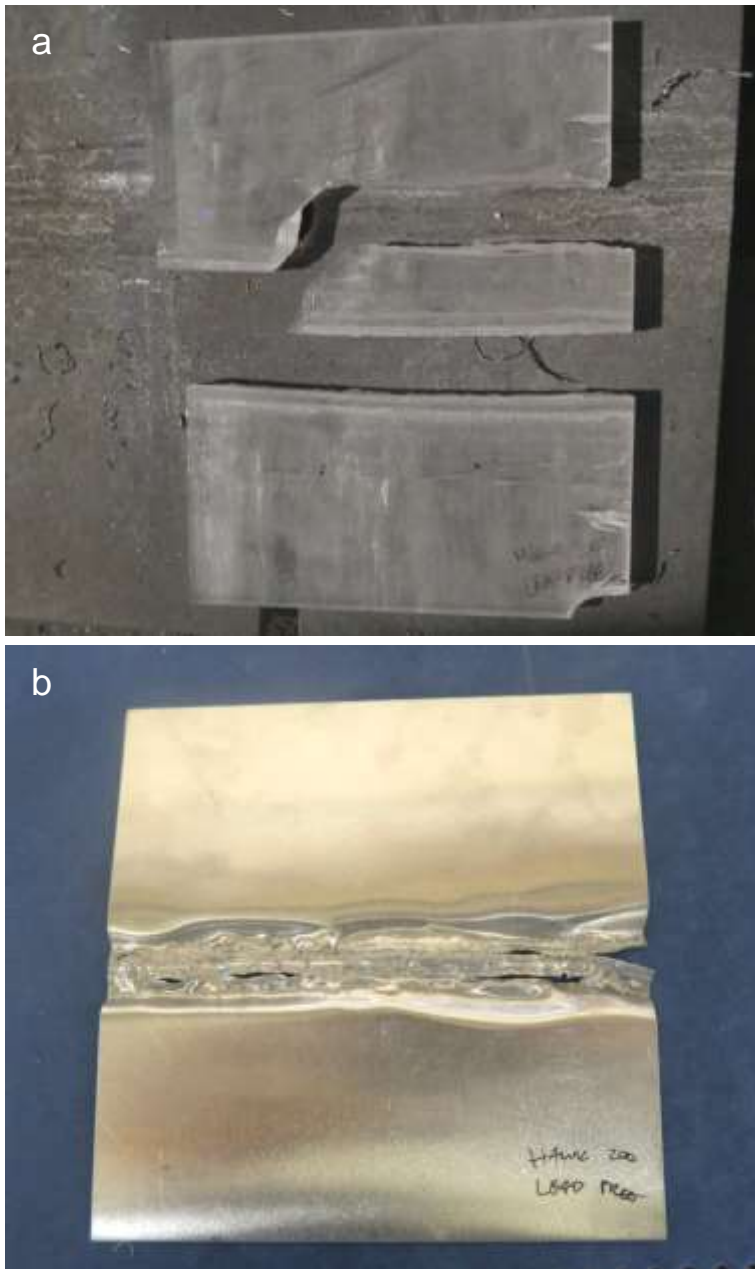


Figure 8.13 Proof results of the R\_SZB-MDC cutting against (a) 10 mm thick cast acrylic plate and (b) aluminium witness plate.

Figure 8.14 presents the photos of the results from proofing of the Sn-Zn-Bi sheathed round MDC against its standard proof target of a cast acrylic block (proof firing #2). It is seen that the cast acrylic block was not completely defeated, rather with an approximate cut depth of less than 1mm (Figure 8.14a). Figure 8.14b is the aluminium witness plate that was placed under the end of the cord, showing that detonation successfully propagated along the full length of the cord.

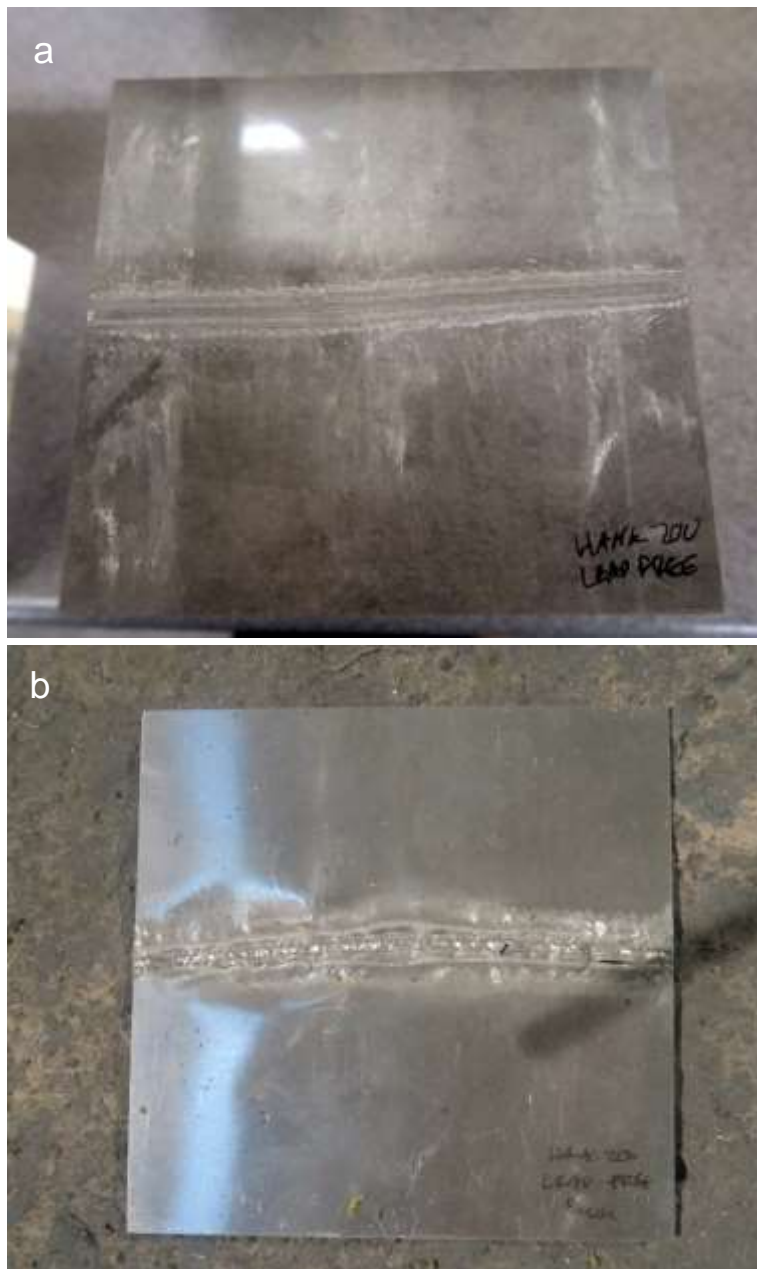


Figure 8.14 Proof results of the R\_SZB-MDC cutting against (a) the cast acrylic block and (b) aluminium witness plate.

Figure 8.15 presents the photos of the results from proofing of the Sn-Zn-Bi sheathed chevron MDC against its standard proof target of the stack of 10×0.5mm thick aluminium plate (proof firing #3). It is proved from Figure 8.15a that four of the ten plates were severed, which met the required number for the current antimonial lead chevron MDC, suggesting that it successfully defeated the target. Figure 8.15b is the aluminium witness plate that was placed under the end of the cord, showing that detonation successfully propagated along the full length of the cord and the cord completely defeated the aluminium witness plate.

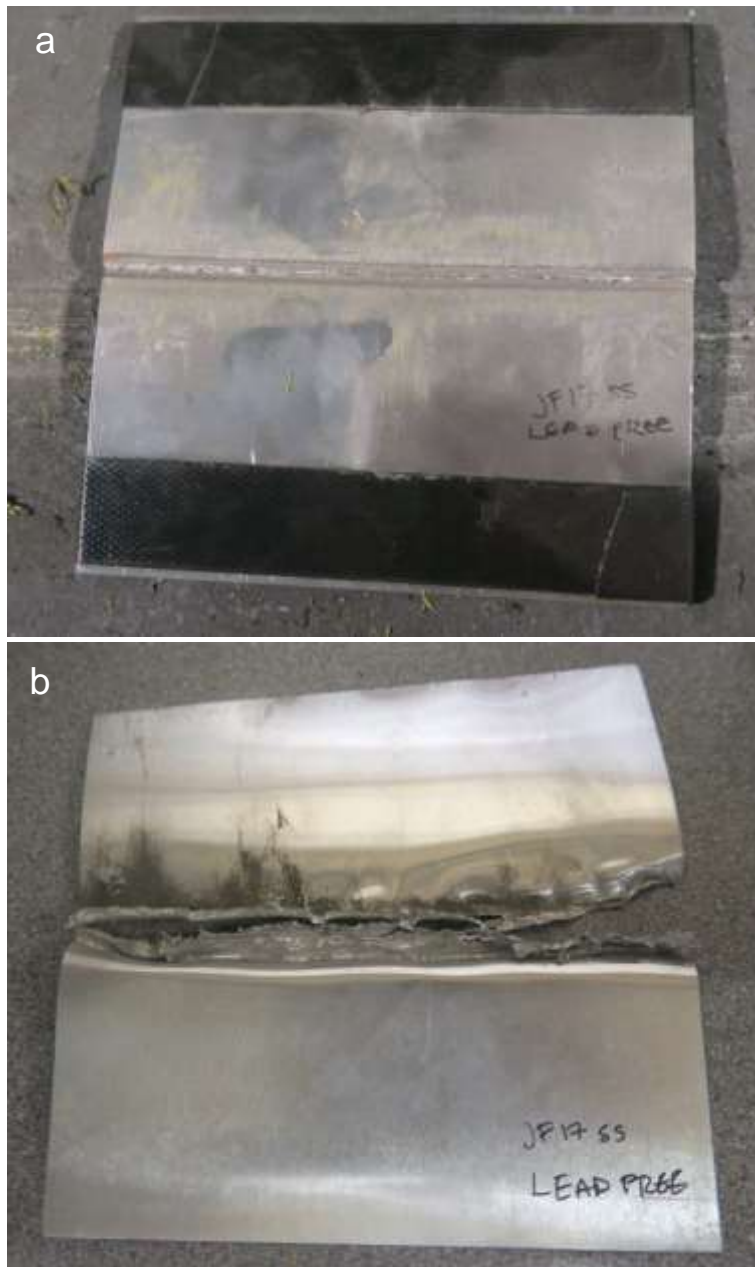


Figure 8.15 Proof results of the C\_SZB-MDC cutting against (a) the stack of 10×0.5mm Al plates and (b) aluminium witness plate.

Figure 8.16 presents the photos of the results from proofing of the Sn-Zn-Bi sheathed chevron MDC against its standard proof target of a cast acrylic block (proof firing #4). It is seen that the cast acrylic block was not completely defeated, with an approximate cut depth of less than 1mm (Figure 8.16a). Figure 8.16b is the aluminium witness plate that was placed under the end of the cord, showing that detonation successfully propagated along the full length of the cord the cord completely severed the aluminium witness plate.

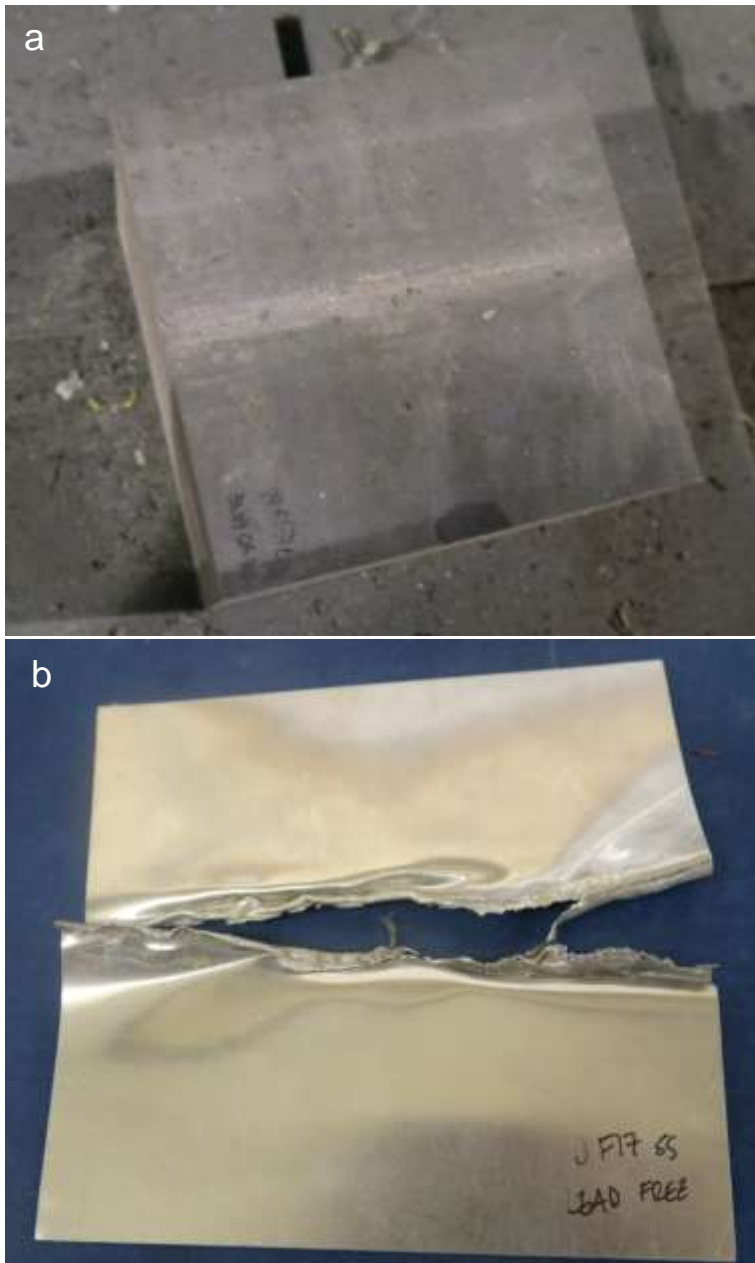


Figure 8.16 Proof results of the C\_SZB-MDC cutting against (a) cast acrylic block and (b) aluminium witness plate.

## 8.4 Summary

This chapter presents the performance simulations for MDCs sheathed by Pb, Pb-5Sb, Sn, and Sn alloys, combined with a relatively light metal sheath of Al, and a heavy metal sheath of Ta. Comparison of the cut depth between the potential lead replacement Sn-based alloys and the current Pb alloys was made. The simulation results showed that when against Al7039 target the Sn-Zn-Bi sheathed cords and Pb sheathed cords displayed close cut depth of 0.16mm (Sn-Zn-Bi alloys) and 0.19mm (lead alloys). Similarly, for acrylic targets the Sn-based cords and Pb-based cords also displayed comparable cut depths of 0.5mm and 0.6mm, respectively. The density difference of sheath materials was believed to be the main cause of the resulting differences in cut depths.

Two types of live MDCs with a round and chevron shape were proofed against different targets including cast acrylic and aluminium plates. The proof results confirmed that cast acrylic plates were successfully defeated for both round and chevron profiled MDCs. Besides, the number of severed aluminium plates met the required for the lead cords. The proof tests have verified that the Sn-Zn-Bi miniature detonating cords are the suitable lead replacements for the application, confirming success of the development.

## Chapter 9 Conclusions

Lead-free tin alloys used as miniature detonating cords in the aircraft canopy severance systems have been developed. Microstructural characteristics, mechanical properties, corrosion properties, and performance simulations for Sn-Cu, Sn-Zn, and Sn-Zn-Bi alloys with different compositions and different processes from casting to rolling have been studied. The main conclusions are drawn as follows:

- Microstructure of as-cast Sn-(0.3-1.0)wt.% Cu alloys consists of Sn solution phase and  $\text{Cu}_6\text{Sn}_5$  intermetallic phase. The rolling does not alter the phase constituent of alloys, but significantly refine the microstructure and enhance the mechanical properties. The rolled hypoeutectic Sn-(0.3-0.5)wt.% Cu alloys offer the yield strength from 26.1 to 31.9MPa, UTS from 30.1 to 34MPa and elongation from 86.4% to 87.5%, which is at a similar level of tensile properties in comparison with the antimonial lead alloys with the UTS from 17 to 27MPa and elongation from 76 to 90%. Sn-Cu alloys exhibit strain softening during tensile tests, which benefits the sheath manufacture and subsequent processing in rolling and drawing after assembly with high-energy explosive materials.
- The rolled Sn-0.5wt.%Cu alloy shows a manifest bimodal grain structure containing over 97% (frequency) of fine grains less than  $30\mu\text{m}$  and small portion of coarse grains in the range of  $50\text{-}150\mu\text{m}$ . DRX plays a crucial role in the deformation. Particle-stimulated nucleation (PSN) phenomenon by the  $\text{Cu}_6\text{Sn}_5$  particles/clusters are the dominant DRX mechanism. The boundary-induced nucleation is detected as another DRX mechanism, which is associated with continuous dynamic recrystallization (CDRX).  $\{301\}$  and  $\{101\}$  type twins are extensively observed as an effective deformation mechanism during rolling. The formation of  $\{301\}$  twin may be closely related to the orientation, which results from a specific orientation relation between the stress and the orientation of deformed grains. The fine DRX nuclei/grains display the  $\langle 001 \rangle // \text{RD}$  fibre texture, which is associated with the specific orientation relationship between the external stress and the  $\text{Cu}_6\text{Sn}_5/\beta\text{-Sn}$  interface. The  $\langle 001 \rangle // \text{RD}$  fibre texture in fine DRX nuclei is weakened and  $\langle 110 \rangle // \text{RD}$  fibre texture becomes strengthened with grain growth, which is ascribed to the growth advantages of specific orientation relationships.
- In Sn-3Zn-xBi (0-5wt.%Bi) alloys, Bi addition modifies the Sn-Zn eutectic morphology from well aligned Zn-rich needles to irregular coarse Zn-rich flakes and results in effective

microstructure refinement. Zn-rich phase, Bi precipitates, and Bi solutes are critical to dynamic recrystallization (DRX). This is because secondary phases on one hand provide more nucleation sites, on the other hand, offer relative obstacles to growth of new crystallized grains. Also, Bi solutes hinder motion of the new grain boundaries. Higher Bi content enhances the strength and elongation of the rolled Sn-Zn-Bi alloys. The Sn-3Zn-5Bi alloy achieved superior mechanical properties, with the UTS, yield strength, and elongation of 84.4MPa, 68.3MPa, and 75.2%, respectively, due to the most homogenous smallest equiaxed grains and the largest proportion of HAGBs.

- The corrosion resistance increases in the order of Sn-3Zn-1Bi, Sn-3Zn-3Bi, Sn-3Zn, Sn-3Zn-5Bi, Sn-3Zn-7Bi. The Zn-rich phase possessing the lowest corrosion potential among all phases serves as the anodic and thus is selectively and preferentially corroded, accompanied by the formation of major corrosion products,  $Zn_5(OH)_8Cl_2 \cdot H_2O$ . Bi addition (1-7 wt.%) can cause dramatic increases in the size of corrosion-vulnerable Zn-rich precipitates and lead to more uniform distribution of these precipitates. This is the reason that addition of 1 wt.% and 3 wt.% Bi increased the corrosion susceptibility of the Sn-3Zn alloy. In Bi-containing Sn-3Zn-*x*Bi alloys, the corrosion resistance is constantly increased with increasing the Bi contents from 1 wt.% to 7 wt.%, due to the enhanced barrier effect of Bi particles. When Bi concentration reaches 5 wt.% and 7 wt.%, the barrier effect of Bi phase can counteract the detrimental effect resulted from the coarsened Zn-rich precipitates, resulting in increased corrosion resistance of Sn-3Zn-5Bi and Sn-3Zn-7Bi in comparison with Sn-3Zn.
- The performance simulations for Al7039 target demonstrate that the tin alloys sheathed cords including pure Sn, Sn-Cu, and Sn-Zn-Bi display the cut depth of approximately 0.16 mm, at a similar level in comparison with the lead sheathed cords (0.19 mm). Similar cut depths against the acrylic target were obtained to be 0.5 and 0.6 mm for Sn-based cords and Pb-based cords. The density difference can be the main cause of the resulting difference in the cut depth. The proof firings confirm that cast acrylic plates have been successfully defeated for both round and chevron profiled Sn-Zn-Bi cords and the number of severed aluminium plates has met the required for the lead cords, confirming that the Sn-Zn-Bi miniature detonating cords are the successful lead replacements for the application.

## Chapter 10 Suggestions for Future Work

In the present study, Sn-Zn-Bi alloys present good mechanical properties, comparable corrosion resistance in comparison with the currently used antimonial lead, relatively homogeneous microstructure caused by rolling. The numerical simulations and proof tests prove the feasibility and reliability of the alloy for the sheath material of miniature detonating cords in the aircraft canopy severance systems. Whereas for better understanding the deformation mechanisms of Sn-Zn-Bi alloys during processing in the manufacturing, and for further assessment of potential lifespan in practical services, several further works may need to be addressed:

- (1) High TEM characterization on the microstructural evolution of Sn-Zn-Bi alloys under rolling, to provide more comprehensive understanding and offer detailed data information in theory for a reference on manufacturing process involving plastic deformation.
- (2) Fatigue measurements based on cyclic bending tests or tensile-compression tests may be carried out to assess the fatigue life, as the cords will serve under conditions that cyclic tensile and compression stresses are applied.

## References

- [1] F. Potts, "Aircrew escape systems". United States Patent 3778010, 1973.
- [2] 2012. [Online]. Available: <https://goo.gl/images/v5jJQ9>.
- [3] J. O'Brien and T. O'Brien, "Diode cutoff and safe packaging system for detonating cord". United State Patent 20080169213A1, 2008.
- [4] E. Kilmer, "Detonating cords loaded with hexanitrostilbene (HNS) recrystallized from acid or organic solvents," White oak laboratory, Silver spring, 1975.
- [5] C. Garrison and W. Southern, "Mild detonating cord confinement". United State Patent 4178853, 1979.
- [6] T. Rogers, "Flexible detonating cord". United State Patent 5223664, 1993.
- [7] G. Abrahamson and G. Huber, "Precision high velocity detonating cord," *Review of scientific instruments*, vol. 30, pp. 934-936, 1959.
- [8] J. Fritz, "Separation Joint Technology," in *39th AIAA/ASME/SAE/ASEE Joint Propulsion Conference*, Huntsville, 2003.
- [9] H. Hannagan, D. Lee and P. Posson, "Tin alloys sheathed explosive device". United State Patent 20040055495A1, 2004.
- [10] X. Bai, J. Liu, S. Li, C. Lv, W. Guo and T. Wu, "Effect of interaction mechanism between jet and target on penetration performance of shaped charge liner," *Materials Science and Engineering: A*, vol. 553, pp. 142-148, 2012.
- [11] R. Lee, M. Woodall, T. Barkley, D. Johnson and S. Kelly, "Detonating cord and methods of making and using the same". United State Patent 20100037793A1, 2010.
- [12] J. Rinehart and R. Cocanower, "Concerning the design of an effective shaped charge for oil well perforating," *Journal of applied physics*, vol. 30, pp. 680-682, 1959.
- [13] G. Norman and H. Siddeley, "Aircrew escape systems". United States Patent 3806069, 1974.
- [14] P. Persson, "Fuse". United State Patent 3590739, 1971.

- [15] J. Chalmers and F. McCaffrey, "Fuse igniting and connecting device". United States Patent 2587694, 1952.
- [16] J. Quail, *The Slow Burning Fuse: The Lost History of the British Anarchists*, Flamingo, 1978.
- [17] "Fuse (explosives)," Wikimedia Foundation Inc, 3 January 2018. [Online]. Available: [https://en.wikipedia.org/wiki/Fuse\\_\(explosives\)](https://en.wikipedia.org/wiki/Fuse_(explosives)).
- [18] [Online]. Available: <http://www.tracefireandsafety.com/VFRE-99/Recognition/Low/SF-Diagram-1.jpg>.
- [19] B. Martin, "Weatherproof safety fuse ingiter". United States Patent 4846067, 1989.
- [20] X. Wen, F. Lu, R. Chen and Y. Lin, "A Theoretical Analysis about the Driving Mechanism of Mild Detonating Fuse," *Propellants, Explosives, Pyrotechnics*, vol. 40, pp. 898-907, 2015.
- [21] L. Cao, Y. Lin, F. Lu, R.Chen and X. Wen, "Study on energy output efficiency of mild detonating fuse in cylinder tube structure," *Materials & Design*, vol. 92, pp. 690-700, 2016.
- [22] M. Schimmel, L. Bement, G. Dubrucq and E. Klein, "Fracture/Severance of Materials". United State Patent 5780763, 1998.
- [23] H. Qualls, "noncontamination linear explosive separation". United States Patent 3453960, 1969.
- [24] C. Garrison, "hydraulic severance shaped explosive". United States Patent 5170004, 1992.
- [25] D. Dadley and P. Haskins, "Linear cutting charge". United States Patent 4693181, 1987.
- [26] J. Smith, "Pyrotechnic shock: A literature survey of the Linear Shaped Charge (LSC)," United States, Huntsville, 1984.
- [27] J. Agrawal, *High energy materials: propellants, explosives and pyrotechnics*, John Wiley & Sons, 2010.
- [28] F. Gálvez, "Proceedings - 23rd International Symposium on Ballistics," in *International Symposium on Ballistics* , Madrid , 2007.
- [29] D. Leidel, "Apparatus for discharging a high speed jet to penetrate a target". United States Patent 5814758A, 1998.

- [30] M. Vigil, "Precision Linear Shaped Charge Analyses for Severance of Metals," Sandia National Laboratories, Albuquerque, 1996.
- [31] D. Vračarić, S. Terzić and D. ILIĆ, "Optimization of the Production Process, Characterization and Efficiency of a linear detonation shaped charge with a small linear mass of the explosive core," *Scientific Technical Review*, vol. 65, pp. 23-30, 2015.
- [32] H. Shekhar, "Theoretical modelling of shaped charges in the last two decades (1990-2010): A review," *Central European Journal of Energetic Materials*, vol. 9, pp. 155-185, 2012.
- [33] S. Rassokha, S. Ladov, G. Kubyshkina and A. Babkin, "Performance Calculation of Shaped Charges With Shear-Formed Liners," *Journal of applied mechanics*, vol. 80, pp. 1-6, 2013.
- [34] M. Liu, G. L, K. Lam and Z. Zong, "Meshfree particle simulation of the detonation process for high explosives in shaped charge unlined cavity configurations," *Shock Waves*, vol. 12, pp. 509-520, 2003.
- [35] A. Doig, "Some metallurgical aspects of shaped charge liners," *Journal of battlefield technology*, vol. 1, pp. 1-3, 1998.
- [36] G. Birkhoff, D. MacDougall, E. Pugh and S. Talor, "Explosive with lined cavities," *Journal of Applied Physics*, vol. 19, pp. 563-582, 1948.
- [37] M. Johnston and S. Lim, "Numerical Observation of the Jet Flight Patterns of Linear Shaped Charges," *Applied sciences*, vol. 2, pp. 629-640, 2012.
- [38] S. Lim, "Steady State Analytical Equation of Motion of Linear Shaped Charges Jet Based on the Modification of Birkhoff Theory," *Applied sciences*, vol. 2, pp. 35-45, 2012.
- [39] S. Lim, "Steady state equation of motion of a linear shaped charges liner," *International Journal of Impact Engineering*, vol. 44, pp. 10-16, 2012.
- [40] S. Lim, "The characteristics of blade formation/cutting process of LSCs," in *Proceeding of the 76th Shock and Vibration Symposium*, Destin, 2005.
- [41] S. Lim, "Jet velocity profile of linear shaped charges based on the arced liner," *Journal of Energetic Materials*, vol. 31, pp. 239-250, 2013a.
- [42] S. Lim, "Jet flight patterns of linear shaped charges," *Journal of energetic materials*, vol. 34, pp. 14-25, 2016.

- [43] M. Held, "Liners for shaped charges," *Journal of battlefield technology*, vol. 4, pp. 1-7, 2001.
- [44] W. Walters and J. Zukas, *Fundamentals of shaped charges*, New York: John Wiley & Sons, 1989.
- [45] D. Novotney and M. Mallery, "Historical development of linear shaped charge," in *43rd AIAA/ASME/SAE/ASEE Joint Propulsion Conference & Exhibit*, 2007.
- [46] O. Ayisit, "The Influence of Asymmetries in Shaped Charge Performance," *International journal of impact engineering*, vol. 35, pp. 1399-1404, 2008.
- [47] N. Nariman-Zadeh, A. Darvizeh, M. Darvizeh and H. Gharababaei, "Modelling of explosive cutting process of plates using GMDH-type neural network and singular value decomposition," *Journal of Materials Processing Technology*, vol. 128, pp. 80-87, 2002.
- [48] R. Gurney, "The initial velocity of fragments from bombs, shells and grenades," Army Ballistic Research Laboratory, 1943.
- [49] R. Barbour, *Pyrotechnics in industry*, New York: McGraw-Hill, 1981.
- [50] V. Bohanek, M. Dobrilović and V. Škrlec, "The efficiency of linear shaped charges," *Tehnički vjesnik*, vol. 21, pp. 525-531, 2014.
- [51] M. Mallery and T. Kozlowski, "Performance Analysis of Linear Shaped Charge for Aerospace Applications," in *41st AIAA/ASME/SAE/ASEE Joint Propulsion Conference & Exhibit*, 2005.
- [52] T. E. Rogers, "Flexible detonating cord". United State Patent 5223664, 1993.
- [53] C. Wendt, D. Betancourt, J. Loehr and J. Reese, "Sintered tungsten liners for shaped charges". United States Patent 6530326B1, 2003.
- [54] M. Held, "Hydrodynamic theory of shaped charge jet penetration," *Journal of explosive and propellants*, vol. 7, pp. 9-24, 1991.
- [55] W. Reese and T. Slagle, "Tungsten enhanced liner for a shaped charge". United States Patent 5656791, 1997.
- [56] T. Wang and H. Zhu, "Copper-Tungsten shaped charge liner and its jet," *Propellants, Explosives, yrotechnics*, Vols. 193-196, p. 21, 1996.
- [57] A. Werner and J. Rider, "Shaped charge liner including bismuth". United States Patent 5221808, 1993.

- [58] D. Brauer, F. Mandigo and D. Tyler, "A Copper alloys for shaped charge liners". United States Patent 5098487, 1992.
- [59] H. Shin, "Dynamic recrystallization in a tantalum shaped charge," *Scripta Metallurgica et Materialia*, vol. 29, pp. 1291-1296, 1993.
- [60] E. Baker, A. Daniels, G. Voorhis, T. Vuong and J. Pearson, "Development of molybdenum shaped charge liners," in *127th Annual Meeting and Exhibition of The Minerals, Metals & Materials Society*, 1998.
- [61] E. Baker, G. Voorhis, R. Campbell and C. Choi, "Development of molybdenum shaped charge liners producing high ductility jets," in *1993, 14th International Symposium on Ballistics*.
- [62] A. Schwartz, M. Kumar and D. Lassila, "Analysis of intergranular impurity concentration and the effects on the ductility of copper-shaped charge jets," *Metallurgical and Materials Transactions A*, vol. 35, pp. 2567-2573, 2004.
- [63] S. Saran, O. Ayisit and M. Yavuz, "Experimental investigations on aluminum shaped charge liners," *Procedia Engineering*, vol. 58, pp. 479-486, 2013.
- [64] M. Yavuz, R. Yıldırım and N. Serin, "Numerical and Experimental Investigation of Jet Formation and Particulation in Shaped Charges with Tulip-like Steel Liners," *Procedia Engineering*, vol. 58, pp. 608-616, 2013.
- [65] Z. Zhao, J. Liu and W. Guo, "Effect of Zn and Ni added in W-Cu alloy on penetration performance and penetration mechanism of shaped charge liner," *International Journal of Refractory Metals and Hard Materials*, vol. 54, pp. 90-97, 2016.
- [66] H. Han, W. Jiang and P. Zhang, "Application of metal powders to shaped charge liner," *Powder Metallurgy Industry*, vol. 3, pp. 1-4, 2004.
- [67] L. Murr and E. Esquivel, "Observations of common microstructural issues associated with dynamic deformation phenomena: Twins, microbands, grain size effects, shear bands, and dynamic recrystallization," *Journal of materials science*, vol. 39, pp. 1153-1168, 2004.
- [68] D. Pratt, D. Wesson and J. Rouse, "Shaped-charge liner". United States Patent 6354219, 2002.
- [69] W. Guo, S. Li and F. Wang, "Dynamic recrystallization of tungsten in a shaped charge liner," *Scripta Materialia*, vol. 60, pp. 329-332, 2009.

- [70] W. Humphrey and P. Gaines, "Penetration and cutting effects of lead-sheathed flexible linear shaped charges and explosive-filled linear shaped-charge containers," Defense Technical Information Center, 1978.
- [71] W. Tian, A. Fan, H. Gao, J. Luo and Z. Wang, "Comparison of microstructures in electroformed copper liners of shaped charges before and after plastic deformation at different strain rates," *Materials Science and Engineering: A*, vol. 350, pp. 160-167, 2003.
- [72] S. Lee, M. Hong, J. Noh and W. Baek, "Microstructural evolution of a shaped-charge liner and target materials during ballistic tests," *Metallurgical and Materials Transactions A*, vol. 33, pp. 1069-1074, 2002.
- [73] D. Blaskett and D. Boxall, *Lead and its alloys*, Chichester: Ellis Horwood Ltd, 1990.
- [74] R. Mahmudi, R. Roumina and B. Raeisinia, "Investigation of stress exponent in the power-law creep of Pb-Sb alloys," *Material Science and Engineering: A*, vol. 382, pp. 15-22, 2004.
- [75] R. Mahmudi, A. Geranmayeh and A. Razaee-Bazzaz, "Impression creep behavior of cast Pb-Sb alloys," *Journal of alloy and compounds*, vol. 427, pp. 124-129, 2007.
- [76] M. Mostafa, "Steady state creep characteristics of the eutectic Pb-Sb alloy," *Physica B: condensed matter*, vol. 349, pp. 56-61, 2004.
- [77] M. Sahota and J. Riddington, "Compressive creep properties of lead alloys," *Material & Design*, vol. 21, pp. 159-167, 2002.
- [78] M. Ashby, "Indentation creep," *Materials Science and Technology*, vol. 8, pp. 594-601, 1992.
- [79] A. Abd El-Khalek and R. Nada, "Effect of structure transformation on the stress-strain characteristics of Pb-3wt% Sb and Pb-3 wt% Sb-1 wt% Sn alloys," *Physica B: Condensed Matter*, vol. 328, pp. 393-398, 2003.
- [80] N. Loizou and R. Sims, "The yield stress of pure lead in compression," *Journal of the Mechanics and Physics of Solids*, vol. 1, pp. 234-243, 1953.
- [81] H. Ye, S. Xue, J. Luo and Y. Li, "Properties and interfacial microstructure of Sn-Zn-Ga solder joint with rare earth Pr addition," *Materials & Design*, vol. 46, pp. 826-823, 2013.
- [82] X. Zhu, K. Kotadia, S. Xu, H. Lu, S. Mannan, C. Bailey and Y. Chan, "Electromigration in Sn-Ag solder thin films under high current density," *Thin Solid Films*, vol. 565, pp. 193-201, 2014.

- [83] W. Osório, J. Spinelli, C. Afonso, L. Peixoto and A. Garcia, "Microstructure, corrosion behaviour and microhardness of a directionally solidified Sn–Cu solder alloy," *Electrochimica Acta*, vol. 56, pp. 8891-8899, 2011.
- [84] K. Moon, W. Boettinger, U. Kattner, F. Biancaniello and C. Handwerker, "Experimental and thermodynamic assessment of Sn–Ag–Cu solder alloys," *Journal of Electronic Materials*, vol. 29, pp. 1122-1136, 2000.
- [85] A. El-Daly, A. F. A. Hammad and D. Nasrallah, "Microstructure, mechanical properties, and deformation behavior of Sn–1.0Ag–0.5Cu solder after Ni and Sb additions," *Materials and Design*, vol. 43, pp. 40-49, 2013.
- [86] J. Graham, "Reactive products having tin and tin alloy liners and sheaths". United States Patent 5827995A, 1998.
- [87] S. Rodney and L. Barr, "Tin alloy sheath material for explosive-pyrotechnic linear products". United States Patent 5333550, 1994.
- [88] Y. Huang, J. Li, J. Liu, H. Su, W. Wang and N. Huang, "Non-lead metal material and application of non-lead metal material to cord type initiating explosive devices". China Patent 102560194A, 2012.
- [89] M. Held, "Particulation of shaped charge jets," in *11th international symposium on ballistics*, Brussels, 1989.
- [90] S. Lim, "Acceleration profile of a flat flyer driven by detonation isentrope," *Propellants, Explosives, Pyrotechnics*, vol. 38, pp. 410-418, 2013.
- [91] G. Noddin and N. Mantua, "Non-rupturing detonating cords". United States Patent 3311056, 1967.
- [92] F. Zhu, L. Zhao, G. Lu and Z. Wang, "Structural response and energy absorption of sandwich panels with an aluminium foam core under blast loading," *Advances in structural engineering*, vol. 11, pp. 525-536, 2008.
- [93] J. Spinelli and A. Garcia, "Microstructural development and mechanical properties of hypereutectic Sn–Cu solder alloys," *Materials Science and Engineering: A*, vol. 568, pp. 195-201, 2013.
- [94] J. Shen, Y. Liu and H. Gao, "Formation of bulk Cu<sub>6</sub>Sn<sub>5</sub> intermetallic compounds in Sn–Cu lead-free solders during solidification," *Journal of materials science*, vol. 42, pp. 5375-5380, 2007.

- [95] S. Seo, S. Kang, D. Shih and H. Lee, "The evolution of microstructure and microhardness of Sn-Ag and Sn-Cu solders during high temperature aging," *Microelectronics Reliability*, vol. 49, pp. 288-295, 2009.
- [96] T. Ventura, S. Terzi, M. Rappaz and A. Dahle, "Effects of solidification kinetics on microstructure formation in binary Sn-Cu solder alloys," *Acta Materialia*, vol. 59, pp. 1651-1658, 2011.
- [97] S. Seo, S. Kang, D. Shih and H. Lee, "An investigation of microstructure and microhardness of Sn-Cu and Sn-Ag solders as functions of alloy composition and cooling rate," *Journal of electronic materials*, vol. 38, pp. 257-265, 2009.
- [98] J. Hunt and K. Jackson, "Binary eutectic solidification," *Transactions of the Metallurgical Society of AIME*, vol. 236, pp. 843-852, 1966.
- [99] S. Seo, S. Kang, D. Shih and H. Lee, "The evolution of microstructure and microhardness of Sn-Ag and Sn-Cu solders during high temperature aging," *Microelectronics Reliability*, vol. 49, pp. 288-295, 2009.
- [100] S. Luo, W. Wang, Z. Xia and B. Wei, "Theoretical prediction and experimental observation for microstructural evolution of undercooled nickel-titanium eutectic type alloys," *Journal of Alloys and Compounds*, vol. 692, pp. 265-273, 2017.
- [101] W. Kurz and D. Fisher, "Dendrite growth in eutectic alloys: the coupled zone," *International Metals Reviews*, vol. 24, pp. 177-204, 1979.
- [102] A. Karma and A. Sarkissian, "Morphological instabilities of lamellar eutectics," *Metallurgical and Materials Transactions A*, vol. 27, pp. 635-656, 1996.
- [103] I. Moura, C. Silva, N. Cheung, P. Goulart, A. Garcia and J. Spinelli, "Cellular to dendritic transition during transient solidification of a eutectic Sn-0.7wt%Cu solder alloy," *Materials Chemistry and Physics*, vol. 132, pp. 203-209, 2012.
- [104] X. Hu, W. Chen and B. Wu, "Microstructure and tensile properties of Sn-1Cu lead-free solder alloy produced by directional solidification," *Materials Science and Engineering: A*, vol. 556, pp. 816-823, 2012.
- [105] A. El-Daly and A. Hammad, "Development of high strength Sn-0.7Cu solders with the addition of small amount of Ag and In," *Journal of Alloys and Compounds*, vol. 509, pp. 8554-8560, 2011.
- [106] L. Snugovsky, C. Cermignani, D. Perovic and J. Rutter, "The solid solubility of Ag and Cu in the Sn phase of eutectic and near-eutectic Sn-Ag-Cu solder alloys," *Journal of electronic materials*, vol. 33, pp. 1313-1315, 2004.

- [107] L. Snugovsky, P. Snugovsky, D. Perovic and J. Rutter, "Effect of cooling rate on microstructure of Ag-Cu-Sn solder alloys," *Materials science and technology*, vol. 21, pp. 61-68, 2005.
- [108] E. Hall, "The deformation and aging of mild steel: III discussion of results," *Proceedings of the Physical Society. Section B*, vol. 64, pp. 747-753, 1951.
- [109] N. Petch, "The cleavage strength of Polycrystals," *Journal of the Iron and Steel Institute*, vol. 174, pp. 25-28, 1953.
- [110] C. Yu, P. Sun, P. Kao and C. Chang, "Mechanical properties of submicron-grained aluminum," *Scripta Materialia*, vol. 52, pp. 359-363, 2005.
- [111] M. Haouaoui, I. Karaman, K. Harwig and H. Maier, "Microstructure evolution and mechanical behavior of bulk copper obtained by consolidation of micro- and nanopowders using equal channel angular extrusion," *Metallurgical and materials transactions A*, vol. 35, pp. 2935-2949, 2004.
- [112] D. Jia, K. Ramesh and E. Ma, "Effects of nanocrystalline and ultrafine grain sizes on constitutive behavior and shear bands in iron," *Acta materialia*, vol. 51, pp. 3495-3509, 2003.
- [113] Y. Li, W. Blum and F. Breuting, "Does nanocrystalline Cu deform by Coble creep near room temperature," *Materials Science and Engineering: A*, vol. 387, pp. 585-589, 2004.
- [114] H. Wilsdorf and D. Kuhlmann-Wilsdorf, "Work softening and Hall-Petch hardening in extruded mechanically alloyed alloys," *Materials Science and Engineering: A*, vol. 164, pp. 1-14, 1993.
- [115] S. Billard, J. Fondere, B. Bacroix and G. Dirras, "Macroscopic and microscopic aspects of the deformation and fracture mechanisms of ultrafine-grained aluminum processed by hot isostatic pressing," *Acta materialia*, vol. 54, pp. 411-421, 2006.
- [116] S. Hariprasad, S. Sastry and K. Jerina, "Deformation behavior of a rapidly solidified fine grained Al-8.5%Fe-1.2%V-1.7%Si alloy," *Acta materialia*, vol. 44, pp. 383-389, 1996.
- [117] F. Tang and J. Schoenung, "Strain softening in nanocrystalline or ultrafine-grained metals: A mechanistic explanation," *Materials Science and Engineering: A*, vol. 493, pp. 101-103, 2008.
- [118] M. Bhatia, I. Adlakha, G. Lu and K. Solanki, "Generalized stacking fault energies and slip in  $\beta$ -tin," *Scripta Materialia*, vol. 123, pp. 21-25, 2016.

- [119] Y. Kinoshita and N. Ohno, “Energetics of slip deformation in beta-Sn: A first-principles study,” *Key Engineering Materials*, vol. 626, pp. 46-49, 2015.
- [120] T. Sakai, A. Belyakov, R. Kaibyshev, H. Miura and J. Jonas, “Dynamic and post-dynamic recrystallization under hot, cold and severe plastic deformation conditions,” *Progress in Materials Science*, vol. 60, pp. 130-207, 2014.
- [121] P. Berbon, M. Furukawa, Z. Horita, M. Nemoto and T. Langdon, “Influence of pressing speed on microstructural development in equal-channel angular pressing,” *Metallurgical and Materials Transactions A*, vol. 30, pp. 1989-1997, 1999.
- [122] G. Liu, S. Ji, L. Grechcini, A. Bentley and Z. Fan, “Microstructure and mechanical properties of Sn-Cu alloys for detonating and explosive cords,” *Journal of materials science and technology*, vol. 33, pp. 1907-1918, 2017.
- [123] K. Ishii and H. Kihō, “Incorporation of slip dislocations in mechanical twins of tin crystals,” *Journal of the Physical Society of Japan*, vol. 18, pp. 1122-1132, 1963.
- [124] L. Lehman, Y. Xing, T. Bieler and E. Cotts, “Cyclic twin nucleation in tin-based solder alloys,” *Acta Materialia*, vol. 58, pp. 3546-3556, 2010.
- [125] C. Sellars, “Recrystallization of metals during hot deformation,” *Philosophical transactions of the royal society A*, vol. 288, pp. 147-158, 1978.
- [126] F. Haessner, *Recrystallization of metallic materials*, Dr. Riederer Verlag, GmbH Stuttgart, 1978.
- [127] H. McQueen and J. Jonas, “Recovery and Recrystallization during High Temperature Deformation,” *Treatise on Materials Science & Technology*, vol. 6, pp. 393-493, 1975.
- [128] S. Wright, M. Nowell and D. Field, “A review of strain analysis using electron backscatter diffraction,” *Microscopy and microanalysis*, vol. 17, pp. 316-329, 2011.
- [129] F. Humphreys and M. Hatherly, *Recrystallization and related annealing phenomena*, Elsevier, 2012.
- [130] P. Darbandi, T. Bieler, F. Pourboghrat and T. Lee, “Crystal plasticity finite-element analysis of deformation behaviour in multiple-grained lead-free solder joints,” *Journal of electronic materials*, vol. 42, pp. 201-214, 2013.
- [131] N. Brar and W. Tyson, “Elastic and plastic anisotropy of white tin,” *Canadian Journal of Physics*, vol. 50, pp. 2257-2264, 1972.

- [132] T. Bieler and A. Telang, "Analysis of slip behaviour in a single shear lap lead-free solder joint during simple shear at 25 C and 0.1/s," *Journal of electronic materials*, vol. 38, pp. 2694-2701, 2009.
- [133] F. Humphreys, "The nucleation of recrystallization at second phase particles in deformed aluminium," *Acta Metallurgica*, vol. 25, pp. 1323-1344, 1977.
- [134] R. Doherty, D. Hughes, F. Humphreys, J. Jonas, D. Jensen, M. Kassner, W. King, T. McNelley, H. McQueen and A. Rollet, "Current issues in recrystallization: a review," *Materials Science and Engineering: A*, vol. 238, pp. 219-274, 1997.
- [135] R. Shahani and T. Clyne, "Recrystallization in fibrous and particulate metal matrix composites," *Materials Science and Engineering: A*, vol. 135, pp. 281-285, 1991.
- [136] J. Robson, D. Henry and B. Davis, "Particle effects on recrystallization in magnesium-manganese alloys: particle-stimulated nucleation," *Acta Materialia*, vol. 57, pp. 2739-2747, 2009.
- [137] A. Wusatowska-Sarnek, H. Miura and T. Sakai, "Nucleation and microtexture development under dynamic recrystallization of copper," *Materials Science and Engineering: A*, vol. 323, pp. 177-186, 2002.
- [138] R. Eleti, T. Bhattacharjee, L. Zhao, P. Bhattacharjee and N. Tsuji, "Hot deformation behaviour of CoCrFeMnNi FCC high entropy alloy," *Materials Chemistry and Physics*, vol. 210, pp. 176-186, 2018.
- [139] A. Imandoust, C. Barrett, A. Oppedal, W. Whittington, Y. Paudel and H. El Kadiri, "Nucleation and preferential growth mechanism of recrystallization texture in high purity binary magnesium-rare earth alloys," *Acta Materialia*, vol. 138, pp. 27-41, 2017.
- [140] J. Bailey and P. Hirsch, "The recrystallization process in some polycrystalline metals," *Proceedings of the Royal Society A: Mathematical, Physical and Engineering Sciences*, vol. 267, pp. 11-30, 1962.
- [141] D. Ponge and G. Gottstein, "Necklace formation during dynamic recrystallization: mechanisms and impact on flow behaviour," *Acta Materialia*, vol. 46, pp. 69-80, 1998.
- [142] B. Shen, L. Deng and X. Wang, "A new dynamic recrystallisation model of an extruded Al-Cu-Li alloy during high-temperature deformation," *Materials Science and Engineering: A*, vol. 625, pp. 288-295, 2015.
- [143] R. Kaibyshev, K. Shipilova, F. Musin and Y. Motohashi, "Continuous dynamic recrystallization in an Al-Li-Mg-Sc alloy during equal-channel angular extrusion," *Materials Science and Engineering: A*, vol. 396, pp. 341-351, 2005.

- [144] K. Tsuzaki, X. Huang and T. Maki, "Mechanism of dynamic continuous recrystallization during superplastic deformation in a microduplex stainless steel," *Acta materialia*, vol. 44, pp. 4491-4499, 1996.
- [145] J. Christian and S. Mahajan, "Deformation twinning," *Progress in materials science*, vol. 39, pp. 1-157, 1995.
- [146] B. Chalmers, "The twinning of single crystals of tin," *Proceedings of the Physical Society*, vol. 47, pp. 733-746, 1935.
- [147] S. Maruyama, "Dynamic behaviour of twinning in tin crystals at various temperatures and strain rates," *Journal of the Physical Society of Japan*, vol. 15, pp. 1243-1251, 1960.
- [148] L. Lehman, Y. Xing, T. Bieler and E. Cotts, "Cyclic twin nucleation in tin-based solder alloys," *Acta Materialia*, vol. 58, pp. 3546-3556, 2010.
- [149] A. Wusatowska-Sarnek, M. H. and T. Sakai, "Nucleation and microtexture development under dynamic recrystallization of copper," *Materials Science and Engineering: A*, vol. 323, pp. 177-186, 2002.
- [150] F. Humphreys, "Particle stimulated nucleation of recrystallization at silica particles in nickel," *Scripta materialia*, vol. 43, pp. 591-596, 2000.
- [151] O. Engler, J. Hirsch and K. Lücke, "Texture development in Al-1.8 wt% Cu depending on the precipitation state-II. Recrystallization textures," *Acta metallurgica et materialia*, vol. 43, pp. 121-138, 1995.
- [152] M. Ferry and F. Humphreys, "The deformation and recrystallization of particle-containing {011} <100> aluminium crystals," *Acta materialia*, vol. 44, pp. 3089-3103, 1996.
- [153] M. Held, "Liners for shaped charges," *Journal of battlefield technology*, vol. 4, pp. 1-6, 2001.
- [154] M. Hammam, F. Allah, E. Gouda, Y. Gendy and H. Aziz, "Aziz, Structure and properties of Sn-9Zn lead-free solder alloy with heat treatment," *Engineering*, vol. 2, pp. 172-178, 2010.
- [155] X. Wei, H. Huang, L. Zhou, M. Zhang and X. Liu, "On the advantages of using a hypoeutectic Sn-Zn as lead-free solder material," *Materials letter*, vol. 61, pp. 655-658, 2007.
- [156] K. Suganuma, "Advances in lead-free electronics soldering," *Current Opinion in Solid State and Materials Science*, vol. 5, pp. 55-64, 2001.

- [157] K. Suganuma and K. Kim, Sn-Zn low temperature solder, Boston: Springer, 2006.
- [158] Y. Kim, K. Kim, C. Hwang and K. Suganuma, "Effect of composition and cooling rate on microstructure and tensile properties of Sn-Zn-Bi alloys," *Journal of alloys and compounds*, vol. 352, pp. 237-245, 2003.
- [159] A. El-Daly, H. Hashem, N. Radwan, F. El-Tantawy, T. Dalloul, N. Mansour, H. Abd-Elmoniem and E. Lotfy, "Robust effects of Bi doping on microstructure development and mechanical properties of hypoeutectic Sn-6.5 Zn solder alloy," *Journal of Materials Science: Materials in Electronics*, vol. 27, pp. 2950-2962, 2016.
- [160] J. Song and Z. Wu, "Variable eutectic temperature caused by inhomogeneous solute distribution in Sn-Zn system," *Scripta Materialia*, vol. 54, pp. 1479-1483, 2006.
- [161] L. Prasad and A. Mikula, "Role of surface properties on the wettability of Sn-Pb-Bi solder alloys," *Journal of alloys and compounds*, vol. 282, pp. 279-285, 1999.
- [162] Y. Kim, K. H. C. Kim and K. Suganuma, "Effect of composition and cooling rate on microstructure and tensile properties of Sn-Zn-Bi alloys," *Journal of alloys and compounds*, vol. 352, pp. 237-245, 2003.
- [163] J. Lendvai, H. Gudladt and V. Gerold, "The deformation-induced dissolution of  $\delta$ 1 precipitates in Al-Li alloys," *Scripta Materialia*, vol. 22, pp. 1755-1760, 1998.
- [164] C. Watanabe, R. Monzen and K. Tazaki, "Effects of Al<sub>3</sub>Sc particle size and precipitate free zones on fatigue behaviour and dislocation structure of an aged Al-Mg-Sc alloy," *International Journal of Fatigue*, vol. 30, pp. 635-641, 2008.
- [165] M. Song, K. Du, Z. Huang, H. Huang, Z. Nie and H. Ye, "Deformation-induced dissolution and growth of precipitates in an Al-Mg-Er alloy during high-cycle fatigue," *Acta Materialia*, vol. 81, pp. 409-419, 2014.
- [166] H. Mecking and G. Gottstein, "Recovery and recrystallization during deformation," *Recrystallization of Metallic Materials*, vol. 1, pp. 195-222, 1978.
- [167] F. Humphreys, "The nucleation of recrystallization at second phase particles in deformed aluminium," *Acta Metallurgica*, vol. 25, pp. 1323-1344, 1977.
- [168] R. Shahani and T. Clyne, "Recrystallization in fibrous and particulate metal matrix composites," *Materials Science and Engineering: A*, vol. 135, pp. 281-285, 1991.
- [169] U. Kattner, "Phase diagrams for lead-free solder alloys," *JOM*, vol. 54, pp. 44-51, 2002.
- [170] J. Cahn, "The impurity-drag effect in grain boundary motion," *Acta Metallurgica*, vol. 10, pp. 789-798, 1962.

- [171] K. Lücke and H. Stüwe, "On the theory of impurity controlled grain boundary motion," *Acta Metallurgica*, vol. 19, pp. 1087-1099, 1971.
- [172] M. Hillert and B. Sundman, "A treatment of the solute drag on moving grain boundaries and phase interfaces in binary alloys," *Acta Metallurgica*, vol. 24, pp. 731-743, 1976.
- [173] R. Gall and J. Jonas, "Solute drag effects during the dynamic recrystallization of nickel," *Acta Materialia*, vol. 47, pp. 4365-4374, 1999.
- [174] D. Cram, X. Fang, H. Zurob, Y. Bréchet and C. Hutchinson, "The effect of solute on discontinuous dynamic recrystallization," *Acta Materialia*, vol. 60, pp. 6390-6404, 2012.
- [175] Y. Kinoshita and N. Ohno, "Energetics of Slip Deformation in Beta-Sn: A First-Principles Study," *Key engineering materials*, vol. 626, pp. 46-49, 2015.
- [176] G. Ren and M. Collins, "The effects of antimony additions on microstructures, thermal and mechanical properties of Sn-8Zn-3Bi alloys," *Materials & Design*, vol. 119, pp. 133-140, 2017.
- [177] E. Hall, "The Deformation and Ageing of Mild Steel: III Discussion of Results," *Proceedings of the physical society. Section B*, vol. 64, pp. 747-753, 1951.
- [178] N. Petch, "The cleavage strength of polycrystals," *The journal of iron and steel institute*, vol. 174, pp. 25-28, 1953.
- [179] A. El-Daly, H. Hashem, N. Radwan, F. El-Tantawy, T. Dalloul, N. Mansour and E. Lotfy, "Robust effects of Bi doping on microstructure development and mechanical properties of hypoeutectic Sn-6.5 Zn solder alloy," *Journal of Materials Science: Materials in Electronics*, vol. 27, pp. 2950-2962, 2016.
- [180] G. Liu and S. Ji, "Effect of Bi on the microstructure and mechanical properties of Sn-Zn alloys processed by rolling," *Materials Characterization*, vol. 137, pp. 39-49, 2018.
- [181] A. Ahmido, S. El Hajjaji, B. Ouaki, A. Sabbar and S. Sebbahi, "Corrosion behavior of Sn-9Zn-xBi lead-free solder alloys in NaCl 3% solution," *Materials Science: An Indian Journal*, vol. 13, pp. 69-76, 2015.
- [182] A. Ahmido, A. Sabbar, H. Zouihri, K. Dakhsi, F. Guedira, M. Serghini-Idrissi and S. El Hajjaji, "Effect of bismuth and silver on the corrosion behaviour of Sn-9Zn alloy in NaCl 3 wt.% solution," *Materials Science and Engineering: B*, vol. 176, pp. 1032-1036, 2011.

- [183] U. Mohanty and K. Lin, "Potentiodynamic polarization measurement of Sn–8.5 Zn–XAl–0.5 Ga alloy in 3.5% NaCl solution," *Journal of the Electrochemical Society*, vol. 153, pp. B319-B324, 2006.
- [184] U. Mohanty and K. Lin, "Electrochemical corrosion behaviour of Pb-free Sn–8.5 Zn–0.05 Al–XGa and Sn–3Ag–0.5 Cu alloys in chloride containing aqueous solution," *Corrosion Science*, vol. 50, pp. 2437-2443, 2008.
- [185] S. Chung, J. Cheng, S. Chiou and H. Shin, "EIS behavior of anodized zinc in chloride environments," *Corrosion Science*, vol. 42, pp. 1249-1268, 2000.
- [186] S. Kapusta and N. Hackerman, "Anodic passivation of tin in slightly alkaline solutions," *Electrochimica Acta*, vol. 25, pp. 1625-1639, 1980.
- [187] D. Abayarathna, E. Hale, T. O'Keefe, Y. Wang and D. Radovic, "Effects of sample orientation on the corrosion of zinc in ammonium sulfate and sodium hydroxide solutions," *Corrosion science*, vol. 32, pp. 755-768, 1991.
- [188] E. McCafferty, "Validation of corrosion rates measured by the Tafel extrapolation method," *Corrosion Science*, vol. 47, pp. 3202-3215, 2005.
- [189] Z. Wang, C. Chen, J. Jiu, S. Nagao, M. Nogi, H. Koga and K. Suganuma, "Electrochemical behaviour of Zn-xSn high-temperature solder alloys in 0.5 M NaCl solution," *Journal of Alloys and Compounds*, vol. 716, pp. 231-239, 2017.
- [190] G. Brug, A. Van Den Eeden, M. Sluyters-Rehbach and J. Sluyters, "The analysis of electrode impedances complicated by the presence of a constant phase element," *Journal of electroanalytical chemistry and interfacial electrochemistry*, vol. 176, pp. 275-295, 1984.
- [191] M. Mori, K. Miura, T. Sasaki and T. Ohtsuka, "Corrosion of tin alloys in sulfuric and nitric acids," *Corrosion Science*, vol. 44, pp. 887-898, 2002.
- [192] J. Liu, Z. Wang, J. Xie, J. Ma, G. Zhang and K. Suganuma, "Understanding corrosion mechanism of Sn–Zn alloys in NaCl solution via corrosion products characterization," *Materials and Corrosion*, vol. 67, pp. 522-530, 2016.
- [193] Z. Wang, "Electrochemical behaviour of Zn-xSn high-temperature solder alloys in 0.5M NaCl solution," *Journal of alloys and compounds*, vol. 716, pp. 231-239, 2017.
- [194] T. Falk, J. Svensson and L. Johansson, "The Influence of CO<sub>2</sub> and NaCl on the Atmospheric Corrosion of Zinc A Laboratory Study," *Journal of the Electrochemical Society*, vol. 145, pp. 2993-2999, 1998.

- [195] L. Garcia, W. Osório, L. Peixoto and A. Garcia, “Mechanical properties of Sn–Zn lead-free solder alloys based on the microstructure array,” *Materials Characterization*, vol. 2010, pp. 212-220, 2010.
- [196] K. Prabhu and P. Deshapande, “Effect of cooling rate during solidification of Sn-9Zn lead-free solder alloy on its microstructure, tensile strength and ductile-brittle transition temperature,” *Materials Science and Engineering: A*, vol. 533, pp. 64-70, 2012.
- [197] J. Liu, G. Zhang, J. Ma and K. Suganuma, “Ti addition to enhance corrosion resistance of Sn–Zn solder alloy by tailoring microstructure,” *Journal of Alloys and Compounds*, vol. 644, pp. 113-118, 2015.
- [198] G. Song and A. Atrens, “Understanding magnesium corrosion—a framework for improved alloy performance,” *Advanced engineering materials*, vol. 5, pp. 837-858, 2003.
- [199] D. Li, P. Conway and C. Liu, “Corrosion characterization of tin–lead and lead free solders in 3.5 wt.% NaCl solution,” *Corrosion Science*, vol. 50, pp. 995-1004, 2008.
- [200] S. Kapusta and N. Hackerman, “odic passivation of tin in slightly alkaline solutions,” *Electrochimica Acta*, vol. 25, pp. 1625-1693, 1980.
- [201] G. Song, A. Atrens, X. Wu and B. Zhang, “Corrosion behaviour of AZ21, AZ501 and AZ91 in sodium chloride,” *Corrosion science*, vol. 40, pp. 1769-1791, 1998.
- [202] G. Song, A. Atrens and M. Dargusch, “Influence of microstructure on the corrosion of diecast AZ91D,” *Corrosion Science*, vol. 41, pp. 249-273, 1999.
- [203] W. Osório, L. Peixoto, P. Goulart and A. Garcia, “Electrochemical corrosion parameters of as-cast Al-Fe alloys in a NaCl solution, Corros. Sci. 52 (2010) 2979-2993.,” *Corrosion Science*, vol. 52, pp. 2979-2993, 2010.
- [204] E. Lee, H. Hornig and J. Kury, “Adiabatic expansion of high explosive detonation products,” Univ. of California Radiation Lab. at Livermore, Univ. of California Radiation Lab. at Livermore, 1968.
- [205] M. Meyers, *Dynamic behavior of materials*, New York: Wiley, 1994.
- [206] S. Marsh, *LASL Shock Hugoniot Data*, California: University of California, Berkeley, 1980.
- [207] G. Johnson and W. Cook, “A constitutive model and data for metals subjected to large strains, high strain rates and high temperatures,” in *Proceedings of the Seventh International Symposium on Ballistic*, The Hague, 1983.